ACS SYMPOSIUM SERIES 1123

Novel Solutions to Water Pollution

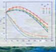

EDITED BY

Satinder Ahuja and Kiril Hristovski

Novel Solutions to Water Pollution

In Novel Solutions to Water Pollution; Ahuja, S., et al.;
ACS Symposium Series; American Chemical Society: Washington, DC, 2013.

ACS SYMPOSIUM SERIES **1123**

Novel Solutions to Water Pollution

Satinder Ahuja, Editor
Ahuja Consulting
Calabash, North Carolina

Kiril Hristovski, Editor
Arizona State University
Tempe, Arizona

Sponsored by the
ACS Division of Environmental Chemistry, Inc.

American Chemical Society, Washington, DC

Distributed in print by Oxford University Press

Downloaded by UNIV LIB UTRECHT on March 20, 2013 | http://pubs.acs.org
Publication Date (Web): March 18, 2013 | doi: 10.1021/bk-2013-1123.fw001

Library of Congress Cataloging-in-Publication Data

Novel solutions to water pollution / Satinder Ahuja, editor, Ahuja Consulting, Calabash, North Carolina, Kiril Hristovski, editor, Arizona State University, Tempe, Arizona ; sponsored by the ACS Division of Environmental Chemistry, Inc.
pages cm. -- (ACS symposium series ; 1123)
Includes bibliographical references and index.
ISBN 978-0-8412-2754-5 (alk. paper)
1. Water--Pollution--Congresses. I. Ahuja, Satinder, 1933, editor of compilation. II. Hristovski, Kiril, editor of compilation. III. American Chemical Society. Division of Environmental Chemistry.
TD419.5.N68 2013
628.1′68--dc23
2012049643

The paper used in this publication meets the minimum requirements of American National Standard for Information Sciences—Permanence of Paper for Printed Library Materials, ANSI Z39.48n1984.

Copyright © 2013 American Chemical Society

Distributed in print by Oxford University Press

All Rights Reserved. Reprographic copying beyond that permitted by Sections 107 or 108 of the U.S. Copyright Act is allowed for internal use only, provided that a per-chapter fee of $40.25 plus $0.75 per page is paid to the Copyright Clearance Center, Inc., 222 Rosewood Drive, Danvers, MA 01923, USA. Republication or reproduction for sale of pages in this book is permitted only under license from ACS. Direct these and other permission requests to ACS Copyright Office, Publications Division, 1155 16th Street, N.W., Washington, DC 20036.

The citation of trade names and/or names of manufacturers in this publication is not to be construed as an endorsement or as approval by ACS of the commercial products or services referenced herein; nor should the mere reference herein to any drawing, specification, chemical process, or other data be regarded as a license or as a conveyance of any right or permission to the holder, reader, or any other person or corporation, to manufacture, reproduce, use, or sell any patented invention or copyrighted work that may in any way be related thereto. Registered names, trademarks, etc., used in this publication, even without specific indication thereof, are not to be considered unprotected by law.

PRINTED IN THE UNITED STATES OF AMERICA

Foreword

The ACS Symposium Series was first published in 1974 to provide a mechanism for publishing symposia quickly in book form. The purpose of the series is to publish timely, comprehensive books developed from the ACS sponsored symposia based on current scientific research. Occasionally, books are developed from symposia sponsored by other organizations when the topic is of keen interest to the chemistry audience.

Before agreeing to publish a book, the proposed table of contents is reviewed for appropriate and comprehensive coverage and for interest to the audience. Some papers may be excluded to better focus the book; others may be added to provide comprehensiveness. When appropriate, overview or introductory chapters are added. Drafts of chapters are peer-reviewed prior to final acceptance or rejection, and manuscripts are prepared in camera-ready format.

As a rule, only original research papers and original review papers are included in the volumes. Verbatim reproductions of previous published papers are not accepted.

ACS Books Department

Preface

We are becoming increasingly aware of the overwhelming pollution of our limited water resources on this planet. And while many contaminants originate from Mother Earth, most water pollution comes as a direct result of anthropogenic activities. This problem has become so immense that it threatens the future of all humanity. If effective measures to reduce and/or remediate water pollution and its sources are not found, it is estimated by UN that 2.7 billion people will face water shortage by 2025 as opposed to 1.2 billion people who do not have access to clean drinking water now. Therefore, development of novel green technologies to address this major problem represents a priority of the highest importance. This book discusses green chemistry and other novel solutions to the water pollution problems which includes some interesting applications of nanoparticles.

Discussion in Chapter 1 is focused on an important problem relating to arsenic contamination of groundwater, which affects nearly 200 million people in various countries, including advanced countries like the United States. Two green chemistry solutions are offered to remediate this horrendous problem. Chapters 12 and 13 discuss some other novel solutions to the problem.

Advanced oxidation and reduction processes, which can be used successfully to remediate water contaminants through the creation of highly reactive radical species are discussed in Chapter 2. Similarly, Chapter 3 illustrates the capacity of ferrate(VI) ion to treat antibiotics in water through an environment-friendly process that could perform a dual function of oxidation and disinfection, forming a nontoxic by-product, iron(III).

A cost-effective and readily accessible woodchip bioreactor for treatment of nitrate-contaminated groundwater below the US EPA maximum contaminant level of 10 mg/L NO_3-N is described in Chapter 4. Two different applications of another novel technology are illustrated in Chapters 5 and 6. These chapters demonstrate the use of zero-valent iron nanoparticles for prevention of mercury methylation and efficient in situ dechlorination of chlorinated solvents in groundwater.

Utilization of inexpensive polycations, as noncovalent bridges that tether anionic surfactant micelles to porous media such as silica or sand, to treat toluene and dichloroethane contamination is discussed in Chapter 7. Oligomerization is a cost-effective way to improve performance of activated carbon for water treatment applications (see Chapter 8).

An innovative concept for removal of heavy metals from acidic solutions utilizes cyclic electrowinning/precipitation is described in Chapter 9. This unique process allows rapid reduction of contaminants and efficient processing of large volumes of contaminated solutions. Removal of two of the most important micronutrients, nitrogen and phosphorus from wasterwater to prevent eutrophication and produce fertilizers, is discussed in Chapter 10.

Feasibility of using a coating of one or two layers that serves as a barrier between the membrane and foulant to reduce membrane fouling is discussed in Chapter 11. Chapters 12 and 13 describe development of hybrid nanoparticle-containing media for simultaneous treatment of multiple contaminants from water. Chapter 12 focuses on synthesis of a hematite nanoparticle granular activated carbon for removal of arsenic and organic co-contaminants. Similarly, Chapter 13 describes the development of an inexpensive and easy-to-fabricate titanium dioxide–based hybrid ion-exchange media and assesses its potential to remove arsenic and nitrate from water.

An overview of applications of zero-valent iron for removing a wide array of contaminants—ranging from microorganisms and chlorinated organic compounds to disinfection by-products and their precursors—is provided in Chapter 14. Chapter 15 demonstrates an application of a full-scale hybrid sequencing batch membrane bioreactor serving 400 residential units and discusses the factors impacting the optimum performance of this system.

We believe that *Novel Solutions to Water Pollution* is a useful and informative text for those engaged in issues of water quality and water pollution remediation at operational, administrative, academic, or regulatory levels.

Satinder Ahuja

Kiril Hristovski

Chapter 1

Green Chemistry and Other Novel Solutions to Water Pollution: Overview

Satinder (Sut) Ahuja*

Ahuja Consulting, 1061 Rutledge Court, Calabash, North Carolina 28467
***E-mail: sutahuja@atmc.net**

To prevent water pollution, effective safety measures should be employed that prevent point-source and nonpoint-source pollution. Green chemistry solutions should be employed, where possible. An effective way to deal with the water pollution problem is to use the least harmful ways to eliminate contaminants. Chromatography and separation chemistry offer a variety of interesting approaches to achieve these goals. Interesting examples of remediation have been provided to help correct arsenic contamination of groundwater, which affects nearly 200 million people worldwide. A variety of novel methods have been included for prevention and remediation of water pollution that entail radical reaction and utilization of nanoparticles.

Introduction

Our drinking water comes from various sources such as rivers, lakes, wells, and natural springs. Unfortunately, these sources can be easily polluted by point and nonpoint source pollutants. Some of the point source problems can be traced to inadequate safety measures relating to production, utilization, and disposal of many inorganic and organic compounds. A number of contaminants also arise from frequently used materials and reactions: coal and oil combustion, gasoline combustion, detergents, disinfectants, drugs (including endocrine disruptors), fertilizers, herbicides, and pesticides. Many contaminants can arise from Mother Earth, e. g., manganese, radionuclides, and arsenic. An overwhelming majority of water-quality problems are caused by diffuse nonpoint sources of pollution that are more difficult to monitor effectively. For example, microbial contamination

In Novel Solutions to Water Pollution; Ahuja, S., et al.;
ACS Symposium Series; American Chemical Society: Washington, DC, 2013.

often results from contamination by animal and human waste that is due to poor sanitary practices. Because of these problems, an estimated 1.2 billion people in the world drink unclean water daily. This chapter will first discuss green chemistry solutions presented by the author at a symposium and then highlight the other presentations from the symposium in the form of an overview.

1. Green Chemistry Solutions

Green chemistry solutions need to be found to resolve water pollution problems. Primarily, these solutions should emphasize effective safety measures that prevent point source pollution. In addition, our vigilance to avoid nonpoint source pollution has to be significantly improved. Realistically, water pollution in modern society seems inevitable. An effective way to deal with pollution problems is to use the least harmful ways to eliminate contaminants (*1*, *2*).

The main objective of green chemistry is to promote research, development, and implementation of innovative chemical technologies that accomplish pollution prevention in a scientifically sound and cost-effective manner. Green chemistry solutions should emphasize effective safety measures that prevent point and nonpoint-source pollution. Listed below are some of the principles of green chemistry that can be applied to solving water pollution problems.

- **Minimize waste:** Ideally, no waste should remain that requires treatment or cleanup.
- **Use catalysts:** Use catalytic rather than stoichiometric reactions that use excess reagents, and work only once.
- **Use safe solvents:** Avoid using unsafe solvents, separation agents, or other auxiliary chemicals. Use innocuous chemicals if it is necessary.
- **Increase energy efficiency:** Run chemical reactions at ambient temperatures and pressures, when possible.
- **Design chemicals and products that degrade after use:** To prevent accumulation in the environment, design chemical products to break down to innocuous substances after use.
- **Analyze in real time:** Include in-process, real-time monitoring and control during syntheses to minimize or eliminate the formation of by-products.

Separation chemistry and chromatography offer a variety of interesting approaches to elimination of contaminants that meet green chemistry requirements. In addition, chemical reactions that meet these requirements can be conducted, when necessary, to minimize the toxicity of a given pollutant. When we conduct chemical reactions to remediate pollution, it is important to assure that the overall impact is minimization of toxicity of the resultant products. An effective way to deal with water pollution problems is to use the least harmful ways to eliminate contaminants.

Discussion below focuses on an important problem relating to arsenic contamination of groundwater, which affects nearly 200 million people in various countries. Even advanced countries like the United States are affected by it. Highlighted below are green chemistry solutions to this horrendous problem.

1.1. Remediation of Arsenic-Contaminated Water

A large number of approaches have been investigated for removing arsenic from drinking water. Several useful papers relating to the problem and its remediation have been published (*3–19*). Various existing and emerging arsenic-removal technologies are listed here.

- Coagulation with ferric chloride, alum, or natural products
- Sorption onto activated alumina
- Sorption onto iron oxide–coated sand particles
- Granulated iron oxide particles
- Polymeric ligand exchange
- Nanomagnetite particles
- Sand with zero-valent iron
- Hybrid cation-exchange resins
- Hybrid anion-exchange resins
- Polymeric anion exchange
- Reverse osmosis

Two effective solutions, based on chromatography and separation chemistry, are highlighted below:

1.1.1. Composite Iron Matrix Filter

The development and deployment of a water filter based on especially made composite iron matrix (SONO filter—Figure 1) for the purification of groundwater to safe potable water. Detailed description may be found in Chapter 12 in reference (*9*). It was approved for public use by the Bangladesh government. The manufacturer claims that the filtered water meets Bangladesh standards (50 ppb of arsenic; the reqirements in the United States are 10 ppb), has no breakthrough, works without any chemical treatment (pre or post), without regeneration or producing toxic waste, based on EPA guidelines. It costs about $40, lasts for five years, and produces 20–30 L/hour for daily drinking and cooking needs of one or two families. Over 35,000 SONO filters have been deployed all over Bangladesh and continue to provide more than a billion liters of safe drinking water. This innovation was recognized by the National Academy of Engineering Grainger Challenge Prize for Sustainability with the highest award for its affordability, reliability, ease of maintenance, social acceptability, and environmental friendliness. The filter requires the replacement of the upper sand layers when the apparent flow rate decreases. Experiments show that the flow rate may decrease 20–30% per year if the groundwater has high iron levels (>5 mg/L), because of[1] formation and deposition of natural HFO in sand layers. The sand layers (about one-inch thick) can be removed, washed and reused, or replaced with new sand.

Figure 1. SONO filter.

Pathogenic bacteria can still be found in drinking water because of unhygienic handling practices or utilization of water from many shallow tube wells located near unsanitary latrines and ponds. A protocol for their elimination must be used once a week in areas where coliform counts are high. It should be noted that, as with all commercial filters, the consumer needs to be alert to manufacturing defects, quality of water related to natural disasters such as flooding, and mechanical damage because of mishandling and transportation.

1.1.2. Wellhead Arsenic-Removal Units

In many remote villages in West Bengal (India), arsenic-contaminated groundwater remains the only viable source of drinking water. Cost-effective arsenic-removal technology is an urgent necessity to provide safe drinking water. The groundwater there is free of other contaminants and is considered safe for drinking. Over 150 wellhead arsenic-removal units containing activated alumina as the adsorbent are currently being operated by local villagers in this Indian state that borders Bangladesh (see Chapter 13 in reference (*9*)). The units are maintained and run by the beneficiaries and do not require any chemical addition, pH adjustment, or electricity for their regular operation. Each of the units serves approximately 250–350 families living within a short distance of the unit; the flow rate is modest at approximately 10 L/minute. Arsenite as well as arsenate from groundwater are effectively removed to render the water safe for drinking and cooking. Regeneration and durability of the adsorbent allow for a low-cost, sustainable solution to the widespread arsenic poisoning in this area. After regeneration, the spent regenerants containing a high concentration of arsenic are converted to a small-volume sludge that is stored under oxidizing conditions, to prevent future arsenic leaching. It has been claimed that this process offers superior economic advantages in regard to treatment and management of dangerous treatment residuals, compared to conventional adsorbent-based processes where regeneration and reuse are not practiced. With conventional processes where the adsorbents are treated as garbage, huge amounts of media in landfills leach out dangerous concentrations of arsenic. Input to the process is groundwater contaminated with arsenic, and caustic soda and acid for regeneration, whereas the output is treated drinking water and neutralized brine solution. Thus, the technology, besides being appropriate for the rural setting of the affected area in terms of ease of use and economics, also offers considerable ecological sustainability.

It has been estimated from the data of 150 running units that, on average, the total volume of water treated by a unit in one year is about 8,000 bed volumes, i.e., 800,000 liters. The calculated cost of the water/1000 L is 85¢ U.S. The estimated amount of arsenic-safe water used for a family of six for drinking and cooking purposes in a month at the rate of 5 L per capita per day is 900 L. The water tariff for a family of six for one month is around 75¢ U.S., or 30 Indian rupees. Regeneration helps reduce the volume of the sludge by about 150 times, and reusability of the adsorbent media significantly helps decrease the cost of the treated water.

2. Ionizing Radiation Techniques To Determine Hydroxyl Radical Efficiencies of Organic Pollutant Mixtures in Treated Wastewaters

Major challenges in ensuring healthful fresh water worldwide are linked to the increasing population, more complex anthropogenic chemicals, numerous outdated water and wastewater treatment facilities, and other conditions. Water reuse practices constitute one of the solutions to these decreased freshwater sources of water, but require additional advanced treatments of wastewater (Chapter 2). Advanced oxidation and reduction processes (AO/RP) can successfully remediate water contaminants through the creation of highly reactive radical species. Gamma irradiations of aqueous solutions are uniquely useful for the creation of radicals of interest and to quantitatively establish this chemistry on a laboratory scale. Hydroxyl radicals are formed in nitrous oxide–saturated aqueous solutions allowing kinetics and radical reaction efficiencies to be computed. Several organic compounds have been studied in pure water solutions to determine the number of contaminant molecules oxidatively transformed for each generated hydroxyl radical. Certain compounds, such as caffeine and *N*,*N*-diethyl-3-methylbenzamide (DEET) react with 100% efficiency, while the experimentally tested sulfa drugs react with about 50% efficiency with the generated hydroxyl radicals, possibly indicative of repair-type reactions in place. Since contaminants are found in complex mixtures in wastewater treatment, mixtures of prototypical model contaminants were tested in both pure water and in wastewater. In pure water, all the individual efficiencies were very similar at values of approximately 85%. To better understand the differences in hydroxyl radical efficiencies in the presence of additional reactive species, kinetic modeling has been implemented using the rate constants, efficiencies, and postulated repair mechanisms of the model compounds. A model that utilized the product of the rate constant and reaction efficiency with the hydroxyl radical showed a level of agreement with the experimental data.

3. Ferrate(VI): A Green Chemistry Oxidant for Removal of Antibiotics in Water

Ferrate(VI) ion is an environment-friendly for water treatment which can perform a dual function of oxidation and disinfection and forms a nontoxic by-product, iron(III). Chapter 3 presents an assessment of the potential of ferrate(VI) to oxidize antibiotics (A). The kinetics, stoichiometry, and products and their antibacterial properties are presented. The second-order rate constants, *k*, of the oxidation reactions at neutral pH were in the range of 5.0×10^{-1}–1.5×103 $M^{-1}s^{-1}$. At a 10 mg L-1 K_2FeO^4 dose, half-lives of the oxidation reaction would be in seconds to minutes at a neutral pH. The values of *k*, and the reaction half-lives, varied with pH. The stoichiometry of the reactions of Fe(VI) with sulfamethoxazole and trimethoprim were 4:1 and 5:1 ([Fe(VI):[A]), respectively. Oxidation products of the reactions were found to be relatively less toxic than parent molecules. The oxidized products of trimethoprim showed no significant antibacterial activity. Examples of efficient removal of antibiotics from the wastewater by Fe(VI) are presented. Overall, ferrate(VI) oxidation could be an effective treatment method for the purification of waters containing antibiotics.

4. Natural Treatment of Surface Water and Groundwater with Woodchip Reactors

Nitrate contamination is considered one of the most serious water quality challenges in California's groundwater basins (Chapter 4). Over-application of nitrogen-containing fertilizers increases nitrate levels in runoff, which in turn increases the nitrate level in shallow aquifers, rivers and lakes. Human consumption of high levels of nitrate in water results in health problems such as the blue baby syndrome, which can result in suffocation of a child from the binding of nitrite to hemoglobin. Cost-effective and readily accessible woodchip bioreactors have been utilized in the Midwest to reduce nitrate levels in surface and drainage waters. A similar laboratory system as that used by Iowa State University researchers for nitrogen-laden tile water was implemented to treat Cal Poly Pomona groundwater that is contaminated with nitrate. When treated in woodchip bioreactors, both tile water and groundwater *nitrate* concentrations were reduced below the drinking water standard (10 mg/L NO_3-N). The retention time and flow rate were observed to be important factors to increase the effectiveness of the biological treatment. Bioreactors were run for at least 6 days to ensure a stable microbial community while the degradation of nitrate was monitored. Nitrate percent removal was higher for tile water than for groundwater, possibly because of a limited source of carbon in the groundwater. For the Iowa tile water, 8-hr retention time was enough to have 96% nitrate removal, while less that 40% was achieved for groundwater at the same retention time. The results indicated a range of 15% to 40% removal rate of nitrate in groundwater. Woodchip bioreactors were amended via addition of soil and succinate to increase microbial population and to stimulate denitrification through an external source of carbon. The groundwater treating system was found to be carbon-limited since addition of succinate increased nitrate removal to 73%. Results from this work show that low-cost systems, like the woodchip reactors, could be used to remediate California's shallow groundwater systems. In a carbon-limited system such as groundwater, denitrification can still be enhanced by addition of a harmless and easily degradable carbon source.

5. In Situ Immobilization of Mercury in Water, Soil, and Sediment Using Carboxymethyl Cellulose Stabilized Iron Sulfide Nanoparticles

Mercury (Hg) is considered one of the most pervasive and toxic metals in the environment. As methyl mercury has been known to be the primary Hg species that accumulates in the food chain, engineered prevention of Hg methylation is considered a key step in remediation of Hg-contaminated water, soil and sediment (Chapter 5). To this end, effective in situ Hg remediation technologies have been consistently sought. In recent years, researchers have been exploring the feasibility of in situ immobilization of Hg through on-site delivery of nanoparticles into Hg-contaminated soil/sediment. This chapter illustrates the concept and promise of the in situ Hg immobilization using a class of newly developed FeS nanoparticles. The nanoparticles were prepared using low-cost, water-soluble carboxymethyl cellulose (CMC) as a stabilizer that can facilitate the deliverability of the nanoparticles into soil/sediment. The nanoaprticles were characterized and investigated with respect to Hg sorption behavior and effectiveness in situ immobilization of Hg in soil/sediment. The stabilized nanoparticles offer some unique advantages: high stability in water, high sorption capacity and affinity for Hg, good mobility and deliverability in soil/sediment, and controllable particle size and transport behavior in porous media. The nanoparticles were able to effectively reduce the water-leachable Hg and the toxicity characteristic leaching procedure (TCLP)-based leachability. Column breakthrough tests demonstrated the deliverability and effectiveness of the nanoparticles for Hg immobilization. Once delivered, the nanoparticles remain virtually immobile under typical groundwater conditions, serving as a long-term sink for Hg. Column Hg elution tests indicated that application of the nanoparticles transferred nearly all water-leachable Hg onto the nanoparticles. As the nanoparticels are incorporated into the geo-media, the Hg adsorbed thereon is immobilized. The nanoparticle-based technology provides a promising alternative for in situ remediation of Hg-contaminated sites.

6. In Situ Dechlorination in Soil and Groundwater Using Stabilized Zero-Valent Iron Nanoparticles: Some Field Experience on Effectiveness and Limitations

To facilitate in situ degradation of chlorinated solvents in the subsurface, Auburn University developed and patented (US7,887,880 B2) a new class of stabilized ZVI nanoparticles using carboxymethyl cellulose (CMC) as a stabilizer (Chapter 6). Laboratory experimental results revealed some unique attributes of CMC-stabilized ZVI nanoparticles:

1. deliverable in soil;
2. offer much greater dechlorination reactivity than non-stabilized counterparts; and
3. can effectively degrade soil-sorbed contaminants such as trichloroethylene (TCE).

These novel features allow the nanoparticles to be delivered into contaminated source zones and facilitate in situ dechlorination in soil and groundwater. Chapter 6 reports preliminary results from two field tests for in situ remediation technology. These field tests confirmed the soil deliverability and reactivity of the nanoparticles for in situ degradation of chlorinated solvents. In a sandy aquifer at Alabama at an injection pressure of <5 psi, the iron nanoparticles were observed to migrate in a range of 10 ft downgradient from the injection well. Following Fe–Pd nanoparticle injections, chlorinated contaminant reduction efficiencies of up to 94% were observed in monitoring wells within the first week. The rapid degradation of chlorinated solvents was evidenced at a California site along with the production of ethane, which is the main abiotic reductive dechlorination product. The concentration of ethane rapidly increased from being not detected to 65 micrograms/L in the groundwater within 2 hours after Fe-Pd nanoparticles were injected. The pilot test at the Alabama site indicated that injection of the nanoparticles boosted a local biological process leading to a long-term reduction of chlorinated contaminants in the subsurface. Some scientific constraints of the technology were also revealed. For instances, while the CMC-stabilized Fe–Pd nanoparticles can degrade soil-sorbed TCE, soil sorption can limit the rate and extent of dechlorination, especially for soils of high organic content. Dissolved organic matter was found to inhibit the degradation rate as well.

7. Polycation-Tethered Micelles as Immobilized Detergents for NAPL Remediation

Applications of permeable reactive barriers to filter contaminants out of groundwater have not taken advantage of surfactant micelles to remove organic contaminants. Such barriers need to have low cost, high capacity, good flow properties and recyclability, requirements not met by organoclays or micellar ultrafiltration. Chapter 7 describes the use of inexpensive polycations as noncovalent bridges that tether anionic surfactant micelles to porous media such as silica or sand. The solubilizing power of the micelles is fully retained. One-step coating processes can be used to optimize the silica–polycation-composite for maximum uptake of pollutants such as toluene and dichloroethane. Since the interactions are electrostatic and noncovalent, variables such as pH and salt can also be used to tune release of nonaqueous phase rich liquid micelles. The effects of such parameters are discussed and the role of the surface charge and porosity of siliceous substrates is described. The temperature-sensitivity of micelle-polycation systems suggests additional ways to tune uptake and release.

8. Novel Production of Activated Carbon for Hampering Oligomerization of Phenolic Compounds

Activated carbon adsorption is widely used in water treatment for removal of various organic micropollutants; nonetheless the presence of oligomerization phenomenon during an adsorption process can reduce its generation efficiency (Chapter 8). To make activated carbon more cost-effective by controlling oligomerization of contaminants during the adsorption process, novel ways need to be be used to produce carbon with optimal pore-size distribution (PSD). Based on the usage of proper raw materials and chemical reagents, combined with optimal activation conditions, it is possible to develop activated carbon which has ideal porous structure for hampering oligomerization. This type of activated carbon can be applied to control oligomerization in both single and multi-component adsorption which is the common situation in real water treatment. Once the oligomerization phenomenon has been well controlled, it is then possible to significantly improve the regeneration efficiency of activated carbon. The extent of the oligomerization can be defined through the difference between adsorptive capacity under anoxic (absence of molecular oxygen) and oxic (presence of molecular oxygen) conditions, respectively. Several successful applications of the novel tailored activated carbon are presented in this chapter.

9. Cyclic Electrowinning/Precipitation (CEP) for the Removal of Heavy Metals from Aqueous Solution Mixtures

Based on the proper raw materials and chemical reagents, combined with optimal activation conditions, it is possible to develop activated carbon that has ideal porous structure for hampering oligomerization (Chapter 9). This type of activated carbon can be applied to control oligomerization in both single solution and also multi-component adsorption, which is the common situation in real water treatment. Once the oligomerization phenomenon has been well controlled, it is then possible to significantly improve the regeneration efficiency of activated carbon. The extent of the oligomerization can be determined from the difference between adsorptive capacity under anoxic (absence of molecular oxygen) and oxic (presence of molecular oxygen) conditions, respectively. Several successful applications of the novel tailored activated carbons will be presented, along with discussion of important activating parameters. The description and operation of a novel cyclic electrowinning/precipitation (CEP) approach with the spouted particulate electrode (SPE) of the CEP system is also presented, specifically for co-electrodeposition of copper and nickel from acidic solution mixtures. As shown, both the quantitative and qualitative behavior of co-electrodeposition of these two metals from their mixtures differs significantly from that of the individual single-metal solutions, primarily because of the metal displacement reaction between Ni0 and Cu^{++}. A numerical model of co-electrodeposition, corrosion, metal displacement, and mass transfer in the SPE is presented, describing the behavior of the experimental data relatively well. Simultaneous removal of mixtures of heavy metals from aqueous solutions is presented in this chapter. CEP combines the advantages of electrowinning in a spouted particulate electrode with that of chemical precipitation and redissolution, to remove heavy metals at low concentrations as solid metal deposits on particulate cathodic particles without exporting toxic metal precipitate sludges from the process.

The overall result is a very large volume reduction of the heavy metal contaminants as a solid metal deposit on particles that can either be safely discarded or further processed to recover particular metals. The performance of this approach is demonstrated with data obtained for the removal of low concentration mixtures of copper, nickel, and cadmium from aqueous solutions, as well as removal from contaminated soil leachates. Separation of these same metals on different sets of cathodic particles is also demonstrated.

10. Macronutrient Removal and Recovery from Tertiary Treatment of Wastewater

Removal of two macronutrients, nitrogen (N) and phosphorus (P), from wastewater is critical before discharging the treated effluent to prevent eutrophication. But N and P are also essential components of any fertilizer; thus, their recovery from wastewater provides an added bonus (Chapter 10). This is especially critical for P since it is a non-renewable resource and its supply potential is diminishing. Details of a process are provided where an inorganic zeolite (clinoptilolite) and a polymeric anion exchanger impregnated with iron oxide nanoparticles are used to achieve selective N and P removal and their simultaneous extraction as a solid-phase fertilizer. Three hybrid polymers were studied: HAIX, DOW-HFO, & DOW-HFO-Cu. Each material combines the durability, robustness, and ease-of-use of a polymeric ion-exchanger with the high sorption affinity of hydrated ferric oxide (HFO) for phosphorus. Laboratory experiments demonstrate that each material can selectively remove P in the presence of competing anions (primarily sulfate) and can also be efficiently regenerated as a solid-phase fertilizer.

11. Functionalized Nanoparticles as Removable Membrane Coatings

Membrane fouling plagues all types of membrane filtration, from large-pore microfiltration to nonporous reverse osmosis (RO). Chapter 11 describes the feasibility of using a coating of one or two layers that serves as a barrier between the membrane and foulant. This coating is electrostatically bound to the membrane at operational pH, then removed with a simple pH adjustment once fouling has reduced operational efficiency. The water treatment polymer polydiallyldimethylammonium chloride (polyDADMAC) was used to create a positive charge on the fully aromatic polyamide membrane surface. Carboxyfunctionalized polyacrylate nanoparticles (NPs) composite with either silver [Ag–PA(-)] or titanium dioxide [TiO_2-PA(-)], both approximately 10 nm in size, were then adsorbed onto the polyDADMAC coating to reinstate an overall negative charge to the membrane surface. Acid washing removed the polyDADMAC coating by protonating the carboxyl groups on the membrane, promoting repulsion from the membrane surface. Coating and removal phases were characterized primarily by measurement of the surface zeta potential with an electrokinetic analyzer. Additional characterization was performed using scanning electron microscopy (SEM) and attenuated total reflectance Fourier transform infrared (ATR-FTIR) spectroscopy. The overall results serve as a proof of concept that these materials could serve as removable coatings for RO membranes.

12. Hematite Nanoparticle Modified Granular Activated Carbon for Removal of Arsenic and Organic Co-Contaminants

The goal of the study described in Chapter 12 was to determine whether hematite nanoparticles could be synthesized within the pores of granular activated carbon (GAC) media by hydrolysis of ferric salt to effectively remove arsenic and organic co-contaminant from water. Five task-oriented objectives were undertaken to address this goal:

1. hematite modified GAC media was fabricated;
2. properties of the fabricated media were characterized;
3. arsenic adsorption capacity was evaluated under batch pseudo-equilibrium conditions in different water matrices;

4. adsorption capacity of the fabricated media was evaluated for model organic co-contaminant (methylene blue) under batch pseudo-equilibrium conditions; and
5. short-bed column tests were conducted to estimate adsorption capacity under continuous flow conditions.

Four different hybrid media were characterized, with iron contents ranging from 0.9% to 4.4% of Fe per dry weight. Longer hydrolysis times in solutions with lower concentrations of ferric salt allow for higher iron content, better distribution of the nanoparticles and formation of pore volume in the macropore region. Characterized by the low Freundlich intensity parameters ($1/n < 1$), the hybrid media with highest iron content exhibited better arsenic adsorption capacity and selectivity in waters with low arsenic concentrations than their counterparts. The introduction of nanoparticles within the pores of the granular activated reduced the adsorption capacity of the hybrid media for the model organic co-contaminant (methylene blue), but it did not affect the energy of adsorption.

13. Titanium Dioxide-Based Hybrid Ion-Exchange Media for Simultaneous Removal of Arsenic and Nitrate

Chapter 13 describes development of an inexpensive and easy to fabricate titanium dioxide–based hybrid ion-exchange media (Ti-HIX) and assess its potential to remove arsenic and nitrate from water. Different Ti-HIX media were fabricated via in situ formation of TiO_2 nanoparticles within the pores of three different commercial IX resins; the Ti-HIX media were characterized; and the arsenic and nitrate removal potential of the most economically feasible Ti-HIX media was assessed in model water under batch pseudo-equilibrium conditions. The Ti-HIX media were characterized with contents ranging between 11% and 21% TiO_2 per media dry mass. The TiO_2-exhibited form of anatase nanoparticles. The Freundlich adsorption intensity parameters ($1/n$) for all the Ti-HIX media were < 1, implying favorable adsorption for arsenic. The estimated maximum adsorption Ti capacity for arsenic expressed per mass of titanium ranged between 16.6, 24.9, and 27.3 mgAs g^{-1} for different types of tested Ti-HIX media, and was several- fold higher than similar reported values in the literature. Nitrate removal performance of the base ion-exchange resins used in synthesis of the Ti-HIX media was not adversely impacted by the synthesis process.

14. Applications of Zero-Valent Iron (ZVI) and Nanoscale ZVI to Municipal and Decentralized Drinking Water Systems—A Review

Zero-valent iron (ZVI) has been used to treat contaminated groundwater for almost two decades, yet its application in environmental engineering to date is still limited to site remediation (Chapter 14). The work in recent years has shown that ZVI is also effective at removing contaminants that are relevant to drinking water, including viruses and bacteria, chlorine, disinfection by-products (DBPs), DBP precursors (e.g., natural organic matter), and metals. The authors suggest that ZVI represents a potential approach to addressing some drinking water problems. This chapter provides a brief summary of recent work on the removal of these contaminants by ZVI and offers examples of potential applications to drinking water systems, i.e., in municipal water treatment plants and small-scale or portable point-of-use (POU) devices. In each example, the specific problems of ZVI are addressed and the expected benefits are discussed. Preliminary results supporting these applications are presented, and possible applications to other water-related problems are considered. The chapter suggests a number of research needs for implementation of the ZVI process.

15. Decentralized Wastewater Treatment for Distributed Water Reclamation and Reuse: The Good, The Bad, and The Ugly—Experience from a Case Study

Cities worldwide are facing a growing water crisis, with challenges from climate change, population growth, and deteriorating infrastructure that threatens economic development, social welfare, and environmental sustainability. New strategies are needed for water/wastewater treatment and distribution that will reduce the need to pump water over long distances and provide opportunities to locally reuse wastewater. A full-scale pilot hybrid sequencing batch membrane bioreactor (SBMBR) wastewater treatment system serving 400 residential units was investigated at the Colorado School of Mines in order to assess the economic and technical feasibility of using the SBMBR process as a sustainable, decentralized approach for on-site water reclamation and reuse of municipal wastewater effluents (Chapter 15). The findings of this study demonstrate that the SBMBR system has the operational flexibility to generate effluent qualities that differ with respect to nitrogen concentrations tailored to local needs generated within a few days, without major system disturbances including no impact on membrane fouling. The largest challenge to implementation of decentralized systems is a much better process understanding that can lead to “smarter” systems for remote operation.

Conclusions

Water pollution in our modern society is inevitable. Effective safety measures that prevent point-source pollutions should be employed. In addition, our vigilance to avoid nonpoint-source pollution must be significantly improved. Green chemistry solutions should be employed, where possible. An effective way to deal with the water pollution problem is to use the least harmful ways to eliminate contaminants. Chromatography and separation chemistry offer a variety of interesting approaches to achieve these goals. Interesting examples of remediation have been provided to help correct arsenic contamination of groundwater, which affects nearly 200 million people worldwide.

A variety of novel methods for prevention and remediation of water pollution that entail radical reaction and utilization of nanoparticles have been considered.

Macronutrient removal and recovery from tertiary treatment of wastewater can provide a solid-phase fertilizer. In addition, a full-scale pilot hybrid sequencing batch membrane bioreactor (SBMBR) wastewater treatment system that can serve 400 residential units is described.

References

1. Ahuja, S. *Green Chemistry Solutions to Water Contamination*, American Chemical Society Meeting, Denver, CO, August 28−September 1, 2011.
2. Ahuja, S. *Handbook of Water Purity and Quality*; Elsevier: Boston, 2009.
3. Ahuja, S. *Assuring Water Purity for Human Consumption*, MARM Meeting, New Brunswick, NJ, 2005
4. Ahuja, S. *Assuring Water Purity by Monitoring Water Contaminants from Arsenic to Zinc*, American Chemical Society Meeting, Atlanta, GA, March 26-30, 2006.
5. McNeil, E. E.; Otson, R.; Miles, W. F.; Rahabalee, F. J. M. *J. Chromatogr.* **1977**, *132*, 277.
6. Ahuja, S. *CHEMTECH* **1980**, *11*, 702.
7. Ahuja, S. *Ultratrace Analysis of Pharmaceutical and Other Compounds of Interest*; Wiley, New York, 1986.
8. Ahuja, S. *Chemical and Engineering News*, November 17, 2008, p 42.
9. Ahuja, S., *Arsenic Contamination of Groundwater: Mechanism, Analysis, and Remediation*; Wiley: New York, 2008.
10. Ahuja, S.; Malin, J. International Conference on Chemistry for Water, Paris, June 21–23, 2004.
11. Ahuja, S. *Arsenic Contamination of Groundwater*, UNESCO Conference on Water Scarcity, Global Changes, and Groundwater Management Responses, Irvine, CA, December 1−5, 2008.
12. Ahuja, S. *Ultratrace Analysis of Pharmaceuticals and Other Compounds of Interest*; Wiley: New York, 1986.
13. Bissen, M.; Frimmel, F. Arsenic—A review. Part I: Occurrence, toxicity, speciation, mobility. *Acta Hydrochim. Hydrobiol.* **2003**, *31*, 9–18.
14. Ng, K.-S; Le-Clech, P.; Ujang, Z. Arsenic removal technologies for drinking water treatment. *Rev. Environ. Sci. Biotechnol.* **2004**, *3*, 43–53.
15. Daus, B.; Weiss, H.; Wennrich, R. Sorption materials for arsenic removal from water: A comparative study. *Water Res.* **2005**, *38*, 2948–2954.
16. Ahuja, S. International Workshop on Arsenic Contamination and Safe Water, Dhaka, Bangladesh, December 11–13, 2005.
17. Ahuja, S.; Malin, J. *Chem. Int.* **2006**, *28* (3), 14–1.
18. Ahuja, S. *Origins and Remediation of Groundwater Contamination by Arsenic: Objectives and Recommendations*, International Workshop on Arsenic Contamination and Safe Water, Dhaka, Bangladesh, December 11−13, 2005.
19. Ahmed, M. F. S.; Ahuja, S.; Alauddin, M.; Huq, S. J.; Lloyd, J. R.; Pfaff, A.; Pichler, T.; Saltikov, C.; Stute, M.; van Geen, A. *Science* **2006**, *314*, 1687–1688.

Chapter 2

Ionizing Radiation Techniques To Determine Hydroxyl Radical Efficiencies of Organic Pollutant Mixtures in Treated Wastewaters

Julie R. Peller,*,[1] Kenneth P. Ishida,[2] and Stephen P. Mezyk[3]

[1]Department of Chemistry, 3400 Broadway, Indiana University Northwest, Gary, Indiana 46408
[2]Research and Development Department, Orange County Water District, Fountain Valley, California 92708
[3]Department of Chemistry and Biochemistry, California State University at Long Beach, Long Beach, California, 90840
***E-mail: jpeller@iun.edu. Phone: 219-980-6744. Fax: 219-980-6673**

The increased challenges in ensuring healthy, fresh water worldwide are linked to rising populations, more complex anthropogenic chemicals, numerous outdated water and wastewater treatment facilities and other conditions. Water reuse practices constitute one of the solutions to these decreased freshwater sources of water, but require additional advanced treatments of wastewater. Advanced oxidation and reduction processes (AO/RPs) can successfully remediate water contaminants through the creation of highly reactive radical species. Gamma irradiations of aqueous solutions are uniquely useful for the creation of these radicals of interest and to quantitatively establish this chemistry on the laboratory scale. Hydroxyl radicals are formed in nitrous oxide saturated aqueous solutions, allowing kinetics and radical reaction efficiencies to be computed. Several organic compounds have been studied in pure water to determine the number of contaminant molecules oxidatively transformed for each generated hydroxyl radical. Certain compounds, such as caffeine and *N,N*-diethyl-3-methylbenzamide (DEET) react with 100% efficiency, while the experimentally tested sulfa drugs react with about 50% efficiency, possibly indicative of repair-type reactions taking place. Since contaminants are found in complex mixtures in wastewater treatment, mixtures of prototypical model contaminants were tested in both pure water and in wastewater. To better understand the differences in hydroxyl radical efficiencies in the presence of additional reactive species, kinetic modeling was implemented using the rate constants, reaction efficiencies and postulated repair mechanisms of the model compounds. A computer model which utilized the product of the rate constant and reaction efficiency with the hydroxyl radical showed reasonable agreement with the experimental data. However, the inclusion of the reactivities of the transient species, as well as the ultimate oxidized products, would be necessary to more accurately quantify the overall hydroxyl radical chemistry.

Introduction

Worldwide, freshwater sources are increasingly threatened by anthropogenic contaminants, water system transformations and rapidly changing patterns of water use, all of which are strong incentives for the implementation of water reuse or water recycling systems (*1–5*). Water reuse is defined as the treatment of wastewater to a sufficient quality for recharge into an aquifer or for use in non-threatening ways to human or environmental health (*6*, *7*). Health and environmental assessments of the recycled water must ensure quality and value for its designated roles (*8*, *9*). Furthermore, water reuse must be acceptable to public opinion, economically viable and competitive with other freshwater sources (*10*). Currently, reused or reclaimed water is utilized in agriculture irrigation, toilet flushing, lawn watering, industrial processing and other functions that do not require potable water.

In the United States, according to the *Clean Watersheds Needs Survey (CWNS) 2004 Report to Congress* (*11*), most municipalities treat wastewater through the secondary treatment stage, and only a small percentage process wastewater beyond this. In the secondary wastewater treatment stage, 85% of biological oxygen demand (BOD) and total suspended solids from the wastewater must be removed, the majority of which is achieved by microbial biodegradation. For recycled wastewaters intended for reuse, treatment beyond the secondary level is required. Additional wastewater contaminants are removed by tertiary treatment using porous media filtration, or by membrane filter steps, such as microfiltration, nanofiltration and reverse osmosis. However, these membranes require cleansing, which leads to concentrated contaminant solutions that must be processed prior to disposal (*12*).

Most tertiary treatment processes do not remove all the dissolved contaminants present in the water and additional procedures are often required for water reuse applications. Some contaminants are recalcitrant and others may be potentially harmful at extremely low concentrations. Furthermore, by-products of biological degradation can be more toxic than the parent compounds (*13–15*). Therefore, additional applications of technologies or treatments in the wastewater process train to eliminate contaminants or chemically remediate contaminants to the point where biological processes can take over are desirable. Advanced oxidation and reduction processes (AO/RPs) largely fulfill these requirements.

Advanced oxidation/reduction processes involve the formation of highly reactive radicals which react to initiate the breakdown of water contaminants (*16*). Technologies such as UV/hydrogen peroxide or ozone/hydrogen peroxide create hydroxyl radicals ($^{\bullet}OH$), which then oxidatively destroy a wide variety of organic contaminants in aqueous solutions (*17–21*). However, the overall removal efficiencies of the $^{\bullet}OH$-mediated process are highly variable depending on the applied technology, its location in the treatment train, the inherent water quality and the contaminants of concern (*22–24*). With certain dissolved organic contaminants, such as *N,N*-diethyl-3-methylbenzamide (DEET), a 100% efficient reaction ensues, where a chemical transformation occurs for every reaction of a DEET molecule with a hydroxyl radical. However, many dissolved organics do not react with 100% efficiency (*22*). For example, sulfa drugs, such as sulfamethoxazole, prove to be approximately 50% efficient in their reaction with the hydroxyl radical (*25*). Moreover, the complexity of these oxidative reactions increases drastically in the presence of other dissolved substances. In multi-component mixtures, such as treated wastewaters, the hydroxyl radical removal of specific contaminants takes place with considerably lower reaction efficiency (*26*).

To properly predict contaminant destruction in AO/RP applications, it makes sense that both hydroxyl radical reaction efficiencies and reaction rate constants be evaluated. To date, numerous hydroxyl rate constants have been determined for a variety of dissolved organics in water solutions. Most are fast, near diffusion controlled, with rate constants in the $10^9 – 10^{10}$ $M^{-1}s^{-1}$ range (*27*, *28*). Conversely, only a small number of hydroxyl radical reaction efficiencies have been tabulated for dissolved organics in pure water solutions, and fewer still in more complicated solution matrices or in contaminant mixtures (*22*, *29*).

When the hydroxyl radical reaction efficiency is combined with the measured rate constant, an effective contaminant removal parameter (ECRP) for a chemical contaminant is generated. We have previously proposed that the ECRP can be achieved by multiplying these two values; for example, sulfamethoxazole's measured rate constant is 8.5 (± 0.3) x 10^9 $M^{-1}s^{-1}$ and its reaction efficiency of oxidation by the hydroxyl radical in pure water was measure as 56 ± 6%. The product of these values, 4.8 (± 0.6) x 10^9 $M^{-1}s^{-1}$, represents the effective contaminant removal rate constant (ECRC), a measure of the speed and permanent transformation of the hydroxyl radical reaction. In another example, caffeine, a compound which reacts 100% efficiently with $^{\bullet}OH$ radicals, has an ECRC equal to its rate constant, 6.9 (± 0.4) x 10^9 $M^{-1}s^{-1}$ (*30*).

We originally proposed that both of these measured values, the rate constant and the reaction efficiency, were required to accurately model hydroxyl radical-mediated contaminant removal in wastewater by AO/RP technologies in wastewater treatment. However, after more thorough investigations, this appeared to be an oversimplified explanation. The data suggests that hydroxyl radical reaction efficiencies of less than 100% may involve a type of “repair” reaction, where after the initial reaction between the radical and the contaminant at the measured rate constant, one pathway for the formed intermediate, or transient, is reaction with another species. With some transients, this pathway will regenerate the parent contaminant, and essentially "repair" the radical transient back to the original contaminant.

While some hydroxyl radical reaction efficiencies have been reported for single component aqueous systems, efficiencies for mixtures of contaminants have not been investigated to the best of our knowledge. To better understand the effectiveness of hydroxyl radical-mediated technologies in advanced wastewater treatments where competition for the hydroxyl radicals exists, overall removal efficiencies of contaminant mixtures must be explored. This reported work takes into account hydroxyl radical rate constants and determinations of efficiencies of single component solutions and multi-component mixtures. Experiments were performed in pure water to obtain reaction efficiencies, and in treated wastewaters to determine overall removal efficiencies and offer insight into the effectiveness of hydroxyl radical-medicated technologies throughout the wastewater treatment train. A few selected experimental values were used in two versions of a simple modeling program to ascertain and predict outcomes of $^{\bullet}OH$-mediated contaminant remediation. Once the reactions of the hydroxyl radicals are better understood in aqueous solutions containing numerous dissolved substances, accurate predictions of contaminant removal and effective implementation of AO/RPs methods in wastewater treatment can be accomplished.

Experimental

Chemicals

Most chemicals used in this study were obtained from the Aldrich Chemical Company at the highest purity available, and used as received. Solutions were made using high purity water produced by a Millipore Milli-Q® system or in filtered secondary- or tertiary-treated wastewater provided by the Orange County Water District, Fountain Valley, CA. Solutions were pre-saturated with high purity N_2O to remove the dissolved oxygen and to simplify our experiments by ensuring only oxidizing conditions.

Steady State Radiolysis Experiments

Although there are many ways to produce hydroxyl radicals in water, the advantage of radiation chemistry techniques incorporated in this study is that they provide a simpler, more direct way to decompose water molecules into AO/RP radicals. This creates a homogeneous solution of radicals with known absolute concentrations, without the addition of large amounts of other reactive chemicals (i.e., H_2O_2, O_3) to the water.

These radiation-based techniques were used to quantitatively form hydroxyl radicals in a variety of aqueous solutions spiked with the chemical contaminants, either singly or mixtures of the compounds. The solution irradiations were performed using a ^{60}Co Gammacell 220 gamma irradiator, housed at the Radiation Laboratory, University of Notre Dame, Notre Dame, IN. During the dates of irradiation, the average dose rate was 0.0029 kGy min^{-1}.

Solutions were made with >18 MΩ-cm deionized water (Millipore Milli-Q®) or in filtered secondary wastewater or reverse osmosis permeate from the Advanced Water Purification Facility (AWPF) of the Orange County Water District in Fountain Valley, CA. The AWPF utilizes a multi-barrier approach to recycle secondary-treated wastewater from the Orange County Sanitation District. This purification process consists of chlorine (NaOCl) addition followed by microfiltration, reverse osmosis and UV/hydrogen peroxide disinfection and advanced oxidation for indirect potable reuse.

The initial high energy radiation of a solution containing less than ~0.1 M solute causes direct ionization and excitation of the water molecules. The ionization immediately creates free electrons and H_2O^+ ions, while the excitation results in O-H bond breakage to make $^\bullet$OH radicals and H$^\bullet$ atoms. The electrons then become hydrated, e^-_{aq} , and H_2O^+ decomposes to give hydroxyl radicals, $^\bullet$OH, and H^+. The subsequent reactions of these initially formed species include formation of H_2O_2 (from combination of two $^\bullet$OH radicals), H$^\bullet$ (from e^-_{aq} and H^+) and H_2 (from reaction of two H$^\bullet$ atoms). It has been quantitatively established that the overall distribution of species produced in pure water (pH 4 – 10) upon radiolysis is constant, and given by reaction (1) (*27*).

$$H_2O \xrightarrow{radiolysis} [0.28]^\bullet OH + [0.06]\,H^\bullet + [0.27]\,e^-_{aq} + [0.05]H_2 + [0.07]H_2O_2 + [0.27]H^+ \quad (1)$$

The numbers in brackets are the G-values (yields) of each species in μM J^{-1} of deposited energy. In N_2O-saturated solution, oxidizing conditions are created due to the reactivity of the hydrated electrons, e_{aq}^-, and hydrogen atoms, H$^\bullet$, with the N_2O according to the following reactions (*27*):

$$e^-_{aq} + N_2O + H_2O \rightarrow N_2 + OH^- + {}^\bullet OH \qquad k_1 = 9.1 \times 10^9\ M^{-1}\ s^{-1} \qquad (2)$$

$$^\bullet H + N_2O \rightarrow {}^\bullet OH + N_2 \qquad k_2 = 2.1 \times 10^6\ M^{-1}\ s^{-1} \qquad (3)$$

Based on experimental measurements, the total hydroxyl radical yield for N_2O-saturated conditions is 0.59 μmol J^{-1} (*31*).

Pulse Radiolysis Experiments

Electron pulse radiolysis was used for the elucidation of hydroxyl radical kinetics. This technique uses short pulses (2-3 ns) of high-energy (8 MeV) electrons from a Linear Accelerator (LINAC) available to us at the Radiation Research Laboratory, University of Notre Dame. The same distribution of radical and molecular species as for gamma radiolysis is initially generated.

In these fast transient kinetic experiments, the absorbed dose by these solutions is determined by using standard dosimetry formed using N_2O-saturated, 1.00 x 10^{-2} M KSCN solutions at $\lambda = 475$ nm, ($G_\varepsilon = 5.2 \times 10^{-4}$ m^2 J^{-1}) with average doses of 3-5 Gy per 2-3 ns pulse, corresponding to ~2-3 μM $^\bullet$OH radicals produced per pulse.

HPLC Analyses

The concentration changes of the contaminant compounds in solution from the gamma irradiations were followed using a Waters HPLC system (Millennium 2010, Waters 717 plus Autosampler, Waters 600 Controller Solvent Pump) equipped with a Supelco Discovery® C18 column, 5 μm (250 mm x 4.6 mm). A solvent flow of 0.85 mL min^{-1} utilized three solvents: water, methanol and dilute acetic acid (1%). In the analyses of bisphenol A (BPA) solutions, the initial solvent mixture consisted of 70% methanol and 30% water. Using a gradient curve, the solvent mixture changed to 30% methanol, 68% water and 2% acetic acid solution at the 13 minute mark. The solvent switched back to the original flow by 16 minutes. The same solvents were utilized in the analyses of the other compounds, with slight variations in the gradients. A photodiode array detector monitored the 200 - 400 nm range and the compounds' detection wavelengths were done at or near the maximum absorbances: caffeine (272 nm), sulfamethoxazole (266 nm), bisphenol A (276 nm) and DEET (247 nm).

Reaction and Removal Efficiency Determinations

Hydroxyl radical removal efficiencies for the studied organic compounds were determined by graphing the absolute change in contaminant concentration (mM) with absorbed radiation dose in kGy units (*25*). To avoid significant interferences from intermediate reaction products, which often effectively compete for hydroxyl radicals, data for contaminant loss of ≤ 30% were used. Initial slope values were determined by fitting the experimental data to a quadratic equation; the linear coefficient of this fit corresponds to the best-fit initial slope and considered the **removal constant**. (Figure 1) The initial slope value was divided by 0.59 μmol J^{-1}, which corresponds to the total $^\bullet$OH yield under N_2O-saturated conditions, and then multiplied by 100 to determine the hydroxyl radical **removal efficiency**. In pure water with only the single solute present, this value was the reaction efficiency. For the treated wastewater/mixtures of compounds, this corresponds to the overall removal efficiency.

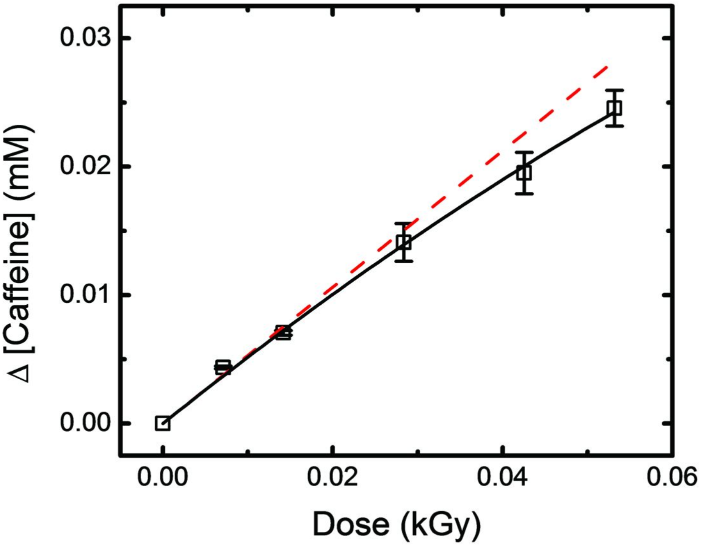

Figure 1. Measured change in a 50 μM caffeine concentration through $^{\bullet}OH$ *radical reaction in* N_2O*-saturated solution of Milli-Q water. Top dashed red line is initial linear component of quadratic fit (solid black line), with slope of 0.591 ± 0.026,* $R^2 = 0.999$*, corresponding to a reaction efficiency of 100.0 ± 4.4%.*

Discussion

Two main experimental parameters, the hydroxyl radical rate constant and the hydroxyl radical reaction efficiency, were gathered to determine the effective contaminant removal parameter, ECRP for four model compounds. The hydroxyl radical reacts rapidly with the model compounds shown in Figure 2, sulfamethoxazole (SX), bisphenol A (BPA), caffeine and *N,N*-diethyl-3-methylbenzamide (DEET), to form hydroxylated products, which can react further with additional radicals and species for the eventual breakdown to smaller, benign carbon compounds. The experimentally determined hydroxyl radical rate constants are 6.9 (± 0.4) x 10^9 and 8.5 (± 0.3) x 10^9 $M^{-1}s^{-1}$, respectively, for caffeine (*30*) and sulfamethoxazole (*22*, *25*, *30*) and 4.9 (± 0.2) x 10^9 and 6.9 (± 0.3) x 10^9 $M^{-1}s^{-1}$ for DEET and BPA (*26*, *32*). While the rate constants for three of the compounds were determined through direct detection of their transient absorptions (see Figure 3 for sulfamethoxazole (*25*)), the direct reaction of hydroxyl radicals with caffeine in high quality water was determined by using competition kinetics (*30*). The standard chosen for these experiments was thiocyanate, which is the same as the dosimetry measurements.

$$^{\bullet}OH + \text{caffeine} \rightarrow \text{products} \qquad k_4 = \text{TBD} \qquad (4)$$

$$^{\bullet}OH + SCN^{-} (+ SCN^{-}) \rightarrow OH^{-} + (SCN)_2^{\bullet-} \qquad k_5 = 1.1 \text{ x } 10^{10} \text{ M}^{-1} \text{ s}^{-1} \quad (5)$$

This competition for hydroxyl radicals by SCN^- and caffeine can be analytically solved to give the expression:

$$\frac{Abs^{o}(SCN)_2^{\bullet-}}{Abs(SCN)_2^{\bullet-}} = 1 + \frac{k_4[Caffeine]}{k_5[SCN^{-}]} \qquad (6)$$

where Abs°$(SCN)_2^{\bullet-}$ is the maximum absorbance determined for the thiocyanate solution without any caffeine and Abs$(SCN)_2^{\bullet-}$ is the reduced absorbance in the presence of this competitor. From monitoring the decrease in $(SCN)_2^{\bullet-}$ absorbance with increasing amounts of caffeine in solution, the rate constant, k_4, was determined from a plot of the ratio of the absorbance intensities against the ratio of concentrations to be 6.9 x 10^9 M^{-1} s^{-1} (*30*).

Using steady state gamma irradiation experiments, the reaction efficiencies were determined to be 100% for both caffeine (see Table 1) and DEET in deionized water (*22*, *32*). For sulfamethoxazole and BPA, the hydroxyl radical reaction efficiencies are significantly lower, at 56% and 76%, respectively, in pure water. Several additional sulfa drugs have also been determined to be about 50% efficiently oxidized by hydroxyl radical-mediated transformations (*25*). For this small compilation of compounds, summarized in Table 1, no discernible correlation exists between rate constants and reaction efficiencies.

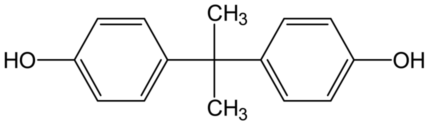 Bisphenol A (2,2-bis(4-hydroxyphenyl)propane)	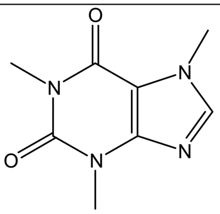 Caffeine (1,3,7-trimethylxanthine)
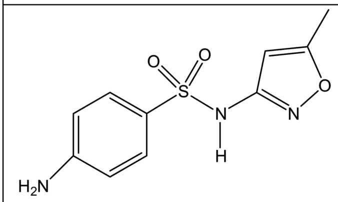 Sulfamethoxazole	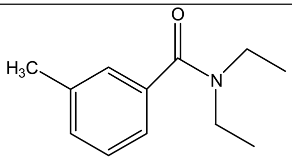 DEET (*N,N*-diethyl-3-methylbenzamide)

Figure 2. Structures of the model contaminants.

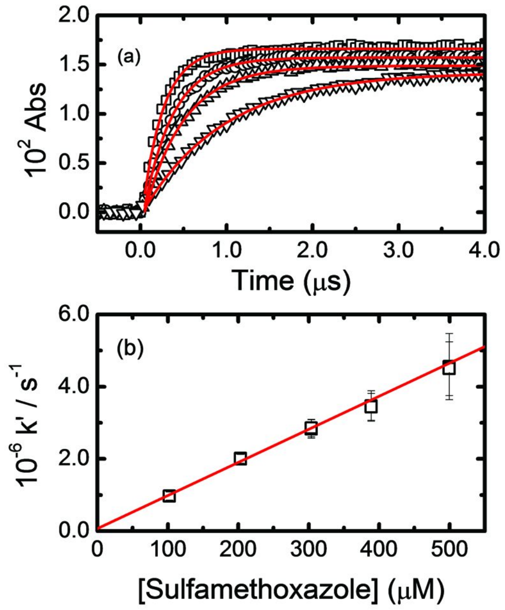

Figure 3. a) Transient growth kinetics observed at 415 nm for hydroxyl radical induced oxidation of sulfamethoxazole in N_2O-saturated solution at pH 7.1 and 21.8°C. Solid red lines correspond to fitted first-order growth kinetics, with corresponding rate constants of (4.50 ± 0.75) x 10^6, (2.86 ± 0.24) x 10^6, (2.00 ± 0.12) x 10^6 and (0.97 ± 0.11) x 10^6 s^{-1}, respectively. b) Second order plot for this oxidation using the kinetic data of a). Solid line is weighted linear fit, with slope corresponding to reaction rate constant of (8.50 ± 0.80) x 10^9 M^{-1} s^{-1} (R^2 = 0.99).

The different reaction efficiency values for these compounds in pure water signify variations in the mechanistic pathways under the controlled hydroxyl radical reaction conditions. In treated wastewaters or natural waters, mixtures of contaminants are present, along with numerous other naturally dissolved substances, which are expected to significantly alter chemical pathways. Since major chemical contaminant concerns exist in the context of treated wastewaters and naturals waters, greater practical value is gained in removal efficiency measurements that involve real water solutions. We previously reported significant decreases in the removal efficiencies of contaminants in treated wastewaters (Table 1), where the hydroxyl radical oxidation efficiencies drop by 50-60% for secondary-treated wastewater (*22*). The main hydroxyl radical scavengers in wastewaters are the carbonate and bicarbonate ions, dissolved organic matter (DOM) and other dissolved species such as metal ions. Thus, it is necessary to determine contaminant removal efficiencies in the presence of numerous dissolved organic contaminants (controlled mixtures), and then in real-world complex matrices.

Table 1. Rate Constants and Efficiencies for Reactions with the Hydroxyl Radical, Determined Using 50 µM Solution Concentrations

Solution/ Contaminant	*BPA*	*Caffeine*	*SX*	*DEET*
Rate Constant DI water, $M^{-1}s^{-1}$	$6.9(\pm 0.3) \times 10^9$	6.9×10^9	$8.5(\pm 0.8) \times 10^9$	$4.9(\pm 0.2) \times 10^9$
Reaction Efficiency (%), DI water	76 ± 7	92 ± 8	56 ± 5	95 ± 9
Removal Efficiency (%), secondary treated wastewater	34 ± 2	37 ± 4	29 ± 7	42 ± 8
Effective Contaminant Removal Rate Constant (ECRC) DI water, $M^{-1}s^{-1}$	$5.2 (\pm 0.2) \times 10^9$	6.3×10^9	$4.6 (\pm 0.8) \times 10^9$	$4.6(\pm 0.2) \times 10^9$

To establish the different efficiencies for mixtures of contaminant chemicals, experiments were conducted in deionized water and in highly treated, post reverse osmosis filtration (RO), treated wastewater. A mixture of 25 µM each of DEET, caffeine and sulfamethoxazole was subjected to radiation-generated hydroxyl radical oxidation, and individual removal constants were determined. These results are summarized in Table 2. In general, the compounds were remediated with similar removal efficiencies: 27, 29 and 29%, respectively, and different from the single component solution results (reaction efficiencies shown in Table 1). If we make the assumption that the radiation generated hydroxyl radicals partition equally among the three compounds, each is remediated with approximately 85% efficiency. This differs greatly from the experimentally determined efficiencies for the single component solutions, where the reactions efficiencies for DEET and caffeine are nearly 100% and that of SX is approximately 50%.

A mixture containing 50 µM each of the same three dissolved organic compounds in deionized water was similarly subjected to hydroxyl radical oxidations and gave the same efficiency values for the hydroxyl radical-mediated removal of these compounds within experimental error. When analogous experiments were performed using highly RO treated wastewater, the sulfamethoxazole removal values were slightly lower, but the caffeine and DEET values were consistent with the deionized water mixtures. In all solution mixtures, the overall removal efficiencies ranged from 76-85%, consistent with the values displayed in Table 2.

Table 2. Removal Efficiencies for DEET, Sulfamethoxazole (SX), and Caffeine Using Mixtures Containing 25 µM of Each

25 µM each: DEET,SX,CAF	*Removal Efficiency, %*
Deionized water	**Average**
Caffeine	29
SX	29
DEET	27
Total	85
Post RO treated wastewater	
Caffeine	27
SX	22
DEET	27
Total	76

In order to explain the observed "leveling effect" of the hydroxyl radical removal efficiencies calculated from the mixtures data, the effective contaminant removal rate constants (combination of reaction efficiency and rate constant), ECRCs, were evaluated. These values, listed in Table 1, may explain, at least to some extent, the relatively equal hydroxyl radical removal efficiencies of the components in the mixture solutions. Since sulfamethoxazole's rate constant is greater than that of caffeine and DEET, the hydroxyl radicals react approximately 20% faster with this sulfa antibiotic. However, upon formation of the hydroxyl radical transient intermediate, only about half of the short-lived radical $^{\bullet}$OH-adducts result in other stable, measureable compounds, according to the reaction efficiency numbers determined from steady state experiments. Essentially, sulfamethoxazole is a better radical scavenger than caffeine or DEET, but the transient that forms does not always lead to a stable product.

We continued our studies of the mixtures by preparing varying concentrations of chemical mixtures in deionized water. A solution of 50 µM caffeine and 10 µM sulfamethoxazole (SX) was saturated with nitrous oxide and subjected to appropriate doses of gamma rays to oxidatively transform less than 30% of the contaminant mixture (see Figure 4). The results of these experiments are summarized in Table 3. Similar to the previous three-component system, the competitive removal leads to different removal efficiencies than those obtained using single component solutions.

Table 3. Experimental and Modeled Average Hydroxyl Radical Removal Constants for Mixed Sulfamethoxazole and Caffeine Solutions

Mixtures in DI, N_2O (g)	*RC for SX (µM/Gy)*	*RC for Caffeine (µM/Gy)*	*Model values SX k_{eff}/Repair*	*Model values Caffeine k_{eff}/Repair*
10 µM SX and 50 µM Caffeine	0.096	0.37	0.068/0.062	0.456/0.415
50 µM SX and 10 µM Caffeine	0.37	0.084	0.415/0.254	0.109/0.074

To better understand and eventually predict the removal of contaminants in wastewater, the data from these latter experiments were modeled. Our simplified computer models used the standard water radiolysis model (*27*) reactions (2) and (3), plus additional equations to describe the oxidation of the two component system. Two separate versions of the model were run; the first model incorporated the known reaction rate constants and efficiencies by multiplying them together to give the effective rate constants:

$$^{\bullet}OH + SX \rightarrow \text{products} \quad k_{eff} = (8.5 \text{ x } 10^9) \text{ x } (0.56) = 4.8 \text{ x } 10^9 \text{ M}^{-1} \text{ s}^{-1} \quad (7)$$

$$^{\bullet}OH + \text{caffeine} \rightarrow \text{products} \quad k_{eff} = (6.9 \text{ x } 10^9) \text{ x } (1.00) = 6.9 \text{ x } 10^9 \text{ M}^{-1} \text{ s}^{-1} \quad (8)$$

The model's predictions, based on these effective rate constants, are shown as the red dashed lines in Figure 4, resulting in a slightly faster removal of these two components than experimentally observed. The removal constant predicted by the model is also given in Table 3. As the degradation products accumulate, they would be expected to compete for the hydroxyl radical, which would slow down the parent degradation, but this is not predicted to be significant at the low doses used in our experiments.

When the computer model was modified to allow "repair reactions" to occur (version 2), the experimentally measured rate constants for both species were used, but only 56% of the sulfamethoxazole was allowed to react to form a stable product (with the other 44% immediately regenerating the parent compound):

$$^{\bullet}OH + SX \rightarrow \text{sulfamethoxazole} \quad k_{eff} = (8.5 \text{ x } 10^9) \text{ x } (0.44) = 3.8 \text{ x } 10^9 \text{ M}^{-1} \text{ s}^{-1} \quad (9)$$

$$^{\bullet}OH + SX \rightarrow \text{products} \quad k_{eff} = (8.5 \text{ x } 10^9) \text{ x } (0.56) = 4.8 \text{ x } 10^9 \text{ M}^{-1} \text{ s}^{-1} \quad (10)$$

The modeling predictions from this approach are represented by the blue dotted lines in Figure 4 and also shown in Table 3. From the graph, it is clear that the predicted values for SX loss were slower than experimentally observed, but provide a slightly better overall agreement for the caffeine data.

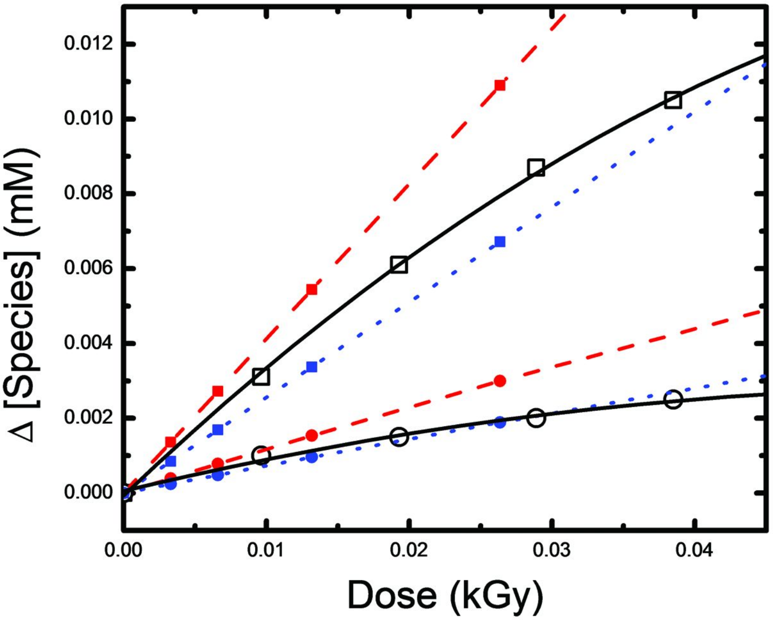

Figure 4. Summary of the computer modeling results of this study. Black open symbols are experimental data for sulfamethoxazole (□) and caffeine (○) concentration changes with applied dose. Solid black lines are quadratic fits, with removal constant values calculated as 0.36 and 0.096, respectively. Red dashed lines are model predictions when using the effective rate constants (k_{meas} x efficiency), and blue dotted lines are the predictions for the "repair" model.

At this time, our simple modeling predictions cannot definitively distinguish which mechanism is most likely involved in the hydroxyl radical oxidations. Based on only calculated values of the removal constant for these two model versions (Table 3), it appears that the first mechanism, incorporating the measured rate constant and efficiency as a product effective rate constant, is in better agreement. This was further supported by our attempts to model the experimental measurements for the opposing ratios, 10 μM SX and 50 μM caffeine. These predicted removal constant values are also shown in Table 3. Under these conditions, both the repair and k_{eff} models under-predict the loss of SX, but with the latter closer to the experimental values. In contrast, both models over-predict the removal of caffeine, with the repair model being in slightly better agreement. It is clear that additional parameters, such as the inclusion of the reactivities of the transient species produced, as well as the ultimate oxidized products, are likely necessary in the modeling to better quantify the overall chemistry. This effort is essential to understand the more complex behavior observed for multiple contaminant removal by AO/RP technologies under real-world wastewater treatment conditions.

References

1. Vorosmarty, C. J.; Green, P.; Salisbury, J.; Lammers, R. B. Global water resources: Vulnerability from climate change and population growth. *Science* **2000**, *289* (5477), 284–288.
2. Miller, G. W. Integrated concepts in water reuse: Managing global water needs. *Desalination* **2006**, *187* (1-3), 65–75.
3. Bischel, H. N.; Simon, G. L.; Frisby, T. M.; Luthy, R. G. Management experiences and trends for water reuse implementation in Northern California. *Environ. Sci. Technol.* **2012**, *46* (1), 180–188.
4. Alcamo, J.; Vorosmarty, C.; Naiman, R.; Lettenmaier, D.; Wostl, C. A grand challenge for freshwater research: Understanding the global water system. *Environ. Res. Lett* **2008**, *3* (010202), 1–6.
5. Gleick, P. H. Roadmap for sustainable water resources in southwestern North America. *Proc. Natl. Acad. Sci. U.S.A.* **2010**, *107* (50), 21300–21305.
6. Gleick, P. H. The changing water paradigm - A look at twenty-first century water resources development. *Water Int.* **2000**, *25* (1), 127–138.
7. Davies, E. G. R.; Simonovic, S. P. Global water resources modeling with an integrated model of the social-economic-environmental system. *Adv. Water Res.* **2011**, *34* (6), 684–700.
8. Tripathi, S. K.; Chintamanie, B. Social and Economic Issues of Farm Produce from Urban Waste Water Irrigation. In *Waste Management and the Environment V*; Popov, V.; et al., Eds.; Wit Press: Southampton, 2010; pp 425−433.
9. Manas, P.; Castro, E.; de las Heras, J. Irrigation with treated wastewater: Effects on soil, lettuce (Lactuca sativa L.) crop and dynamics of microorganisms. *J. Environ. Sci. Health, Part A: Toxic/Hazard. Subst. Environ. Eng.* **2009**, *44* (12), 1261–1273.
10. Exall, K.; Marsalek, J.; Schaefer, K. A review of water reuse and recycling, with reference to Canadian practice and potential: 1. Incentives and implementation. *Water Qual. Res. J. Can.* **2004**, *39* (1), 1–12.
11. *Clean Watersheds Needs Survey 2004: Report to Congress*; U.S. Environmental Protection Agency, Washington, DC, 2004.
12. Reungoat, J.; Escher, B. I.; Macova, M.; Argaud, F. X.; Gernjak, W.; Keller, J. Ozonation and biological activated carbon filtration of wastewater treatment plant effluents. *Water Res.* **2012**, *46* (3), 863–872.
13. Basile, T.; Petrella, A.; Petrella, M.; Boghetich, G.; Petruzzelli, V.; Colasuonno, S.; Petruzzelli, D. Review of endocrine-disrupting-compound removal technologies in water and wastewater treatment plants: An EU perspective. *Ind. Eng. Chem. Res.* **2011**, *50* (14), 8389–8401.
14. Nghiem, L. D.; Manis, A.; Soldenhoff, K.; Schafer, A. I. Estrogenic hormone removal from wastewater using NF/RO membranes. *J. Membr. Sci.* **2004**, *242* (1-2), 37–45.
15. Petrovic, M.; Gonzales, S.; Barcelo, D. Analysis and removal of emerging contaminants in wastewater and drinking water. *Trends Anal. Chem.* **2003**, *22* (10), 685–696.

16. Mezyk, S. P.; Rickman, K. A.; Hirsch, C. M.; Dail, M. K.; Scheeler, J.; Faust, T. Advanced Oxidation and Reduction Process (AO/RP) Radical Generation in the Laboratory and at Large Scale: An Overview. In *Sustaining Water Quality*; Ahuja, S. , Ed.; Elsevier, 2012.
17. von Sonntag, C. Advanced oxidation processes: Mechanistic aspects. *Water Sci. Technol.* **2008**, *58*, 1015–1021.
18. Andreozzi, R.; Caprio, V.; Insola, A.; Marotta, R. Advanced oxidation processes (AOP) for water purification and recovery. *Catal. Today* **1999**, *53* (1), 51–59.
19. Ikehata, K.; El-Din, M. G. Aqueous pesticide degradation by hydrogen peroxide/ultraviolet irradiation and Fenton-type advanced oxidation processes: A review. *J. Environ. Eng. Sci.* **2006**, *5* (2), 81–135.
20. Ikehata, K.; El-Din, M. G. Degradation of recalcitrant surfactants in wasterwater by ozonation and advances oxidation processes: A review. *Ozone: Sci. Eng.* **2004**, *26* (4), 327–343.
21. Gültekin, I.; Ince, N. H. Synthetic endocrine disruptors in the environment and water remediation by advanced oxidation processes. *J. Environ. Manage.* **2007**, *85* (4), 816–832.
22. Peller, J. R.; Cooper, W. J.; Ishida, K. P.; Mezyk, S. P. Evaluation of parameters influencing removal efficiencies for organic contaminant degradation in advanced oxidation processes. *AQUA* **2011**, *60*, 69–78.
23. Katsoyiannis, I. A.; Canonica, S.; von Gunten, U. Efficiency and energy requirements for the transformation of organic micropollutants by ozone, O-3/H_2O_2 and UV/H_2O_2. *Water Res.* **2011**, *45* (13), 3811–3822.
24. De la Cruz, N.; Gimenez, J.; Esplugas, S.; Grandjean, D.; de Alencastro, L. F.; Pulgarin, C. Degradation of 32 emergent contaminants by UV and neutral photo-fenton in domestic wastewater effluent previously treated by activated sludge. *Water Res.* **2012**, *46* (6), 1947–1957.
25. Mezyk, S. P.; Neubauer, T.; Cooper, W. J.; Peller, J. R. Free-radical-induced oxidative and reductive degradation of sulfa drugs in water: absolute kinetics and efficiencies of hydroxyl radical and hydrated electron reactions. *J. Phys. Chem. A* **2007**, *111* (37), 9019–9024.
26. Peller, J.; Mezyk, S. P.; Cooper, W. J. Bisphenol A reactions with hydroxyl radicals: Diverse pathways determined between deionized water and tertiary treated wastewater solutions. *Res. Chem. Intermed.* **2009**, *35*, 21–34.
27. Buxton, G.; Greenstock, C.; Helman, W. P.; Ross, A. B. Critical review of rate constants for reactions of hydrated electrons, hydrogen atoms and hydroxyl radicals ($OH/O^{\cdot -}$) in aqueous solution. *J. Phys. Chem. Ref. Data* **1988**, *17* (2), 513–886.
28. Cooper, W., J.; Snyder, S.; Mezyk, A. S.; Peller, P. , J. R.; Nickelsen, M. G. *Reaction Rates and Mechanisms of Advanced Oxidation Processes (AOPs) for Water Reuse*; Watereuse Foundation: Alexandria, VA, 2009.
29. Swancutt, K. L.; Dail, M. K.; Mezyk, S. P.; Ishida, K. P. Absolute kinetics and reaction efficiencies of hydroxyl-radical-induced degradation of methyl isothiocyanate (MITC) in different quality waters. *Chemosphere* **2010**, *81* (3), 339–344.

30. Kesavan, P. C.; Powers, E. L. Differential modification of oxic and anoxic components of radiation damage in *Bacillus megaterium* spores by caffeine. *Int. J. Radiat. Biol.* **1985**, *48*, 223–233.
31. Buxton, G. V.; Stuart, C. R. Re-evaluation of the thiocyanate dosimeter for pulse radiolysis. *J. Chem. Soc. Faraday, Trans.* **1995**, *91*, 279–281.
32. Song, W.; Cooper, W. J.; Peake, B. M.; Mezyk, S. P.; Nickelson, M. G.; O'Shea, K. E. Free radical destruction of N,N′-diethyl-m-toluamide (DEET) in aqueous solution. *Water Res.* **2009**, *43*, 635–642.

Chapter 3

Ferrate(VI): A Green Chemistry Oxidant for Removal of Antibiotics in Water

Virender K. Sharma,*,1 George Anquandah,[1] Hyunook Kim,[2]
Jia-Qian Jiang,[3] and Radek Zboril[4]

[1]Department of Chemistry and Center of Ferrate Excellence,
Florida Institute of Technology, Melbourne, Florida 32901, United States
[2]The University of Seoul, Dept. of Environmental Engineering,
90 Jeonnong-dong Dongdaemun-gu, Seoul 130-743, Korea
[3]School of Engineering and Built Environment, Glasgow Caledonian University, Cowcaddens Road, Glasgow, Scotland, G4 0BA, United Kingdom
[4]Regional Centre of Advanced Technologies and Materials, Departments of Experimental Physics and Physical Chemistry, Faculty of Science, Palacky University, Slechtitelu 11, 78371 Olomouc, Czech Republic
[*]E-mail : vsharma@fit.edu

Ferrate(VI) ($Fe^{VI}O_4^{2-}$, Fe(VI)) ion is an environmentally-friendly chemical for water treatment, which can peform a dual function of oxidation and disinfection and forms a non-toxic byproduct, iron(III). This chapter presents an assessment of the potential of ferrate(VI) to oxidize antibiotics (A). The kinetics, stoichiometry, and products and their antibacterial properties are presented. The second-order rate constants, k, of the oxidation reactions at neutral pH were in the range from 5.0×10^{-1} - 1.5×10^{3} $M^{-1}s^{-1}$. At a 10 mg L^{-1} K_2FeO_4 dose, half-lives of the oxidation reaction would be in seconds to minutes at a neutral pH. The values of k, and the reaction half-lives, varied with pH. The stoichiometry of the reactions of Fe(VI) with sulfamethoxazole and trimethoprim were 4:1 and 5:1 ([Fe(VI):[A]), respectively. Oxidation products of the reactions were found to be relatively less toxic than parent molecule. The oxidized products of trimethoprim showed no significant antibacterial activity. Examples of efficient removal of antibiotics from the wastewater by Fe(VI) are presented.

In Novel Solutions to Water Pollution; Ahuja, S., et al.;
ACS Symposium Series; American Chemical Society: Washington, DC, 2013.

Overall, ferrate(VI) oxidation could be an effective treatment method for the purification of waters containing antibiotics.

Introduction

There is a great concern of occurrence of antibiotics in the aquatic environment (*1*). The use of antibiotics in aquaculture has been banned in the European Union. Currently used water and wastewater treatment processes are not adequate to remove antibiotics. Antibiotics are therefore frequnetly detected in effluents and sludge from municipal wastewater treatment plants in the concentration ranges from ng L^{-1} to μg L^{-1} in water and from μg kg^{-1} to mg kg^{-1} in sludge (*1–6*). A low level of antibiotics in the water may not be of concern, but the presence of antibibiotic-resistent pathogens is a growing global problem (*7–9*). According to World Health Organization (WHO), the antibiotic resistance is one of the biggest human health issues of this century (*10*). Effective treatment processes are needed to remove antibiotics in water in order to circumvalent the spread of antibiotic-resistant bacteria.

Advanced oxidation processes (AOPs) have been demonstrated to eliminate antibiotics from water (*11–19*). Ozone is effective in removing antibiotics, but a study showed that the transformed products were biologically active (*20*). Chlorination though remove antibiotics, however, chlorination byproducts may be more toxic than the parent molecules (*21–24*). Chlorine dioxide has also been investgated to oxidize antibiotics (Navalon et al. 2008; Wang et al. 2010). The transformation of antibiotics under typical ClO_2 disinfection doses may not eliminate antibacterial activity (*25*). In recent years, ferrate(VI) ($Fe^{VI}O_4^{2-}$, Fe(VI)) is emerging an novel oxidant to remove micropollutants in water (*26–28*).

This chapter summarizes the kinetics and products of the oxidation of antibiotics by Fe(VI), followed by a brief discussion on the mechanism of the reactions. Examples are presented on the removal of antibiotics in wastewater effluents.

Ferrate(VI)

Ferrate(VI) is a tetra-oxy anion in which four oxygen atoms are coordinated tetrahederally with the iron atom (*29*). A number of salts of the anion have been synthesized, but sodium and potassium salts (Na_2FeO_4 and K_2FeO_4) are commonly applied in performing studies relavant to environmental remediation. Numeous methods can be applied to quantify the concentrations of Fe(VI) ion in solid and solutions phases and these methods have recently been reviewed (*30*). Fe(VI) ion in alkaline solution has a characteristic visible spectrum ($\varepsilon_{510\,nm} = 1150\ M^{-1}cm^{-1}$), which is frequently used to determine its concentration at pH 9.0. The fundamental properties of Fe(VI) has recently been summarized (*31*). Ferrate(VI) has shown a significant capability as a coagulant (*32*, *33*). The final reduced by-product of Fe(VI) is a non-toxic ferric ion, Fe(III), which is an effective coagulant for removing metals, non-metals, radionuclides, nutrients, and humic acids (*32–43*). Examples include the treatment of arsenic, metal cyanides, and phosphate (*34*, *39*, *44*). Fe(VI) is also an effective disinfectant (*45*). A number of microorganisms can be treated with Fe(VI) and species that are susceptible to Fe(VI) include virus *f2,* Virus *Qβ*, *Escherichia coli*, *Bacillus cereus*, *Bacillus subtils, Streptococcus bovis*, *Staphylococcus aureus*, *Shigella flexneri*, *Streptococci faecalis*, *Salmonella typhimurium*, and *Canadida albican* (*41*, *42*, *46–49*). Recent studies showed that Fe(VI) is highly effective in treating *Ichthyophthirius multifiliis* (*50*, *51*). This species can effect freshwater fish and Fe(VI) treatment can thus prevent economic loss to the aquaculture industry. Removal of microcystin-LR by Fe(VI) has also been suggested (*52*).

The redox potentials of Fe(VI) ion are +2.20 V and +0.72 V in acidic and alkaline solutions, respectively (*53*). The redox potential in acidic media is the higher than most of the oxidants currently used in water and wastewater treatment (*33*, *47*, *54*, *55*). Fe(VI) has a relatively high reactivity with sulfur and nitrogen containing pollutants (*27*, *33*, *56*, *57*) and most of pollutants can be removed in seconds to minutes time scales (*26*, *28*, *58*, *59*). Mechanism of the reactions have been described in detail (*31*, *58*, *60*). Fe(VI) can effectively oxidize micropollutants such as endocrine disruptors, and pharmaceuticals and personal care products (*11*, *48*, *61–66*). The following sections focuses on the oxidative transformations of antibiotics by Fe(VI).

Kinectics

The rate-law for the oxidation of antibiotics (A) by F(VI) were found to be first-order for each reactant (Eq. 1)

$$-d[\mathrm{Fe(VI)}]/dt = k[\mathrm{Fe(VI)}]_{\mathrm{tot}}[\mathrm{A}]_{\mathrm{tot}} \tag{1}$$

where k represents the second-order rate constant for the reaction of Fe(VI) with santibiotics, $[\mathrm{Fe(VI)}]_{\mathrm{tot}}$ represents the total concentration of Fe(VI) species, and $[\mathrm{A}]_{\mathrm{tot}}$ represents the total concentration of antibiotics. The observed second-order rate constants decreased non-linearly with increasing pH (*13*, *39*, *67*, *68*). The values of k at pH 8.0 and 7.0 at 25 °C are given in Table 1. Sulfonamide contains two moieties, an aniline ring and a five- or six-membered heterocyclic aromatic group, connected to both sides of sulfonamide linkage (-NH-SO_2-). At pH 7.0, the reactivity of sulfonamides with Fe(VI) is of the order of 10^2 – 10^3 $M^{-1}s^{-1}$, which indicate their effective removal by Fe(VI). Ciprofloxacin has secondary amine moiety and can react with Fe(VI) with second-order rate constants of the order of $k_{\mathrm{app}} \sim 10^2$ $M^{-1}s^{-1}$ (Table 1). Enrofloxacin and trimethoprim have tertiary amine moieties and reacted with Fe(VI) at a slower rate than that of ciprofloxacine. This is consistent with the general trend of reactivity of amines with Fe(VI) (*69–71*).

Table 1. Second-Order Rate Constants for Selected Antibiotics in Reaction with Ferrate(VI) (pH 7.0 and 8.0; 25 °C)

Compound	*k ($M^{-1}s^{-1}$)*	*$t_{1/2}$**	*k ($M^{-1}s^{-1}$)*	*$t_{1/2}$**
	pH 8.0		*pH 7.0*	
Sulfisoxazole[a]	3.5×10^{2}	39.3 s	1.5×10^{3}	9.2 s
Sulfamethazine[a]	1.1×10^{2}	125 s	1.1×10^{3}	13.2 s
Sulfamethizole[a]	3.8×10^{1}	365 s	4.1×10^{2}	33.9 s
Sulfadimethoxine[a]	–	–	7.9×10^{1}	175 s
Sulfamethoxazole[a]	4.6×10^{1}	301 s	1.3×10^{3}	10.4 s
Ciprofloxacin[c]	1.7×10^{2}	81 s	4.7×10^{2}	29 s
Enrofloxacin[c]	2.4×10^{1}	573 s	4.7×10^{1}	290 s
Trimethoprim[b]	3.4×10^{0}	4080 s	4.3×10^{1}	318 s

* Assuming 10 mg/L K_2FeO_4 dose. [a] From ref (*68*). [b] From ref (*67*). [c] From ref (*39*).

Under the conditions of Fe(VI) concentration (10 mgL^{-1} K_2FeO_4), as might be expected in practice, the half-lives of the reactions would be in the range from 29 to 573 at pH 8.0 (Table 1). At pH 7.0 under the same conditions, the half-lives would be very short from 9.2 – 290 s (Table 1). Because the reaction rates are also temperature dependent, it gives rise to different activation energies of the reaction (*68*), and the reaction half-lives will vary significantly with the environmental conditions.

Stoichiometry and Products

Very little is known on the stoichiometric factor, η, of the reactions of Fe(VI) with antibiotics. The η is the number of Fe(VI) molecules consumed per molecule of antibiotic. Only reported values of η are known for the oxidation of sulfamethoxazole (SMX) and trimethoprim (TMP), which are ~ 4 and ~ 5, respectively, at pH 9.0 (Eqs. 2 and 3).

$$4\,\mathrm{Fe(VI)} + \mathrm{SMX} \rightarrow 4\,\mathrm{Fe(III)} + \mathrm{Products} \tag{2}$$

$$5\,\mathrm{Fe(VI)} + \mathrm{TMP} \rightarrow 4\,\mathrm{Fe(III)} + \mathrm{Products} \tag{3}$$

Values of η more than one has suggested that Fe(VI) reacts not only react with a parent molecule, but also with intermediate(s) of the reaction. Furthermore, η > 1indicates that the values of *k* reported in Table 1, which were obtained from the monitoring of Fe(VI), must be assessed with caution in order to predict the degradation of antibiotics.

The products of the oxidation of SMX by Fe(VI) at pH 9.0 showed that Fe(VI) attacked on the isoxazole and aniline moieties of the SMX (*68*). The isoxazole ring was opened and aniline was transformed to nitro group and hence products obtained were expected to be relatively non-toxic. The detail product analysis was also performed on the oxidation of TMP by Fe(VI) at pH 7.0. The cleavage of TMP by Fe(VI) resulted in 3,4,5-trimethoxybenzaladehyde (TMBA) and 2,4-dinitropyrimidine (DNP). A systematic analysis of products at different molar ratios of Fe(VI) to TMP using liquid chromatography-tandem mass spectrometry (LC-MS/MS) proposed a reaction scheme of oxidation reaction (Figure 1). Fe(VI) preferentially attacked an activated bridging methylene group of TMP to yield TMP-OH (Pathway 1). A further reaction of TMP-OH formed a ketone product, TMP=O (Pathway 2). Cleavage of TMP-OH also occurred to form TMBA and diamianopyrimidine (DAP) (Pathway 3). A reaction of Fe(VI) with DAP gave DNP (Pathway 4).

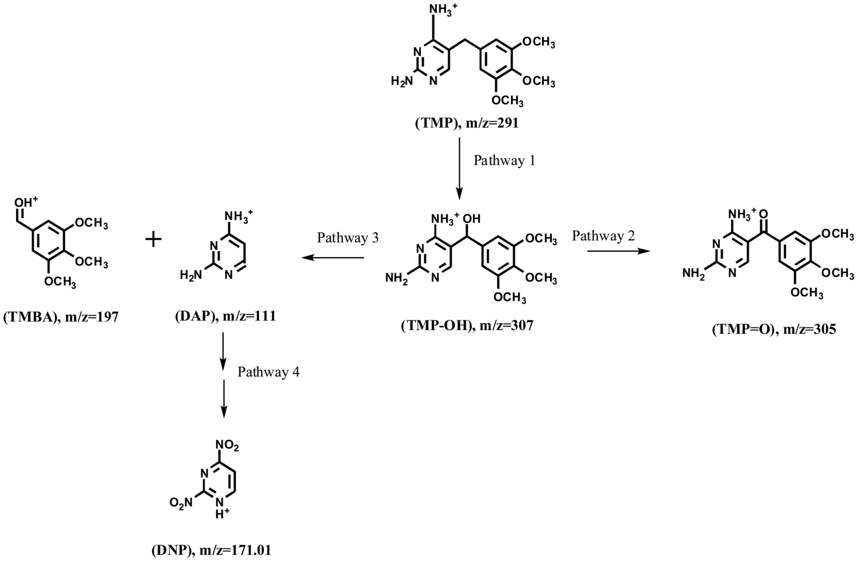

Figure 1. Reaction pathways for oxidation of TMP by Fe(VI). (Adapted from (67) with permission of American Chemical Society).

An elimination of DAP by Fe(VI) to yield DNP as a final product is significant because the antibacterial properties of TMP has been attributed to the DAP moiety (*72*, *73*). Since DAP moity completely transferred to DNP, elimination of TMP by Fe(VI) was expected to have no antibacterial activity. This was confirmed by testing antibacterial property of the reaction mixture solutions againsts *E. coli*. In these experiments dose-response plots were constructed and details are given elsewhere (*67*). Estimated values of MIC and EC_{50} were ~0.2 $x10^{-6}$ M and ~ 8.0 × 10^{-6} M, respectively. From the dose-response plots, a potency equivalent quotient (PEQ) value was calculated (Eq. 4).

$$PEQ = EC_{50,0}/EC_{50,X} \qquad (4)$$

$EC_{50,0}$ in Eq. 4 is the EC_{50} value calculated from the measured dose-response relationship for the TMP without any Fe(VI) oxidant added and $EC_{50,x}$ is the EC_{50} for the corresponding plots with × M Fe(VI) dosed to the TMP to cause oxidation.

Figure 2A shows the plot of individual calculated PEQs versus the $[TMP]/[TMP]_o$ in each sample. The straight line demonstrate a loss of one mole of TMP would result in the loss of one PEQ of the TMP antibacterial properties. A negative deviation of the experimental data in Figure 2A indicates that not only the oxidation products had no antibacterial properties, but also interfered with the inhibition properties of TMP. The non-linear negative deviation from the ideal suggests that the oxidation products of TMP formed at various dosages of Fe(VI) caused different interference(s) to the inhibition properties of TMP. Results of Figure 2A clearly indicate that products formed from the reactions of Fe(VI) and TMP had insignificant antibacterial potency compared to the TMP. Results of ozone oxidation of TMP were different from that of Fe(VI) (Figure 2B). However, TMP was deactivated by O_3 with a stoichiometry of approximately 1 PEQ lost for each mole fraction equivalent consumed by reaction with O_3 (*74*) This is also in agreement with the target moiety attack on TMP by O_3 (*74*).

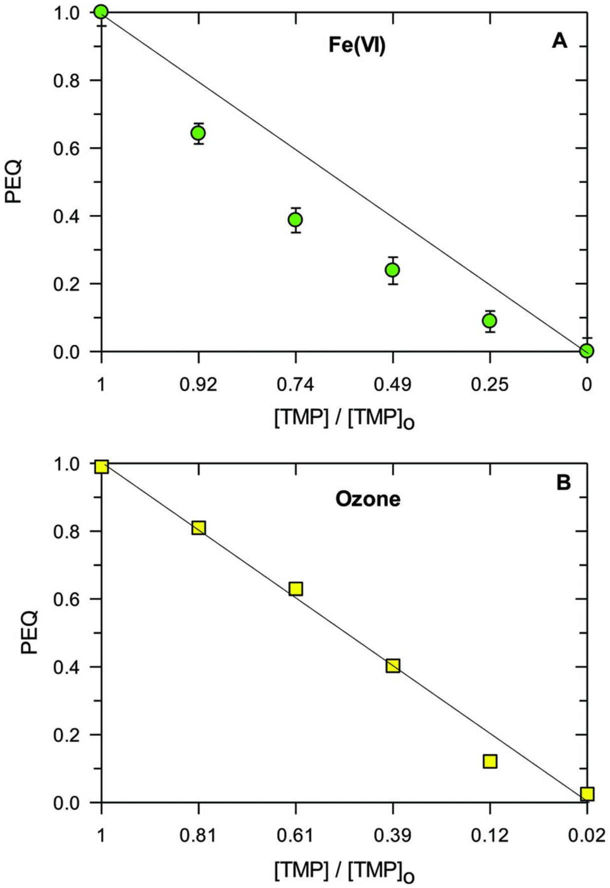

Figure 2. Potency equivalent quotient plots with corresponding TMP oxidation by Fe(VI) (A) and (B). (Adapted from (67) and (74) with the permission of the American Chemical Society).

Removals

A study on the oxidative elimination of tetracycline by Fe(VI) in buffered solution at different pH and molar ratios has been performed (*75*). The optimal pH range for degradation of tetracycline was 9-10 and most of tetracycline was degraded (> 90 %) in 1 min. However, degradation of dissolved organic carbon was below 15 %; suggesting incomplete mineralization to carbon dioxide. It is likely that naphthol ring in the tetracycline could not be transformed by Fe(VI).

Removal of ciprofloxacine by Fe(VI) has been sought in the model wastewater (*76*). At a concentration of 100 μg L^{-1} of ciprofloxacine in model wastewater, Fe(VI) dose of less than 0.3 mg L^{-1} could remove 60 % of the antibiotic. Increase of Fe(VI) dosage up to 1 mg L^{-1} could achieve only 80 % ciprofloxacine. In other study, elimination of ciprofloxacine of > 85 % in a secondary effluent from a pilot wastewater treatment plant was obtained at a Fe(VI) dose of 5 mg Fe L^{-1} at pH 8.0 (*11*, *39*). At this dose of Fe(VI), other antibiotics, sulfamethoxazole and enrofloxacine, could also be eliminated more than 90 %.

A detailed study on the removal of selected pharmaceuticals in secondary wastewater effluents by Fe(VI) has been performed (*77*). Results of the study are presented in Figure 3. Removal of antibiotics were from 74 – 99 %. Removals of sulfonamide and trimethoprim were expected bases on aniline moieties in these molecules, which could easily be attacked by Fe(VI). Removal of trimethoprim has also been demonstrated in the secondary effluent (*67*). Fluoroquinolones, ciprofloxacin, lemefloxacine and norfloxacin have piperazine's secondary amine moieties, which could react at faster rates with Fe(VI) to result in their high removal (Table 1). Enrofloxacine contains the tertiary amine and reacted slower with Fe(VI); hence lower removal of it compared to secondary amines containing fluoroquinolones (Figure 3). Tercyclines have phenolic moieties, which have shown rapid reactions with Fe(VI) (*78–81*). Therefore, Fe(VI) had high potential to remove tetracyclines (Figure 3). Among the macrolides, erythromycin did not react with Fe(VI) while roxithromycin and oleandomycin could be removed by Fe(VI) (Figure 3) (*77*). It is possible that dehydration of erythromycin on the 14-membered lactone ring would make it difficult to attack the aniline moiety (*77*). More research is needed to describe no reactivity of erythromycin with Fe(VI).

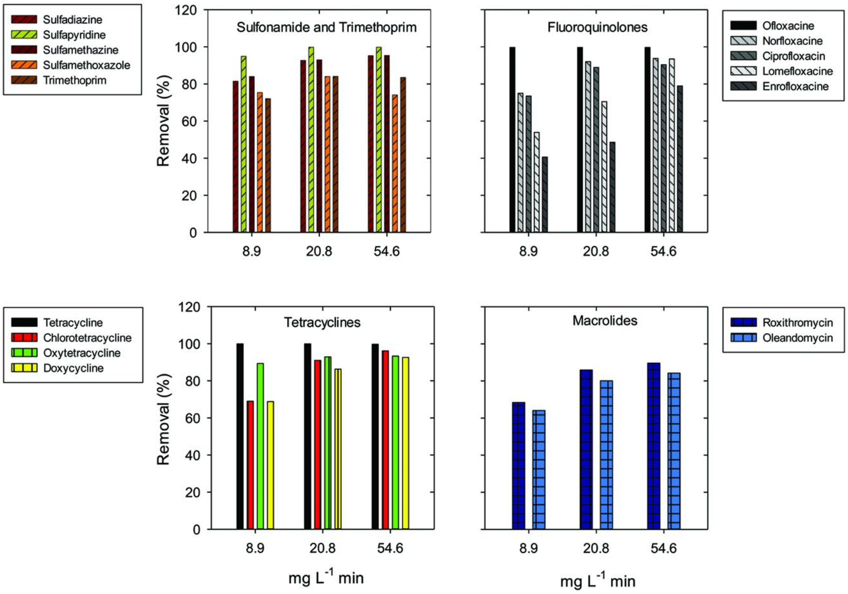

Figure 3. Removal (%) of selected antibiotics spiked in wastewater during Fe(VI) treatment. (data were taken from (77))

Conclusions

The kinetics of studied reactions of Fe(VI) with antibiotics suggests the high potential of the removal of antibiotics in water and wastewater. High removal of antibiotics spiked into wastewater matric also support the kinetics results, however, kinetics of reactions are known for only few antibiotics and more studies are needed to determine rate constants of the oxidation of antibiotics having different moieties. Stoichiometry of the reactions of the reactions between Fe(VI) and antibiotics are known only for very few molecules and a future research should include the determination of stoichiometric ratio in order to estimate the removal efficiency of antibiotics by Fe(VI) from the rate studies. Also, detailed products and their antibacterial activities are limited to only trimethoprim and more research in this area is required to assess fully if Fe(VI) fully removes antibacterial property after transforming the parent antibiotic molecule. Finally, a role of organic matter in removing of antibiotics by Fe(VI) is lacking and a systematic investigation using different kinds of organic matter is needed.

Acknowledgments

V.K. Sharma wishes to acknowledge United States National Science Foundation (CBET 1236331) for ferrate research. The authors gratefully acknowledge the support by the Operational Program Research and Development for Innovations - European Regional Development Fund (project CZ.1.05/2.1.00/03.0058) and by the Operational Program Education for Competitiveness - European Social Fund (project CZ.1.07/2.3.00/20.0056) of the Ministry of Education, Youth and Sports of the Czech Republic.

References

1. Li, B.; Zhang, T. PH significantly affects removal of trace antibiotics in chlorination of municipal wastewater. *Water Res.* **2012**, *46*, 3703–3713.
2. Yu, K.; Li, B.; Zhang, T. Direct rapid analysis of multiple PPCPs in municipal wastewater using ultrahigh performance liquid chromatography-tandem mass spectrometry without SPE pre-concentration. *Anal. Chim. Acta* **2012**.
3. De la Cruz, N.; Giménez, J.; Esplugas, S.; Grandjean, D.; De Alencastro, L. F.; Pulgarín, C. Degradation of 32 emergent contaminants by UV and neutral photo-fenton in domestic wastewater effluent previously treated by activated sludge. *Water Res.* **2012**, *46*, 1947–1957.
4. López-Roldán, R.; de Alda, M. L.; Gros, M.; Petrovic, M.; Martín-Alonso, J.; Barceló, D. Advanced monitoring of pharmaceuticals and estrogens in the Llobregat River basin (Spain) by liquid chromatography-triple quadrupole-tandem mass spectrometry in combination with ultra performance liquid chromatography-time of flight-mass spectrometry. *Chemosphere* **2010**, *80*, 1337–1344.
5. Zhang, T.; Li, B. Occurrence, transformation, and fate of antibiotics in municipal wastewater treatment plants. *Crit. Rev. Environ. Sci. Technol.* **2011**, *41*, 951–998.

In Novel Solutions to Water Pollution; Ahuja, S., et al.;
ACS Symposium Series; American Chemical Society: Washington, DC, 2013.

6. Le-Minh, N.; Khan, S. J.; Drewes, J. E.; Stuetz, R. M. Fate of antibiotics during municipal water recycling treatment processes. *Water Res.* **2010**, *44*, 4295–4323.
7. Storteboom, H.; Arabi, M.; Davis, J. G.; Crimi, B.; Pruden, A. Identification of antibiotic-resistance-gene molecular signatures suitable as tracers of pristine river, urban, and agricultural sources. *Environ. Sci. Technol.* **2010**, *44*, 1947–1953.
8. Lapara, T. M.; Burch, T. R.; McNamara, P. J.; Tan, D. T.; Yan, M.; Eichmiller, J. J. Tertiary-treated municipal wastewater is a significant point source of antibiotic resistance genes into Duluth-Superior Harbor. *Environ. Sci. Technol.* **2011**, *45*, 9543–9549.
9. Gao, P.; Mao, D.; Luo, Y.; Wang, L.; Xu, B.; Xu, L. Occurrence of sulfonamide and tetracycline-resistant bacteria and resistance genes in aquaculture environment. *Water Res.* **2012**, *46*, 2355–2364.
10. Levy, S. B. The challenge of antibiotic resistance. *Sci. Am.* **1998**, *278*, 46–53.
11. Lee, Y.; Gunten, U. V. Oxidative transformation of micropollutants during municipal wastewater treatment: Comparison of kinetic aspects of selective (chlorine, chlorine dioxide, ferrate^{VI}, and ozone) and non-selective oxidants (hydroxyl radical). *Water Res.* **2010**, *44*, 555–566.
12. Sharma, V. K. Oxidative transformations of environmental pharmaceuticals by Cl_2, ClO_2, O_3, and Fe(VI): Kinetics assessment. *Chemosphere* **2008**, *73*, 1379–1386.
13. Sharma, V. K.; Li, X. Z.; Graham, N.; Doong, R. A. Ferrate(VI) oxidation of endocrine disruptors and antimicrobials in water. *J. Water Supply: Res. Technol.--AQUA.* **2008**, *57*, 419–426.
14. Hu, L.; Stemig, A. M.; Wammer, K. H.; Strathmann, T. J. Oxidation of antibiotics during water treatment with potassium permanganate: Reaction pathways and deactivation. *Environ. Sci. Technol.* **2011**, *45*, 3635–3642.
15. Martin Ruel, S.; Choubert, J. M.; Esperanza, M.; Miège, C.; Navalón Madrigal, P.; Budzinski, H.; Le Ménach, K.; Lazarova, V.; Coquery, M. On-site evaluation of the removal of 100 micro-pollutants through advanced wastewater treatment processes for reuse applications. *Water Sci.Technol.* **2011**, *63*, 2486–2497.
16. Navalon, S.; Alvaro, M.; Garcia, H. Reaction of chlorine dioxide with emergent water pollutants: Product study of the reaction of three β-lactam antibiotics with ClO_2. *Water Res.* **2008**, *42*, 1935–1942.
17. Sirtori, C.; Agüera, A.; Gernjak, W.; Malato, S. Effect of water-matrix composition on trimethoprim solar photodegradation kinetics and pathways. *Water Res.* **2010**, *44*, 2735–2744.
18. Wang, P.; He, Y.-L.; Huang, C.-H. Reactions of tetracycline antibiotics with chlorine dioxide and free chlorine. *Water Res.* **2011**, *45*, 1838–1846.
19. Luo, X.; Zheng, Z.; Greaves, J.; Cooper, W. J.; Song, W. Trimethoprim: Kinetic and mechanistic considerations in photochemical environmental fate and AOP treatment. *Water Res.* **2012**, *46*, 1327–1336.
20. Radjenovic, J.; Godehardt, M.; Petrovic, M.; Hein, A.; Farre, M.; Jekel, M.; Barcelo, D. Evidencing generation of persistent ozonation products of

antibiotics roxithromycin and trimethoprim. *Environ. Sci. Technol.* **2009**, *43*, 6808–6815.

21. Kosjek, T.; Heath, E. Applications of mass spectrometry to identifying pharmaceutical transformation products in water treatment. *TrAC, Trends Anal. Chem.* **2008**, *27*, 807–820.
22. Fatta-Kassinos, D.; Meric, S.; Nikolaou, A. Pharmaceutical residues in environmental waters and wastewater: Current state of knowledge and future research. *Anal. Bioanal. Chem.* **2011**, *399*, 251–275.
23. Bulloch, D. N.; Lavado, R.; Forsgren, K. L.; Beni, S.; Schlenk, D.; Larive, C. K. Analytical and biological characterization of halogenated gemfibrozil produced through chlorination of wastewater. *Environ. Sci. Technol.* **2012**, *46*, 5583–5589.
24. Quintana, J. B.; Rodil, R.; López-Mahía, P.; Muniategui-Lorenzo, S.; Prada-Rodríguez, D. Investigating the chlorination of acidic pharmaceuticals and by-product formation aided by an experimental design methodology. *Water Res.* **2010**, *44*, 243–255.
25. Wang, P.; He, Y.-L.; Huang, C.-H. Oxidation of fluoroquinolone antibiotics and structurally related amines by chlorine dioxide: Reaction kinetics, product and pathway evaluation. *Water Res.* **2010**, *44*, 5989–5998.
26. Sharma, V. K. Kinetics and mechanism of formation and destruction of N-nitrosodimethylamine in water: A review. *Sep. Purif. Technol.* **2012**, *88*, 1–10.
27. Sharma, V. K. Oxidation of nitrogen containing pollutants by novel ferrate(VI) technology: A review. *J. Environ. Sci. Health, Part A: Toxic/Hazard. Subst. Environ. Eng.* **2010**, *45*, 645–667.
28. Sharma, V. K. Potassium ferrate(VI): Environmental friendly oxidant. *Adv. Environ. Res.* **2002**, *6*, 143–156.
29. Hoppe, M. L.; Schlemper, E. O.; Murman, R. K. Structure of potassium ferrate(VI). *Acta Crystallogr.* **1982**, *B38*, 2237–2239.
30. Luo, Z.; Strouse, M.; Jiang, J. Q.; Sharma, V. K. Methodologies for the analytical determination of ferrate(VI): A review. *J. Environ. Sci. Health, Part A: Toxic/Hazard. Subst. Environ. Eng.* **2011**, *46*, 453–460.
31. Sharma, V. K. Oxidation of inorganic contaminants by ferrates(Fe(VI), Fe(V), and Fe(IV)) - Kinetics and mechanisms - A review. *J. Environ. Manage.* **2011**, *92*, 1051–1073.
32. Jiang, J. Q.; Wang, S. enhanced coagulation with potassium ferrate(VI) for removing humic substances. *Environ. Eng. Sci.* **2003**, *20*, 627–633.
33. Jiang, J.; Lloyd, B. Progress in the development and use of ferrate(VI) salt as an oxidant and coagulant for water and wastewater treatment. *Water Res.* **2002**, *36*, 1397–1408.
34. Filip, J.; Yngard, R. A.; Siskova, K.; Marusak, Z.; Ettler, V.; Sajdl, P.; Sharma, V. K.; Zboril, R. Mechanisms and efficiency of the simultaneous removal of metals and cyanides by using ferrate(VI): Crucial roles of nanocrystalline iron(III) oxyhydroxides and metal carbonates. *Chem. Eur. J.* **2011**, *17*, 10097–10105.
35. Sharma, V. K.; Sohn, M. Aquatic arsenic: Toxicity, speciation, transformations, and remediation. *Environ. Int.* **2009**, *35*, 743–759.

In Novel Solutions to Water Pollution; Ahuja, S., et al.;
ACS Symposium Series; American Chemical Society: Washington, DC, 2013.

36. Sharma, V. K.; Yngard, R. A.; Cabelli, D. E.; Clayton Baum, J. Ferrate(VI) and ferrate(V) oxidation of cyanide, thiocyanate, and copper(I) cyanide. *Radiat. Phys. Chem.* **2008**, *77*, 761–767.
37. Yngard, R.; Damrongsiri, S.; Osathaphan, K.; Sharma, V. K. Ferrate(VI) oxidation of zinc-cyanide complex. *Chemosphere* **2007**, *69*, 729–735.
38. Yngard, R. A.; Sharma, V. K.; Filip, J.; Zboril, R. Ferrate(VI) oxidation of weak-acid dissociable cyanides. *Environ. Sci. Technol.* **2008**, *42*, 3005–3010.
39. Lee, Y.; Zimmermann, S. G.; Kieu, A. T.; Gunten, G. V. Ferrate (Fe(VI)) application for municipal wastewater treatment: A novel process for simultaneous micropollutant oxidation and phosphate removal. *Environ. Sci. Technol.* **2009**, *43*, 3831–3838.
40. Jiang, J. Q; Stanford, C.; Alsheyab, M. The online generation and application of ferrate(VI) for sewage treatment: A pilot scale trial. *Sep. Purif. Technol.* **2009**, *68*, 227–231.
41. Jiang, J. Q.; Wang, S.; Panagoulopoulos, A. The role of potassium ferrate(VI) in the inactivation of Escherichia coli and in the reduction of COD for water remediation. *Desalination* **2007**, *210*, 266–273.
42. Jiang, J. Q.; Wang, S.; Panagoulopoulos, A. The exploration of potassium ferrate(VI) as a disinfectant/coagulant in water and wastewater treatment. *Chemosphere* **2006**, *63*, 212–219.
43. Jiang, J. Q.; Lloyd, B.; Grigore, L. Preparation and evaluation of potassium ferrate as an oxidant and coagulant for potable water treatment. *Environ. Eng. Sci.* **2001**, *18*, 323–328.
44. Jain, A.; Sharma, V. K.; Mbuya, M. S. Removal of arsenite by Fe(VI), Fe(VI)/Fe(III), and Fe(VI)/Al(III) salts: Effect of pH and anions. *J. Hazard. Mater.* **2009**, *169*, 339–344.
45. Sharma, V. K. Disinfection performance of Fe(VI) in water and wastewater:A review. *Water Sci. Technol.* **2007**, *55*, 225–232.
46. Makky, E. A.; Park, G.-S.; Choi, I.-W.; Cho, S.-I.; Kim, H. Comparison of Fe(VI) (FeO_4^{2-}) and ozone in inactivating *Bacillus subtilis* spores. *Chemosphere* **2011**, *83*, 1228–1233.
47. Sharma, V. K.; Kazama, F.; Jiangyong, H.; Ray, A. K. Ferrates as environmentally friendly oxidants and disinfectants. *J. Water Health* **2005**, *3*, 45–58.
48. Jiang, J. Q. Research progress in the use of ferrate(VI) for the environmental remediation. *J. Hazard. Mater.* **2007**, *146*, 617–623.
49. Kim, H.; Sharma, V. K. Innovative Ferrate [iron(VI)] Technology in Sludge Treatment. In *Innovative Ferrate(VI) Technology in Water and Wastewater Treatment*; Sharma, V. K., Jiang, J. Q., Bouzek, K., Eds.; Proceedings of the International Symposium, May 31, 2004, Prague, Czech Republic; pp 74−82.
50. Ling, F.; Wang, J.-G.; Wang, G.-X.; Gong, X.-N. Effect of potassium ferrate(VI) on survival and reproduction of *Ichthyophthirius multifiliis* tomonts. *Parasitol. Res.* **2011**, *109*, 1423–1428.
51. Ling, F.; Wang, J.-G.; Liu, Q.-F.; Li, M.; Ye, L.-T.; Gong, X.-N. Prevention of *Ichthyophthirius multifiliis* infestation in goldfish (*Carassius auratus*) by potassium ferrate(VI) treatment. *Vet. Parasitol.* **2010**, *168*, 212–216.

52. Sharma, V. K.; Triantis, T. M.; Antoniou, M. G.; He, X.; Pelaez, M.; Han, C.; Song, W.; O'Shea, K. E.; De La Cruz, A. A.; Kaloudis, T.; Hiskia, A.; Dionysiou, D. D. Destruction of microcystins by conventional and advanced oxidation processes: A review. *Sep. Purif. Technol.* **2012**, *91*, 3–17.
53. Wood, P. M. The redox potential for dimethyl sulfoxide reduction to dimethyl sulfide. *FEBS Lett.* **1981**, *124*, 11–14.
54. Sharma, V. K. Use of iron(VI) and iron(V) in water and wastewater treatment. *Water Sci. Technol.* **2004**, *49*, 69–74.
55. Anquandah, G.; Ray, M. B.; Ray, A. K.; Al-Abduly, A. J.; Sharma, V. K. Oxidation of X-ray compound ditrizoic acid by ferrate(VI). *Environ. Technol.* **2011**, *32*, 261–267.
56. Eng, Y. Y.; Sharma, V. K.; Ray, A. K. Ferrate(VI): Green chemistry oxidant for degradation of cationic surfactant. *Chemosphere* **2006**, *63*, 1785–1790.
57. Ghernaout, D.; Naceur, M. W. Ferrate(VI): In situ generation and water treatment – A review. *Desalin. Water Treat.* **2011**, *30*, 319–332.
58. Sharma, V. K.; Luther, G. W., III; Millero, F. J. Mechanisms of oxidation of organosulfur compounds by ferrate(VI). *Chemosphere* **2011**, 1083–1089.
59. He, C.; Li, X.; Sharma, V. K.; Li, S. Elimination of sludge odor by oxidizing sulfur-containing compounds with ferrate(VI). *Environ. Sci. Technol.* **2009**, *43*, 5890–5895.
60. Sharma, V. K. Oxidation of inorganic compounds by ferrate (VI) and ferrate(V): One-electron and two-electron transfer steps. *Environ. Sci. Technol.* **2010**, *44*, 5148–5152.
61. Sharma, V. K.; Anquandah, G. A. K.; Nesnas, N. Kinetics of the oxidation of endocrine disruptor nonylphenol by ferrate(VI). *Environ. Chem. Lett.* **2009**, *7*, 115–119.
62. Sharma, V. K.; Anquandah, G. A. K.; Yngard, R. A.; Kim, H.; Fekete, J.; Bouzek, K.; Ray, A. K.; Golovko, D. Nonylphenol, octylphenol, and bisphenol-A in the aquatic environment: A review on occurrence, fate, and treatment. *J. Environ. Sci. Health, Part A: Toxic/Hazard. Subst. Environ. Eng.* **2009**, *44*, 423–442.
63. Anquandah, G. A. K.; Sharma, V. K. Oxidation of octylphenol by ferrate(VI). *J. Environ. Sci. Health, Part A: Toxic/Hazard. Subst. Environ. Eng.* **2009**, *44*, 62–66.
64. Hu, L.; Page, M.; Marinas, B.; Shisler, J. L.; Strathmann, T. J. Treatment of emerging pathogens and micropollutants with potassium ferrate (VI). *Proc. - Water Qual. Technol. Conf. Expo.* **2010**, hu11/1–hu11/8.
65. Hu, L.; Martin, H. M.; Arce-Bulted, O.; Sugihara, M. N.; Keating, K. A.; Strathmann, T. J. Oxidation of carbamazepine by Mn(VII) and Fe(VI): Reaction kinetics and mechanism. *Environ. Sci. Technol.* **2009**, *43*, 509–515.
66. Zimmermann, S. G.; Schmukat, A.; Schulz, M.; Benner, J.; Gunten, U. V.; Ternes, T. A. Kinetic and mechanistic investigations of the oxidation of tramadol by ferrate and ozone. *Environ.l Sci. Technol.* **2012**, *46*, 876–884.
67. Anquandah, G. A. K.; Sharma, V. K.; Knight, D. A.; Batchu, S. R.; Gardinali, P. R. Oxidation of trimethoprim by ferrate(VI): Kinetics, products, and antibacterial activity. *Environ. Sci. Technol.* **2011**, *45*, 10575–10581.

68. Sharma, V. K.; Mishra, S. K.; Nesnas, N. Oxidation of sulfonamide antimicrobials by ferrate(VI) [$Fe^{VI}O_4^{2-}$]. *Environ. Sci. Technol.* **2006**, *40*, 7222–7227.
69. Noorhasan, N. N.; Sharma, V. K.; Cabelli, D. Reactivity of ferrate(V) (FeVO43-) with aminopolycarboxylates in alkaline medium: A premix pulse radiolysis. *Inorg. Chim. Acta* **2008**, *361*, 1041–1046.
70. Noorhasan, N.; Patel, B.; Sharma, V. K. Ferrate(VI) oxidation of glycine and glycylglycine: Kinetics and products. *Water Res.* **2010**, *44*, 927–937.
71. Carr, J. D. Kinetics and Product Identification of Oxidation by Ferrate(Vi) of Water and Aqueous Nitrogen Containing Solutes. In *Ferrates: Synthesis, Properties, and Applications in Water and Wastewater Treatment*; Sharma, V. K., Ed.; ACS Symposium Series 985; American Chemical Society: Washington, DC, 2008; pp 189−196.
72. Simo, B.; Perello, L.; Ortiz, R.; Castineiras, A.; Latorre, J.; Canton, E. Interactions of metal ions with a 2,4-diaminopyrimidine derivative (trimethoprim). Antibacterial studies. *J. Inorg. Biochem.* **2000**, *81*, 275–283.
73. Vandanyan, R.; Hruby, V. *Synthesis of Essential Drugs*. Elsevier: Amsterdam, The Netherlands, 2006.
74. Dodd, M. C.; Kohler, H. P. E.; Gunten, U. V. Oxidation of antibacterial compounds by ozone and hydroxyl radical: Elimination of biological activity during aqueous ozonation processes. *Environ. Sci Technol.* **2009**, *43*, 2498–2504.
75. Ma, Y.; Gao, N.; Li, C. Degradation and pathway of tetracycline hydrochloride in aqueous solution by potassium ferrate. *Environ. Eng. Sci.* **2012**, *29*, 357–362.
76. Jiang, J. Q.; Zhou, Z.; Pahl, O. Preliminary study of ciprofloxacin (cip) removal by potassium ferrate(VI). *Sep. Purif. Technol.* **2012**, *88*, 95–98.
77. Yang, B.; Ying, G.-G.; Zhao, J.-L.; Liu, S.; Zhou, L.-J.; Chen, F. Removal of selected endocrine disrupting chemicals (EDCs) and pharmaceuticals and personal care products (PPCPs) during ferrate(VI) treatment of secondary wastewater effluents. *Water Res.* **2012**, *46*, 2194–2204.
78. Huang, H.; Sommerfield, D.; Dunn, B. C.; Erying, E. M.; Lloyd, C. R. Ferrate(VI) oxidation of aqueous phenol: Kinetics and mechanism. *J. Phys. Chem. A* **2001**, *195*, 3536–3541.
79. Rush, J. D.; Cyr, J. E.; Zhao, Z.; Bielski, B. H. The oxidation of phenol by ferrate(VI) and ferrate(V). A pulse radiolysis and stopped-flow study. *Free Radical Res.* **1995**, *22*, 349–360.
80. Lee, Y.; Yoon, J.; von Gunten, U. Kinetics of the oxidation of phenols and phenolic endocrine disruptors during water treatment with ferrate (Fe(VI)). *Environ. Sci. Technol.* **2005**, *39*, 8978–8984.
81. Sharma, V. K. Ferrate(VI) and ferrate(V) oxidation of organic compounds: Kinetics and mechanism. *Coord. Chem. Rev.* **2012**, *257*, 495–510.

Chapter 4

Natural Treatment of Surface Water and Groundwater with Woodchip Reactors

M. Palomo,*,[1] A. Bhandari,[2] H. Enriquez,[2] and W. Rodriguez[1]

**[1]Department of Civil Engineering, California State Polytechnic University,
3801 West Temple Avenue, Pomona, California 91768
[2]Department of Civil Engineering, Kansas State University,
2118 Fielder Hall, Manhattan, Kansas 66506
*Phone: 909-869-4144. Fax: 909-869-4342.
E-mail: mpalomo@csupomona.edu**

Nitrate contamination is one of the most serious water quality challenges in California's groundwater basins. Over-application of nitrogen-containing fertilizers increases nitrate levels in runoff, which in turn increases the nitrate level in shallow aquifers, rivers and lakes. In natural water systems, high concentration of nutrients like nitrate can cause the occurrence of eutrophication and hypoxia, or degradation of the groundwater quality by the increased concentration of dissolved solids in potential sources of drinking water. Human consumption of water with nitrate concentrations above maximum contaminant levels results in health problems such as blue-baby syndrome and cancer. Cost-effective and readily accessible woodchips bioreactors have been used in field-scale systems in the Midwest to reduce nitrate levels in surface and drainage waters. A laboratory bench-scale system, similar to that used in the field, was used to treat nitrogen-laden tile water in Iowa State University (ISU) and to treat Cal Poly Pomona groundwater that was naturally contaminated with nitrate. At universities, ISU and Cal Poly Pomona identical bioreactors where used to study the effectiveness of the systems. When treated in woodchip bioreactors, both tile water and groundwater nitrate concentrations were reduced below the drinking water standard (10 mg/L NO_3-N). Retention time and flow rate were important factors to increase the effectiveness of the biological treatment. Bioreactors were run for at least 6 days to ensure stable microbial community while the degradation of nitrate was monitored. Nitrate percent removal was higher for tile water than for groundwater. For the Iowa tile water 8-hr retention time was enough to achieve 96 % nitrate removal, while less that 40% was achieved for groundwater at the same retention time. Our results indicated a range 15% to 40% removal rate of nitrate in groundwater. Woodchip bioreactors were amended with soil and succinate to increase microbial population and to stimulate denitrification through an external source of carbon. Addition of succinate increased nitrate removal to 73% in the groundwater system, indicating that the groundwater system was carbon-limited for optimum denitrification, but that denitrification can be enhanced by the addition of a harmless, easily degradable carbon source. Woodchip reactors are a low-cost system that can contribute to the remediation of California's shallow groundwater systems.

Introduction

Excessive fertilizer use in urban and agricultural areas and wastewater overflows have caused serious nitrate pollution in surface water, groundwater and marine environments (*1*). Efforts to differentiate agricultural from other anthropogenic sources of nitrates in groundwater have been investigated in existing literature (*2*, *3*), nevertheless, the total nitrate present in groundwater is the concern of this study. Nitrate that is not assimilated by plants is leached from soils and can percolate into ground waters and/or be washed into freshwater reservoirs and discharged into the ocean through urban storm water systems (*4*–*6*). Excess nitrate enhances algal growth, resulting in uncontrolled algae blooms in freshwater, which reduces dissolved oxygen and affects aquatic ecosystems through degradation of the water quality. Red tide blooms (algae blooms) caused by high nitrate concentrations are frequently observed off the coast of Southern California (*7*). Hypoxia produced by decay of such blooms is associated with mortality of marine fauna (*7*, *8*). In recharge basins, uncontrolled algae growth promotes precipitation of suspended solids to the bottom of the basins, reducing infiltration rates in groundwater recharge activities. Algae layers accumulating in the bottom of the basins increase the annual cost of operation and maintenance of basins that receive reclaimed water with high nitrate concentrations.

Many groundwater basins in Southern California, including the groundwater used by California State Polytechnic University, Pomona campus (Cal Poly Pomona), have been historically underused due to high nitrate concentrations (*9*). Consumption of drinking water with high nitrate levels has been associated with methemoglobinemia (blue-baby syndrome) (*10*) and with increased risk of cancer (*11*). Groundwater sources with nitrate levels above the EPA maximum (10 mg/L N), must be treated before its use for drinking water. Currently in Southern California the two most commonly used processes, for the removal of nitrate, for production of safe drinking water are ion exchange (IE), and reverse osmosis (RO). However, both are energy intensive processes which are not 100% efficient, and generate brine waters that are frequently discharged into the sea or sent out for treatment to the LA Sanitation District wastewater treatment facilities.

Water scarcity in Southern California has made the reclamation of groundwater, runoff water, wastewater (*12*), and available local surface water a critical task to be able to meet the water demands in the region. High dependence on imported water (water from Northern California and the Colorado River) to satisfy Southern California water demands, and recent reductions of water allocations from the north due to environmental issues in the Bay-Delta area, have led State and public agencies to seek ways to maximize the use of local water resources to satisfy Southern California water demands while reducing dependence on imported water sources (*13–16*).

According to the California Department of Public Health (CDPH), biological treatment for drinking water production is not allowed. However, CDPH has allowed a minimum of six months of soil aquifer treatment (SAT) of recharged reclaimed water before pumping for drinking water production (*17*). Groundwater recharge of reclaimed water has been practiced by Agencies like Orange County Water District and the Inland Empire Utilities Agency among others. Thus, reclamation of groundwater via natural treatment systems like woodchip reactors could be feasible if CDPH requirements are met.

In the Midwest, natural and engineered approaches have been used to remediate surface water and drainage containing nitrate. Engineered woodchip bio-reactors have been used in agricultural and urban applications and appear to be the most cost effective and lowest maintenance option for nitrate reduction via microbial denitrification (*10*, *18–21*). Microbial denitrification requires a carbon source (derived from woodchips and/or total carbon in the water), anoxic conditions, denitrifying bacteria, and the presence of nitrate in the water. Under the appropriate conditions, bacteria naturally present in the woodchips, form complex communities that act to reduce nitrate to N_2, a process known as respiratory or dissimalatory denitrification (DNR). Initially, all oxygen available in the bio-reactor is consumed by microbial respiration. When nitrate is introduced to the bioreactor, and dissolved oxygen (DO) is depleted, bacteria capable of denitrification induce the production of a set of alternative respiratory enzymes that reduce nitrate to nitrite, then to nitric oxide and nitrous oxide, and ultimately to N_2 gas ($NO_3^- \rightarrow NO_2^- \rightarrow NO + N_2O \rightarrow N_2$ (g)) (*22*, *23*). Under anaerobic conditions, where DO concentrations are under 2 mg/L, NO_3^- acts as the primary electron acceptor, thus starting the conversion process of NO_3^- to N_2 gas, thus achieving the reduction of nitrate present in water.

Field-scale woodchip reactors used in the Midwest have not required bacterial inoculation, just a constant source of nitrate and anoxic conditions. Effectiveness of such field-system has been observed even after 7 years of placement (*24*). The work presented here shows the results from a bench-scale system that mimics the field-scale systems used in Midwest agricultural fields to reduce nutrients in runoff water to improve stream quality. In addition, this study shows how a similar bench-scale system could be used in Southern California to remediate shallow groundwater contaminated with nitrate (*7*, *25*, *26*). The proposed system is not intended to replace drinking water production systems, but to improve quality of groundwater that could be further exposed to SAT (*17*).

In Southern California, groundwater is a more reliable and less expensive local water source than imported water resources (*27*). The city of Pomona (one of the largest cities in LA County) and Cal Poly Pomona use groundwater to satisfy part of their water demands. Groundwater is pumped out of the Spadra Basin (Figure 1). The water quality of the Spadra basin has been degraded due to the overuse of fertilizers (such as ammonium nitrate- NH_4NO_3) for agricultural, gardening, and animal grazing activities (*6*). These have led to runoff and infiltration of nitrate into the groundwater. Groundwater pumped out at Cal Poly Pomona contains nitrate concentrations above the drinking water standard (10 mg/L as N). Due to the increasing water demands and increasing cost of imported water, in 1992, the City of Pomona started the operations of an ion exchange facility to treat groundwater and produce 15 MGD of drinking water. Drinking water demands at Cal Poly Pomona have been met by producing drinking water through the blending of disinfected groundwater with treated imported surface water. In 2011, Cal Poly Pomona received funds from a Department of Public Health grant to build a "Cal Poly Pomona Water Filtration Facility", which will be completed in May of 2013. The facility will treat nitrate and organics in groundwater, producing approximately 340,000 GPD (~80% campus demand) by means of reverse osmosis.

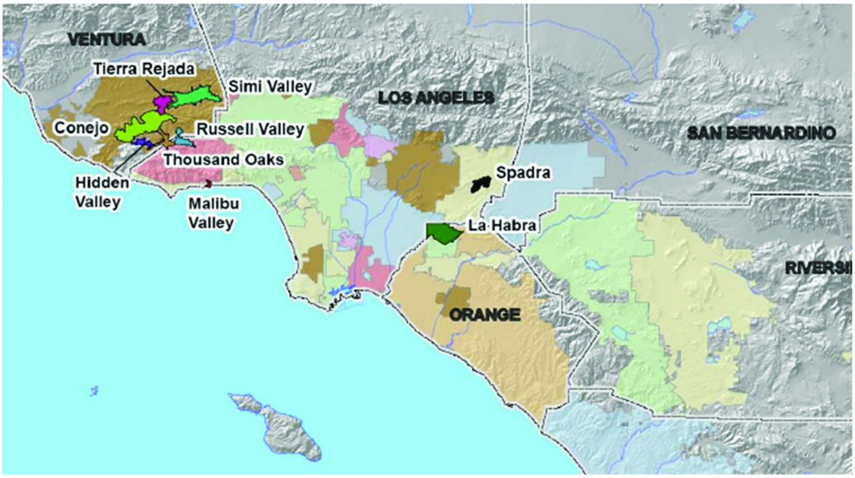

Figure 1. Location of Spadra Basin within the LA area. Figure taken from MWD 2007, Groundwater Assessment Study (authorized use from MWD).

The high water demands in the LA area have required the use of advance technology to reclaim water sources that otherwise would not be used for the production of safe drinking water (*17*). Changes in nutrient management practices, like reduction in fertilizer application, and improvement of nutrient storage facilities, have been acknowledged as sources to improve groundwater quality (*28*). However, remediation of groundwater and surface water sources via natural treatment systems should be explored as a way to sustain the environment and to possibly reduce costs of advance treatment once the quality of the water sources has been improved. The goal of the work presented here is to show how a bench-scale natural treatment system that works to improve surface water quality (similar to those used in the field in the Midwest) could be successfully used to reclaim valuable groundwater sources in Southern California. Natural treatment of groundwater could potentially reduce the high capital investment required to produce drinking water by advance water treatment systems and reduce the production of the undesirable brine.

Methods and Materials

Nalgen bottles, 1050 mL volume, were used along with varied mass of wood chips (ranging from 220 to 390 g of woodchips per bottle depending on the source of woodchips: Golden Valley Hardscapes, Story City, IA, or, in California, Garden EarthGro-The Natural Choice, Scotts Lawn Care, ½″ x 1″ chipped wood). The porosity of the columns varied from 72% (Iowa) to 54% (California). Porosity was determined by dividing the volume of water in the bottle with woodchips by total bottle volume, expressed as a percent. Field tile water was used as reactor influent for the study at ISU, while field groundwater was used for the experiments conducted at Cal Poly Pomona (GW- Cal Poly Pomona well 1).

Column replicates were run using two pumps (MasterFlex, C/L) with dual channels to run replicates. Tile water or groundwater was continuously added to the system with the aid of the pumps at a flow rate varying from 0.9 ml/min to 1.6 ml/min, depending on the desired contact time. Influent was pumped through 1.40 mm diameter tubing. Columns were conditioned with DI water for seven days before starting the first experiment, to allow establishment of constant pumping rate and stable microbial community before influent and effluent parameter measurements began. Influent water was replenished every 24 hours. Samples from influent and effluent were collected and tested every 24 hours for the duration of the study. Influent and effluent were analyzed for color (Hach programs platinum cobalt standard method, 5 to 500 units), total dissolved solids (gravimetric method), conductivity (HQ440d Benchtop Dual Input, Multi-Parameter Meter with an IntelliCAL™ CDC40101 digital, graphite, 4-pole conductivity probe), turbidity (Hach 2100N), alkalinity (titration), hardness (Hach programs- method 8030) and total organic carbon (TOC) (Hach direct method 101209- LR 0.3 to 20 mg C/L). In Iowa, nitrate was quantified using an Automated Flow Injection Ion Analyzer (Lachat, QuickChem 8000); while in California a Dionex Ion chromatograph ICS 1100 (Pump, degasser, injection valve, conductivity Detector with anion self-regenerating suppressor ASRS 300 4 mm, IonPac AS19 Analytical Column, and an ionPac AG19 guard column) was used.

Column Setup

Three column experiments were performed with different retention times. In Iowa, retention times of 4.2, 6.3, and 8 hours with flow rates of 3, 2 and 1.58 ml/min, respectively, were recorded. In California retention, times of 6, 8, 10, and 12 hours with flow rates of 1.34, 1.25, 0.99, and 0.72 ml/min were used. The tubing was inserted from the top of the bottle with the opening of the tube pushed to the bottom so that the influent could be pumped upward. The column set up is shown in Figure 2. Experiments were run in the laboratory at room temperature; averaging 22° C. To test if additional bacteria would further enhance denitrification, soil was used at each contact time to amend the column media in the Iowa systems. Fifteen grams of soil were added to a column for each of the above contact times. In California, an additional experiment was conducted where succinate was added to the groundwater as a labile carbon source (*29*) to enhance denitrification (8.35 hours of retention time and a flow rate of 0.944 ml/min).

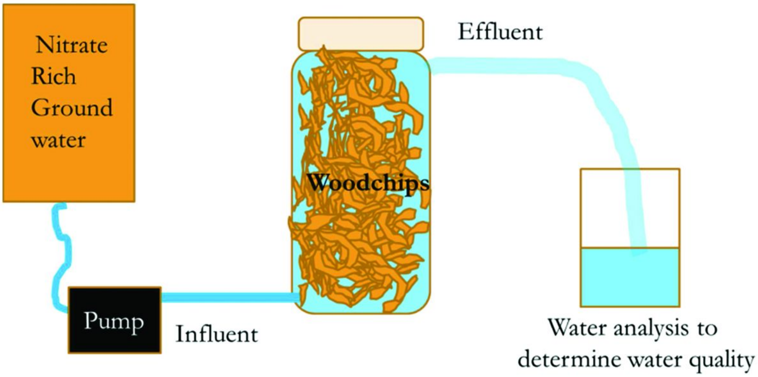

Figure 2. Column experimental set up used to study nitrate removal from tile water and groundwater.

Results and Discussion

Cal Poly Pomona

Historically the nitrate level in groundwater pumped from the Spadra basin averaged 55 mg/L NO_3^- (*4–6*). Table 1 shows the minimum and maximum NO_3^- concentrations as determined by Cal Poly Pomona facilities. Currently, Cal Poly Pomona is blending groundwater with imported water from the Colorado River to reduce nitrate levels to approximately 26 mg/L NO_3^-. Imported water nitrate levels are minimal compared to groundwater, so blending has heretofore been a good solution to satisfy Cal Poly Pomona campus water demand.

However, reductions in imported water allocation, dependence on the imported water source to reduce nitrate concentrations, and at-risk pumping rights due to limiting pumping flow rates have led the Cal Poly Pomona facilities manager to seek the construction of a reverse osmosis facility to increase pumping rates, while producing good quality water and having the benefit of eliminating dependence on imported water.

Table 1. Cal Poly Pomona Groundwater System Nitrate Concentration. (Adapted from Cal Poly Pomona Water Quality Reports, 2009, 2010, 2011)

Chemical or Constituents (ppm as NO_3^-)	*MCL*	*MCLG*	*MWD Supply*		*Cal Poly Groundwater System*	
			Range	*Average*	*Range*	*Average*
Nitrate [2009]	45	45	1.2-1.8	1.5	50-60	57 25.5*
Nitrate [2010]	45	45	1.4-2.2	1.8	38-60	55 27.0*
Nitrate [2010]	45	45	1.4-2.2	1.8	52-57	54 27.0*

* Based on weekly sampling of blend of well water and MWD water that is supplied to the campus.

Efficiency of the Woodchips System Treating Tile Water

The influent used was from field tile water (ISU Farm, Ames, IA) that had an average electrical conductivity of 765 µS. Figure 3 shows the nitrate concentration in the influent and effluent from three column experiments performed with retention times of 4.2, 6.3, and 8 hours, with flow rates of 3, 2 and 1.58 mL/min, respectively. Influent nitrate concentration was fairly constant with values around 11 mg/L NO_3-N, higher than the 10 mg/L standard recommended by EPA. Influent TOC in the tile water was typically between 3 and 5 mg/L. Treatment of tile water with woodchips alone showed that at any of the studied detention times, nitrate can be removed by the system to below 10 mg/L. However, as contact time increased the removal of nitrate increased. While after 4.2 hours of contact 7 mg/L NO_3-N were left in the water, after 6 and 8 hours, only 3 and 1 mg/L of NO_3-N, respectively, were detected. Results are in agreement with contact times and removal rates reported for in-field pilot scale drainage bioreactors (*21*).

The results from the bioreactors amended with 15 grams of soil are shown in Figure 1. Results are observed at three different retention times. The results at 4.2 hours of contact showed that nitrate was slightly lowered but not removed to levels lower than 6 mg/L. In contrast, beyond 6 hours of contact, nitrate was removed almost completely from the system, leaving only approximately 1- 2 mg/L NO_3^-N. Though addition of soil to the woodchip reactor does not represent the real field condition, it helped to augment treatment efficiency by increasing microbial activity and possibly due to the extra source of easily degradable carbon required for the denitrification process. The experimental set up was shown to be effective at removing nitrate from surface water, with efficiency that varied depending on the retention time of the systems.

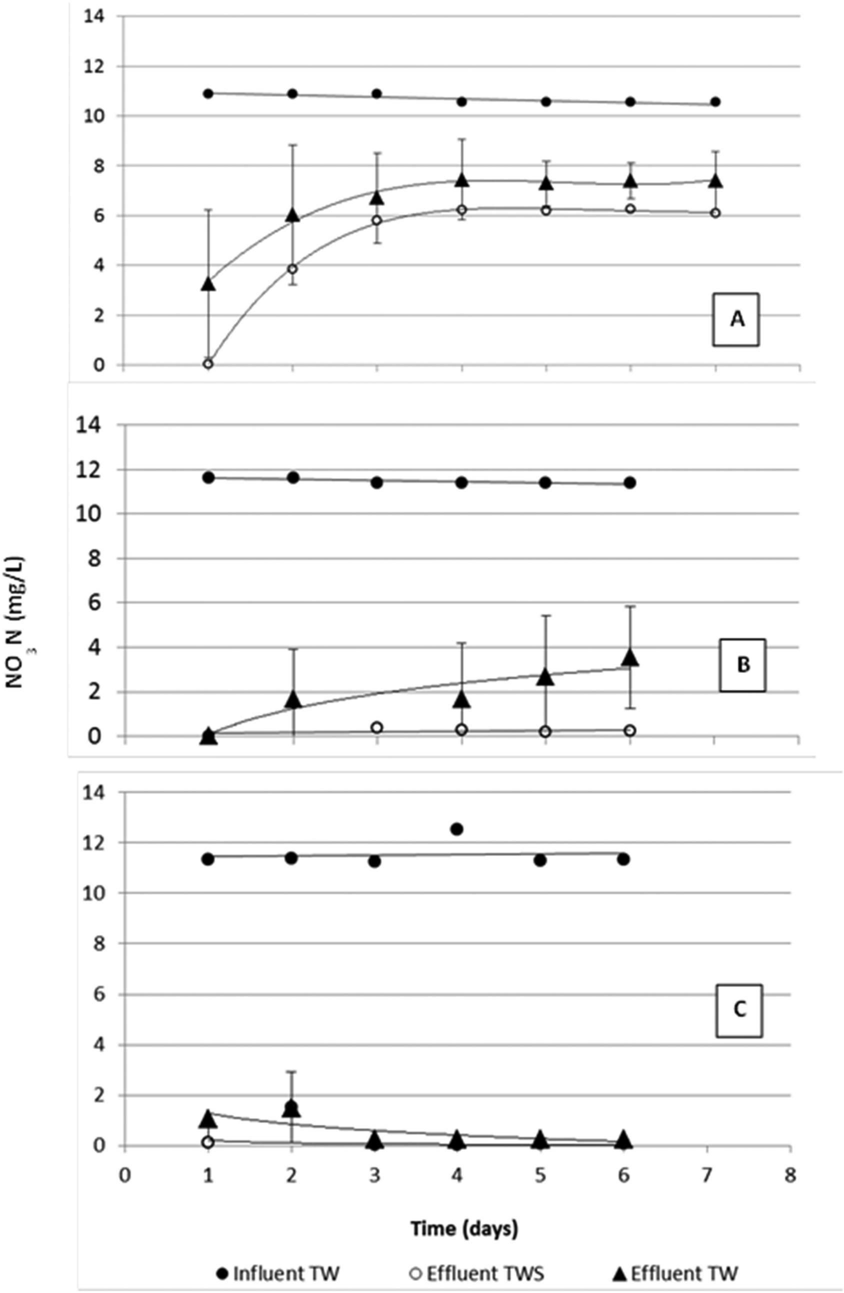

Figure 3. Removal of nitrate from tile water (TW) using woodchip reactors in Ames, Iowa. Effluent nitrate concentrations in reactors with woodchips only (Effluent TW) and in reactors amended with soil (Effluent TWS) at A) 4.2 hours, B) 6 hours and C) 8 hours.

Efficiency of the Woodchips Systems Treating Cal Poly Pomona's Groundwater

Since the system used for surface water in Iowa was proven to effectively remove nitrate from surface water, it was hypothesized that a similar system would be effective at removing nitrate from groundwater at Cal Poly Pomona. Though historically groundwater extracted from the Spadra basin contained nitrate levels well above the drinking water standards, such high levels were not observed in two of the experiments conducted. Additionally, nitrate levels were highly variable within the period of studies. The average values of various water quality parameters of the groundwater are shown in Table 2. Visual inspection of the groundwater did not allow distinguishing from tap water.

Table 2. Groundwater Quality Analysis

Groundwater Quality Parameters	*Average Value*
pH	7.17
Turbidity	0.21 NTU
Total dissolved solids	559 mg/L
Color	5 PtCo
Conductivity	1,100 μS
Total Organic Carbon	0.30 mg/L
Total hardness	322 mg/L $CaCO_3$
Total alkalinity	376 mg/L as $CaCO_3$

While groundwater commonly contains low suspended solids, low organics and high salt concentration, surface water has higher content of suspended solids and more organic carbon due to the exposure to atmosphere (*30*). Thus, to ensure that effective removal of nitrate was achieved under the bench-scale conditions, specifically at low organic carbon, the shortest retention time used to treat groundwater was 6 hours.

Figure 4 shows the results of nitrate removal from groundwater at four different contact times. Independently of influent nitrate concentration of 6, 8 and 10 hours of retention, effluent nitrate concentration ranged from 9 to 7 mg/L NO_3^--N. However, after 12 hours only 4 mg/L of nitrate were recorded. This result should be contrasted with the tile water at 6 hours, where approximately 4 mg/L of nitrate were left in the effluent; groundwater required twice the time to reach the same nitrate concentration as surface water.

Although the woodchip system was not as effective at removing nitrate to levels below the drinking water standard for groundwater as for tile water, the system did improve the groundwater quality to acceptable nitrate levels. The difference in the type of woodchips used could contribute to the difference in effectiveness. However, the chemistry of groundwater is significantly different from that of surface water, thus it was hypothesized that a source of labile carbon was necessary to eliminate the possibility of a carbon-limiting condition in the denitrification system. In the case of the groundwater study no soil was added to the woodchip reactors because it would not represent a possible field practice, since it would be a potential contaminant for a drinking water source. Thus, no microbial enhancement was done, but addition of succinate as a source of carbon provided stimulation of the microorganisms in the reactor.

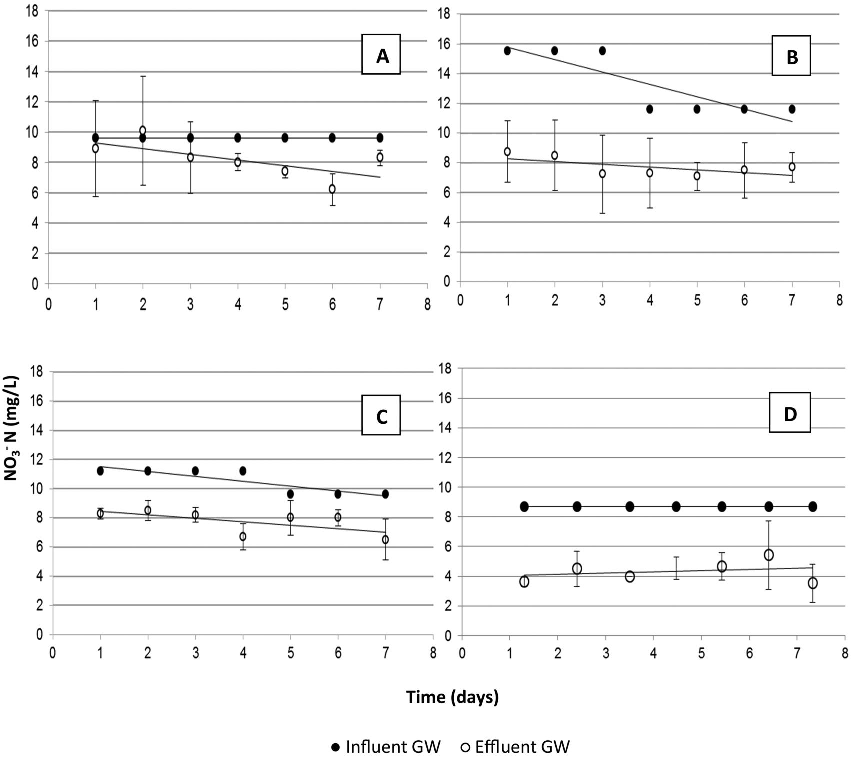

Figure 4. Nitrate removal from groundwater (GW) using woodchip reactors in Cal Poly Pomona. Effluent nitrate concentrations for reactors with woodchips only (Effluent GW) at A) 6 hours, B) 8 hours and C) 10 hours, and D) 12 hours.

Groundwater Treatment System with a Labile Carbon Source

In order for denitrification to occur, four conditions must be achieved a) constant source of nitrate, b) anaerobic conditions, c) carbon source and d) presence of denitrifying bacteria. Figure 5 A) shows the nitrate concentration in the influent and effluent of the succinate-enriched system. Succinate-enriched systems were observed to be very effective enhancing nitrate removal, leaving a residual nitrate concentration of approximately 1 mg/L, regardless of the inlet nitrate concentration. Results suggested that the woodchip reactors were carbon-limited and that addition of succinate alleviated the problem. During the eight days of experimentation, the influent nitrate concentration varied significantly. However, as shown in Figure 5 B) nitrate percent removal varied from 73 to 93%, being higher at higher influent nitrate concentrations. The system performance was improved when higher nitrate concentration were recorded in the influent line. In the presence of succinate, even at low influent concentration, the effluent nitrate was less than 2 mg/L. This result is comparable to 6 hours of treatment for tile water with soil or with any of the 8-hour experiments in Iowa.

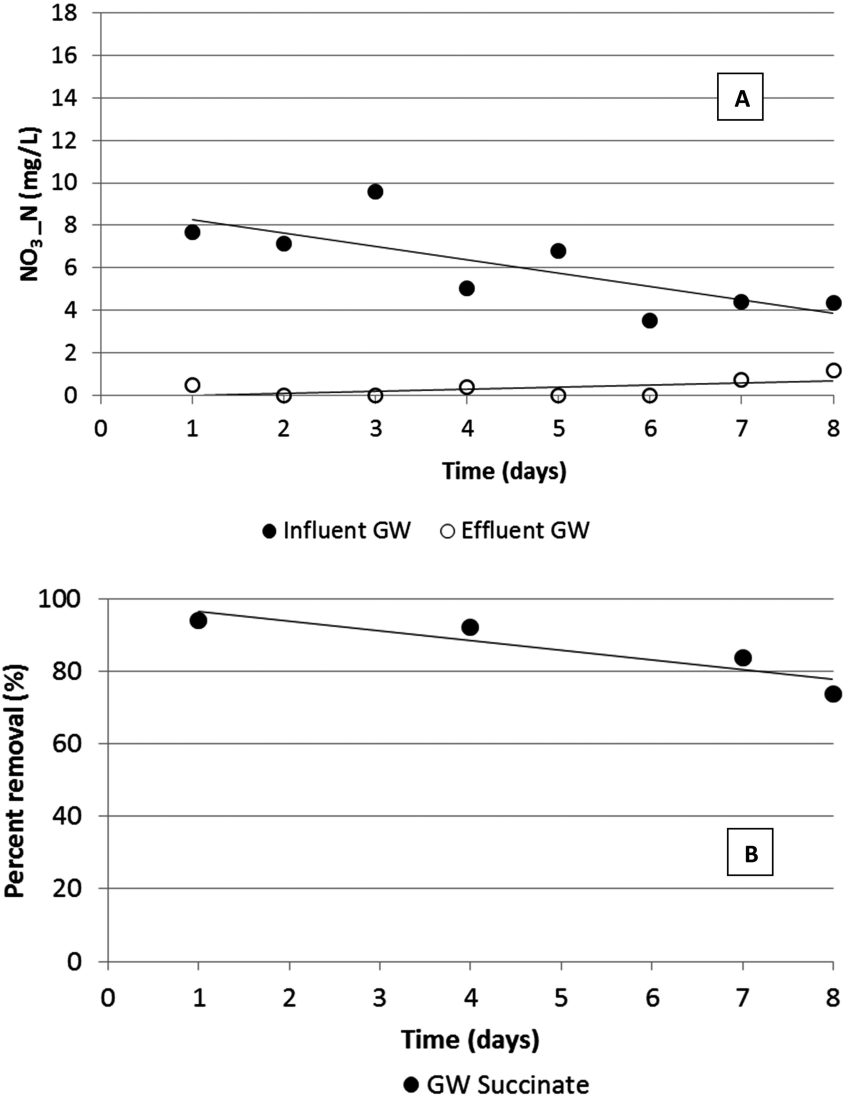

Figure 5. A) Removal of nitrate from groundwater (GW) using woodchip reactors amended with succinate, retention time of 8.35 hours and flow rate of 0.94 ml/min. B) Percent of nitrate removal in the woodchip reactors amended with succinate.

Figure 6 shows the comparison of the percent nitrate removal from tile water and from groundwater systems, both without amendment. The higher performance of the woodchip systems with tile water should be due to the higher concentration of organic carbon found in surface water, thus, the systems are not carbon limited. In the case of the groundwater the highest removal (~50%) was observed at 12 hours of retention time. Succinate addition to the system improved the removal of nitrate increasing it to 73% in 8 hours. Control of retention time in the field is a critical factor for successful use of these systems on a practical scale. Table 3 summarizes the percent nitrate removal in all the systems evaluated in this study. The best removal rates were reported when the treatment systems were amended with soil or succinate. However, in the case of tile water, 8 hours of contact were enough to reach near full removal of nitrate. In contrast, for groundwater no more than 50% of nitrate was removed after 12 hours of retention. Addition of succinate greatly improved the removal but the efficiency was never as good as the one reported for tile water.

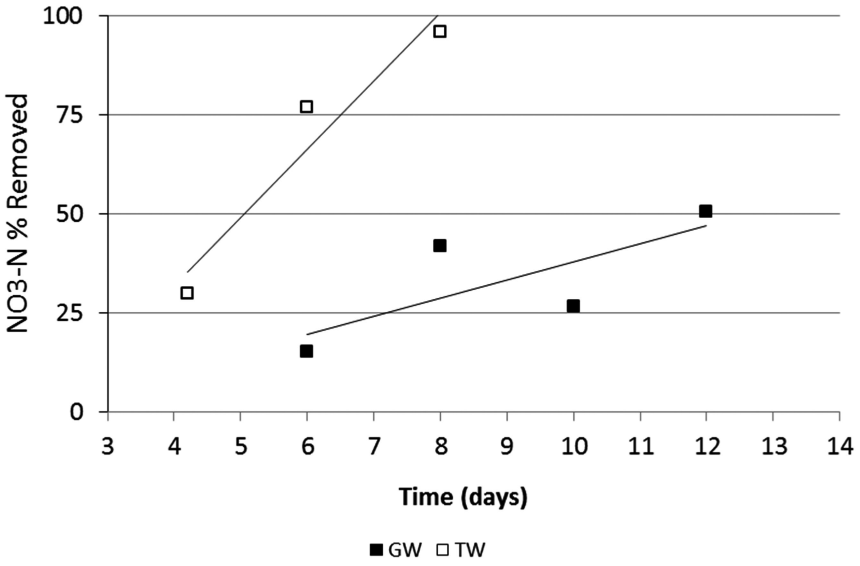

Figure 6. Comparison of the efficiency of the woodchips reactors to remove nitrate from two different water sources. No soil or succinate was added to the systems.

Table 3. Removal efficiencies for woodchip reactors

Detention time (hours)	*GW*	*GW Succinate*	*TW*	*TWS*
	% Percent Removal			
4.2	ND	ND	30	40
6.0	15	ND	77	97
8.0	42	73*	96	99
10.0	26	ND	ND	ND
12.0	50	ND	ND	ND

* Average flow rate was 8.35 ml/hr.

Conclusions

In the Midwest, bioreactors packed with woodchips seem to be a cost effective method to reduce nitrate levels in drainage water. This study evaluated the effectiveness of laboratory bench scale woodchip reactors in reducing nitrate concentration from tile water and groundwater. The efficacy of this bioreactor is proven effective at different contact times and by amending the system with extra labile carbon. Retention time was an important factor to increase efficiency of the bioreactors. Iowa's tile water yielded higher removal rate compared to Cal Poly Pomona's groundwater because of the difference in water quality. The effectiveness of an inexpensive carbon source, such as woodchips and succinate, to reduce nitrate levels in groundwater that is a potential drinking water source was evident from the effluent nitrate level results.

Higher retention times could have improved the removal rate of groundwater nitrate levels. However, a 12-hour retention time or longer is not practical at larger scales. The use of an external carbon source such as succinate to increase nitrate reduction and control of the bacterial community in the bioreactor could potentially give the means to engineer the denitrfication process in such field reactors. The results of this study indicate that woodchip reactors could be used to improve the quality of the groundwater in California, which could reduce cost of advance treatment to produce drinking water.

Acknowledgments

This research was supported by the Department of Education's College Cost Reduction & Access Act (CCRAA), the Cal Poly Pomona Kellogg Endowment Fund Kellogg Legacy Project Endowment at Cal Poly Pomona, as well as the Cal Poly Pomona President's Research, Scholarship, and Creative Activities Program. The authors would like to thank and acknowledge the constant support of Facilities Planning & Management Department at Cal Poly Pomona, especially Joe Phillipy, Leon Krebs and George Lwin for facilitating the groundwater sampling, and Dr. Marcia Murry-Ewers from the Biological Sciences Department at Cal Poly Pomona for providing the succinate. Additionally, the authors would like to acknowledge the assistance provided by undergraduate students Cindy Khov, Pedro Alvarez, Ian Berkland, and Jorge Rubalcava with the groundwater collection and testing, and Manu Ajmani, Laura Christianson and Loren Shiers at Iowa State University.

References

1. Public Drinking Water Systems. California Department of Health Services, 2004. http://www.dhs.ca.gov/ps/ddwem/chemicals/monitoring/results94-03.htm.
2. Moore, K. B.; Ekwurzel, B.; Esser, B. K.; Hudson, G. B.; Moran, J. E. *Appl. Geochem.* **2006**, *21*, 1016–1029.
3. Choi, W.-J.; Lee, S.-M.; Ro, H.-M. *Geosci. J.* **2003**, *7*, 81–87.
4. Cal Poly Pomona, Water Quality Report 2009.
5. Cal Poly Pomona, Water Quality Report 2010.
6. Cal Poly Pomona, Water Quality Report 2011.
7. Hunter, W. J. *J. Contam. Hydro.* **2001**, *53*, 119–131.
8. Rabalais, N. N.; Turner, R. E.; Justic, D.; Dortch, Q.; Wiseman, W. J.; Gupta, B. K. S. *Estuaries* **1996**, *19*, 386–407.
9. *Metropolitan Water District of Southern California*, Number 1308, 2007. http://www.mwdh2o.com/mwdh2o/pages/yourwater/supply/groundwater/gwas.html.
10. Blowes, D. W.; Robertson, W. D.; Ptacek, C. J.; Merkey, C. *J. Contam. Hydrol.* **1994**, *15*, 207–221.
11. Weyer, P. J.; Cerhan, J. R.; Kross, B. C.; Hallberg, G. R.; Kantamneni, J.; Breuer, G; Jones, M. P.; Zheng, W.; Lynch, C. F. *Epidemiol.* **2001**, *11*, 327–338.
12. Mansell, B.; Schroeder, E. *Wat. Res.* **1999**, *33*, 1845–1850.
13. *Department of Water Resources, Sacramento (DWR)*, 2005. http://www.waterplan.water.ca.gov/
14. Freeman, G. *Securing Reliable Water Supplies for Southern California*; Los Angeles County Economic Development Corporation: Los Angeles, 2008.
15. Freeman, G.; Poghosyan, M.; Lee, M. *Where Will We Get the Water? Assessing Southern California's Future Water Strategies*; Los Angeles County Economic Development Corporation: Los Angeles, 2008.
16. Colorado River Basin Water Supply & Demand Study, Interim Report No.1. U.S. Bureau of Reclamation, 2012. http://www.usbr.gov/lc/region/programs/crbstudy/report1.html
17. Asano, T.; Cotruvo, J. A. *Wat. Res.* **2004**, *38*, 1941–1951.
18. R. A. Cooke; Doheny, A. M.; Hirschi, M. C. Bio-Reactors for Edge-of-Field Treatment of Tile Outflow; ASABE Paper 0120181-17; American Society of Agricultural and Biological Engineers: St. Joseph, MI , 2001.
19. Diaz, R.; Garcia, J.; Mujeriego, R.; Lucas, M. *Environ. Eng. Sci.* **2003**, *20*, 93–702.
20. Christianson, L.; Castello, A.; Christianson, R.; Helmers, M.; Bhandari, A. *Appl. Eng. Agric.* **2010**, *26* (5), 849–854.

21. Christianson, L.; Bhandari, A.; Helmars, M. J. *J. Environ. Eng.* **2011**, *137* (4), 213–220.
22. Greben, H. A.; Tjatji, M.; Talma, S. *Proc. 2004 Water Institute Southern Africa (WISA) Biennial Conf.*, 1070–1077.
23. Zumft, W. G. In *The Prokaryotes*, 2nd ed.; Balows, A., Trüper, H. G., Dworkin, M., Harder, W., Schleifer, K. H., Eds.; Springer-Verlag: New York, 1992; pp 554–582.
24. Robertson, W. D. *Ecol. Eng.* **2010**, *36*, 1581–1587.
25. Bedessem, M. E.; Edgar, T. V.; Roll, R. *J. Environ. Qual.* **2005**, *34*, 936–942.
26. Greenan, C. M.; Moorman, T. B.; Kaspar, T. C.; Parkin, T. B.; Jaynes, D. B. *J. Environ. Qual.* **2006**, *35*, 824–829.
27. *Department of Water Resources, Sacramento (DWR)*. 2012. http://www.waterplan.water.ca.gov/cwpu2013/2012-mar-rms/index.cfm.
28. Harter, T.; Lund, J. R.; Darby, J.; Fogg, G. E.; Howitt, R.; Jessoe, K. K.; Pettygrove, G. S.; Quinn, J. F.; Viers, J. H.; Boyle, D. B.; Canada, H. E.; DeLaMora, N.; Dzurella, K. N.; Fryjoff-Hung, A.; Hollander, A. D.; Honeycutt, K. L.; Jenkins, M. W.; Jensen, V. B.; King, A. M.; Kourakos, G.; Liptzin, D.; Lopez, E. M.; Mayzelle, M. M.; McNally, A.; Medellin-Azuara, J.; Rosenstock, T. S. *Addressing Nitrate in California's Drinking Water*; Report for the State Water Resources Control Board Report to the Legislature, Groundwater Nitrate Project, Implementation of Senate Bill X2 1; University of California, Davis: Davis, CA, 2012.
29. Gierczak, R. F.; Devlin, J. F.; Rudoloph, D. L. *J. Contam. Hydrol.* **2007**, *89*, 48–70.
30. *California Department of Water Resources and Bureau of Reclamation*, 2003. http://www.water.ca.gov/groundwater/index.cfm#.

Chapter 5

In Situ Immobilization of Mercury in Water, Soil, and Sediment Using Carboxymethyl Cellulose Stabilized Iron Sulfide Nanoparticles

Yanyan Gong and Dongye Zhao[*]

**Environmental Engineering Program, Department of Civil Engineering,
Auburn University, Auburn, Alabama 36849
[*]E-mail: zhaodon@auburn.edu**

Mercury (Hg) is considered one of the most pervasive and toxic metals in the environment. As methyl mercury has been known to be the primary Hg species that accumulates in the food chain, engineered prevention of Hg methtylation is considered a key step in remediation of Hg-contaminated water, soil and sediment. To this end, effective in situ Hg remediation technologies have been consistently sought. In recent years, researchers have been exploring the feasibility of in situ immobilization of Hg through on-site delivering nanoparticles into Hg-contaminated soil/sediment. This chapter illustrates the concept and promise of the in situ Hg immobilization using a class of newly developed FeS nanoparticles. The nanoparticles were prepared using a low-cost, water-soluble carboxymethyl cellulose (CMC) as a stabilizer that can facilitate the deliverability of the nanoparticles into soil/sediment. The nanoaprticles were characterized and investigated with respect to Hg sorption behavior and effectiveness for in situ immobilization of Hg in soil/sediment. The stabilized nanoparticles offer some unique advantages, namely, high stability in water, high sorption capacity and affinity for Hg, good mobility and deliverability in soil/sediment, and controllable particle size and transport behavior in porous media. The nanoparticles were able to effectively reduce the water-leachable Hg and the TCLP (toxicity characteristic leaching procedure) based leachability. Column breakthrough

In Novel Solutions to Water Pollution; Ahuja, S., et al.;
ACS Symposium Series; American Chemical Society: Washington, DC, 2013.

tests demonstrated the deliverability and effectiveness of the nanoparticles for Hg immobilization. Once delivered, the nanoparticles remain virtually immobile under typical groundwater conditions, serving as a long-term sink for Hg. Column Hg elution tests indicated that application of the nanoparticles transferred nearly all water-leachable Hg onto the nanoparticles. As the nanoparticles are incorporated into the geo-media, the Hg adsorbed thereon is immobilized. The nanoparticle based technology provides a promising alternative for in situ remediation of Hg-contaminated sites.

Introduction

Mercury (Hg) has been known to be one of the most pervasive and bio-accumulative neurotoxins in the environment (*1*, *2*). A number of anthropogenic activities have been found responsible for elevated levels of Hg in water, soil and sediment, including mining activities, oil and coal combustion, waste incineration, crematoria, chlor-alkali industries, paper and pulp, pharmaceutical and battery manufacturing, municipal wastes, and sewage sludge incineration (*3–5*).

Hg has three valence states (+I, +II and 0), and the ready interconversion of inorganic and organic forms. Among the most cited health effects of Hg are damage of the central nervous system and the gastrointestinal tract, mental and motor dysfunction, impairment of pulmonary and kidney function, and chest pain (*6–8*). Mercury methylation takes place in anaerobic soil/sediment mediated by sulfate reducing bacteria, and the methylated Hg can then accumulate at high levels in the aquatic food chain (*9–11*). Consequently, controlling Hg methylation is considered a key step to mitigate human exposure to Hg.

To mitigate human exposure, the U.S. Environmental Protection Agency (EPA) has set a maximum contaminant level (MCL) of 2 μg/L for mercury in drinking water .

In the subsurface, Hg can be a long-term contaminant source to groundwater and surface water (*4*). Various technologies have been studied to remove Hg from contaminated sites, including phytoremediation, bioremediation, excavation and thermal treatments, and constructed wetland (*12*). However, these processes require some critical constraints. For instance, excavation and *ex situ* treatment of contaminated soil/sediment is environmentally disruptive, and costly if the contamination is distributed over a large area and/or extends deep in the ground (*4*). Phytoremediation employs special plants which can assimilate and concentrate Hg in their root and leaf tissues from soils, yet, subsequent harvesting and combustion of plants are needed (*13*). In addition, phytoremediation can only reach relatively shallow soil and can take prolonged remediation timeframe, during which access to the vegetation by wildlife will be limited (*14*). Furthermore, conventional technologies are not accessible to Hg plumes located deep in the groundwater acuqifer or underneath existing infrastrucures.

Consequently, innovative in situ remediation technologies to immobilize Hg in contaminated soils or sediments are urgently needed.

Sulfide minerals have been known to be effective sorbents for Hg (*15*). The strong affinity of sulfide for Hg can be revealed by the extremely low solubility product of HgS ($K_{sp} = 2\times10^{-53}$) (*16*). In sulfidic sediments, the dominant mineral phases are generally pyrite (FeS_2), greigite (Fe_3S_4), amorphous FeS, and mackinawite (FeS) (*17*). Of all the sulfide minerals, iron sulfide (FeS) has drawn a lot of attention because it is first formed in most anoxic environments, and has been accepted to be a major constituent of acid-volatile sulfides (*18–20*). Because of the high sorption capacity for Hg^{2+}, its ubiquitous presence and long-term stability in anoxic sediments, FeS holds the potential for immobilizing Hg^{2+} in the subsurface environment (*2*). FeS can immobilize Hg through adsorption, structural incorporation and precipitation as a discrete sulfide phase (HgS (s)) (*2*, *21*), as depicted in equations (1-3):

$$\mathrm{FeS} + \mathrm{Hg}^{2+} \rightarrow \mathrm{Fe}-\mathrm{S}-\mathrm{Hg}^{2+} \text{ (Hg adsorption onto FeS)} \tag{1}$$

$$\mathrm{Fe}-\mathrm{S}-\mathrm{Hg}^{2+} \rightarrow \mathrm{Fe(Hg)S} + \mathrm{Fe}^{2+} \text{ (Hg inclusion into FeS)} \tag{2}$$

$$\mathrm{FeS} + \mathrm{Hg}^{2+} \rightarrow \mathrm{HgS} + \mathrm{Fe}^{2+} \text{ (Ion exchange reaction)} \tag{3}$$

Numerous studies have shown that FeS can effectively immobilize Hg from aqueous solutions (*2*, *22*). For example, at an initial FeS solid concentration range of 0.28-0.40 g/L, 100% of 200 mg/L Hg was removed from the aqueous system within 24 hours (*22*). The maximum sorption capacity was determined to be 1.70 g/g (0.75 mol Hg^{2+}/mol FeS) at pH 5.6 (*22*). However, natural or conventionally synthesized FeS particles are typically in the millimeter or larger scale, which are too big to be delivered into Hg-contaminated soil or sediment. Consequenlty, these macroscale particles are not deliverable into the contaminant source zones, and thus, not suitable for in situ immobilization of Hg in soil or sediment.

Stabilization of FeS Nanoparticles

Compared to conventional technologies, the in situ remediation through direct injection of the nanoparticles into contaminant source zones offers some unique advantages, such as reduced remediation time, less environmental disruption, and easy accessibility to contaminant plumes deep in the ground or underneath built infrastructures (*23–27*). To facilitate direct delivery of the nanoparticles into the target contaminated zone, the nanoparticles must be stable in the aqueous phase, i.e., the nanoparticles must remain in the nanoscale without aggregation and precipitation. Previous studies have demonstrated that the application of the stabilizer could not only improve the transportability of the nanoparticles in the subsurface, but also enhance particle reactivity with contaminants due to the reduced particle size and greater surface area (*24*, *27*). For example, polysaccharide stabilized Fe-Pd nanoparticles can be transported in a loamy-sand soil, and the nanoparticles degraded trichloroethene (TCE) 17 times faster than non-stabilized particles (*24*).

A variety of particle stabilization strategies have been explored to prepare FeS nanoparticles with controlled particle morphology and size distribution in recent years (*28–32*). These technologies include reverse micelle (*28*), sulfate reducing bacteria-assisted production (*32*), high-energy mechanical milling (*29*), polymer-stabilized wet-chemical synthesis (*30*), and poly(amidoamine) dendrimer-stabilization (*31*). However, the preparation of functionalized FeS nanoparticles that are suitable for in situ Hg remediation remains challenging.

For environmental remediation uses, a stabilizer must satisfy some critical features: 1) the stabilizer is able to effectively prevent particle agglomeration, and facilitate particle size control; 2) the stabilizer should not cause significant alternation of soil/sediment properties, such as hydraulic conductivity; and 3) the stabilizer must be cost-effective; and 4) it is environmental benign.

Carboxymethyl cellulose (CMC) is a modified polysaccharide with a pK_a value of 4.3 (*24*). CMC can effectively stabilize various metal or semiconductive nanoparticles through concurrent steric and electrostatic stabilization mechanisms (*24*, *35*). The strong stabilizing effect of CMC along with its low cost and environmental compatibility makes it an ideal choice (*33*). When applied during the nanoparticle preparation stage, CMC can facilitate the particle nucleation and growth, thereby controlling the the nanoparticle size distribution (*34*). CMC has been widely employed in facilitating size control of various metals and metal compounds, such as zerovalent iron (*35*), magnetite (*36*), iron phosphate (*37*), and Fe-Mn oxide (*23*).

Xiong et al. (*1*) and Gong et al. (*38*) demonstrated that CMC can serve as an effective stabilizer for preparing FeS nanoparticles that are suitable for the desired in situ immobilization of Hg in soil/sediment. Figure 1 depicts the scheme for synthesizing CMC-stabilized FeS nanoparticles.

The preparation is conducted in flasks under anaerobic conditions. First, a CMC (typically, molecular weight = 90k) solution is prepared with DI water. Then, a $FeSO_4$ solution is added to the CMC solution under N_2 purging. The molar ratio of CMC to Fe (or type of CMC) can be varied to yield nanoparticles with different particle sizes. Subsequently, a stoichiometric amount of Na_2S solution is introduced into the solution dropwise under shaking and vacuum to yield a solution with desired FeS and stabilizer concentrations. To ensure complete reaction and full growth of nanoparticles, the nanoparticle suspension is sealed and aged for 24 hours before use. Based on the chemical cost calculation, the preparation of the nanoparticles is very cost-effective (1.12 $/lb-FeS).

Figure 2(a-b) compares images of lab-prepared FeS aggregates and CMC-stabilized FeS nanoparticles (*38*). Non-stabilized FeS formed aggregates rapidly due to the high surface energy and precipitated in five minutes; in contrast, stabilized FeS nanoparticles remained fully dispersed in water. Based on work by He et al. (*24*), the carboxymethyl and hydroxyl groups of CMC molecules can interact with particles, resulting in a layer of negative charges attached to the surface of particles. The attached CMC can provide strong interparticle electrostatic and steric repulsions to overweigh the attractive forces, and thereby suppressing the agglomeration of FeS. As shown in the TEM images, non-stabilized FeS presented as aggregated flocs, while stabilized FeS appeared as clearly defined and discrete nanoparticles. The mean particle size of stabilized FeS nanoparticles was determined to be 34.31±8.34 nm (standard deviation).

The DLS (dynamic light scattering) based hydrodynamic diameter was determined to be 222.5±3.2 and 1632.0±7.0 nm (99.9% particles by number), respectively, for CMC-stabilized nanoparticles and sonicated non-stabilized FeS (*38*). Because DLS directly measures the nanoparticle suspension and is based on the particle diffusivity, the DLS-based size is considered more relevant to the transport of the nanoparticles.

CMC-stabilized FeS nanoparticles displayed a rather negative surface with a zeta potential (ζ) value ranging from -43 to -68 mV over the pH range of 5-11, confirming that the stabilization of the nanoparticles is attributed to the electrosteric repulsion induced by the attachment of negatively charged CMC (pKa = 4.3) on the surface of the FeS particles (*24*, *38*).

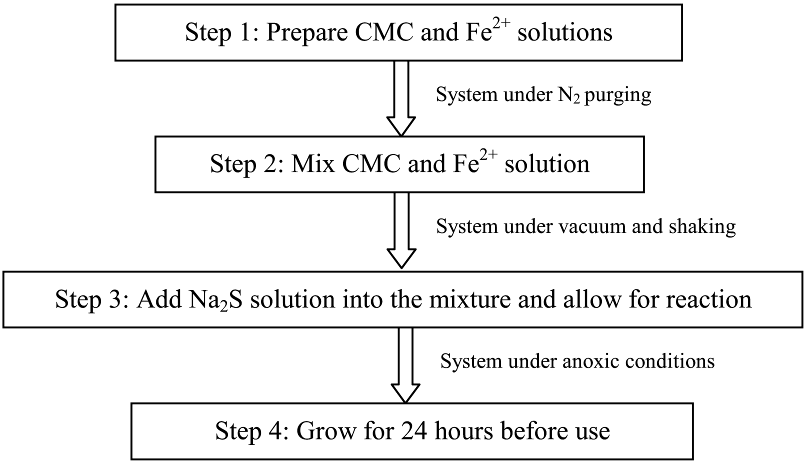

Figure 1. Procedure for synthesizing CMC-stabilized FeS nanoparticles.

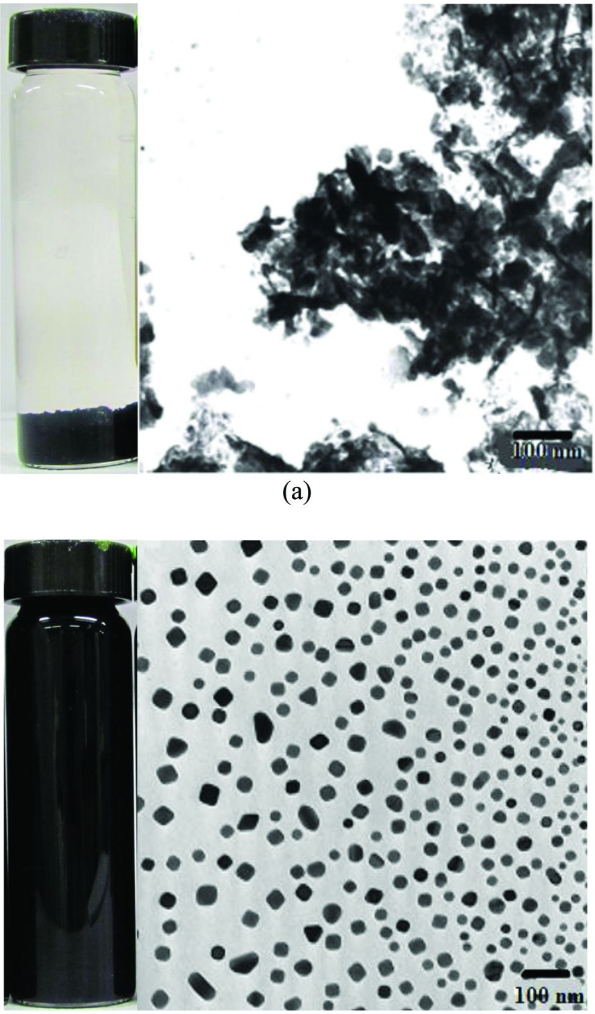

Figure 2. Digital photographs and TEM images of (a) non-stabilized FeS aggregates, and (b) CMC-stabilized FeS nanoparticles (FeS = 0.5 g/L, CMC = 0.05%). "Reproduced with permission from Reference (38). Copyright 2012, IOP Science".

Immobilization of Hg in Water and Soil/Sediment Using CMC-Stabilized FeS Nanoparticles

Sorption of Hg(II) in Water

The CMC-stabilized FeS nanoparticles displayed greater sorption capacity than non-stabilized particles when used for immobilization of Hg in aqueous solution (*39*). Liu et al. (*39*) showed that at an initial FeS nanoparticle concentration of 12 mg/L, 86% of 40 mg/L Hg was immobilized after 6 hours, corresponding to a sorption capacity of 2656 mg/g, which is 13% higher than that for non-stabilized FeS aggregates. The increase in Hg sorption capacity can be attributed to the larger specific surface area (36.9 m^2/g) of the stabilized nanoparticles.

Immobilization of Hg in Soil/Sediment

Batch Hg Immobilization Tests

Gong et al. (*38*) demonstrated the effectiveness of CMC-stabilized FeS nanoparticles for immobilization of Hg in contaminated soil/sediment through a series of batch tests at various dosages of the nanoparticles. Figure 3 shows the transient release of Hg when 2.7 g of a sediment denoted as AL1 or a field contaminated soil designated as NJ4 was mixed with 27 mL of the FeS nanoparticle suspension at various concentrations. For comparison, Hg leaching rates with DI water were also superimposed. Note the sediment AL1 contained freshly loaded Hg, while NJ4 was contaminated with historically aged Hg. For sediment AL1, when the sediment was mixed with DI water, the aqueous phase Hg concentration reached 87.13±9.08 μg/L during the leaching period of 48 hours. In contrast, in the presence of 100, 200, 500, and 1000 mg/L of the CMC-stabilized FeS nanoparticles, the Hg released was reduced by 83%, 92%, 95% and 96%, respectively. Similar phenomena were observed for the soil NJ4. The Hg leached was lowered by 79% and 92% after 16 hours when the soil samples were subjected to 500 and 1000 mg/L of the FeS nanoparticles. These results clearly demonstrate that the nanoparticles can effectively transfer water soluble Hg into the nanoparticle phase, thereby reducing the Hg leachability in the contaminated soil/sediment.

The relative affinity of FeS nanoparticles toward Hg can be quantified by the equilibrium Hg distribution coefficient (K_d) between the aqueous phase and the solid phase as shown in equation (4):

$$K_d = \frac{q}{C} \qquad (4)$$

where q and C are Hg concentrations in the solid and aqueous phases, respectively. Separate Hg sorption isotherm tests with FeS nanoparticles revealed an average K_d value of 19,131 L/g over an equilibrium aqueous-phase Hg concentration (C) of 0-140 μg/L (linear isotherm in this concentration range) (*39*). This K_d value is more than three orders of magnitude greater than the K_d values for the sediment AL1 (2.8 L/g), and the soil NJ4 (16.2 L/g) (*38*).

Table 1 presents the measured K_d values when the Hg-laden soil was subjected to various concentrations of the FeS nanoparticles. Evidently, the presence of the nanoparticles greatly decreased the desorption of soil/sediment sorbed Hg into the aqueous phase. Furthermore, increasing the nanoparticle concentration markedly increased the K_d values. This observation confirmed that the nanoparticles can greatly enhance the solid (FeS+soil/sediment) phase Hg sorption capacity and affinity.

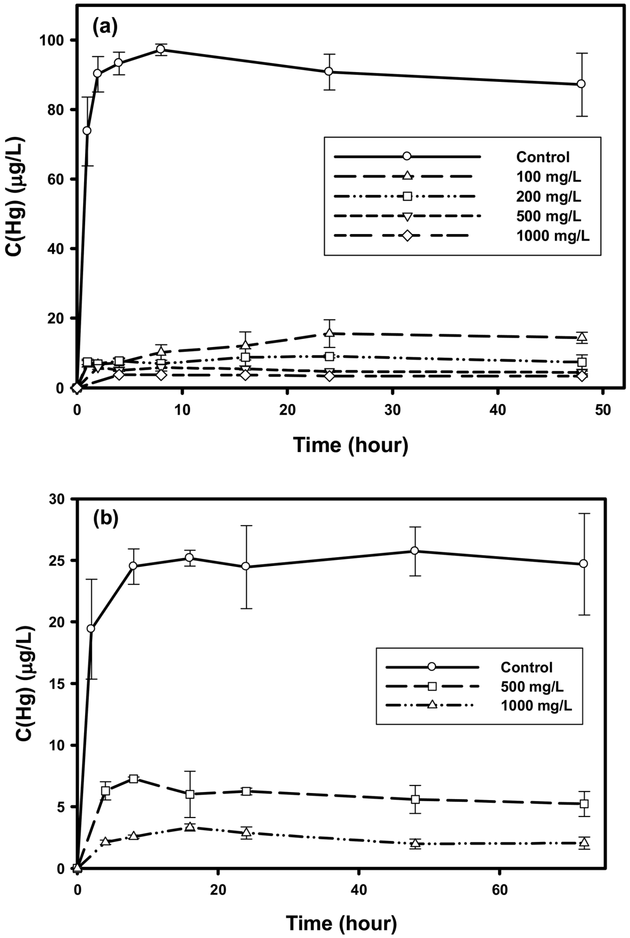

Figure 3. Hg leaching rates in the aqueous phase from (a) sediment AL1, and (b) soil NJ4 with DI water or in the presence of various concentrations of CMC-stabilized FeS nanoparticles. Initial Hg content was 248 mg/kg for AL1 and 401 mg/kg for NJ4. The pH value was kept constant during the reaction period (7.0 for AL1, and 7.8 for NJ4). "Reproduced with permission from Reference (38). Copyright 2012, IOP Science".

Table 1. **Equilibrium Hg Distribution Coefficients (*K_d*) for Sediment and Soil Samples in the Absence or Presence of Various Concentrations of FeS Nanoparticles (*38*)[a]**

Sample	*FeS nanoparticles (mg/L)*	*C (µg/L)*	*K_d (L/g)*
Sediment AL1	0	87.1	2.8
	100	14.4	17.2
	200	7.4	33.6
	500	4.5	55.4
	1000	3.4	73.0
Soil NJ4	0	24.7	16.2
	500	5.2	76.2
	1000	2.0	196.3

[a] K_d was calculated based on total Hg in the solid phase (FeS+soil/sediment) and Hg dissolved in water (*C*).

Of various chemical forms of Hg, methylmercury has been considered as the culprit to both wildlife and humans (*40*). Hg methylation is generally thought to occur in anoxic sediments through a sulfate-reducing bacteria mediated process (*9*, *41*), and it has been suggested that the availability of Hg for methylation is only controlled by neutral dissolved Hg complexes (e.g. HgS^0 and $Hg(HS)_2{}^0$) which are capable of passive diffusion across the cell membrane (*42*). As a result, the extent of Hg methylation can be governed by reducing the formation of these uncharged soluble species. Mehrotra et al. (*43*) found that the addition of Fe^{2+} to sulfidic wetland sediments decreased the extent of Hg methylation by decreasing S^{2-} activity, and hence the formation of Hg soluble complexes. Xiong et al. (*1*) pointed out that the nanoparticle treatment of a Hg-contaminated sediment can greatly suppress the concentration of the bioavailable Hg species. Figure 4 plots the dissolved Hg complexes concentration as a function of FeS nanoparticles dosage. Increasing the noparticles concentration from 1.1×10^{-5} M to 5.1×10^{-3} M lowered these species by nearly three orders of magnitude.

The nanoparticles treatment also reduces the leachability of Hg based on the TCLP (toxicity characteristic leaching procedure) tests. Xiong et al. (*1*) observed that the equilibrium Hg concentration in the TCLP extract amounted to 212 µg/L for the untreated Hg-spiked sediment (initial Hg content = 177 mg/kg), compared to only ~72 µg/L when the same sediment was treated with 15.6 mg/L of nanoparticle suspension at pH 7.0. When the nanoparticles dosage was increased to 206 mg/L, the Hg concentration was further lowered to 2 µg/L, a 99% reduction. Remarkable reduction in TCLP-leached Hg concentration was also reported for field-contaminated soils or sediments upon similar brief nanoparticle treatments (*38*).

Based on the experimental results of batch tests, the CMC-stabilized FeS nanoparticles can not only offer high sorption capacity and strong affinity for Hg, but also are likely to effectively inhibit the process of Hg methylation.

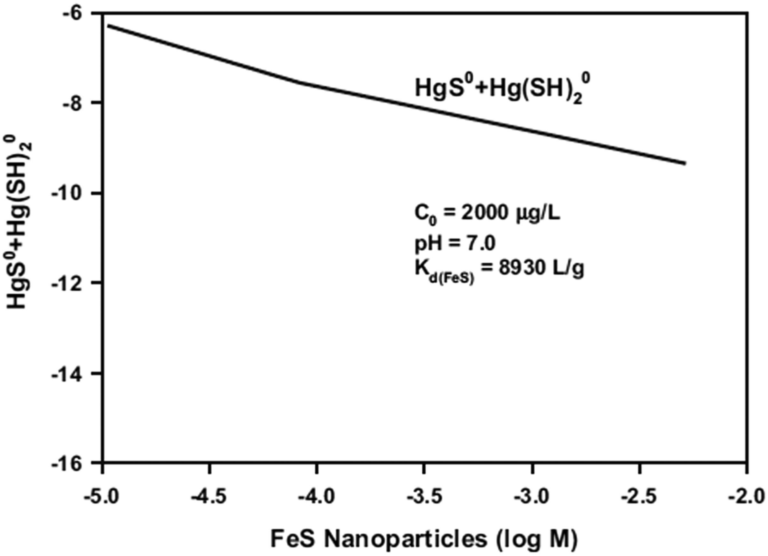

Figure 4. Removal of bioavailable Hg complexes as a function of FeS nanoparticle concentration. Visual MINTEQ (version 2.53) was used to calculate the equilibrium Hg speciation in the solution phase. "Reproduced with permission from Reference (1). Copyright 2009, Elsevier".

Transport of CMC-Stabilized FeS Nanoparticles in Porous Media

For the intended in situ remediation application, the nanoparticles must satisfy the following features: 1) the nanoparticles should be deliverable into the subsurface, i.e., they should be mobile under a certain injection pressure to ensure delivery into the targeted contaminant zones, 2) the nanoparticles should offer high sorption capacity and strong affinity for Hg, 3) the delivered nanoparticles should be virtually immobile under typical natural groundwater flow conditions, i.e., once the external pressure is released, the nanoparticles should remain immobile, or in a confined domain, providing prolonged Hg immobilization capacity, 4) the nanoparticles should not cause significant alteration of soil/sediment properties, such as conductivity and chemistry, and 5) the nanoparticles should not cause any environmental harm.

Gong et al. (*38*) tested the soil/sediment deliverability and transport behaviors of the stabilized FeS nanoparticles by measuring the breakthrough curves of the nanoparticles through 1-D column experiments. Figure 5 (a-b) shows breakthrough profiles of a conservative tracer (KBr) and the nanoparticles through a fixed-bed column packed with the sediment AL1 and the soil NJ4, respectively. For AL1, under an external pressure of 0.4 psi, full breakthrough of the nanoparticles ($C/C_0 = 0.7$) occurred at ~9 pore volumes (PVs), compared to ~7 PVs for the tracer ($C/C_0 = 1.0$). Approximately 30% of the introduced nanoparticles were retained in the sediment bed after ~42 PVs of the nanoparticles passed through the bed. For NJ4, under an external pressure of 0.5 psi, full breakthrough of the nanoparticles ($C/C_0 = 0.8$) occurred at ~12 PVs, compared to ~8 PVs for the tracer ($C/C_0 = 1.0$). Approximately 20% of the nanoparticles were retained in the soil after ~50 PVs of the nanoparticles passed through the bed. Similar breakthrough profiles were also reported by An and Zhao (*23*) who tested the transport behavior of CMC-stabilized Fe-Mn nanoparticles through a sandy soil. For comparison, column tests of non-stabilized FeS aggregates were also carried out under otherwise identical conditions. However, nearly all the particles were retained on the top layer of the sediment/soil. The results indicate that the nanoparticles are deliverable in the field contaminated sites under moderate external injection pressure. Based on the classical filtration theory (*44*), the partial deposition of fine nanoparticles to the porous media can be attributed to Brownian diffusing, interception, and/or gravitational sedimentation.

The size of the nanoparticles is critical in ensuring effective delivery. He and Zhao (*35*) found that various sizes of zerovalent iron (ZVI) nanoparticles can be prepared by manipulating the concentration or type of CMC stabilizers and controlling the synthesizing conditions, such as CMC-to-Fe molar ratios, temperature, and pH. As a rule, the higher CMC-to-Fe ratio, the smaller nanoparticles are obtained; CMC of higher molecular weight yileds smaller nanoparticles though the resultant nanoparticle suspension bears with higher viscosity.

The flow velocity is another important parameter affecting the nanoparticles' transport and deposition in porous media. He et al. (*45*) studied breakthrough behaviors of CMC-stabilized ZVI nanoparticles under the pore flow velocity range of 0.0176-0.0706 cm/s. They observed that at a pore velocity of 0.0353 cm/s, the effluent ZVI concentration rapidly reached a plateau ($C/C_0 = 0.88$) at ~2 PVs. Doubling the pore velocity to 0.0706 cm/s increased the full breakthrough C/C_0 level to 0.99. Conversely, decreasing the pore velocity to 0.0176 cm/s lowered the full breakthrough C/C_0 level to 0.82, i.e. 6% more nanoparticles were retained in the sand bed. Based on the breakthrough profiles and the filtration modeling approach, He et al. (*45*) calculated the maximum travel distance (MTD) of the nanoparticles as a function of the flow velocity. Figure 6 shows that the mobility of the nanoparticles as a function of pore velocity. Evidently, the effective area or particle travel distance can be manipulated by controlling the injection velocity, i.e. injection pressure. Based on the same approach, Gong et al. (*38*) predicted the MTD for the CMC-stabilized FeS nanoparticles to be 1.11 m under 0.4 psi injection pressure. When the pressure was doubled, the MTD was increased to 1.85 m. However, once the external pressure was released, the MTD was determined to be 18 cm under a typical groundwater flow velocity of 0.1 m/d. Moreover, CMC stabilizers are expected to break down in weeks to months (*27*). Consequently, the mobility of the nanoparticles will be further diminished as CMC is degraded. Eventually, the delivered FeS nanoparticles will be incorporated in the ambient geo-media, serving as a long-term sink for Hg immobilization.

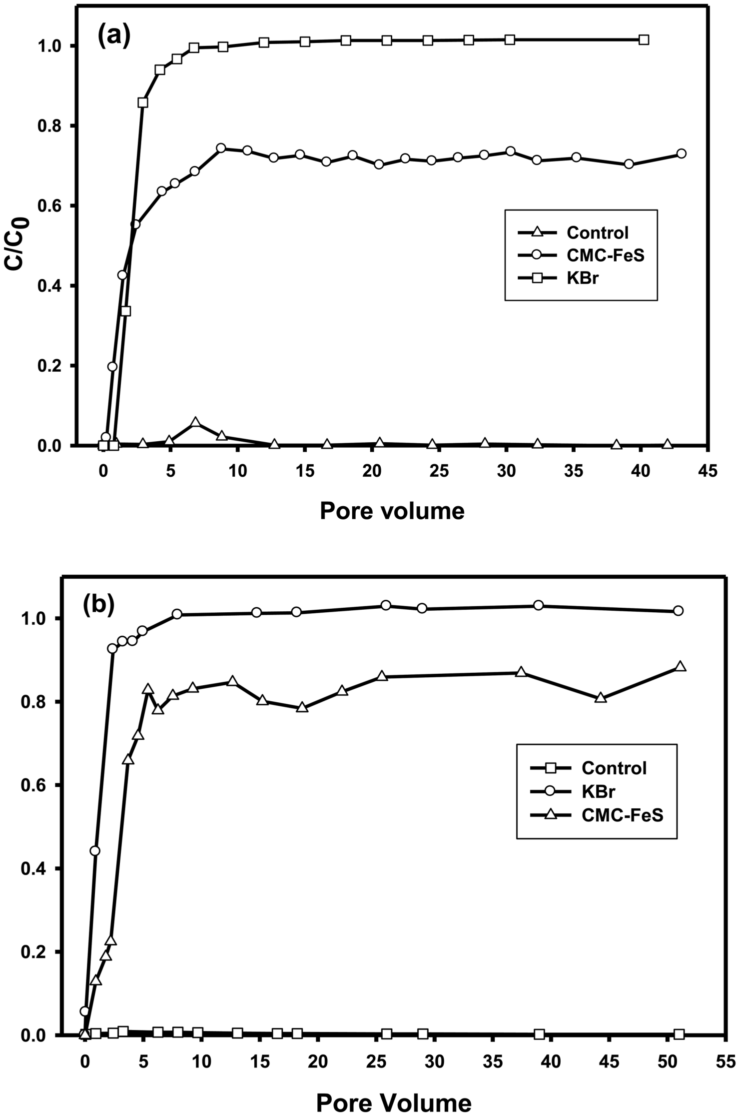

Figure 5. Breakthrough curves of a tracer (KBr) and CMC-FeS nanoparticles through (a) sediment AL1 (KBr = 50 mg/L, FeS = 500 mg/L, CMC = 0.05%, pore velocity = 0.22 cm/min, EBCT = 113 min), and (b) soil NJ4 (KBr = 50 mg/L, FeS = 500 mg/L, CMC = 0.05%, pore velocity = 0.10 cm/min, EBCT = 102 min). "Reproduced with permission from Reference (38). Copyright 2012, IOP Science".

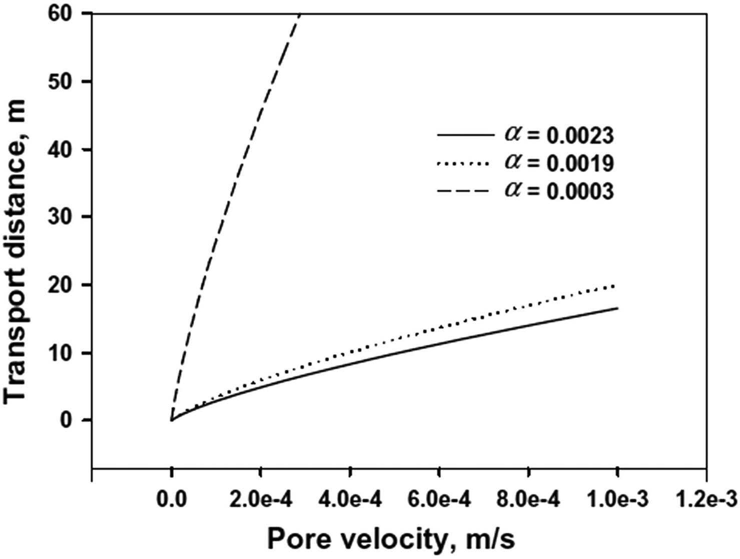

Figure 6. Relationship between the maximum travel distance of CMC-stabilized ZVI nanoparticles and interstitial liquid velocity in a fixed bed sand column. "Reproduced with permission from Reference (45). Copyright 2009, Elsevier".

In Situ Immobilization of Hg in Soil/Sediment Using CMC-Stabilized FeS Nanoparticles

For the in situ application, the delivered nanoparticles should offer high sorption capacity and strong affinity for Hg. Gong et al. (*38*) investigated the effectiveness of the CMC-stabilized FeS nanoparticles for in situ immobilization of Hg in soil and sediment through a series of fixed-bed column experiments. Figure 7 compares elution histories of total Hg and dissolved Hg from the sediment AL1 bed when a suspension of the CMC-stabilized FeS nanoparticles was pumped through the sediment bed. For comparison, the same elution test was also carried out using a solution containing 0.05 wt.% CMC without the nanoparticles under otherwise identical conditions. Based on mass balance calculations, the dissolved Hg leached during the 95 PVs of elution tests was reduced from ~1% (without the nanoparticles) to 0.1% (with the nanoparticles), a 90% reduction.

When the effluent samples were analyzed for total Hg (i.e. both dissolved and naonoparticle-sorbed Hg), the nanoparticle suspension eluted ~5% of Hg initially sorbed in the sediment, while the CMC solution eluted only 1 % of Hg from the sediment. Furthermore, 99% of the eluted Hg by the nanoparticle suspension was associated with the nanoparticles, indicating nearly all soluble Hg is transferred to the nanoparticle phase. As mentioned before, once the external injection pressure is released, the nanoparticles are virtually immobile under natural groundwater conditions. As a result, Hg associated with the nanoparticles is immobilized. Such transferring of the labile form of Hg in soil/sediment to the nanoparticle-associated form would render Hg less bioavailable for methylation.

The sharp initial Hg peaking is indicative of a stage-by-stage desorption process of Hg binding in the sediment at sites of different binding energies. When the Hg-free influents (CMC solution or FeS nanoparticles) were passed through the Hg-contaminated sediment bed, dissolved Hg complexes in the pore water were first eluted, followed by Hg species associated with the weak binding sites of the sediment, such as oxygen- and nitrogen-bearing functional groups along with some mineral lattice of the sediment (*1*, *46*). As a result, an abrupt rise in Hg concentration was observed. As more effluents passed, Hg species associated with the stronger binding sites, mainly reduced sulfur groups, were slowly released into the surrounding solution (*46*). From a kinetic viewpoint, the observed Hg elution profile denotes that the most efficient Hg mass transfer occurred within the first 10 PVs of nanoparticles treatment, and the nanoparticles thereafter primarily serve as an added long-term sink or an in situ built sorptive barrier that scavenges any bleeding Hg (*38*).

Following the elution tests, the TCLP leachability of Hg remaining in the samples was determined. The Hg concentration in the TCLP extractant was 51 µg/L for the untreated sediment. However, upon the brief nanoparticle treatment, the TCLP-leached Hg was reduced to 4.4 µg/L, a reduction of 91%. The nanoparticle amendment rendered the Hg concentration far below the TCLP threshold of 25 µg/L for land disposal of Hg wastes.

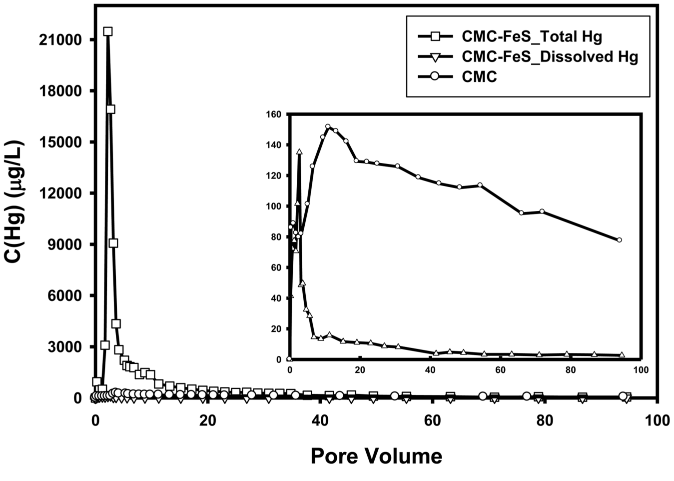

Figure 7. Elution histories of total and dissolved Hg from Hg-contaminated sediment AL1 when subjected to a suspension of 500 mg/L of CMC-stabilized FeS nanoparticles or a 0.05 wt.% CMC solution (pore velocity = 0.22 cm/min, EBCT = 113 min). Inset: a close-up of dissolved Hg concentration histories under the two elution conditions (with or without the nanoparticles). Total Hg refers to all Hg in the effluent (both dissoveld and FeS-sorbed); Dissolved Hg denotes Hg that is dissolved in the solution. "Reproduced with permission from Reference (38). Copyright 2012, IOP Science".

Conclusions

Contamination of Hg in soil and sediment has been one of the most challenging environmental issues. However, because of the extent, scope and mobility of the contaminant, effective in situ Hg remediation technologies have been lacking. The CMC-stabilized FeS nanopartciles offer some unique properties, such as the small particle size, large surface area, soil deliverability, and strong affinity for Hg, and thus, hold the promise to develop a more cost-effective in situ Hg remediation technology in contaminated sediment, soil and groundwater. Once delivered, the nanoparticles will remain in the local soil/sediment matrix and serve as a long term sink for Hg, reducing soluble Hg and biological methylation of Hg. The particle stabilization strategy using polysaccharides offers a simple and effective way to control size and transport behavior of the nanoparticles. Batch and column experimental results confirmed the effectiveness of the nanoparticles for sorption and immobilization of Hg. This in situ remediation technology greatly decreases Hg leachability and bioavailability, reduces the overall remediation time, and offers a powerful remediation strategy for remediaton of contaminant plumes that are not accessible by conventional technologies. Further pilot- or field-scale tests are warranted to further demonstrate the effectiveness and long-term technical viability of the technology.

References

1. Xiong, Z.; He, F.; Zhao, D.; Barnett, M. O. *Water Res.* **2009**, *43*, 5171–5179.
2. Jeong, H. Y.; Klaue, B.; Blum, J. D.; Hayes, K. F. *Environ. Sci. Technol.* **2007**, *41*, 7699–7705.
3. Anirudhan, T. S.; Divya, L.; Ramachandran, M. *J. Hazard. Mater.* **2008**, *157*, 620–627.
4. Bower, J.; Savage, K. S.; Weinman, B.; Barnett, M. O.; Hamilton, W. P.; Harper, W. F. *Environ. Pollut.* **2008**, *156*, 504–514.
5. Fitzgerald, W. F.; Engstrom, D. R.; Mason, R. P.; Nater, E. A. *Environ. Sci. Technol.* **1998**, *32*, 1–7.
6. Bayramoglu, G.; Arica, M. Y. *J. Hazard. Mater.* **2007**, *144*, 449–457.
7. Sweet, L. I.; Zelikoff, J. T. *J. Toxicol. Environ. Health, Part B* **2001**, *4*, 161–205.
8. Mercone, D.; Thomson, J.; Croudace, I. W.; Troelstra, S. R. *Geochim. Cosmochim. Acta* **1999**, *63*, 1481–1488.
9. Gilmour, C. C.; Henry, E. A.; Mitchell, R. *Environ. Sci. Technol.* **1992**, *26*, 2281–2287.
10. Kerin, E. J.; Gilmour, C. C.; Roden, E.; Suzuki, M. T.; Coates, J. D.; Mason, R. P. *Appl. Environ. Microbiol.* **2006**, *72*, 7919–7921.
11. Stein, E. D.; Cohen, Y.; Winer, A. M. *Crit. Rev. Env. Sci. Technol.* **1996**, *26*, 1–43.
12. Atwood, D.; Zaman, M. *Mercury Removal from Water Recent Developments in Mercury Science*; Atwood, D., Ed.; Springer: Berlin/Heidelberg, 2006; Vol. 120, pp 163−182.

13. Riddle, S. G.; Tran, H. H.; Dewitt, J. G.; Andrews, J. C. *Environ. Sci. Technol.* **2002**, *36*, 1965–1970.
14. Hinton, J.; Veiga, M. Mercury Contaminated Sites: A Review of Remedial Solutions. In *Proceedings of the NIMD (National Institute for Minamata Disease) Forum*, Minamata, Japan, 2001.
15. Brown, J. R.; Bancroft, G. M.; Fyfe, W. S.; McLean, R. A. N. *Environ. Sci. Technol.* **1979**, *13*, 1142–1144.
16. Barnett, M. O.; Turner, R. R.; Singer, P. C. *Appl. Geochem.* **2001**, *16*, 1499–1512.
17. Morse, J. W.; Arakaki, T. *Geochim. Cosmochim. Acta* **1993**, *57*, 3635–3640.
18. Rickard, D.; Schoonen, M. A. A.; Luther, G. W., III Chemistry of Iron Sulfides in Sedimentary Environments. In *Geochemical Transformations of Sedimentary Sulfur*; Vairavamurthy, M. A., Schoonen, M. A. A., Eglinton, T. I. , Luther, G. W., III, Manowitz, B., Eds.; ACS Symposium Series 612; American Chemical Society: Washington, DC, 1995; pp 168−193.
19. Berner, R. A. *J. Geol.* **1964**, *72*, 293–306.
20. Rickard, D. T. *Am. J. Sci.* **1974**, *274*, 941–952.
21. Wolfenden, S.; Charnock, J. M.; Hilton, J.; Livens, F. R.; Vaughan, D. J. *Environ. Sci. Technol.* **2005**, *39*, 6644–6648.
22. Liu, J.; Valsaraj, K. T.; Devai, I.; DeLaune, R. D. *J. Hazard. Mater.* **2008**, *157*, 432–440.
23. An, B.; Zhao, D. *J. Hazard. Mater.* **2012**.
24. He, F.; Zhao, D.; Liu, J.; Roberts, C. B. *Ind. Eng. Chem.* **2006**, *46*, 29–34.
25. Liu, R.; Zhao, D. *Water Res.* **2007**, *41*, 2491–2502.
26. Pan, G.; Li, L.; Zhao, D.; Chen, H. *Environ. Pollut.* **2010**, *158*, 35–40.
27. Xu, Y.; Zhao, D. *Water Res.* **2007**, *41*, 2101–2108.
28. Chadha, A.; Sharma, R. K.; Stinespring, C. D.; Dadyburjor, D. B. *Ind. Eng. Chem. Res.* **1996**, *35*, 2916–2919.
29. Chin, P. P.; Ding, J.; Yi, J. B.; Liu, B. H. *J. Alloys Compd.* **2005**, *390*, 255–260.
30. Paknikar, K. M.; Nagpal, V.; Pethkar, A. V.; Rajwade, J. M. *Sci. Technol. Adv. Mat.* **2005**, *6*, 370.
31. Shi, X.; Sun, K.; Balogh, L. P.; Jr, J. R. B. *Nanotechnology* **2006**, *17*, 4554.
32. Watson, J. H. P.; Croudace, I. W.; Warwick, P. E.; James, P. A. B.; Charnock, J. M.; Ellwood, D. C. *Sep. Sci. Technol.* **2001**, *36*, 2571–2607.
33. He, F.; Zhao, D. *Appl. Catal., B* **2008**, *84*, 533–540.
34. Shimmin, R. G.; Schoch, A. B.; Braun, P. V. *Langmuir* **2004**, *20*, 5613–5620.
35. He, F.; Zhao, D. *Environ. Sci. Technol.* **2007**, *41*, 6216–6221.
36. Liang, Q.; Zhao, D.; Qian, T.; Freeland, K.; Feng, Y. *Ind. Eng. Chem. Res.* **2011**, *51*, 2407–2418.
37. Liu, R.; Zhao, D. *Chemosphere* **2007**, *68*, 1867–1876.
38. Gong, Y. Y.; Liu, Y. Y.; Xiong, Z.; Kaback, D.; Zhao, D. Y. *Nanotechnology* **2012**, *23*.
39. Liu, Y. Y.; Gong, Y. Y.; Xiong, Z.; Kaback, D.; Zhao, D. Y. *Water Res.* **2012**, in preparation.
40. Boening, D. W. *Chemosphere* **2000**, *40*, 1335–1351.

41. King, J. K.; Kostka, J. E.; Frischer, M. E.; Saunders, F. M. *Appl. Environ. Microb.* **2000**, *66*, 2430–2437.
42. Benoit, J. M.; Gilmour, C. C.; Mason, R. P.; Heyes, A. *Environ. Sci. Technol.* **1999**, *33*, 951–957.
43. Mehrotra, A. S.; Horne, A. J.; Sedlak, D. L. *Environ. Sci. Technol.* **2003**, *37*, 3018–3023.
44. Kretzschmar, R.; Borkovec, M.; Grolimund, D.; Elimelech, M. Mobile Subsurface Colloids and Their Role in Contaminant Transport. In *Advances in Agronomy*; Donald, L. S., Ed.; Academic Press: San Diego, 1999; Vol.66, pp 121−193.
45. He, F.; Zhang, M.; Qian, T.; Zhao, D. *J. Colloid Interface Sci.* **2009**, *334*, 96–102.
46. Kot, F. S.; Rapoport, V. L.; Kharitonova, G. V. *Cent. Eur. J. Chem.* **2007**, *5*, 846–857.

Chapter 6

In Situ Dechlorination in Soil and Groundwater Using Stabilized Zero-Valent Iron Nanoparticles: Some Field Experience on Effectiveness and Limitations

Man Zhang and Dongye Zhao*

Environmental Engineering Program, Department of Civil Engineering, 238 Harbert Engineering Center, Auburn University,
Auburn, Alabama 36849, United States
***Phone: (334) 844 6277. Fax: (334) 844 6290. E-mail: zhaodon@auburn.edu**

To facilitate in situ degradation of chlorinated solvents in the subsurface, Auburn university developed and patented (US7,887,880 B2) a new class of stabilized ZVI nanoparticles using carboxymethyl cellulose (CMC) as a stabilizer. Laboratory experimental results revealed some unique attributes of CMC-stabilized ZVI nanoparticles: 1) they are deliverable in soil; 2) they offer much greater dechlorination reactivity than non-stabilized counterparts; and 3) the particles can effectively degrade soil-sorbed contaminants such as trichloroethylene (TCE). These novel features allow the nanoparticles to be delivered into contaminated source zones and facilitate in situ dechlorination in soil and groundwater. This chapter reports preliminary results from two field tests of the in situ remediation technology. These field tests confirmed the soil deliverability and reactivity of the nanoparticles for in situ degradation of chlorinated solvents. In a sandy aquifer at Alabama, at an injection pressure of <5 psi, the iron nanoparticles were observed to migrate up to 10 ft downgradient from the injection well. Following Fe-Pd nanoparticle injections, chlorinated contaminant reduction efficiencies of up to 94% were observed in monitoring wells within the first week. The rapid degradation of chlorinated solvents was evidenced at a California site along with the production of ethane, which is the main abiotic

In Novel Solutions to Water Pollution; Ahuja, S., et al.;
ACS Symposium Series; American Chemical Society: Washington, DC, 2013.

reductive dechlorination product. The concentration of ethane rapidly increased from being not detected to 65µg/L in the groundwater within 2 hours after Fe-Pd nanoparticles were injected. The pilot test at Alabama site indicated that injection of the nanoparticles boosted a local biological process leading to a long-term reduction of chlorinated contaminants in the subsurface. Some technical constraints of the technology were also revealed. For instances, while the CMC-stabilized Fe-Pd nanoparticles can degrade soil-sorbed TCE, soil sorption can limit the rate and extent of dechlorination especially for soils of high organic content. Dissolved organic matter was found to inhibit the degradation rate as well.

Introduction

In the last decade or so, zero-valent iron (ZVI) nanoparticles have drawn remarkable interest for in situ remediation of soil and groundwater contaminated with chlorinated solvents. Gillham and O'Hannesin (*1*) reported that ZVI could effectively degrade 14 chlorinated methanes, ethanes and ethenes through reductive dechlorination. In 1997, Wang and Zhang (*2*) first reported that ZVI nanoparticles prepared through the conventional borohydride reduction approach were able to degrade trichloroethylene (TCE) and polychlorinated biphenyl (PCBs). Despite the aggregation problems, the lab-prepared Fe-Pd particles exhibited >100 times greater reactivity than commercially available iron powders.

Reduction of chlorinated compounds by Fe-Pd bimetallic particles is a hydrodechlorination process, where Fe acts as the electron source and Pd (typically at 0.1 wt% of Fe) as a catalyst. The presence of trace amounts of Pd greatly facilitates generation and sorption of the reactive atomic hydrogen, which is critical in the dechlorination reaction. In addition, the galvanic couples formed between iron and paaladium are critical for the generation of the reactive atomic hydrogen. Under ambient conditions, TCE is reduced by ZVI nanoparticles to environmentally innocuous compounds, such as acetylene, ethylene and ethane. Some chlorinated intermediates (cis-1,2,-dichloroethylene (DCE), 1,1-DCE, vinyl chloride (VC)) may be produced but usually account for less than 1% of the TCE degraded (*3*).

Compared to conventional granular iron, which has been commonly applied in permeable reactive barriers (PRBs), truly nanoscale iron particles offer the advantage that the nanoparticles can be injected into the contaminated source zones or other down-gradient contaminant plumes, thereby facilitating in situ degradation of chlorinated solvents (*4*, *5*). Compared to conventional remediation technologies such as PRBs and pump-and-treat, such a proactive in situ approach by means of the nanoparticles is expected to greatly shorten the remediation timeframe and reduce the overall remediation cost. In addition, the in situ remediation technology can often reach contaminant zones that are located deep in the ground or underneath built infrastructures, which are not accessible by conventional technologies.

ZVI nanoparticles tend to aggregate into micro- or milli-meter scale particles due to strong magnetic and electrostatic interactions. The aggregated particles are no longer transportable through the porous media, even through sand (*6*, *7*), and thus, cannot be delivered or dispersed in the target subsurface contaminated zones. In addition, particle agglomeration also reduces the specific surface area of iron particles, thereby reducing the available active surface sites and the chemical reactivity.

To prevent nanoparticle aggregation and facilitate particles deliverability, various particle stabilization techniques have been developed. For examples, nanoparticles are stabilized using emulsified oil (*8*), carrier supports (*9*, *10*), polymers (*11*, *12*) or surfactants (*13*, *14*). To facilitate soil deliverability of ZVI nanoparticles, Auburn University researchers developed a new class of highly dispersible palladized iron (Fe-Pd) nanoparticles using sodium carboxymethyl cellulose (CMC) as a stabilizer (*7*). Unlike traditional methods, the CMC stabilizer was added during the particle synthesis, which allows better control of nanoparticle nucleation and growth by manipulating the type and concentration of the stabilizer. In addition to its macromolecular structure, the adsorption of negatively charged CMC molecules ($pK_a = 4.3$) onto the ZVI nanoparticles results in an electrical double layer on the surface of the nanoparticles. Consequently, the nanoparticles are stabilized through the concurrent coulombic repulsion between the CMC-capped particles and steric hindrance due to the coated CMC macromolecules. Figure 1 shows the TEM image of CMC-stabiblized Fe-Pd nanoparticles with an average particle diameter of 4.3±1.8 nm.

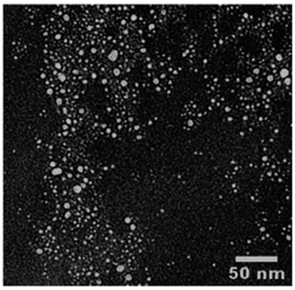

Figure 1. TEM image of freshly prepared CMC-stabilized Fe-Pd nanoparticles. Fe = 0.1 g/L; Pd/Fe = 0.1 wt%; CMC (sodium form)= 0.2 % (7). Reproduced with permission from Refererence (7). Copyright 2007, American Chemical Society.

Laboratory studies have revealed that CMC-stabilized ZVI nanoparticles offer much improved deliverability through various porous media ranging from sand to field soil (*15*). Based on column breakthrough curves and filtration modeling, the particle travel distance in soil was found strongly dependent on the groundwater flow rate (or injection pressure). For example, CMC-stabilized ZVI nanoparticles could travel only 16 cm at a groundwater pore velocity of 0.1 m/day in a sandy soil. However, the travel distance can be extended to 146 m when the pore water velocity is elevated to 61 m/day under the otherwise identical conditions (*16*). Therefore, the effective area of the ZVI nanoparticles can be controlled by regulating the injection pressure. In addition, it is noteworthy that once delivered, the nanoparticles will remained in a very confined domain under typical groundwater conditions.

The stabilized Fe-Pd nanoparticles also exhibited superior dechlorination reactivity. Compared to the non-stabilized counterparts, the stabilized nanoparticles exhibited 17 times higher reactivity for reductive dechlorination of TCE. With 0.2 g/L of CMC-stabilized Fe-Pd nanoparticles (Pd = 0.1 wt.% of Fe), 50 mg/L of TCE was completely degraded to chloride in less than one hour without detection of byproducts such as DCE and VC (*7*).

While numerous laboratory studies have been reported, field data have been rather limited on the deliverability and dechlorination effectiveness of CMC-stabilized Fe-Pd nanoparticles. In addition to the complex hydrogeochemical conditions in the field, the spatial and temporal variation of contamination (*14*) and soil heterogeneity (*17*) are likely to affect the effectiveness of the dechlorination. In addition, soil sorption and dissolved organic matter also affect the efficacy. This study summarizes results from two field demonstration experiments that were designed to investigate the deliverability and dechlorination reactivity of the CMC-stabilized Fe-Pd nanoparticles under field conditions (*18*, *19*). In addition, this study reports laboratory investigation on the effectiveness of CMC-stabilized iron nanoparticles for soil-sorbed TCE, and on the effect of dissolved organic matter on the reactivity of the nanoparticles (*20*).

Field Test at a California Site

A series of single-well, push-pull tests were conducted at an aerospace facility near San Francisco Bay in California. The goal was to test the soil deliverability of CMC-stabilized ZVI nanoparticles into the subsurface and the dechlorination reactivity towards chlorinated contaminants such as TCE and Tetrachloroethylene (PCE). The push-pull test was carried out by first injecting a suspension of CMC-stabilized ZVI nanoparticle into an injection well; and then, an extraction was performed from the same well and recovery of the injected nanoparticles was determined. A conservative tracer (KBr) was mixed in the nanoparticle suspension to provide insight into the hydrodynamic characteristics of the fluid in the groundwater aquifer. Details on this field experiments have been reported by Bennett et al. (*18*).

The test area mainly consists of silts and clays, interlined with coarse-grained channel deposits. The coarse-grained sediments were the primary permeable and water-bearing zones in the subsurface. Three water-bearing zones were detected at depths from 3.8 ~4.8 m, 6.4 ~6.5 m and 9.2 ~9.8 m below ground surface (bgs), where the uppermost water-bearing zones was confined. Soil samples collected from 4.1 m bgs and 9.5 m bgs were characterized as poorly degraded sands and the corresponding hydraulic conductivity were estimated to be approximately 105 and 28 m/day, respectively.

The test site was primarily contaminated by a dissolved TCE/PCE plume originating from the upgradient of the groundwater flow. Some typical biological dechlorination byproducts such as cis-DCE and vinyl chloride were detected in the groundwater, suggesting active biological dechlorination is operative at the site. Soil samples collected from the depth of 4.7 m and 9.5 m contained TCE at 0.29 and 2.1 mg/kg, respectively; however, there was no chlorinated ethenes detected in the soil samples from 2.3 m and 6.4 m bgs (detection limit = 0.25 mg/kg). A significant amount of chlorinated ethenes were detected from 9.3 m to 10 m bgs.

A multi-level injection well I-1 was constructed for both nanoparticle injection and groundwater extraction. The well was screened at three depth intervals, which corresponded to the three water-bearing zones in the subsurface. Three push-pull tests were performed with CMC-stabilized iron nanoparticles at three different screened intervals. Approximately 117 L of 1.0 g/L (CMC = 0.8 wt%), 110 L of 0.2g/L (CMC = 0.4 wt%) of ZVI nanoparticles and 110 L of 0.35 g/L Fe-Pd bimetallic nanoparticles (CMC = 0.8 wt%, Pd = 0.1 wt.% of Fe) were prepared and injected in three separate injection events on April 25, 2006, April 26, 2006 and May 1, 2006, respectively.

The CMC-stabilized ZVI nanoparticles were synthesized on site before each injection through the aqueous phase reduction of ferrous iron by sodium borohydride in the presence of CMC. The freshly-prepared nanoparticles were then injected into the water-bearing stratum of the aquifer along with a conservative tracer (bromide) and then extracted with the groundwater from the same well. The groundwater samples were collected during the extraction stage to assess the nanoparticle recovery and dechlorination reactivity.

The mass recovery of the injected iron was compared with that of the injected tracer to evaluate the transportability of the nanoparticles within the aquifer. Figure 2 shows the concentration histories of total iron and bromide in the groundwater collected from I-1 during the extraction ("pull") stage during the third push-pull test (*18*). The area under curves were used to estimate the total mass of iron/bromide recovered. There was no lag time between the injection and extraction test, i.e. the nanoparticles/groundwater mixture drawn towards I-1 immediately after injection. Mass balance calculations indicated that approximately 31% of total iron (113 g) was recovered during the extraction compared to 76% for bromide, suggesting that the stabilized nanoparticles are partially transportable in the aquifer. A lower recovery of iron nanoparticles was observed when there was a residence time between the end of injection and the beginning of extraction, as was the case in the first and second push-pull tests. For example, in the first push-pull test, when the extraction was initiated about 13 h after the end of injection, only 2.6 % of the total iron was recovered against 61% of bromide recovery. The prolonged residence time of the nanoparticles in the aquifer may facilitate the adsorption of iron in the soil phase (*20*) and render the nanoparticles less mobile over time.

Upon injection of three batches of ZVI nanoparticles, the ORP (oxidation-reduction potential) of groundwater rapidly decreased from the baseline value of -173 ~-234 mV to -400 ~-500 mV (*18*), indicating formation of a strong reducing environment at the site. The decrease of ORP is attributed to the strong reducing power of Fe-Pd nanoparticles and consumption of pre-existing oxidants such as dissolved oxygen.

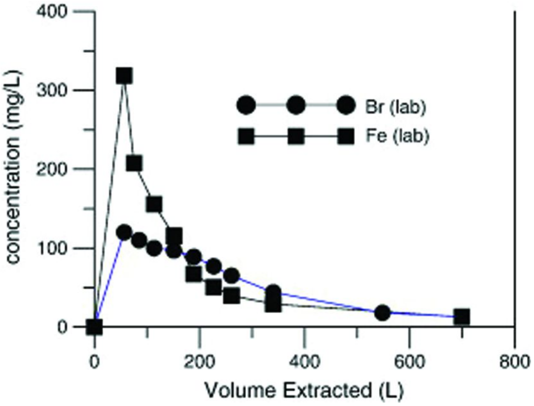

Figure 2. Corrected iron concentration and bromide concentration versus volume extracted (18). Reproduced with permission from Refererence (18). Copyright 2010, Elsevier.

Concentrations of dissolved chlorinated contaminants in groundwater were monitored during the extraction phase of the push-pull tests. In a control test when tap water, instead of ZVI nanoparticles, was pumped to the underneath aquifer during the injection phase, the total chlorinated contaminant concentration at the end of extraction phase ($V_{ext}/V_{inj} > 1.5$) was approximately 35 % lower compared to the baseline condition (*18*), although more than 90% of the injection bromide was successfully recovered. The lower rebound concentration of chlorinated contaminants suggested that a direct comparison of the pre- and post-injection chlorinated contaminant concentrations could not provide reliable evidence for effective degradation of chlorinated contaminants in this study.

Consequently, the accumulation of daughter products associated with reductive dechlorination using ZVI nanoparticles, such as ethane and ethene, was used as an indicator for in-situ abiotic degradation. Ethane, which is the primary product of abiotic dechlorination using Fe-Pd nanoparticles (*21*), was reported under the detection limit (5 μg/L) in all of baseline samples (*18*). As shown in Figure 3, immediately after the injection of the stabilized Fe-Pd nanoparticles in the third push-pull test, ethane increased significantly from being non-detected to 65 μg/L in less than 2 h, suggesting the occurrenc of an effective and complete degradation of the chlorinated contaminants in the vicinity of injection well I-1. The high concentration of ethane was observed in the early extraction stage (Vext/Vinj <0.5) and its concentration gradually decreased thereafter as more groundwater was extracted from the test aquifer, suggesting that the abiotic degradation of chlorinated containments mainly occurred in the soil pore space near the injection well I-1. Different from ethane, the concentration of ethene continuously increased in the extraction stage. It is plausible because the injection of Fe-Pd nanoparticles could facilitate the indigenous biodegradation of chlorinated contaminants (*22*) and promote the production of ethene, which is the main degradation product for biodechlorination process (*23*).

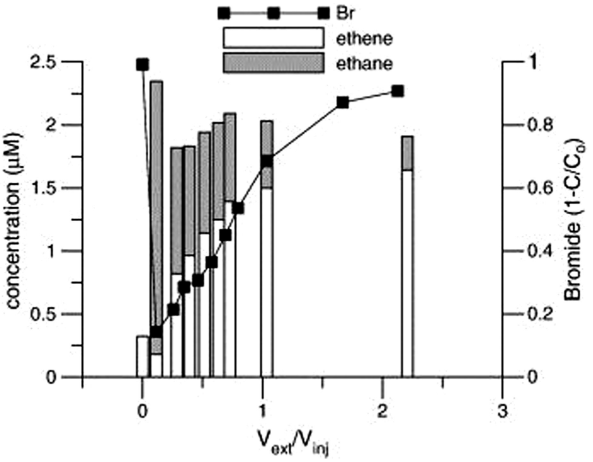

Figure 3. Ethene and ethane concentrations as a function of volume of groundwater being extracted over volume of injected nanoparticle suspension (V_{ext}/V_{inj}) during the third push-pull test (18). Reproduced with permission from Refererence (18). Copyright 2010, Elsevier.

The push-pull tests confirmed the mobility of CMC-stabilized ZVI nanoparticles in this coarse-grained sediment and its effectiveness in degradation of chlorinated contaminants in the subsurface. However, each push-pull test only lasted less than two days. Detailed quantitative information is yet to be acquired on the radius of influence of the iron nanoparticles following the injections and the long-term dechlorination performance of the CMC-stabilized iron nanoparticles in the subsurface.

Field Test at an Alabama Site

A more comprehensive, two-year field study was conducted at a former manufacturing facility located in Alabama. Details of this field test have been reported by He et al. (*19*). The soil at the site predominately consists of silty clay but mixed with some limestone-gravels and sands, which renders the subsurface aquifer relatively permeable. The hydraulic conductivity within the test area was determined to be 5.6 ft/day and the pore velocity of the groundwater flow was estimated about 0.22 ft/day (*19*). A number of chlorinated contaminants including PCE, TCE, PCB1242 and cis-DCE were detected in the test area.

The dimensions of the test area were approximately 15 ft by 10 ft. As shown in Figure 4, four testing wells were installed along with the groundwater flow path, including one injection well (IW-1), two monitoring wells (MW-1 and MW-2) located at 5-ft and 10-ft down-gradient, respectively, and another monitoring well (MW-3) at 5-ft up-gradient. The wells IW-1, MW-1 and MW-3 were screened from 45 ft bgs to 50 ft bgs, while MW-2 was screened from 40 ft bgs to 45 ft bgs due to the change of the bed rock elevation.

CMC-stabilized Fe-Pd nanoparticles were prepared on site following the same approach as at the California site. The resultant stabilized Fe-Pd nanoparticles were able to completely pass through a Fisher filter paper P5. Two separate injection events were conducted at the site. About 150 gallons of a nanoparticle suspension containing 0.2 g/L Fe-Pd (Pd = 0.1 wt.% of Fe, CMC= 0.1%) were gravity-fed into the test aquifer on January 29, 2007. Another batch of 150 gallons of 1.0 g/L of Fe-Pd (Pd = 0.1 wt.% of Fe, CMC=0.6%) were injected at an injection pressure of ~5 psi on February 26, 2007. KBr was mixed with the nanoparticle suspension as a conservative tracer prior to injection. Groundwater sampling and analysis were conducted in monitoring wells to access the nanoparticle mobility and the change in groundwater hydrogeochemical conditions and chlorinated contaminant concentrations before and after the Fe-Pd nanoparticle injections.

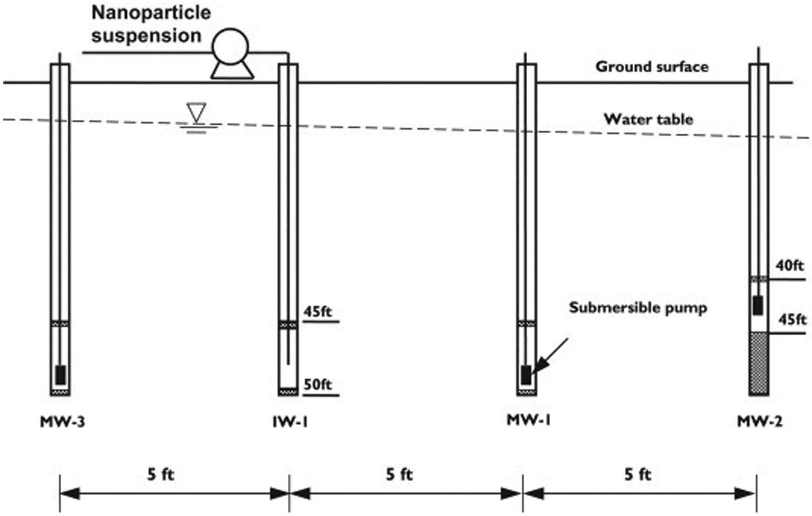

Figure 4. A cross-sectional view of the testing site and schematic of the in-situ injection of CMC-stabilized Fe-Pd nanoparticles (19). Reproduced with permission from Refererence (19). Copyright 2010, Elsevier.

The stabilized Fe-Pd nanoparticles could be easily delivered into the subsurface and dispersed in the test area. Figure 5 shows the normalized concentration (C/C_0) of bromide and Fe-Pd nanoparticles (measured as the total Fe concentration) in the downgradient monitoring wells after each injection event. C_0 is the concentration of bromide or Fe-Pd nanoparticles in the injected nanoparticle suspension. The normalized mass of Fe-Pd nanoparticles (represented by the area under the normalized concentration curves) transported towards the monitoring wells was compared to that of bromide to determine the nanoparticle mobility. After Injection #1, the normalized mass of Fe-Pd nanoparticles transported to MW-1 was about 37.4% of that for the tracer. The higher retention of Fe nanoparticles compared to the tracer could be attributed to filtration and adsorption effect in soil (*15*, *20*). Much enhanced mobility for both bromide and the nanoparticles was observed at the higher injection pressure or flow rate. When the injection flow rate was doubled from 0.67 gallon/min (Injection #1) to 1.34 gallon/min (Injection #2), the nanoparticles transported to MW-1 increased to 70% of that for the tracer bromide. Meanwhile, the normalized peak concentrations of bromide and Fe-Pd nanoparticles approached almost 100% and 84%, respectively. This observation was in concord with our laboratory results that the mobility and travel distance of stabilized ZVI nanoparticles increased with the groundwater flow velocity (*15*). At MW-2 which is located 10 ft down gradient from IW-1, as shown in Figure 5b, the normalized peak concentrations of bromide and Fe-Pd nanoparticles remained less than 3% throughout two injection events, suggesting that the injection pressure applied was exhausted at MW-1 and/or a poor hydraulic connection between MW-1 and MW-2 (*24*).

The observations were similar to those at California site: the injection of Fe-Pd nanoparticles led to a rapid decrease in ORP of groundwater in MW-1 and MW-2 from baseline values of -63 and -73 mV to -355 and -179 mV, respectively, in 2 h after Injection #2. The ORP value remained strongly negative in 6 days and gradually bounced back to the baseline levels after 8 to 10 days due to the exhaustion of the Fe-Pd nanoparticles.

Rapid degradation of chlorinated contaminants was observed in the two down-gradient monitoring wells MW-1 and MW-2 after injection of Fe-Pd nanoparticles, as shown in Figure 6. In MW-1, a sharp concentration peak to 1.6 ~2.8 of their baseline concentrations was observed for TCE, PCE and PCB1242 immediately after Injection #1 ions, which may stem from solubilization and re-mobilization of soil-sorbed contaminants by the injected fluid. Shortly, the concentrations of chlorinated contaminants quickly reduced in 15 hours and remained as low as 25% of their baseline concentrations for 7 days, indicating a substantial and rapid degradation of these chlorinated contaminants occurred after Fe-Pd nanoparticles injection. 5 days after Injection #1, the contaminant concentrations started to increase slowly along with the consumption of the reducing power of Fe-Pd nanoparticles. Laboratory studies showed that the degradation rate of TCE in DI water using 9-day aged Fe-Pd nanoparticles was only 2.8% of that for freshly-prepared nanoparticles (*19*).

It is noteworthy that the concentrations for chlorinated contaminants decreased again after two weeks. On Day 29, the concentrations of TCE and PCE were only 4% and 41% of the baseline concentrations in MW-1 (Figure 5a). Considering that the reducing power of the ZVI nanoparticles would have been exhausted within two weeks, the observed lasting reduction of chlorinated contaminants was attributed to a biological degradation that was likely boosted through introduction of the CMC-stabilized Fe-Pd nanoparticles. Anaerobic microorganisms are favorably promoted by the hydrogen gas produced from the corrosion of the iron nanoparticles (*25*, *26*) and the polysaccharide stabilizer CMC would serve as carbon source to support the bacteria growth. Figure 7a shows that the concentrations of TCE and PCE remained less than 10% of the baseline concentration after 567 days of the second injection, indicating the long-lasting potential of the nanoparticle boosted biological dechlorination process.

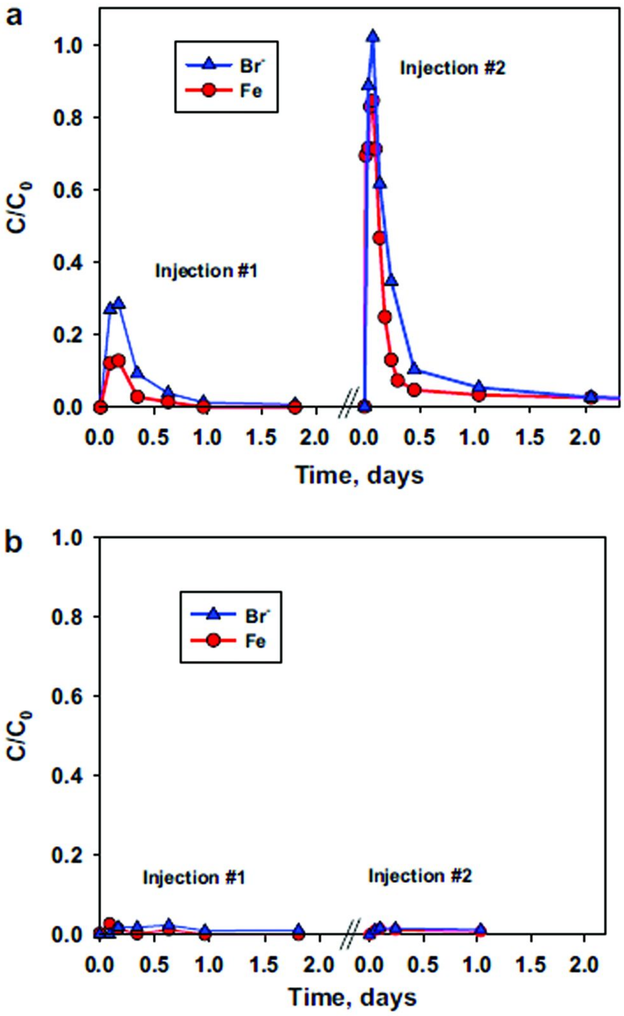

Figure 5. Transport of the tracer and CMC-stabilized ZVI nanoparticles to monitoring well (a) MW-1 and (b) MW-2 during Injection #1 and #2. The background total iron concentration in MW-1 and MW-2 were less than 1mg/L. For Injection #1, $C_{0,\ Fe}$=0.2 g/L, $C_{0,\ Br}$= 0.04 g/L. For Injection #2, $C_{0,\ Fe}$=1.0 g/L, $C_{0,\ Br}$= 0.07 g/L (19). Reproduced with permission from Refererence (19). Copyright 2010, Elsevier.

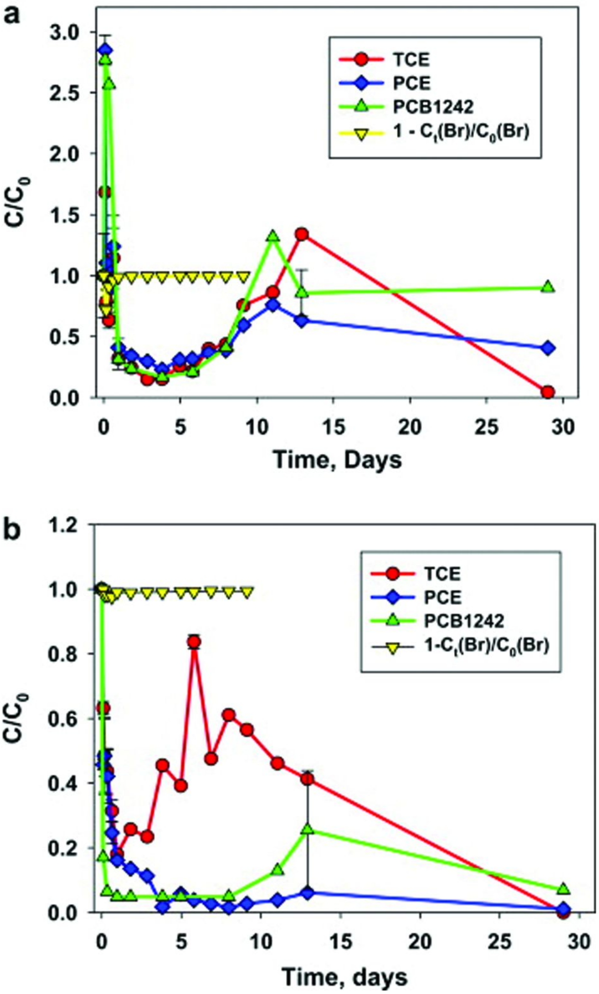

Figure 6. Concentration evolutions of PCE, TCE and PCB1242 in groundwater from (a) MW-1 and (b) MW-2 following injection #1. The baseline concentration C_0 of PCE, TCE and PCB1242 in MW-1 were 1225ppb, 1655ppb, and 21ppb, respectively. The baseline concentration C_0 of PCE, TCE and PCB1242 in MW-2 were 4133ppb, 3710ppb, and 62 ppb, respectively (19). Reproduced with permission from Refererence (19). Copyright 2010, Elsevier.

Figure 6b plots the normalized concentrations of chlorinated contaminants over time in MW-2. As in the case of MW-1, the concentrations of the chlorinated contaminants in MW-2 reduced rapidly following the injection of the Fe-Pd nanoparticles, but tended to bounce back after 3 to 5 days. For example, the TCE concentration was reduced to approximately 20% of the baseline concentration, but bounced back to ~85% after 6 days of the injection, and then went down again and reached almost undetectable on Day 29, confirming the initial abiotic process followed by a boosted biotic dechlorination. The PCE concentration remained below 6% of the baseline concentration. PCB1242 increased to 22% on Day 13 and later decreased to less than 7% of the baseline concentration on Day 29. The decrease of the chlorinated contaminants in MW-2 could be attributed to the abiotic reduction of chlorinated contaminants existing in the area between MW-1 and MW-2 and a decrease in chlorinated contaminant mass coming from the up-gradient groundwater. The long-term biodegradation was also evidenced in MW-2. As shown in Figure 7b, PCE, TCE and PCB1242 remained at <4%, < 4% and ~13%, respectively, of their baseline concentrations in MW-2 after 567 days of the second injection.

During the 596 days of experimental period, the total concentration of chlorinated ethenes (PCE, TCE, cis-DCE and VC) decreased by 40% and 61% in MW-1 and MW-2, respectively (*19*). The fractions for cis-DCE and vinyl chloride, which are typical reduction byproducts of biological dechlorination (*27*), increased from 73 % to 98 % and from 62 % to 98 % of the total chlorinated compounds, respectively, in MW-1 and MW-2 (*19*). The increase in the fractions of cis-DCE and VC further confirmed the role of the nanoparticle-boosted biological degradation in the lasting chlorination process. It should be noted that although the fraction of cis-DCE and vinyl chloride increased, the concentrations of cis-DCE and VC in MW-1 and MW-2 decreased from 9.6 to 7.7 mg/L and from 15.2 to 9.4 mg/L, respectively, on Day 596 after the first injection (*19*).

The field test at this Alabama site further confirmed that CMC-stabilized Fe-Pd nanoparticles were deliverable into a contaminated sandy soil under modest external pressure. The nanoparticles were able to reach at least 10 feet down-gradient from the injection well. If desired, the effective distance can be further extended by increasing the injection pressure. Rapid abiotic degradation of various chlorinated contaminants was observed immediately after the Fe-Pd nanoparticles injection and the dechlorination last for ~12 days. Then, the stabilized nanoparticles boosted a strong biological degradation process, which offered long-tem reduction of chlorinated contaminants.

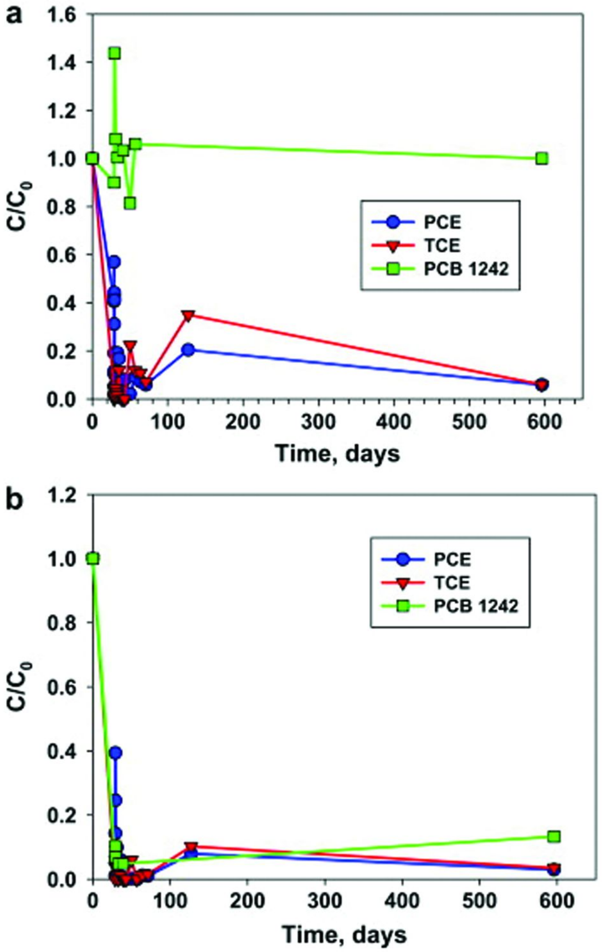

Figure 7. The long-term concentration histories of PCE, TCE and PCB1242 in groundwater from (a) MW-1 and (b) MW-2, following two injections of CMC-stabilized Fe-Pd nanoparticles (19). Reproduced with permission from Refererence (19). Copyright 2010, Elsevier.

Constraints of the in Situ Remediation Technology

It should be noted that the foregoing two field tests were performed at sites that have a relatively high hydraulic conductivity and the organic matter content in the soil. In addition, the aquifers are either well confined or well defined with a impermeable bed rock. To better understand the constraints of the stabilized Fe-Pd nanoparticles for degrading soil-sorbed contaminants and to investigate the effects of soil sorption and dissolved organic matter on TCE degradation, Zhang et al. (*20*) carried out detailed laboratory batch and column studies with two model soils (a potting soil and a Smith Farm Soil) using CMC-stabilized Fe-Pd nanoparticles.

The potting soil contained a high organic matter of 8.2%, whereas the Smith Farm soil had a low organic matter content of 0.7%. About 0.52 mg/g and 0.45 mg/g TCE were pre-sorbed on the potting soil and Smith Farm soil, respectively, prior to each degradation test. CMC-stabilized Fe-Pd nanoparticles were prepared at 0.3 g/L as Fe (Pd = 0.1 wt.% of Fe, CMC = 0.24%).

The degradation kinetic tests were initiated by mixing ~58 mL of the 0.3 g/L Fe-Pd nanoparticles with 12 g TCE-sorbed soil in 67 mL glass vials. The mixtures were then shaken on a rotator at 60 rpm at 21±1°C. At selected time intervals, the glass vials were centrifuged to separate the soil and liquid suspension. 100 μL of each supernatant was transferred into 1 mL of hexane for extraction. TCE and degradation products in hexane were then analyzed on an HP 6890 Gas Chromatograph equipped with an electron capture detector (ECD) (*28*). The TCE remaining in the soil was extracted with 50 mL methanol in a hot water bath at 70°C for 2 days twice consecutively and analyzed by gas chromatograph.

Figure 8 plots the degradation kinetic data of TCE that were pre-sorbed on the two model soils and TCE dissolved in DI water. The CMC-stabilized Fe-Pd nanoparticles degraded about 44% and 82% of sorbed TCE in the potting soil and Smith Farm within 27 h, respectively. In contract, the same nanoparticles completely degraded water-dissolved TCE within 4 hours at the identical ZVI to TCE mass ratio, with a pseudo-first-order reaction rate constant of 1.64 h^{-1}. A comparison of the degradation kinetics of soil-sorbed TCE to that of dissolved TCE reveals that the TCE degradation rate and extent is strongly limited by its sorption on soil. Between the two soils, the potting soil contains much higher organic matter, and thus, offers a greater TCE sorption capacity and stronger affinity to TCE (*20*, *29*). As a result, a smaller percentage of sorbed TCE was desorbed and degraded for the potting soil, leaving 66% of TCE remaining in the soil phase after 27 h. This observation indicates that soil organic matter can greatly reduce the availability of TCE for reductive dechlorination by the stabilized iron nanoparticles.

Zhang et al. (*20*) found that the presence of soluble organic matter in the aqueous phase severely inhibited TCE degradation by the nanoparticles. Figure 9 shows the TCE degradation rates in the aqueous phase by CMC-stabilized Fe-Pd nanoparticles in the presence of soluble soil organic matter that was pre-extracted by DI water from the potting soil. The presence 40 mg/L as TOC of the dissolved organic matter, the observed pseudo-first-order reaction rate constant was reduced from 1.22 h^{-1} (without the organic matter) to 0.81 h^{-1}. The reaction rate constant further decreased to 0.41 h^{-1} when the organic matter concentration was raised to 350 mg/L as TOC. Chen et al. (*30*) also reported that the pseudo-first-order reaction rate constant of reductive dechlorination by commercial ZVI nanoparticles decreased from 0.018 to 0.014 h^{-1} when 10 mg/L of the Suwannee River humic acid was exerted.

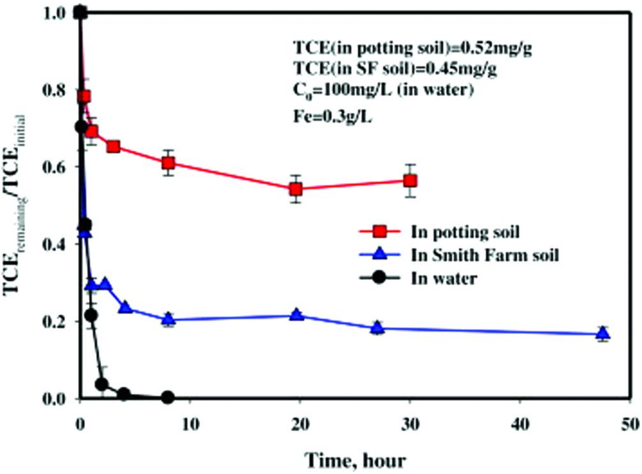

Figure 8. Dechlorination of soil-sorbed and water-dissolved TCE with CMC-stabilized Fe-Pd nanoparticles with two model soils. Initial TCE in potting soil and Smith Farm soil was 0.52 mg/g and 0.45 mg/g, respectively; The ZVI to TCE mass ratio is 6.24: 17.4 and 5.4:17.4 and 1:3 for potting soil, Smith Farm soil, and solution-only system, respectively; C_0 *= 100 mg/L (initial TCE concentration in the solution only degradation tests); Fe = 0.3 g/L; Pd/Fe = 0.1 wt%; CMC (sodium form)= 0.24 % (20). Reproduced with permission from Refererence (20). Copyright 2011, Elsevier.*

A number of factors can be held responsible for the observed inhibitive effect of dissolved organic matter on the TCE dechlorination. Firstly, the organic molecules may compete with the CMC molecules for the surface sites on the ZVI nanoparticles, thereby interfering with the stabilization of the nanoparticles. The hydrodynamic diameter of the CMC-stabilized ZVI nanoparticles was measured with a suspension containing 0.2 g/L Fe and 0.2 wt.% CMC at pH 7.9 and at room temperature (25 °C). A dynamic light scattering (DLS) Zetasizer Nano ZS (Malvern Instruments Ltd, Malvern, Southborough, MA, USA) was used. The result indicated that the presence of 350 mg/L as TOC of dissolved organic matter increased the mean hydrodynamic diameter of the CMC-stabilized ZVI nanoparticles from 155 nm to 200 nm (*20*). The increase of the particle size lessens the available reaction sites on the surface of the nanoparticles and lower the reaction rate. Secondly, adsorption of dissolved organic matter on the ZVI surface decreases the reactive sites for TCE degradation and exerts an additional mass transfer barrier for TCE. Tratnyek et al. (*31*) reported that dissolved organic matter from a Suwannee River water sample exhibited faster adsorption equilibrium and higher adsorption affinity to ZVI than TCE, suggesting that natural organic matter will compete with TCE for the available reactive sites on the ZVI surface.

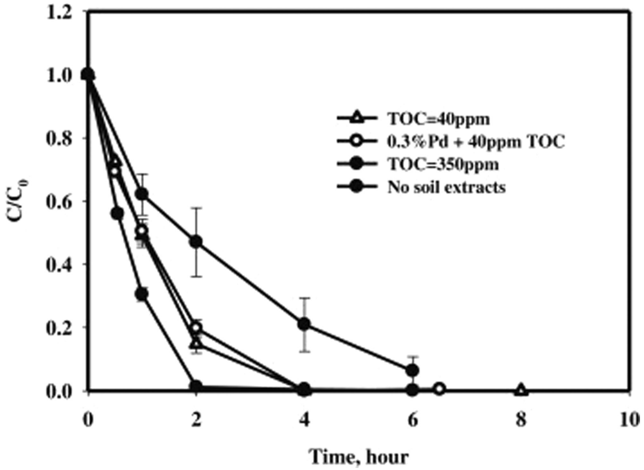

Figure 9. Reductive dechlorination of TCE in water by CMC-stabilized Fe-Pd nanoparticles with or without soil extracts. Initial TCE concentration was 100 mg/L, Fe = 0.3 g/L, CMC (sodium form)= 0.24 %, Pd = 0.1 wt% of Fe except for one case where Pd = 0.3 wt.% of Fe. Organic matter extracted from the Soil was quantified as TOC in the aqueous phase (20). Reproduced with permission from Refererence (20). Copyright 2011, Elsevier.

Concluding Remarks

Numerous laboratory test data have demonstrated that Fe-Pd nanoparticles can effectively degrade various chlorinated solvents in the solution phase. However, limited information is available on the field performance of the nanoparticles. For field in situ remediation uses, the CMC-stabilized ZVI nanoparticles have shown promising in terms of particle deliverability and reactivity. This chapter summarizes results from two field tests where CMC-stabilized Fe-Pd nanoparticles were delivered into aquifers of relatively high hydraulic conductivity. In both cases, the nanoparticles were found transportable through the soil under modest external injection pressure. The particle retention or travel distance can be manipulated by controlling the injection pressure or flow rate. Rapid and complete dechlorination reaction was observed during the initial stage (~12 days) following each injection. Following the initial abiotic dechlorination, the delivered nanoparticles were able to induce a long-standing biological dechlorination process, resulting in a sustained dechlorination (40%-61% reduction in total mass of chlorinated solvents) over the experimental period of 596 days at the Alabama site. However, this technology has the following constraints: 1) the hydraulic conductivity must be reasonably high to facilitate effective delivery of the nanoparticles, 2) the presence of high concentrations of dissolved organic matter may inhibit the reactivity of the nanoparticles, 3) soil sorption of chlorinated compounds may limit the dechlorination arte and extent, and thus, caution should be exercised for soil rich of organic matter.

References

1. Gillham, R.W.; Ohannesin, S.F. *Ground Water* **1994**, *32*, 958–967.
2. Wang, C. B.; Zhang, W. X. *Environ. Sci. Technol.* **1997**, *31*, 2154–2156.
3. Liu, Y.Q.; Majetich, S.A.; Tilton, R.D.; Sholl, D.S.; Lowry, G.V. *Environ. Sci. Technol.* **2005**, *39*, 1338–1345.
4. Elliott, D. W.; Zhang, W. X. *Environ. Sci. Technol.* **2001**, *35*, 4922–4926.
5. Taghavy, A.; Costanza, J.; Pennell, K. D.; Abriola, L. M. *J. Contam. Hydrol.* **2010**, *118*, 128–142.
6. Schrick, B.; Hydutsky, B. W.; Blough, J. L.; Mallouk, T. E. *Chem. Mater.* **2004**, *16*, 2187–2193.
7. He, F.; Zhao, D. Y.; Liu, J. C.; Roberts, C. B. *Ind. Eng. Chem. Res.* **2007**, *46*, 29–34.
8. Quinn, J.; Geiger, C.; Clausen, C.; Brooks, K.; Coon, C.; O’Hara, S.; Krug, T.; Major, D.; Yoon, W. S.; Gavaskar, A.; Holdsworth, T. *Environ. Sci. Technol.* **2005**, *39*, 1309–1318.
9. Zhan, J. J.; Zheng, T. H.; Piringer, G.; Day, C.; McPherson, G. L.; Lu, Y. F.; Papadopoulos, K.; John, V. T. *Environ. Sci. Technol.* **2008**, *42*, 8871–8876.
10. Zhan, J. J.; Sunkara, B.; Le, L.; John, V. T.; He, J. B.; McPherson, G. L.; Piringer, G.; Lu, Y. F. *Environ. Sci. Technol.* **2009**, *43*, 8616–8621.
11. Phenrat, T.; Fagerlund, F.; Illangasekare, T.; Lowry, G. V.; Tilton, R. D. *Environ. Sci. Technol.* **2011**, *45*, 6102–6109.
12. Ponder, S. M.; Darab, J. G.; Mallouk, T. E. *Environ. Sci. Technol.* **2000**, *34*, 2564–2569.
13. Kanel, S. R.; Nepal, D.; Manning, B.; Choi, H. *J. Nanopart. Res.* **2007**, *9*, 725–735.
14. Sun, Y. P.; Li, X. Q.; Zhang, W. X.; Wang, H. P. *Colloids Surf., A* **2007**, *308*, 60–66.
15. He, F.; Zhang, M.; Qian, T. W.; Zhao, D. Y. *J. Colloid Interface Sci.* **2009**, *334*, 96–102.
16. Marvin, C. H.; Painter, S.; Tomy, G. T.; Stern, G. A.; Braekevelt, E.; Muir, D. C. G. *Environ. Sci. Technol.* **2003**, *37*, 4561–4568.
17. Rehfeldt, K. R.; Boggs, J. M.; Gelhar, L. W. *Water Resour. Res.* **1992**, *28*, 3309–3324.
18. Bennett, P.; He, F.; Zhao, D. Y.; Aiken, B.; Feldman, L. *J. Contam. Hydrol.* **2010**, *116*, 35–46.
19. He, F.; Zhao, D. Y.; Paul, C. *Water Res.* **2010**, *44*, 2360–2370.
20. Zhang, M.; He, F.; Zhao, D. Y.; Hao, X. D. *Water Res.* **2011**, *45*, 2401–2414.
21. Lien, H. L.; Zhang, W. X. *Colloid Surf., A* **2001**, *191*, 97–105.
22. Kirschling, T. L.; Gregory, K. B.; Minkley, J. E. G.; Lowry, G. V.; Tilton, R. D. *Environ. Sci. Technol.* **2010**, *44*, 3474–3480.

23. MaymoGatell, X.; Chien, Y. T.; Gossett, J. M.; Zinder, S. H. *Science* **1997**, *276*, 1568–1571.
24. Sanford, W. E.; Cook, P. G.; Robinson, N. I.; Weatherill, D. *Ground Water* **2006**, *44*, 564–573.
25. DiStefano, T. D.; Gossett, J.; Zinder, S. *Appl. Environ. Microbiol.* **1992**, *58*, 3622–3629.
26. Maymo-Gatell, X.; Tandoi, V.; Gossett, J. M.; Zinder, S. H. *Appl. Environ. Microbiol.* **1995**, *61*, 3928–3933.
27. Magnuson, J. K.; Stern, R. V.; Gossett, J. M.; Zinder, S. H.; Burris, D. R. *Appl. Environ. Microbiol.* **1998**, *64*, 1270–1275.
28. He, F.; Zhao, D. Y. *Environ. Sci. Technol.* **2005**, *39*, 3314–3320.
29. Chiou, C. T.; Porter, P. E.; Schmedding, D. W. *Environ. Sci. Technol.* **1983**, *17*, 227–231.
30. Chen, J.; Xiu, Z.; Lowry, G. V.; Alvarez, P. J. J. *Water Res.* **2011**, *45*, 1995–2001.
31. Tratnyek, P. G.; Scherer, M. M.; Deng, B.; Hu, S. *Water Res.* **2001**, *35*, 4435–4443.

Chapter 7

Polycation-Tethered Micelles as Immobilized Detergents for NAPL Remediation

Paul Dubin,[1,*] Jessica Schiffman,[2] and Bingqian Zheng[1]

[1]Department of Chemistry, University of Massachusetts,
710 N. Pleasant Street, Amherst, Massachusetts, 01003
[2]Chemical Engineering, University of Massachusetts,
710 N. Pleasant Street, Amherst, Massachusetts 01003
[*]E-mail: dubin@chem.umass.edu

Applications of permeable reactive barriers to filter contaminants out of groundwater have not taken advantage of surfactant micelles to remove organic contaminants. Such barriers need to have low cost, high capacity, good flow properties and recyclability, requirements not met by organoclays or micellar ultrafiltration. We describe the use of inexpensive and GRAS (genrally recognized as safe) polycations as noncovalent bridges that tether anionic surfactant micelles to porous media such as silica or sand. The solubilizing power of the micelles is fully retained. One-step coating processes can be used to optimize the silica-polycation-composite for maximum uptake of pollutants such as toluene and dichlorethane. Since the interactions are electrostatic and noncovalent, variables such as pH and salt can be used to also tune release of micelles rich in NAPL's (nonaqueous phase liquids). We discuss the effects of such parameters and describe the role of the surface charge and porosity of siliceous substrates. The temperature-sensitivity of micelle-polycation systems suggest additional ways to tune uptake and release.

In Novel Solutions to Water Pollution; Ahuja, S., et al.;
ACS Symposium Series; American Chemical Society: Washington, DC, 2013.

Introduction and Background

The need for inexpensive, versatile materials to remediate groundwater polluted by agrochemical, petroleum, and industrial wastes is rapidly increasing as the *per capita* supply of potable water is decreasing. While "permeable reactive barriers (*1*)" provide an alternative to Herculean pump-and-treat methods, they largely fail to address organophilic non-aqueous phase liquids (NAPLs). The ability to solubilize these with surfactants forms the basis of remediation by organoclays (*2*) or micelle-enhanced ultrafiltration (*3*). However, the former lacks capacity since the surfactant layer is rapidly saturated, and the latter leads to highly diluted NAPL solutions, and requires micelle retention along with high rates of NAPL permeation, hence avoiding membrane fouling.

The problem of NAPL remediation would ideally be met by an inexpensive removable substrate with application mode flexibility, that retains the solubilization efficiency of micelles, along with resistance to dilution. This need could be met if polymers could bind and tether micelles to a versatile range of inactive substrates. This is feasible via noncovalent electrostatic interactions for two reasons. First, the complexation of polelectrolytes to oppositely charge micelles is strong (although reversible) (*4*), but does not appear to degrade solubilizing efficiency (*5*). Second, polyelectrolytes, polycations in particular, are highly substantive to many surfaces.

Several pieces of evidence attest to the integrity of anionic/nonionic micelles (mole fraction of anionic $=Y$) in complexes with polyelectrolytes, either in solution or in more condensed state. The remarkably high MW of intrapolymer poly(dimethyldiallylammonium chloride) (PDADMAC)-SDS/TX100 complexes can only be explained if a single chain can bind many micelles (*6*). CryoTEM images of complexes and coacervates (*7*) show that ca. 15 nm particles abundant at $Y<Y_c$ (a micelle surface charge density too low to lead to polyelectrolyte binding) and too small to be polyelectrolyte (PE), are confined within ca. 200 nm regions for $Y>Y_c$. At such conditions conducive to binding, the critical micelle concentration is identical in the presence or absence of PE. Most significant for the work here, it can be shown as in Figure 1 that the solubilization of a model NAPL (Orange OT, [(2-methylphenyl)azo]-2-naphthol) is identical regardless of PE-complexation state as long as total surfactant concentration (anionic + nonionic) is fixed[5]. Indeed, Scamehorn and co-workers used polyelectrolyte-surfanctant complexes, including PDADMAC-SDS in micellar ultrafiltration to decrease surfactant permeation (*8*). However, in contrast the PDADMAC-SDS system, the PDADMAC-SDS/TX100 system allows for the modulation of the polycation-micelle interaction by tuning the micelle surface charge density via Y. These allows tuning of the complex phase state, which would default to precipitate for pure SDS ($Y=1$).

Ample evidence demonstrates the avid binding of polycations to siliceous media. The adsorption of PDADMAC, an inexpensive and non-toxic cationic polymer produced in large scale for waste water treatment, has been used by us to modify porous glass (*9*), silicon (SiO_2) surfaces (*10*), and electrophoresis capillaries (*11*). In all cases the adsorbed polycation was able to bind proteins *selectively* showing that the colloid interaction of this cationic polyelectrolyte in solution was retained in its adsorbed state. Given the propensity of PDADMAC to bind anionic/nonionic (SDS/TX100) anionic/micelles in solution (*12*), it is likely that a similar mechanism would allow for the tethering of micelles (SDS/TX100) to siliceous surfaces. Since adsorption of cationic polyelectrolytes to negative surfaces is highly durable, even irreversible (*13*), while the binding of anionic/nonionic micelles to the same polycations can be reversed in several ways, it should therefore be possible to release micelles in a controlled manner after they have been used to remove an organic pollutant from an aqueous phase.

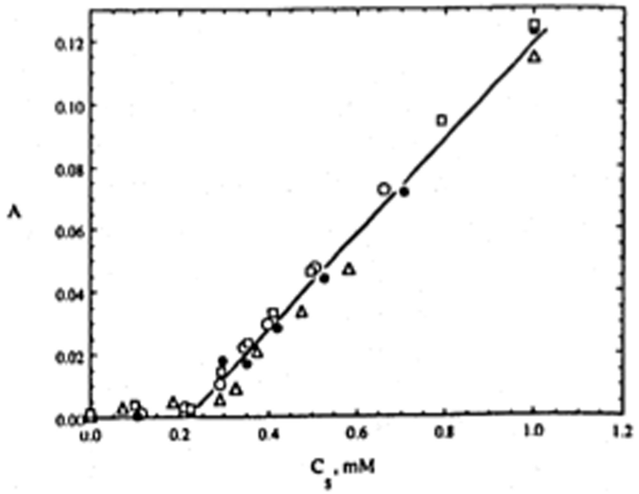

Figure 1. Absorbance of solubilized Orange OT (model NAPL) in solutions of SDS/TX100 (Y = 0.23) at 0.40 M NaCl. C_S is the molar concentration of total surfactant. Concentrations of PDADMAC (Merquat 100, nominal MW 2x10^5): C_p(g/L) = 0 (l), 0.10 (m), and 0.20 (q). Concentration allowed to vary with C_S (s). Critical micelle concentration, cmc, unaltered by polycation binding indicates little perturbation of micelle. (Reproduced with permission from ref. (5). Copyright 1991 Elsevier).

The PDADMAC-SDS/TX100 system shows a number of interesting and important features. The polycation-micelle interaction can be modulated by the mole fraction of anionic in the surfactant mixture, i.e. the fraction of micelle head groups that carry a charge. This variable, *Y*, ranging from 0 (pure nonionic) to 1 (pure anionic) effectively tunes the micelle surface charge density. As shown in Figure 2, with increasing *Y* at low salt, the system progresses from (I) a non-interacting system, to (II) complexes with excess PE (net positive complexes), to (IV) complexes with excess micelle (net negative), and finally (V) phase separation (precipitation) (*14*). At most ionic strengths, region III is observed. Here, complexes of near zero charge are susceptible to liquid-liquid phase separation, i.e., coacervation may occur. The second key parameter modulating the phase states is the ionic strength, *I*, and Figure 1 shows the interdependence of *Y* and *I* as a set of phase boundaries. Together, *Y* and *I* represent micelle surface potential ψ_0 and screening length κ^{-1}, where κ, the

Debye-Hückel screening parameter, varies as $I^{1/2}$. Theoretical foundations for the ionic strength dependence for critical binding of polyelectrolytes to spherical particles have recently been put forward quite comprehensively by Cherstvy and Winkler (*15*) Since the micelle-PE interaction energy increases with ψ_0 and decreases with added salt, the negative slopes of the phase boundary lines in Figure 1 show the opposing effects of micelle charge and ionic strength. The phase boundary lines can be considered to identify conditions in which Y/I is just large enough for the interaction energy to cause incipient complexation (at Y_c), or if significantly larger, enough to expel all counterions (at precipitation – Y_p). The response of the system to ionic strength provides a way to bind or release micelles from polycation.

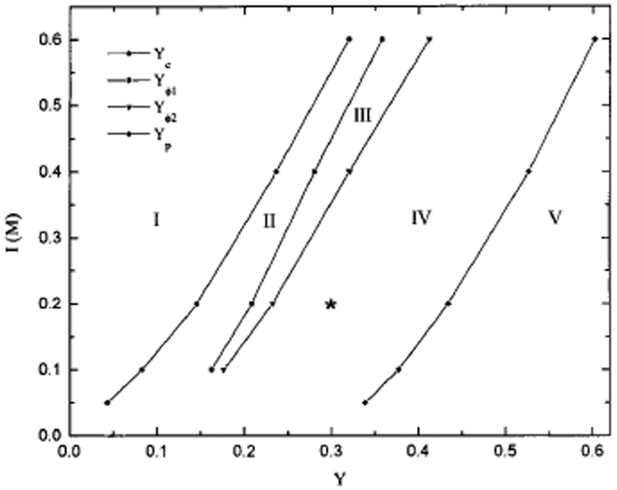

Figure 2. Phase boundaries for the PDADMAC-SDS/TX100 polycation-mixed micelle system, presented as ionic strength I and mixed micelle anionic:nonionic mole ratio (Y). From left to right: (I) non-interacting system, (II) soluble polycation-micelle complex (excess polycation), (III) coacervate, (IV) soluble polycation-micelle complex (excess micelle), and (V) precipitate. The ratio of SDS charge to polycation charge ([+]/[-]) progresses from zero to infinity, passing through unity in region III. Boundaries II/III and III/IV depend also on polymer MW, and polymer:surfactant stoichiometry; regarding I/II, Y_c depends exclusively on I. (Reproduced with permission from ref. (14). Copyright 1996 American Chemical Society).

In addition to effects of *Y* and *I*, PDADMAC-SDS/TX100 solutions display thermally induced phase transitions (*16*), of considerable interest in that temperature may be changed more continuously and reversibly than ionic strength. Coacervation, the liquid-liquid phase separation that occurs in region III in Figure 2, is induced at critical temperatures T_φ that can be modulated by e.g. ionic strength, polymer MW and SDS:TX100 ratio. Figure 3 shows this LCST (lower critical solution temperature) as a function of *Y* for different polymer concentrations and polymer MW's. This temperature dependence has two-fold significance for NAPL remediation. First, a solution of PDADMAC-SDS/TX100 that is saturated with pollutant can be concentrated by more than 10-fold by simply raising the temperature above T_{φ}, which allows for easy removal of pollutant after settling or centrifugation, as will be shown in Figure 10. Second, the same desolvation is expected for PE-micelles immobilized on surfaces.

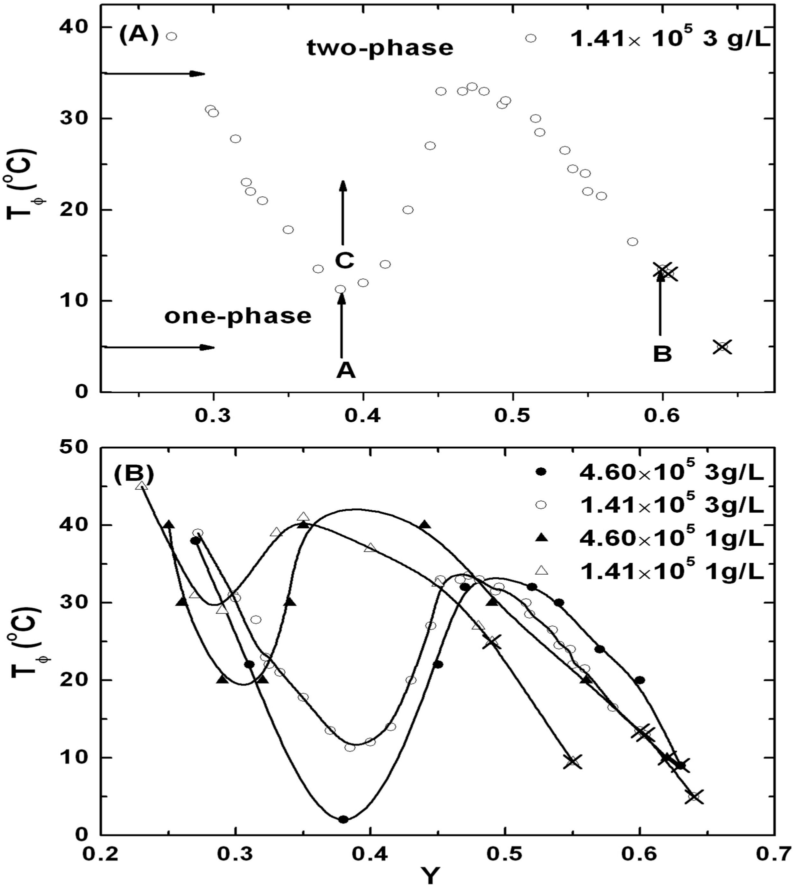

Figure 3. (A) Temperature-induced phase separation in PDADMAC-SDS/TX100 in 0.4 M NaCl solutions shown as LCST (lower critical solution temperature) dependence on surfactant composition Y. (B) Effects of polymer MW and concentration. "x" symbols correspond to dense phases appearing as precipitates rather than coacervates. (Reproduced with permission from ref. (14). Copyright 1996 American Chemical Society).

While Figure 3 does portray an LCST, it is certainly not directly comparable to polymer solution phase diagrams, as solute concentration is not a variable and thus tie-lines do not exist. While we have speculated on the entropic contributions of counterion loss and chain configuration to T_{φ} in ref. (*16*), the rich phenomenology of this liquid-liquid transition is still under investigation (*17*).

Results and Discussion

SPIM: Silica-Polyelectrolyte Immobilized Micelles

Proof of Concept

A simple proof of concept in Figure 4 shows a column packed with standard quartz sand, with an intermediate layer of sand treated first with PDADMAC, then with SDS/TX100 (followed by washing to remove unbound surfactant). When a methanol-water solution of Orange OT is eluted through the column, all the dye is absorbed by the intermediate layer of treated sand, and the eluant is water white. When white sea sand was used in place of the non-white quartz sand, no dye adsorption occurred, an unexpected result due to the lack of surface charge on $CaCO_3$ and the consequent lack of polycation adsorption. For purposes of visualization, the following experiments are conducted with white CPG glass, which offers the important advantages of being well-characterized with respect to particle size, and particularly, pore size.

Figure 4. A SPIM "sand-wich". Treated polycation-micelle sand is layered between untreated sand and Orange OT (in MeOH-water) is eluted. All dye is trapped in the SPIM layer.

Optimization of Polymer and Micelle Loading

Many variables could influence the efficiency of organophile uptake. As a starting assumption we proposed that the uptake of NAPL per unit mass of substrate (e.g. sand) would be linear with the surfactant loading, which in turn, would be linear with polycation loading. First, in order to explore the optimization of conditions for polycation adsorption, PDADMAC was replaced with poly-4-vinylpyridine, quaternized with methyl iodide (QPVP) with a readily quantitated UV chromophore; the substrate sand was replaced with the more reproducible and better characterized "Corning porous glass", CPG (*18*); and toluene was used as more representative of polluting NAPLS. At pH 9.5 in 0.5 M NaCl, the adsorbed amount of QPVP in mg/m^2 glass, Γ, was found to reach a plateau within one hour, as expected for adsorption on a porous surface. This equilibrium value Γ_{eq} was measured at pH 9.5 as a function of *I* and found to attain a local maximum of 0.3 mg/m^2 in 1.0 M NaCl, with rather little change at higher salt. When Γ_{eq} was measured at 0.5M NaCl for polymer concentrations ranging from 0-20 g/L, a linear binding isotherm was observed, rather than a plateau at high QPVP concentration. Slow equilibria, strong binding at high salt, and linear isotherms are not typical for polyelectrolyte adsorption, and suggest a more complex situation for porous glass as opposed to planar surfaces.

In order to establish whether maximizing polycation binding would indeed achieve maximum micelle loading, varying amounts of QPVP were adsorbed onto CPG (7.5 nm pore diameter) prior to adsorption of mixed micelles and rinsing. The unexpected result shown in Figure 5[15] was a *decrease* in micelle loading as Γ_{eq} increased from 0.1 to 0.4 mg/m^2. On the other hand, the efficiency of toluene binding per micelle increased substantially with Γ_{eq}, as shown in Figure 6. One implication of these results is that the conformation of the polycation is dependent on Γ_{eq}, and that the amount of micelle bound per polycation — or its solubilization efficiency — could be affected by polycation conformation.

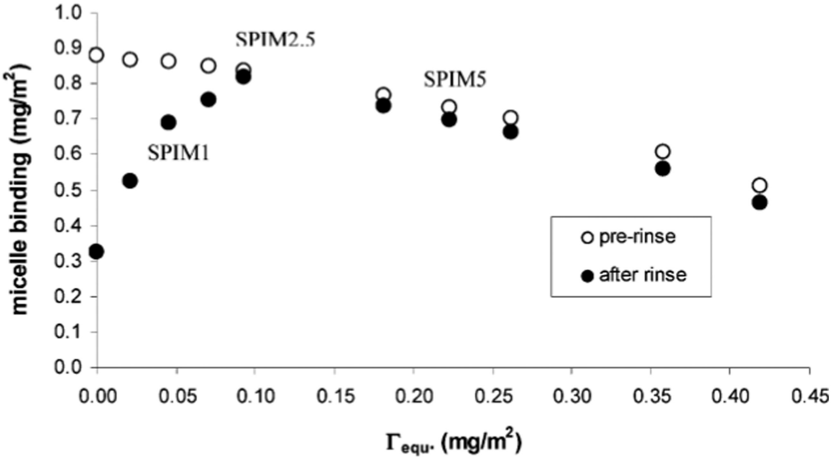

Figure 5. Dependence of micelle loading on the amount of pre-adsorbed polycation (QPVP). (Reproduced with permission from ref. (16). Copyright 2005 American Chemical Society).

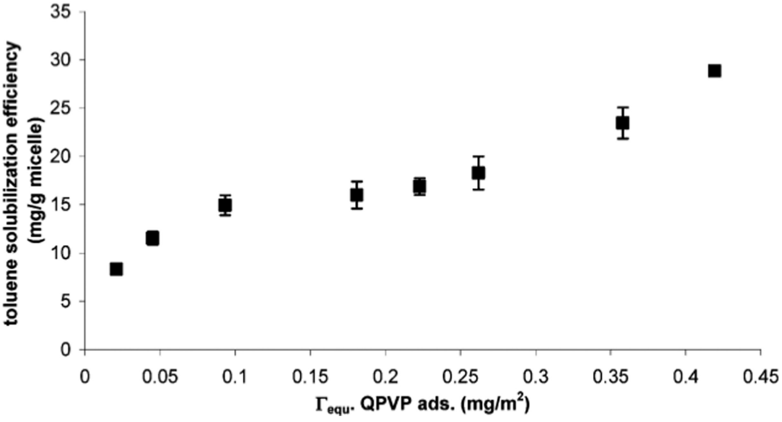

Figure 6. Dependence of micelle solubilization efficiency — mg toluene (g adsorbed micelle)$^{-1}$ — as a function of the degree of polycation adsorption prior to micelle loading. (Reproduced with permission from ref. (16). Copyright 2005 American Chemical Society).

Optimization of Pore Size and Configuration of Adsorbed Polymer

To explore the role of the conformation of the adsorbed polycation, we varied the ratio of polymer size to pore size using CPG with pore diameters from 7.5 to 285 nm ($0.6 < r_p / R_h < 460$) (*19*). The surprising results are shown in Figure 7. On an area basis (7B), polycation adsorption is maximized at $r_p / R_h > 4$, while micelle uptake is maximized at $r_p / R_h = 2$. On a weight basis (7A), polycation adsorption is maximum at $r_p / R_h = 2$, but micelle uptake appears to increase down to the smallest pore size, where $r_p / R_h = 0.3$, and the pores are smaller than the micelle! The two salient facts — (1) polycations *larger* than pores are adsorbed effectively, and (2) micelle binding per unit mass of polymer is largest for pores smaller than the polymer – are best explained using the model of Lin and Deen (*20*). First, their calculations explain adsorption at $r_p < R_h$: the increased negative electrostatic potential within a small pore produces a relative gain in energy even if only some of the polymer is confined upon adsorption. Second, this leaves an array of unconfined polymer segments available for micelle binding as depicted schematically in Figure 8.

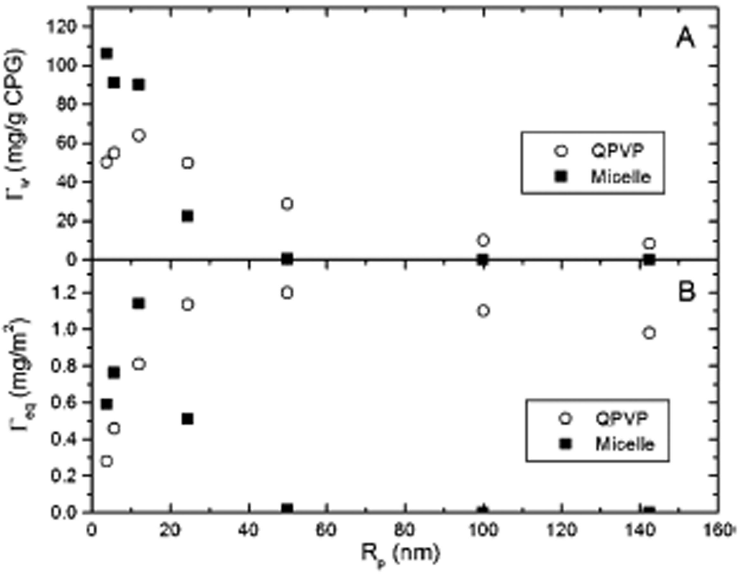

Figure 7. QPVP and micelle uptake (mg/g CPG, or mg/m² CPG, A and B, respectively). For QPVP, R_h = 6.2 mm. pH 9.5, I= 0.5 M NaCl. (Reproduced with permission from ref. (17). Copyright 2005 American Chemical Society).

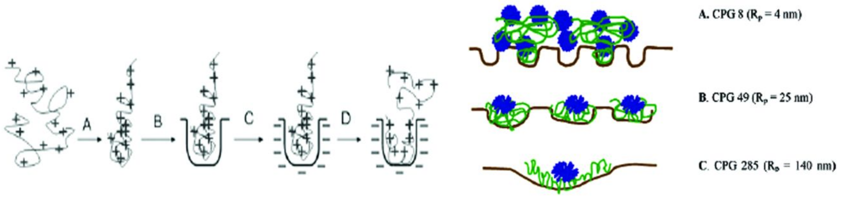

Figure 8. Left: Hypothetical steps in the adsorption of a polycation for r_p /R_h <1, leading to partially confined chains. Energy expended in compression in neutral pore (A) compensated by interaction of compressed polycation with charge pore (C). Right: Schematic depiction of micelle uptake on polycation adsorbed on this "mushroom" configuration. (Reproduced with permission from ref. (18). Copyright 2007 American Chemical Society).

Sequential vs. One-Step Loading

While sequential coating procedures might offer more control of final properties, we were surprised to find that similar ultimate properties could be obtained in a single step wherein PE-micelle complexes were added to porous glass (Figure 9, middle) (*21*). This result has an intriguing similarity to the recent finding that a layer-by-layer buildup of polyanion-polycation films can effectively be replaced by repeated application (spin-coating) of polyanion-polycation *mixture* (*22*). This result suggests that a reorganization of the coating solution occurs leading to the preferential location vicinal to the prior surface of the macroion of opposite charge. It was further proposed that such reorganization is promoted by shear forces.

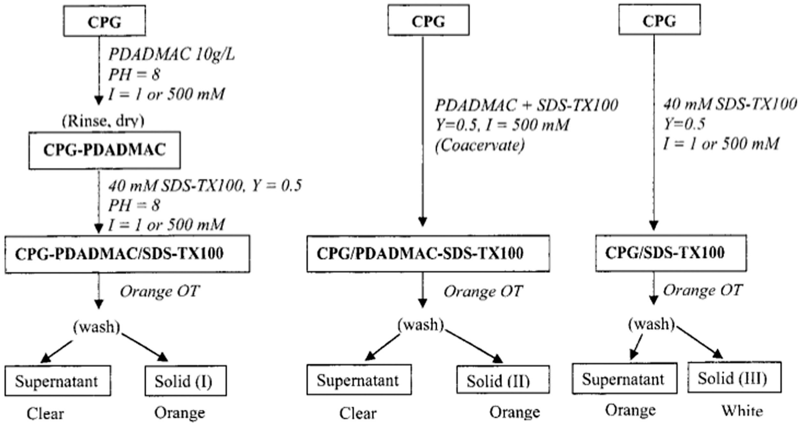

Figure 9. Sequential (left) and simultaneous application of polycation and micelles, followed by qualitative visualization of Orange OT uptake. (Reproduced with permission from ref. (20). Copyright 2001 American Chemical Society).

Uptake of Organic Pollutants

SPIM samples were added at 2 wt% to solutions of standard purgeable halocarbon/aromatic mixtures (400-2000 ppb) in water. The most significant results were obtained for halocarbons, with 2-4 fold reductions for dichlorobenenes, carbon tetrachloride, tetrachloroethene and chlorobenzene. The application of SPIM-like materials in filtration mode would clearly yield more dramatic results.

Temperature-Dependent NAPL Concentration

Materna et al[3] pointed out the use of surfactant cloud point separation to enhance the capture of phenolics after ultrafiltration. A similar approach can be applied with the polycation-micelle system described here, Figure 3 showing the wide range of phase separation temperatures that can be achieved. The resultant coacervates, containing surfactant concentrations as high as 30% w/w, could contain NAPL's is a dense fluid state. To test this proposal, a solution of 3g/L PDADMAC and 20mM TX100 was titrated with 60mM SDS to Y=0.35, saturated with Orange OT, then filtered. Centrifugation for 30 min at a temperature slightly above T_φ. As shown in Figure 10, coacervation has concentrated more than 90% of the original solubilized dye into <2% of the original volume. Similar effects might be expected for micelles adsorbed on spherical particles with polycation brushes.

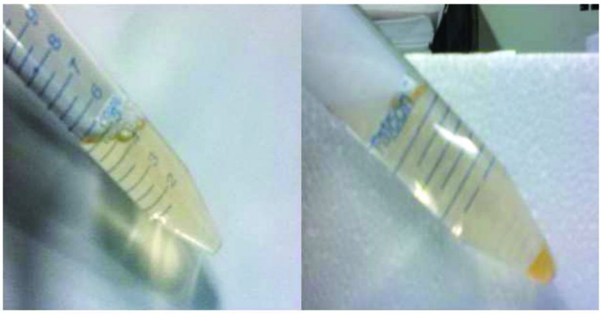

Figure 10. Concentration of Orange OT from polycation-micelle solution by temperature-induced coacervation. Solutions before (left) and after (right) warming to $T > T_\varphi$.

Conclusions and Prospects

The ability of polycations to bridge surfactant micelles with negatively charged surfaces could be utilized in many modes for water remediation. These include static applications, such as emplacement of polycation/micelle-coated sand in regions around buried fuel tanks to inhibit diffusion; quiescent placement in porous containers in wells threatened by polluted aquifers; and active filtration systems in which micelles are adsorbed on fiberglass mesh. An additional opportunity arises from the temperature-induced phase separation of the polycation-micelle system, which could combine advantages of reduced diffusivity vis-à-vis micellar ultrafiltration[8] with the concentrating power of reversible phase separation (*22*). The temperature-induced collapse of solubilizate-saturated polycation-bound micelles shown in Figure 10, suggests analogous behavior for polycation-bound micelles on particulate substrates, and the use of such thermal switching in manipulating NAPL uptake and release.

References

1. Ake, C. L; Wiles, M. C; Huebner, H. J. Porous organoclay composite for the sorption of polycyclic aromatic hydrocarbons and pentachlorophenol from groundwater. *Chemosphere* **2003**, *51*, 835–854.
2. Khan, F. I.; Husain, T.; Hejazi, R. An overview and analysis of site remediation technologies. *J. Environ. Manage.* **2004**, *71*, 95–122.
3. Materna, K; Goralska, E; Sobczynska, A; et al. Recovery of various phenols and phenylamines by micellar enhanced ultrafiltration and cloud point separation. *Green Chem.* **2004**, *6*, 176–182.

4. Kizilay, E.; Kayitmazer, A. B.; Dubin, P. L. Complexation and coacervation of polyelectrolytes with oppositely charged colloids. *Adv. Colloid Interface Scie.* **2011**, *167*, 24–37n.
5. Sudbeck, E.; Curran, M. E.; Skelton, J. Dye solubilization in polyelectrolyte-micelle complexes. *J. Colloid Interface Sci.* **1991**, *142*, 512–517.
6. Xia, J.; Zhang, H.; Rigsbee, D. R.; Dubin, P. L.; Shaikh, T. Structural elucidation of soluble polyelectrolyte-micelle complexes: Intra- vs interpolymer association. *Macromolecules* **1993**, *26*, 2759–2766.
7. SwansonVethamuthu, M; Dubin, P. L; Almgren, M. Cryo-TEM of polyelectrolyte-micelle complexes. *J. Colloid Interface Sci.* **1997**, *186*, 414–419.
8. Guo, W.; Uchiyama, H.; Tucker, E. E.; Christian, S. D.; Scamehorn, J. F. Use of polyelectrolyte-surfactant complexes in colloid-enhanced ultrafiltration. *Colloids Surf., A.* **1997**, *123*, 695–703.
9. Dubin, P. L.; Wang, Y. Protein binding on polyelectrolyte-treated glass: Effect of structure of adsorbed polyelectrolyte. *J. Chromatogr.* **1998**, *808*, 61–70.
10. Silva, R. M.; Urzúla, R. M.; Petri, D. F. S.; Dubin, P. L. Protein adsorption onto polyelectrolyte layers: Effects of protein hydrophobicity and charge anisotropy. *Langmuir* **2010**, *26*, 14032–14038.
11. Wang, Y.; Dubin, P. Capillary modification by noncovalent polycation adsorption: Effects of polymer molecular weight and adsorption ionic strength. *Anal. Chem.* **1999**, *71*, 3463–3468.
12. Kizilay, E.; Maccarrone, S.; Foun, E.; Dinsmore, A. D.; Dubin, P. L. Cluster formation in polyelectrolyte-micelle complex coacervation. *J. Phys. Chem.* **2011**, *115*, 7256–7263.
13. Hammond, P. T. Form and function in multilayer assembly: New applications at the nanoscale. *Adv. Mater.* **2004**, *16*, 1271–1293.
14. Wang, Y.; Kimura, K.; Huang, Q.; Dubin, P. L.; Jaeger, W. Effects of salt on polyelectrolyte-micelle coacervation. *Macromolecules* **1999**, *32*, 7128–7134.
15. Cherstvy, A. G.; Winkler, R. G. Polyelectrolytes adsorption onto oppositely charged interfaces: unified approach for plane, cylinder, and sphere. *Phys. Chem. Chem. Phys.* **2011**, *13*, 11686–11693.
16. Kumar, A.; Dubin, P. L.; Hernon, M. J.; Jaeger, W. Temperature-dependent phase behavior of polyelectrolyte-mixed micelle systems. *J. Phys. Chem B.* **2007**, *11*, 8468–8476.
17. Kizilay, E.; Maccarrone, S.; Foun, E.; Dinsmore, A. D.; Dubin, P. L. Cluster formation in polyelectrolyte-micelle complex coacervation. *J. Phys. Chem.* **2011**, *115*, 7256–7263.
18. Mishael, Y.; Dubin, P. L. Uptake of organic pollutants by silica-polycation immobilized micelles. *Environ. Sci. Technol.* **2005**, *39*, 8475–8480.
19. Mishael, Y. G.; Dubin, P. L.; de Vries, R.; Kayitmazer, A. B. Effect of pore size on adsorption of a polyelectrolyte to porous glass. *Langmuir* **2007**, *23*, 2510–2516.

20. Lin, N. P.; Deen, W. M. Charge effects on the diffusion of polystyrene sulfonate through porous membranes. *J. Colloid Interface Sci.* **1992**, *153*, 483–492.
21. Wang, Y. L.; Banziger, J.; Dubin, P. L.; Filippeli, G. Adsorptive partitioning of an organic compound onto polyelectrolyte-immobilized micelles on porous glass and sand. *Environ. Sci. Technol.* **2001**, *15*, 2608–2611.
22. Saint-Aubin, C.; Hemmerlé, J.; Boulmedais, F.; Vallat, M. F.; Nardin, M.; Schaaf, P. New 2-in-1 polyelectrolyte step-by-step film buildup without solution alternation: From PEDOT-PSS to polyelectrolyte complexes. *Langmuir* **2012**, *28*, 8681–8691.

Chapter 8

Novel Production of Activated Carbon for Hampering Oligomerization of Phenolic Compounds

Liang Yan and George A. Sorial[*]

**School of Energy, Environmental, Biological, and Medical Engineering,
University of Cincinnati, Cincinnati, Ohio 45221-0071, United States
[*]E-mail: George.Sorial@uc.edu**

The overall objective of this research was to develop novel activated carbon by KOH activation of bituminous coal for hampering oligomerization of phenolic compounds on its surface. A matrix of 24 activated carbon samples with different microporosity and BET surface area were created to systematically evaluate the effect of the different activation variables (KOH/bituminous coal ratio, heating temperature, activation time, and flow rate of nitrogen gas). The effectiveness of activated carbon sample on hampering oligomerization was then systematically examined. Anoxic and oxic isotherm adsorption of single solute (phenol, 2-Methylphenol and 2,4-dimethylphenol) and binary solute (2-methylphenol/2,4-dimethylphenol) were studied, using Carbon$_{exp}$ and commercial granular activated carbon (GAC) F400. Both single solute adosption and binary solute adsorption on Carbon$_{exp}$ indicated no impact of the presence of molecular oxygen on the adsorptive capacity which is manifested by no significant differences between oxic and anoxic environment. Carbon$_{exp}$ sample proved to be effective in hampering the oligomerization of phenolic compounds under oxic conditions. On the other hand, F400, which have lower Microporosity and acidic functional contents, significant increases in the adsorptive capacity had been observed when molecular oxygen was present.

In Novel Solutions to Water Pollution; Ahuja, S., et al.;
ACS Symposium Series; American Chemical Society: Washington, DC, 2013.

Introduction

Phenolic derivatives are a group of common environmental contaminants and widely exist in industrial waste water. Phenolic compounds have the potential to induce obvious adverse effects to human health, and the removal of these compounds through common water treatment processes is, therefore, an emerging concern. Among all treatment processes, adsorption by activated carbon is the best and most frequently used technology in phenolic compounds removal because of its good adsorption capacity and flexibility (*1–3*).

In the past several decades, removal efficiencies of activated carbon adsorption processes for phenolic compounds have been evaluated using either bench- (*4*, *5*) or pilot-scale systems (*6*, *7*), in addition to surveys at full-scale drinking water treatment plants (*8*). However, the regeneration efficiency of activated carbon after adsorption were found generally not to be satisfactory (*2*). The poor efficiency in carbon regeneration is attributable to the oligomerization of phenolic compounds. Oligomerization can produce macromolecular compounds, including dimers, trimers and tetramers of phenolic compounds, which can severely reduce carbon regeneration efficiency. Many investigations have demonstrated that the presence of molecular oxygen in the aqueous phase promotes chemical transformation, such as oligomerization of the organic compounds absorbed onto the carbon surface (*9*, *10*). Since economic use has been a major concern in granular activated carbon (GAC) usage due to poor regeneration efficiency of activated carbon, development and further application of novel activated carbon that can control oligomerization and supply high regeneration efficiency is impeded.

Generally the adsorptive properties of activated carbon are determined first of all by its surface chemistry such as surface groups and metal complexes. However, many studies have pointed out that the chemical characteristics of activated carbon have no dominant effects on oligomerization of phenolic compounds. The impact of surface functional groups on oligomerization was first investigated by Vidic et al (*2*). According to their results the oxygen-containing basic surface functional groups have little influence while the effect of acid functional groups was much less pronounced. Similarly, Uranowski et al. (*9*) found that acid-washable metals and metal oxides are not a key factor in promoting oligomerization of adsorbates on the surface of activated carbons. In contrast, the porous structure of activated carbon was found to have significant impact on oligomerization. Lu & Sorial (*11*) tested 5 types of activated carbon fibers (ACF) with different pore size distribution (PSD) and found that the molecular size of competing compounds relative to the pore size distribution of activated carbon determined the effect of PSD of activated carbon on the extent of oligomerization of phenolic compounds. According to this study, considerable oligomerization only happens on the surface of activated carbon with wide pore size distribution and relative big pore diameter. Consequently, adsorbents with small pore diameters like ACF ACC-10 (microporosity above 90%) are very effective for control of adsorption oligomerization. Therefore, activated carbon with similar pore structure as ACC-10 (having their pore volume mostly distributed in micropores and low critical pore diameter) needs to be developed and used for hampering oligomerization in order to make activated carbon more cost effective.

There are two principal methods for manufacturing activated carbon, namely, physical activation and chemical activation. Physical activation comprises carbonization of the raw material followed by steam gasification. In chemical activation, the carbonaceous precursor is impregnated by a chemical reagent and then pyrolysed (*12*). Compared with physical activation, chemical activation is more often carried out due to intrinsic advantages such as lower energy consumption, higher product yields and better porous structure (*13*). In addition, the chemical activation method by potassium hydroxide has been widely applied and has shown to be effective in development carbon with both high BET surface area and well-developed porosity (*14*, *15*). Therefore, it was chosen for this study to develop activated carbon with narrow carbon PSD and high BET surface area. Bituminous coal was chosen as the carbonaceous precursor to develop activated carbon with high microporosity due to hardness and high density. It is worth to note that all the pores of activated carbon are developed through the removal of carbon atoms during the activation process. Therefore, only optimum activation can guarantee a carbon with the optimum combination of microporosity and surface area. The use of KOH chemical activation were examined in numerous studies for carbon development (*16*, *17*). However, one of the main obstacles of using this approach is that these empirical conditions are case-specific and could not necessarily limit oligomerization. The current study included four activation parameters (KOH/coal ratio, activation temperature, activation time and inert gas flow rate). Interpretations of these parameters could provide their contributions in the overall carbon porous structure. More importantly, the effect of the developed activated carbon ($\mathrm{Carbon_{exp}}$) on control of oligomerization by conducting anoxic and oxic isotherm adsorption were investigated with multicomponent solute system. The results can represent the adsorption behavior of $\mathrm{Carbon_{exp}}$ in practical usage of activated carbon treatment.

Materials and Methods

Preparation and Activation of Carbon

Colorado bituminous coal (American Educational Products) with an 8.2 wt% of ash content was used as the precursor in the present study. The investigation of four critical activation parameters was carried out using a progressive method. The coal was firstly crushed with a ball mill and sieved to a uniform size of 400-600 μm. An amount of 3 g bituminous coal was mixed with KOH solution in a ceramic boat at various weight ratios of KOH to the raw material (1:1, 2:1, 3:1, 4:1 or 5:1). 1 ml DI water per 1 g activating agent was added. The slurry was put into a horizontal cylindrical furnace and was dried at 110 °C for 16 hours under nitrogen atmosphere. Subsequently, the activation process of sample was carried out. The heat treatment consisted of a heating ramp from 110 °C to the final heat treatment temperature at a heating rate of 5 °C min^{-1}, followed by a plateau of 0.5, 1, 2, 3 or 4 h under a set nitrogen flow rate. The system was then cooled back to the initial temperature. The carbon samples were washed repeatedly with a 5 M solution of

HCl and later with distilled water until they are free of chloride ions and the pH of the rinse water is the same as the pH of distilled water. The name of each carbon sample consists of bituminous coal's name (BC), KOH/coal ratio (i.e. 3/1 would be 31), the heating temperature in centigrade, the heating time in hours, and the flow rate in ml/min. Thus, for an activated carbon prepared with a KOH/bituminous coal ratio of 4/1 and which was heated at 600 °C for 2h, and with flow rate 200 ml/min, the nomenclature would be BC-41-600-2-200.

Physical Characterizations of Adsorbents

The porous structure of the activated carbon samples was characterized by adsorption of N_2 at 77 K using a micromeritics analyzer (TRI3000). Beforehand, the samples were degassed at 423K under nitrogen for 2h. The T-plot equation was applied to the N_2 isotherms for calculating the micropore size distribution, and the BJH theory was utilized in order to obtain meso- and macro-pore size distribution. From the N_2 adsorption data, the total pore volume and the apparent BET surface areas were also obtained. To determine the optimum pore structures of activated carbon samples, conventional bituminous GAC Filtrasorb 400 (Calgon, Pittsburgh, PA), was used as reference.

Chemical Characterizations of Adsorbents

Total Acidity and Basicity

The determination of total acidic and basic groups on the carbon surface was performed by NaOH and HCl uptake. Vials with 100 mg of carbon and 20 ml of 0.05 N NaOH or HCl solution were mixed for 2 days in a Tumbler at room temperature. Blanks were also added as controls. The solutions were filtered with a 0.45μm filter. 10 ml of the carbon solution was titrated with either 0.05 N NaOH or HCl. The amount of base consumed was calculated by using the amount needed to titrate the blank to a pH of 4.5 and taking the difference of the amount needed to titrate the solution to the same end point. The amount of acid consumed used the same process but with an end point of pH 11.5. All measurements were expressed as meq/g (*18*).

pH of Point of Zero Charge (pHpzc)

Batch equilibrium method was used for determining pHpzc of the selected Carbonexp and F400. Autoclaved DI water was prepared with different pH values ranging from 2-11. pH adjustments were made using 0.5 N HCl or NaOH solutions. 100 mg of carbon sample was placed in vials with 10 ml autoclaved DI water at different initial pH values. The vials were sealed and shaken for 2 days at 50 rpm at room temperature. The carbon was allowed to settle before pH testing. The final pH was tested using a pH meter (Accumet Research AR 50). The pH_{pzc} is the pH of the solution that remains unchanged after contact with the sample (*18*).

Adsorption Isotherms

Adsorbates

The target adsorbates in this study are phenol (99%), 2-methylphenol (98%), and 2,4-Dimethylphenol (99%) (Aldrich Chemical Co., Inc., Milwaukee, WI). They were chosen because they represent commonly encountered phenolic pollutants in water and wastewater treatment. Meanwhile, the three phenolic compounds have various molecular structures. Phenol is two dimensional while 2-methylphenol and 2,4-dimethylphenol are three dimensional. The molecular sizes of phenol, 2-methylphenol and 2,4-diemthylphenol are 5.76 Å × 4.17 Å, 5.69 Å × 5.32 Å × 1.63 Å and 5.68 Å × 5.62 Å × 1.63 Å, respectively (Advanced Chemistry Development-ACD Labs 5.0 software, Toronto, Canada).

Adsorbents

The activated carbon sample with best porous characteristics developed from activation experiments was used to conduct the adsorption isotherm. Furthermore, F400 (Filtrasorb 400) (400-600 μm) was chosen as a typical commercial GAC (Calgon Carbon Corporation, Pittsburgh, PA) for comparison. This bituminous base activated carbon is selected because it represents commonly used commercial GAC for removal of organic compounds in water treatment. Prior to use in the study, the GAC was rinsed several times with de-ionized water to remove the dust (<0.45μm), dried in an oven at 105 °C for two days, and then stored in a desiccator until use.

Isotherm Procedure

The bottle point method was used for conducting the adsorption isotherms at 23°C ± 1°C. Two initial concentration (200 and 1000 mg/L) were used for the single solute system and two initial concentration combinations (Table 4) were used for the binary system. Different masses (calculated based on the myers equation) of activated carbon was added to the bottles. To clearly demonstrate the implication of oligomerization of phenolic compounds, two adsorption conditions were considered, anoxic (absence of molecular oxygen) isotherms and oxic (presence of molecular oxygen) isotherms. The anoxic condition was attained by purging the adsorbents with nitrogen for about 1 min, twice a day for 3 days; moreover, the buffered water used for preparing the adsorbate solution, prior to the addition of the adsorbate, was also purged with nitrogen to expel any dissolved oxygen and finally each isotherm bottle (125ml) was completely filled with the adsorbate solution. For the oxic isotherms 100ml of adsorbate solution was added in each 125ml bottle and the head space purged by oxygen gas for a minute in order to ensure no oxygen limitation is attained during the adsorption isotherm equilibration time. Two blanks per set bottles served as controls during the isotherm experiments. The sealed bottles were then placed in a rotary tumbler for 2 weeks.

Extraction Experiment

After adsorption,the comparison of regeneration efficiency between $\text{Carbon}_{\text{exp}}$ and F400 was also investigated by conducting extraction experiments. In this study, the adsorbent loaded with phenolic compounds after oxic adsorption isotherm experiments were extracted using a soxhlet apparatus. Carbon samples were extracted with methanol for one day followed by three days of extraction with dichloromethane (DCM). The extraction method used is described in other studies (*9*, *19*).

Analytical Procedure

The adsorbate concentrations for the single isotherm, multicomponent isothem, and extraction experiment were measured by High Performance Liquid Chromatography (HPLC) (Agilent 1100 series; Agilent Technologies, Wilmington, DE) equipped with Chemstation software, a model G1322A degasser, a model G1311A Quatpump, a model G1316A Thermostatted column oven, and a model G1315A Diode-array detection system. The column used was a 150mm * 4.6mm inner diameter, 3μm particle size, C18 ODS HYPERSIL column (Thermo scientific, Waltham, MA), operated at 30 °C. The mobile phase consisted of 0.1% (v/v) formic acid in water (eluent A) and of acetic acid, methanol and acetonitrile (5:5:90, v/v/v; eluent B), and the flow rate was controlled to 1.0 ml/min. The gradient program was as follows: 10% A to 90% B (2 min), 20% A to 80% B (4 min), 40% A to 60% B (6 min), 60% A to 40% B (8 min), 90% A to 10% B (10 min). Total run time is 12 min. Phenolic compounds were monitored separately at 270 nm (phenol and 2-methylphenol) and 280 nm (2,4-dimethylphenol). Additionally, UV/Vis spectra were recorded in the range of 270-300 nm. The retention time for phenol was 6.2 min, 2-methylphenol 6.9 min, and 2, 4-dimethylphenol 8.5 min under the conditions used.

Myers Equation

In this study, the Myers equation (1) was used to correlate the single solute isotherm adsorption data.

$$C_e = \frac{q_e}{H} \times \exp(K{q_e}^{p}) \tag{1}$$

where Ce is the equilibrium liquid-phase concencentration, mM, qe is the surface loading, mmol/g, H(L/g), K(mmol/g), and P (dimensionless) are regression parameters (*20*).

At low concentration, the Myers equation becomes linear equation (2), i.e., following Henry's law equation,

$$\frac{dC_e}{dq_e} = \frac{1}{H};\ q_e \rightarrow 0 \tag{2}$$

This criterion is very important when predicting multicomponent adsorption systems by the ideal adsorption theory (IAST) because of the integration limits in the Gibbs adsorption equation (*11*). Meanwhile, q_e (mmol/g) was calculated from mass balance equation (3):

$$q_e = \frac{(C_O - C_e)V}{M} \tag{3}$$

where Co (mM) is initial liquid-phase concentration; M (g) is the mass of adsorbent; V (L) is the adsorbate volume. The adsorbate volume, V, was 0.125 L for the anoxic isotherms and 0.1 L for the oxic isotherms.

Ideal Adsorbed Solution Theory (IAST)

Ideal Adsorbed Solution Theory (IAST) was used in this study because it is the most common approach used to predict the multicomponent adsorption isotherms onto activated carbon by using only single solute equilibrium data (*21*, *22*). The IAST is based on the assumption that the adsorbed mixture forms an ideal solution at a constant spreading pressure. The model can be represented by the following equation (4):

$$C_{e,i} = \frac{C_i^o(\Pi \mathrm{m}, \mathrm{T})\, q_{e,i}}{\sum_{i=1}^{i=N} q_{e,i}} \tag{4}$$

Where $\mathrm{C_i^o}(\Pi_\mathrm{m}, \mathrm{T})$ is equilibrium liquid-phase concentration of pure solute i at the same temperature T and spreading pressure Π_m of the mixture with N components.

$$\sum_{i=1}^{i=N} \frac{q_{e,i}}{q_i^o} = \sum_{i=1}^{i=N} \frac{C_{e,i}}{C_i^o} = 1 \tag{5}$$

The above equation (5) is the expression of the relationship between mixture equilibrium solid-phase concentration $q_{e,i}$ and single solute equilibrium concentrations q^o_i in the case of an ideal multicomponent system.

$$\frac{A_s\pi_i}{RT} = \int_0^{q_i^o} \frac{q_i^o}{C_i^o}\frac{dC_i^o}{dq_i^o}\, dq_i^o \qquad (6)$$

In addition, a further relation is established between the spreading pressure and directly measurable quantities as equation (6). Where As is external surface area per unit mass of adsorbent and π_i is the spreading pressure of single component i. This method did not consider the chemical effects during the adsorption process. Therefore, this approach will not accurately predict adsorption equilibrium of trace organic contaminants under oxic condition due to oligomerization of adsorbates on the surface of the activated carbon. However, it's very suitable to examine the effectiveness of $\text{Carbon}_{\text{exp}}$ in hampering oligomerization under oxic conditions in multicomponent adsorption.

Results and Discussion

The strategy to optimize porous properties involved stepwise changes in different parameters such as the KOH/coal mass ratio, activation temperature, activation time and nitrogen flow rate. The activation conditions that were studied in detail are summarized in Table 1. Two of these parameters had a significant effect on the final pore characteristics of the activated carbon.

Table 1. Porous Properties of GAC F400 and Activated Carbon by Using KOH as the Activating Agent

Sample	*Activation Parameters*	*S_{BET}[a] (m^2/g)*	*Vmicro[b] (cm^3/g)*	*Vmeso+ Vmacro[c] (cm^3/g)*	*V_{Total}[d] (cm^3/g)*	*Micropore Percentage[e] (%)*
	KOH/Coal ratio					
F400	–	993	0.373	0.242	0.615	60.7
BC-11-700-1-400	1:1	354	0.162	0.064	0.226	71.6
BC-21-700-1-400	2:1	971	0.405	0.154	0.559	72.4
BC-31-700-1-400	3:1	1158	0.434	0.235	0.669	64.9
BC-41-700-1-400	4:1	1247	0.389	0.348	0.737	52.8

Continued on next page.

Table 1. (Continued). Porous Properties of GAC F400 and Activated Carbon by Using KOH as the Activating Agent

Sample	*Activation Parameters*	*S_{BET}[a] (m^2/g)*	*Vmicro[b] (cm^3/g)*	*Vmeso+ Vmacro[c] (cm^3/g)*	*V_{Total}[d] (cm^3/g)*	*Micropore Percentage[e] (%)*
BC-51-700-1-400	5:1	920	0.295	0.242	0.537	55.0
	Temperature					
BC-21-600-1-400	600	845	0.381	0.104	0.485	78.4
BC-21-650-1-400	650	1128	0.507	0.144	0.651	77.9
BC-21-700-1-400	700	971	0.405	0.154	0.559	72.4
BC-21-750-1-400	750	1335	0.529	0.236	0.765	69.2
BC-21-800-1-400	800	1451	0.516	0.319	0.835	61.8
BC-21-850-1-400	850	1285	0.329	0.430	0.759	43.4
	Time					
BC-21-650-0.5-400	0.5	1085	0.499	0.122	0.621	80.3
BC-21-650-1-400	1	1128	0.507	0.144	0.651	77.9
BC-21-650-2-400	2	1476	0.684	0.157	0.841	81.3
BC-21-650-3-400	3	1107	0.499	0.139	0.638	78.3
BC-21-650-4-400	4	903	0.415	0.109	0.524	79.2
	N_2 flow rate					
BC-21-650-2-100	100	1203	0.534	0.158	0.692	77.1
BC-21-650-2-200	200	1472	0.676	0.179	0.855	79.0

Continued on next page.

Table 1. (Continued). Porous Properties of GAC F400 and Activated Carbon by Using KOH as the Activating Agent

Sample	*Activation Parameters*	S_{BET}[a] (m^2/g)	*Vmicro*[b] (cm^3/g)	*Vmeso+ Vmacro*[c] (cm^3/g)	V_{Total}[d] (cm^3/g)	*Micropore Percentage*[e] *(%)*
BC-21-650-2-400	400	1476	0.683	0.158	0.841	81.3
BC-21-650-2-600	600	1091	0.480	0.153	0.633	75.8

[a] S_{BET} is BET surface area. [b] *Vmicro* is the volume of micropore. [c] $Vmeso+Vmacro = V_{Total}-Vmicro$. [d] V_{Total} is the total pore volume. [e] *Micropore percentage* $= Vmicro/V_{Total} \times 100\%$.

KOH/Coal Ratio

The chemical reagent ratio is an essential identifying parameter of activation since this parameter has a significant impact on the micropore size distribution and thus influences the effectiveness of carbon in hampering oligomerization. In order to investigate the optimum KOH/coal ratio, the ratio was varied in the range 1/1 to 5/1 while keeping the other factors constant (activation temperature 700 °C, activation time 1 h and nitrogen flow rate 400 ml/min, respectively). All evaluated textural parameters of these carbon samples are presented in Table 1. It is remarkable to note that the lower the KOH/coal ratio the higher the micropore volume percentage, up to a KOH/coal ratio 2/1, reflecting a decrease in the pore size. In addition, it is shown that the sample with the narrowest pore size distribution is the sample prepared with KOH/coal ratio 1/1 and 2/1, which agrees with the micropore volumes percentage calculated from the micropore volume and the total pore volume. However, the BET surface area (354 m^2/g) and micropore volume (0.162 cm^3/g) of the sample using KOH/coal ratio 1/1 are significantly lower than F400. On the other hand, the BET surface area (971 m^2/g) and micropore pore volume (0.405 cm^3/g) of the sample with a 2/1 ratio are similar or better than F400. Therefore, the sample with the most ideal BET surface area and microporosity is the sample with a 2/1 ratio.

Activation Temperature

The activation temperature was varied from 600 to 900 °C while keeping the rest of the parameters constant (KOH/Coal ratio, activation time and nitrogen flow rate were 2/1, 1 h and 400 mL/min, respectively). As shown in Table 1, the BET surface area increases with activation temperature from 650 to 850 °C. Furthermore, the BET surface area of all the samples were larger than F400. But the total BET surface area decreased significantly with activation temperature below 650 °C, mainly due to lack of proper activation of the resulting material. In addition, the higher activation temperature, the lower micropore volume percentage. Consequently, the mesopore and macropore volume were increasing at higher temperatures. As expected, the carbon microporosity was inversely proportional to the activation temperature due to the elimination of the most reactive carbon atoms after the over activation process. In summary, the activation temperature is a very important parameter in developing activated carbon with suitable structure required for controlling oligomerization. Activated samples with a high level of microporosity can be obtained at 650 °C (BC-21-650-1-400).

Activation Time

In order to examine the best activation time on the activated carbon, this parameter was varied from 0.5 to 4 h while keeping the other parameters constant. As shown in Table 1, the differences of total BET surface area between carbon activated for 2 h and 4 h were significant. However, the differences in the BET surface area between carbons activated for 2, 3 or 4 h were very small. On the other hand, the microporosity of the activated carbons corresponded to pore sizes in the range 0–2 nm were similarly formed with reaction time longer than 0.5 h. All activated samples showed similar micropore percentage at around 80%, indicating that their micropore structure was maintained to some extent after certain activation time. This means that the effect of the activation time at this activation temperature on the micropore percentage is not particularly significant. Furthermore, it can be seen that, in all cases, the activated carbon samples activated for 2 h can provide the highest largest micropore volume, highest micropore percentage and highest BET surface area. Therefore, an activation time of 2 hours could be considered to be optimum for the preparation of a good activated carbon for oligomerization control.

Nitrogen Flow Rate

In the activation process, nitrogen is used as a protection gas. To select the best nitrogen flow rate, the nitrogen flow rate was varied in the range 100 - 600 mL/min with the values of the other parameters kept constant (KOH/coal ratio of 2:1, activation temperature of 650 °C and activation time of 2h). From Table 1, it can be seen that increasing N_2 flow rates favored the development of total BET surface area until a value of 400 mL/min was reached. It can be seen that a further increase in the N_2 flow rate led to a decrease in the surface area. This fact can also be confirmed from the microporosity of activated carbon samples, which shows the sample with highest micropore percentage is obtained by using nitrogen flow rate of 400 ml/min. These finding is consistent with other reported in the literature (*23*, *24*). This pore opening behavior could be explained on the basis that the gaseous products (containing CO_2, CO, H_2O etc.) evolved during the activation process. Previous studies reported that the removal of CO, CO_2 and H_2 would favor the activation process while the removal of H_2O formed during the pyrolysis reaction work against the activation, In addition, a too high nitrogen flow rate could result in removing a large amount of H_2O from the reactive site and this would be detrimental to the porous properties of the carbon, while a too low nitrogen flow rate would probably not remove sufficient amounts of CO, CO_2, which would be also in detrimental to the activation.Therefore, a balance between these two removal processes must be reached under a medium nitrogen flow rate (400 ml/min).

The above results indicate that BC-21-650-2-400 sample, which is prepared under activation condition (KOH/coal = 2/1, activation temperature = 650 °C, Activation time = 2 hours and nitrogen flow rate = 400 ml/min), has the best potential for controlling oligomerization of phenolic compounds. This carbon sample will be referred to as $\text{Carbon}_{\text{exp}}$. Based on the titration test, the $\text{Carbon}_{\text{exp}}$ was found to be an acidic carbon with total acidity and total basicity are 0.54 meq/g and 0 meq/g, respectively. In contrast, the total acidity and total basicity for F400 is 0.15 meq/g and 0.475 meq/g. On the other hand, the values of pHpzc for $\text{Carbon}_{\text{exp}}$ and F400 are 3.4 and 7.1, respectively.

Single Solute Adsorption

The experimental data obtained under both conditions are represented in Figures 1−3. The experimental data were correlated to the Myers equation. Evaluation of the Myers equation was done by calculating the sum of squares of relative error (SSRE). The correlation parameters for the Myers equation are presented in Table 2.

Table 2. Myers Isotherm Equation Parameters

		H *(L g^{-1})*	*K* *(mmol g^{-1})$^{-p}$*	*P*	*Sum of squares of relative residual*
Phenol					
Anoxic	$\text{Carbon}_{\text{exp}}$	16878.9	6.33	0.429	0.15
	F400	16878.9	5.88	0.633	0.52
Oxic	$\text{Carbon}_{\text{exp}}$	16878.9	5.55	0.518	0.27
	F400	16878.9	4.75	0.653	0.24
2-Methylphenol					
Anoxic	$\text{Carbon}_{\text{exp}}$	24337.0	5.44	0.474	0.243
	F400	24337.0	7.11	0.389	0.15
Oxic	$\text{Carbon}_{\text{exp}}$	24337.0	4.68	0.574	0.31
	F400	24337.0	5.13	0.501	0.224
2,4-Diemthylphenol					
Anoxic	$\text{Carbon}_{\text{exp}}$	25000.0	4.32	0.727	0.29

Continued on next page.

Table 2. (Continued). Myers Isotherm Equation Parameters

		H *(L g⁻¹)*	*K* *(mmol g⁻¹)⁻ᵖ*	*P*	*Sum of squares of relative residual*
	F400	15000.0	5.01	0.712	0.26
Oxic	$\text{Carbon}_{\text{exp}}$	25000.0	2.31	1.196	0.46
	F400	15000.0	1.90	1.405	0.36

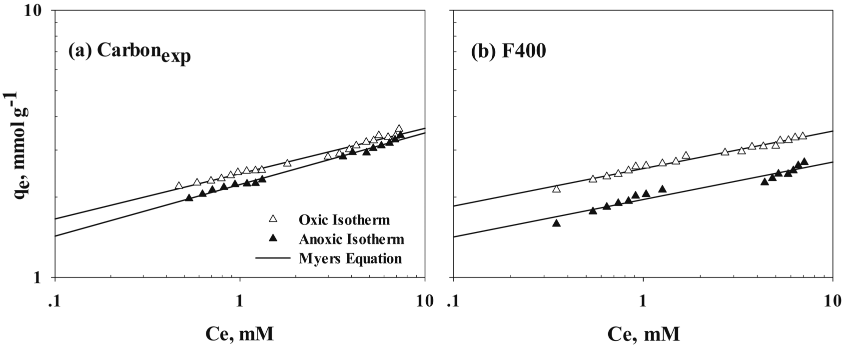

Figure 1. Single solute adsorption isotherm of phenol: (a) on $\text{Carbon}_{\text{exp}}$; and (b) on F400.

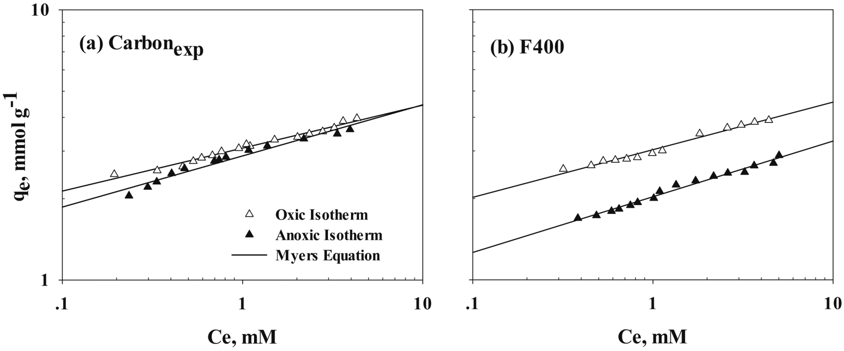

Figure 2. Single solute adsorption isotherm of 2-methylphenol: (a) on $\text{Carbon}_{\text{exp}}$; and (b) on F400.

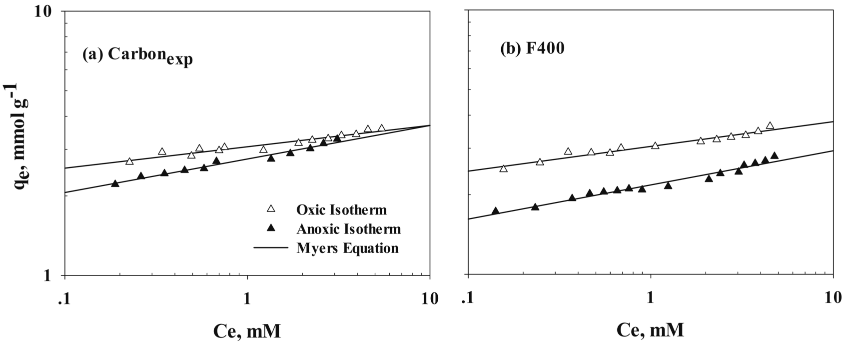

Figure 3. Single solute adsorption isotherm of 2,4-dimethylphenol: (a) on Carbon$_{exp}$; and (b) on F400.

Analysis of the data in Figures 1−3 reveals that much higher adsorptive capacities of all phenolic compounds for F400 are attainable under oxic conditions. And the increase in capacity is more pronounced in the lower concentration ranges than for higher concentrations. Furthermore, it is worthwhile to note that the difference in the 2-methylphenol adsorptive capacity obtained for F400 under oxic and anoxic conditions is more significant than that for phenol and 2,4-dimethylphenol. However, the presence of molecular oxygen in the test environment didn't have a tremendous impact on the adsorptive capacity of Carbon$_{exp}$.

The capacity increase in the presence of oxygen was compared between Carbon$_{exp}$ and F400, at corresponding equilibrium concentrations of 0.5 mM and 5 mM (Table 3). These two limits were selected in order to represent the low and high carbon dosage. The adsorptive capacity for F400 in the presence of oxygen increased by 32.2% and 32.7% for phenol, 42.3% and 52.5% for 2-methylphenol, 30.2% and 43.7% for 2,4-dimethylphenol respectively at two equilibrium concentrations. This increase in capacity under oxic conditions has been attributed to oligomerization reactions that take place on the carbon surface. It is also worthwhile to note that the three compounds used in this study exhibited different degrees of oligomerization, with 2-methylphenol being the most reactive and phenol exhibiting the least effect. The distinct performance can be attributed to the differences of critical oxidation potential (COP) of these phenolic compounds. The COP for 2-methylphenol is 1.040 V while that for phenol and 2,4-dimethylphenol is 1.089 and 1.052 V.

Table 3. Comparison of Anoxic and Oxic Adsorption Capacity

	Ce (mM)	*Phenol*			*2-Methylphenol*			*2,4-Dimethylphenol*		
		Anoxic q_e (mmol/g)	*Oxic q_e (mmol/g)*	*q_e (%)*	*Anoxic q_e (mmol/g)*	*Oxic q_e (mmol/g)*	*Δq_e (%)*	*Anoxic q_e (mmol/g)*	*Oxic q_e (mmol/g)*	*Δq_e (%)*
$\text{Carbon}_{\text{exp}}$	0.5	1.943	2.182	12.3	2.552	2.796	9.54	2.530	2.918	15.3
	5	3.195	3.010	6.12	4.185	4.341	3.70	3.844	3.604	-6.25
F400	0.5	1.854	2.461	32.7	1.760	2.683	52.5	1.970	2.831	43.7
	5	2.401	3.174	32.2	2.828	4.027	42.3	2.881	3.749	30.2

As is apparent from Table 3, the differences between the oxic and anoxic adsorption isotherms for the three phenolic compounds were all very slight for $Carbon_{exp}$ as compared to F400. This indicated that there was no appreciable effect of molecular oxygen on the exhibited adsorptive capacity of $Carbon_{exp}$. Therefore, $Carbon_{exp}$ has a significant positive impact on hampering oligomerization of phenolic compounds on its surface. This distinct performance can be attributed to the significant higher micropore percentage than F400. Keeping in mind that the possibility of forming larger stable oligomerized molecular products decreases with an decrease in the size of activated carbon pores. It is obvious that F400 has a broad pore PSD from 10-500 Ǻ and oligomerization would not be constricted by its pore PSD. However, the $Carbon_{exp}$ has a critical pore diameter of 10 Ǻ and a narrow PSD. The second widest dimensions of phenol, 2-methylphenol and 2-ethylphenol are 4.17, 5.32 and 5.70 Ǻ, respectively. Therefore, it is reasonable to assume that it is possible for phenol to form dimers, while the 2-methylphenol and 2,4-dimethylphenol is even impossible to get oligomerized. In addition, the difference of adsorption performance between $Carbon_{exp}$ and F400 could be partially attributed to the surface basicity difference. Previous study of Vidic et al. (*2*) has mentioned that higher surface basicity can promote the oligomerization of phenolic compounds. Based on the results of titration measurement, the total basicity for $Carbon_{exp}$ and F400 are 0 meq/g and 0.475 meq/g, respectively. Thus the more basic surface functional of GAC F400 can also promote phenolic compounds oligomerization.

Finally, the extraction efficiency for $Carbon_{exp}$ after phenol, 2-methylphenol and 2,4-dimethylphenol adsorption were 70.1-87.2%, 50.1-67.2%, and 54.1-71.9%, respectively. While the extraction efficiency for F400 were only 21-32%, 17-26.2%, and 26.4 -30.3 %, respectively. The extraction efficiency obtained from F400 was significantly lower as compared to $Carbon_{exp}$. This is an indication of the serious irreversible oligomerization of phenolic compounds, unlike $Carbon_{exp}$, the wide PSD and more basicity surface chemistry of F400 did not have any noticeable effect on hampering oligomerization.

Multicomponent Isotherm Tests

In this study, binary adsorption of 2-methylphenol/2,4-dimethylphenol was performed on F400 and $Carbon_{exp}$. Figures 4 (a) and (b) present the binary adsorption isotherms of phenol/2-methylphenol for F400 and $Carbon_{exp}$, respectively. Meanwhile, the Myers parameters obtained from the single solute anoxic isotherm was applied into IAST model to predict the competitive adsorption behavior. Evaluation of the predictability of IAST was also done by calculating the sum of SSREs. All the detailed concentration combination and SSRE values of both runs for both adsorbents are shown in Table 4.

Figure 4 (a) demonstrates that the presence of molecular oxygen had a significant impact on the binary adsorptive properties of F400. The obvious differences between oxic and anoxic binary adsorption isotherms due to oligomerization on the carbon surface was observed for both 2-methylphenol and 2,4-dimethylphenol. On the other hand, the anoxic adsorption isotherms can be well predicted by IAST. However, the oxic adsorption isotherms for both 2-methylphenol and 2,4-dimethylphenol are obviously higher than oxic adsorption value predicted by IAST. The under prediction of the IAST is due to the oligomerization behavior which is taking place in the presence of molecular oxygen which is not accounted for in IAST.

In contrast, $\text{Carbon}_{\text{exp}}$ (see Figure 4(b)) showed remarkable different binary adsorption behavior than that documented for F400. For the binary adsorption studied, oligomerization could happen in various ways, such as 2-methylphenol molecules, 2-methylphenol and 2,4-dimethylphenol, or 2,4-dimethylphenol molecules. Therefore, it seems there are more opportunities than single solute adsorption. However, it is apparent from Figure 4 (b) that the oxic and anoxic isotherm lines are really close to each other for both adsorbates on $\text{Carbon}_{\text{exp}}$. This observation can be attributed to three reasons. Firstly, regarding multicomponent adsorption, the possibility for either compound to get oligomerized becomes less as compared to the single solute system because of the competitive effect that would lead to less available sites. Secondly, the narrow PSD also leads to the oligomerization constriction effect on binary adsorption. Thirdly, $\text{Carbon}_{\text{exp}}$ is a more acidic carbon which is unfavorable for oligomerization of phenolic compounds. It is seen from Figure 4(b) that the binary adsorptive behavior of $\text{Carbon}_{\text{exp}}$ agreed with those predicted by the IAST model for both oxic and anoxic binary system. Therefore, the good prediction (see Table 4) for the both oxic and anoxic binary adsorption on $\text{Carbon}_{\text{exp}}$ by IAST confirmed again the effectiveness of $\text{Carbon}_{\text{exp}}$ in hampering oligomerization for binary solute system adsorption.

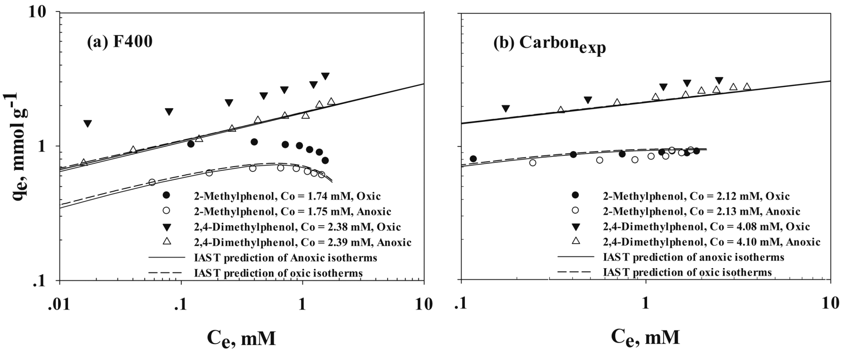

Figure 4. Binary adsorption isotherms of 2-methylphenol and 2,4-dimethylphenol: (a) on F400; and (b) on $\text{Carbon}_{\text{exp}}$.

Table 4. Summary of the Multicomponent Adsorption System

Adsorbent	*Conditions*	*Binary adsorption*			
		Initial concentration (mM)		*SSRE*	
		2-Methylphenol	*2,4-Dimethylphenol*	*2-Methylphenol*	*2,4-Dimethylphenol*
F400	Anoxic	1.75	2.39	0.0655	0.0201
	Oxic	1.74	2.38	0.8094	0.4581
$\text{Carbon}_{\text{exp}}$	Anoxic	2.13	4.10	0.1294	0.029
	Oxic	2.12	4.08	0.0257	0.1810

Conclusions

Chemical activation of bituminous coal by KOH was conducted in this study to evaluate the effectiveness of $\mathrm{Carbon_{exp}}$ in hampering oligomerization of phenolic compounds. This study demonstrated that the best conditions for activation which could provide a highly microporous and BET surface area seems to be a moderate KOH/coal ratio (2/1), a medium activation temperature (650 °C), a medium activation time (2 h) with a 400 ml/min nitrogen flow rate.

Both single-solute and binary-solute adsorption isotherms demonstrated that $\mathrm{Carbon_{exp}}$ was very effective in hampering oligomerization of phenolic compounds on the surface of the adsorbent. All adsorption isotherms reveal that the presence of molecular oxygen causes a significant increase in the F400 adsorptive capacity for the phenolic compounds used in this study. This increase is much less pronounced for $\mathrm{Carbon_{exp}}$ due to its higher micropore percentage and more acidic surface characteristics. Furthermore, $\mathrm{Carbon_{exp}}$ also shows higher adsorptive capacity than F400 under both oxic and anoxic conditions due to its higher BET surface area. Therefore, $\mathrm{Carbon_{exp}}$ developed in this study is not only more effective in hampering oligomerization as compared to commercial GAC but also leads to better adsorptive capacity. Finally, higher regeneration efficiency was achieved for $\mathrm{Carbon_{exp}}$ than GAC F400 which further confirms the effective control of oligomerization on $\mathrm{Carbon_{exp}}$.

In summary, through chemical activation of bituminous coal by KOH, it is possible to generate $\mathrm{Carbon_{exp}}$ having both high microporosity and high BET surface area. $\mathrm{Carbon_{exp}}$ with narrow PSD is much more effective in hampering oligomerization as compared to commercial activated carbon which has a wide PSD.

References

1. Cooney, D. O.; Xi, Z. P. *AIChE J.* **1994**, *40*, 361–364.
2. Vidic, R. D.; Tessmer, C. H.; Uranowski, L. J. *Carbon* **1997**, *35*, 1349–1359.
3. Hamdaoui, O.; Naffrechoux, E. *J. Hazard. Mater.* **2007**, *147*, 381–394.
4. Choi, K. J.; Kim, S. G.; Kim, C. W.; Kim, S. H. *Chemosphere* **2005**, *58*, 1535–1545.
5. Snyder, S. A.; Adham, S.; Redding, A. M.; Cannon, F. S.; DeCarolis, J.; Oppenheimer, J.; Wert, E. C.; Yoon, Y. *Desalination* **2007**, *202*, 156–181.
6. Ternes, T. A.; Meisenheimer, M.; McDowell, D.; Sacher, F.; Brauch, H. J.; Gulde, B. H.; Preuss, G.; Wilme, U.; Seibert, N. Z. *Environ. Sci. Technol.* **2002**, *36*, 3855–3863.
7. Vieno, N. M.; Harkki, H.; Tuhkanen, T.; Kronberg, L. *Environ. Sci. Technol.* **2007**, *41*, 5077–5084.
8. Stackelberg, P. E.; Furlong, E. T.; Meyer, M. T.; Zaugg, S. D.; Henderson, A. K.; Reissman, D. B. *Sci. Total Environ.* **2004**, *329*, 99–113.
9. Uranowski, L. J.; Tessmer, C. H.; Vidic, R. D. *Water Res.* **1998**, *32*, 1841–1851.
10. Grant, T. M.; King, C. J. *Ind. Eng. Chem. Res.* **1990**, *29*, 264–271.
11. Lu, Q. L.; Sorial, G. A. *Chemosphere* **2004**, *55*, 671–679.

12. Molinasabio, M.; Rodriguezreinoso, F.; Caturla, F.; Selles, M. J. *Carbon* **1995**, *33*, 1105–1113.
13. Lozano-Castello, D.; Calo, J. M.; Cazorla-Amoros, D.; Linares-Solano, A. *Carbon* **2007**, *45*, 2529–2536.
14. Lillo-Rodenas, M. A.; Juan-Juan, J.; Cazorla-Amoros, D.; Linares-Solano, A. *Carbon* **2004**, *42*, 1371–1375.
15. Lillo-Rodenas, M. A.; Cazorla-Amoros, D.; Linares-Solano, A. *Carbon* **2003**, *41*, 267–275.
16. Fuente, E.; Gil, R. R.; Giron, R. P.; Lillo-Rodenas, M. A.; Montes-Moran, M. A.; Martin, M. J.; Linares-Solano, A. *Carbon* **2010**, *48*, 1032–1037.
17. Kalderis, D.; Bethanis, S.; Paraskeva, P.; Diamadopoulos, E. *Bioresour. Technol.* **2008**, *99*, 6809–6816.
18. Dastgheib, S. A.; Karanfil, T.; Cheng, W. *Carbon* **2004**, *42*, 547–557.
19. Vidic, R. D.; Suidan, M. T. *Water Environ. Res.* **1992**, *64*, 798–804.
20. Sorial, G. A.; Suidan, M. T.; Vidic, R. D.; Maloney, S. W. *J. Environ. Eng.* **1993**, *119*, 1026–1043.
21. Myers, A. L.; Prausnitz, J. M. *AIChE J.* **1965**, *11*, 121–127.
22. Radke, C. J.; Prausnit, Jm *Ind. Eng. Chem. Fundam.* **1972**, *11*, 445–451.
23. Jimenez, V.; Diaz, J. A.; Sanchez, P.; Valverde, J. L.; Romero, A. *Chem. Eng. J.* **2009**, *155*, 931–940.
24. Jiang, Q.; Zhao, Y. *Microporous Mesoporous Mater.* **2004**, *76*, 215–219.

Chapter 9

Cyclic Electrowinning/Precipitation (CEP) for the Removal of Heavy Metals from Aqueous Solution Mixtures

J. M. Calo,[*] P. Grimshaw, and G. Hradil

School of Engineering, Brown University, Providence, Rhode Island 02912
[*]E-mail: JMCalo@brown.edu

The description and operation of a novel cyclic electrowinning/precipitation (CEP) approach for the simultaneous removal of mixtures of heavy metals from aqueous solutions are presented. CEP combines the advantages of electrowinning in a spouted particulate electrode (SPE) with that of chemical precipitation and redissolution, to remove heavy metals at low concentrations as solid metal deposits on particulate cathodic particles without exporting toxic metal precipitate sludges from the process. The overall result is very large volume reduction of the heavy metal contaminants as a solid metal deposit on particles that can either be safely discarded or further processed to recover particular metals. The performance of this approach is demonstrated with data obtained for the removal of low concentration mixtures of copper, nickel, and cadmium from aqueous solutions, as well as removal from contaminated soil leachates. Separation of these same metals on different sets of cathodic particles is also demonstrated. An analysis of co-electrodeposition of copper and nickel from acidic solution mixtures is also presented, as an example of the processes that occur in the SPE of the CEP system. The quantitative and qualitative behavior of co-electrodeposition of these two metals from their mixtures differs significantly from that of the individual single-metal solutions, primarily due to the metal displacement reaction between Ni^0 and Cu^{++}. A numerical model of co-electrodeposition, corrosion, metal displacement,

In Novel Solutions to Water Pollution; Ahuja, S., et al.;
ACS Symposium Series; American Chemical Society: Washington, DC, 2013.

and mass transfer in the SPE is presented that describes the behavior of the experimental data relatively well.

Introduction

Chemical precipitation of metal ions is perhaps the simplest and most widely used method of heavy metal removal from aqueous solutions (*1*). Traditionally, hydroxide precipitants such as lime and caustic soda have been favored over their sulfide counterparts, due to the higher cost of chemically produced hydrogen sulfide and associated hazards. The use of sodium hydroxide introduces the least amount of additional mass to the precipitate sludge, but the volume of sulfide precipitate sludge is generally less. This has significant economic impact on waste management strategies for waste metal producers, since smaller volumes result in lower disposal and reclamation costs. In addition, the solubilities of metal sulfides are generally less than their corresponding hydroxides or carbonates. Even moderate sulfide addition can effectively reduce dissolved metal levels to below those permitted for discharge (*2*). In addition, in certain cases metals can be recovered from sulfide sludges (*3*). Metal precipitation with sulfides and hydroxides is well documented in the literature (*4–7*).

Electrowinning, electrolytic removal/recovery (ER), or electroextraction, is another technique that has been used to remove heavy metals from contaminated water. This approach involves electrodeposition or reduction of metal ions from an electrolyte. In ER, a current is passed between the electrodes and metal cations diffuse to the surface of the cathode where they form a surface complex, receive electrons, and are reduced to the metallic state. Metal removal/recovery rates by ER can be augmented by increasing current density, cathode surface area, and liquid phase agitation to improve mass transfer rates. The major drawback of ER of metals from dilute solutions is low current efficiencies.

There are also a number of other methods that have been demonstrated to be quite effective for the removal of heavy metals from complex aqueous mixtures, such as colloidal foam flotation (*8*) and nondispersive membrane liquid extraction (*9*). Indeed, such techniques may also be coupled to ER in a manner somewhat similar to what is presented here for chemical precipitation. However, ER exhibits the additional advantages of producing a solid metallic material that provides considerable volume reduction, which is also convenient for further metal purification and recovery.

Although packed beds have been used as ER cathodes (*10*, *11*), their operability is limited by agglomeration of bed particles due to bridging of metal deposits between particles and the accompanying unacceptable increase in pressure drop (*12*, *13*). Fluidized beds have also been used as ER cathodes (*14–16*). These types of systems offer good liquid-solid contacting and do not generally suffer from particle agglomeration. However, they usually exhibit randomized, poor electrical contact between particles, inhomogeneous electrical potentials, and particle segregation effects (*17*). The existence of anodic zones in fluidized bed electrodes that are not observed in unexpanded fixed beds of the same particles, has also been reported (*18*, *19*). In addition, the range of overpotentials tends to be spatially distributed (*13*).

Spouted (or recirculating) particulate electrodes (SPE) utilize conductive particles that are circulated hydrodynamically as a low-density, liquid-solid mixture in an entrained flow mode, and form a denser moving bed in the cathode region. Thus, in a sense, they are hybrids of fixed and fluidized (entrained) bed electrodes, incorporating advantages of both, while minimizing some of their disadvantages. For example, the cathodic particles do not agglomerate due to metal electrodeposition as long as spouting and particle movement are maintained. We have investigated electrowinning of copper (*20*) and nickel (*21*) in a SPE.

Here we report on our investigations of the removal of mixtures of copper, nickel, and cadmium to low concentrations with a Cyclic Electrowinning/Precipitation (CEP) system that combines the positive characteristics of both chemical precipitation and electrowinning, while avoiding/minimizing some of their individual inherent drawbacks (*22*). In a CEP system, chemical precipitation/redissolution is used in two ways: to increase metal concentrations for more efficient electrowinning, and as a *finishing* step for reducing metal concentrations in the final effluent water. When operated in a cyclic fashion, metal precipitates are formed and redissolved, but no toxic sludge leaves the process. The process effluents are the solid particles with the accumulated electrodeposited metal, and decontaminated effluent water. In addition, related work is presented on the electrowinning of bimetallic mixtures (Cu/Ni) from aqueous solutions (*23*) that elucidates the processes that occur in the SPE of the CEP system.

Experimental

CEP System Apparatus and Materials

The CEP system is an automated and programmable apparatus for the removal of heavy metals from aqueous solutions using a cyclic combination of electrowinning and in-process precipitation and redissolution steps. As shown in the schematic in Figure 1 and the image in Figure 2, it consists of two principal components: the spouted particulate electrode (SPE), and the precipitation/redissolution (P/R) tank. Metal ion-containing water is pumped into the P/R tank from the wastewater reservoir. The solution pH is then increased with 1N NaOH, and the resultant precipitation of the metal ions as insoluble hydroxides removes the metals in the supernatant water to concentrations on the order of 0.3-1.5 ppm. The filtered solution is then pumped to the clean solution reservoir. Additional contaminated water is then introduced into the P/R tank, and the entire solution is re-acidified with 1N H_2SO_4 and remixed with the metal hydroxide sludge, which redissolves and produces a solution with higher metal ion concentrations with each cycle. *Via* multiple P/R steps, the metal ion concentrations are increased sufficiently to enable electrowinning (metal ion reduction) onto the solid cathodic particles in the SPE at good current efficiencies.

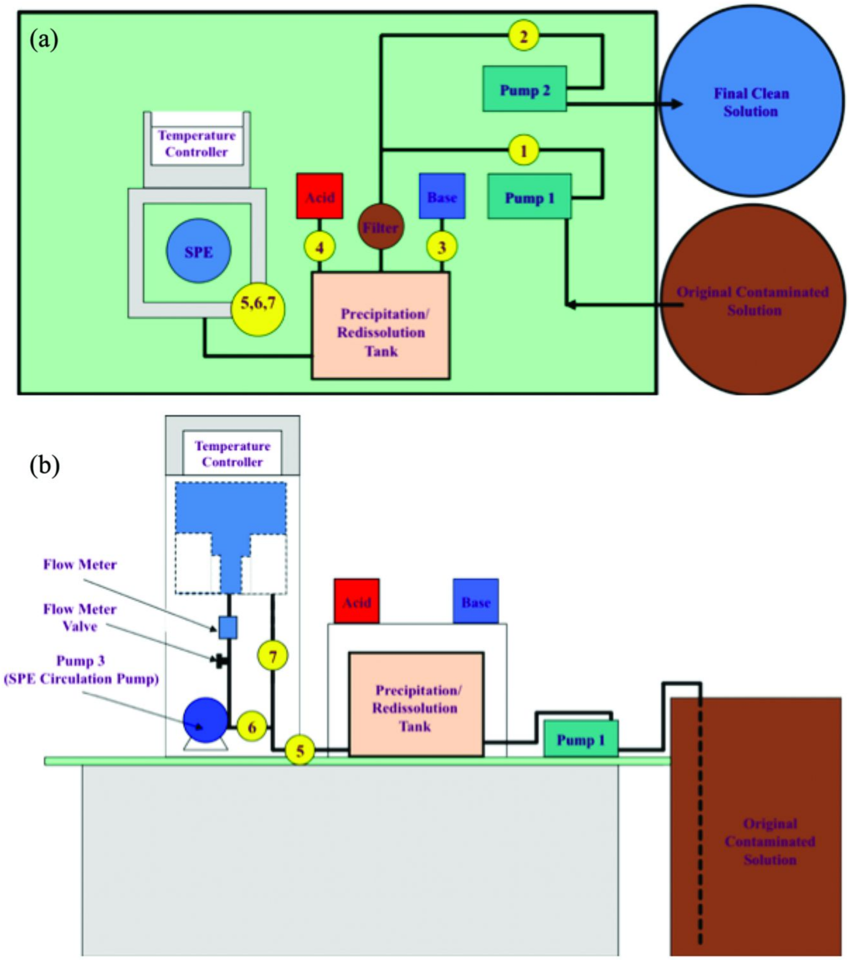

Figure 1. Schematic of Cyclic Electrowinning/Precipitation (CEP) system: (a) top view; (b) side view.

A schematic of the SPE used in the CEP system (constructed by Technic, Inc., Cranston, RI) is presented in Figure 3. Its operation is similar to that of a spouted bed electrochemical reactor used and described in our previous work (*20*, *21*, *23*) Essentially, conductive particles are entrained in the electrolyte jet and convected upwards in the central draft tube. The entrained particles disengage from the liquid flow as the velocity decreases in the freeboard region, and then fall on the inverted conical distributor. The collector/distributor cone channels the particles to the periphery, where they fall onto and become part of the particulate moving bed cathode, which transports them inward and downward on the bottom cone back to the entrainment region. The pumping action of the spout circulates the particles through the vessel in a toroidal fashion - upwards in the spout, and downwards in the moving bed. Electrowinning occurs only on the bottom conical section of the vessel, where the particles form a cathodic moving bed in contact with the current feeder.

Figure 2. Image of the Cyclic Electrowinning/Precipitation (CEP) system.

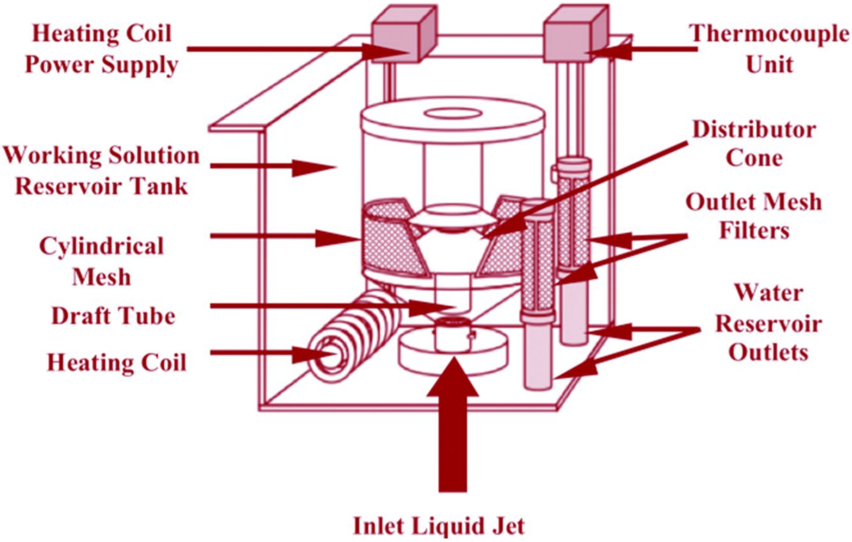

Figure 3. Schematic of Spouted Particulate Electrode (SPE).

A variable 50A DC power supply was used to deliver current to the SPE. The electrolyte solution was circulated with a magnetically coupled centrifugal pump (Iwaki MD-40RT), equipped with a bypass valve for flow rate control. A paddle wheel flow meter (Signet 3-2535) was used to measure the liquid flow rate. A heater (CAL Controls Ltd. CAL3300) located at the bottom of external holding chamber, and a cooler consisting 1/16” plastic tubing coils circulating cooling water, located on the wall of the reservoir chamber, are used simultaneously to set the solution temperature. An automatic pH controller (Barnant, model HD-PHP) was used to maintain constant pH by the addition of potassium hydroxide solution to the SPE reservoir.

Electrically actuated ball valves (ASAHI America 05E01660F) and pumps (Iwaki MD-30RT-115ML) were used to control the solution flows. A mixer (IKA, Eurostar power CV S1) was employed to stir the solution during addition of sulfuric acid or sodium hydroxide solution to the P/R tank. A 20 µm inline filter (ISC, Model No SJC-40-20) was used to retain metal hydroxide precipitate particles. A computer (Dell Optiplex 320), LabView™ software, and electronics interface (National Instruments, NI PCI-6221, M series DAQ; SCB-68 noise rejecting, shielded I/O connector block; and USB-9211A 4 Ch) were used to automatically control all CEP system operations.

The electrolyte solution in the SPE reservoir was sparged with 3.5 SLM (standard L min^{-1}) of nitrogen to reduce the dissolved oxygen concentration and reduce metal corrosion from the cathodic particles. The sparger was constructed from 0.635 cm diameter nylon tubing arranged in a square, 16.5 cm on a side, drilled with 0.35 mm diameter holes. The water flow rate was 16.2 L min^{-1}. Approximately 400 cm^3 of conductive bed media (2.0 mm diameter plastic spheres, metallized with copper - Bead House LLC, CMC02.0/CP) were used.

The initial metal ion concentrations for all the CEP experiments were approximately 20 ppm each in the fresh solutions, consisting of 14.1 g $CuSO_4 \cdot 5H_2O$ (>98%, Aldrich), 16.3 g $NiSO_4 \cdot 6H_2O$(>98%, Aldrich), and 8.3 g $CdSO_4 \cdot 5H_2O$ (>98%, Aldrich) added to 180 L of water for the ternary mixture. 550 g of Na_2SO_4 (granular, >99%, Aldrich) and 600 g H_3BO_3 (to suppress hydrogen evolution and stabilize pH in the vicinity of the cathodic particles (*24*)), were added to the precipitation tank just prior electrowinning in the SPE.

Metal concentrations in the aqueous samples were determined with an ICP Optical Emission Spectrometer (ICP-OES; Jobin Yvon, JY2000). Sufficient sulfuric acid (1M, Mallinkrodt) and potassium hydroxide (1M, Fisher Scientific) were added automatically to obtain the desired pH values of 4 for redissolution and electrowinning, and 11 for precipitation in the P/R tank.

CEP System Program

A LabView™ control program was used to automate and control the CEP system so that it could be programmed to accommodate a wide variety of metal removal/remediation/ recovery scenarios that may be found in practice. The control program consists of a front panel and block panel modules. The front panel serves as the programmatic interface. Controls and indicators on the front panel allow for inputting and exhibiting data and the status of all the system elements, such as pumps, valves, and pH. The block panel incorporates the code for the control program. The time sequence is the main frame of the program. The precipitation/redissolution tank and SPE processes are executed in the order specified by the program. The "on/off" status of the pumps and the "open/closed" status of the valves are controlled by the program. The pH and level sensors provide input to the program *via* the data acquisition system. The program then sends out the appropriate digital signals to control the corresponding pumps and valves to execute each step in the program.

The CEP System program was run for a specified time, or until the metal ion concentrations reached a desired level, or with programs executing various different CEP cycles. The sequence of fluid handling operations during the *precipitation/redissolution cycle* and the *electrowinning cycle* are outlined in the Appendix.

Results

Metal Co-Removal from a Cu/Ni Mixture with a Spouted Particulate Electrode (SPE)

The co-removal/recovery of multiple metals from complex mixtures is of practical import in a number of applications, including electrowinning in the SPE of the CEP system. In order to elucidate the primary mechanisms of import in electrowinning complex metal mixtures, here we present an analysis of co-removal of Cu and Ni from aqueous solution mixtures.

Co-electrodeposition of copper and nickel and examination of the resultant alloy structures have been conducted in rotating cylinder electrodes (*25–27*). It has been shown that the co-electrodeposition of these metals is not independent (*25*), but that a displacement reaction occurs between deposited nickel metal and copper ions in solution (*28*). Bradley and Landolt (*29*) investigated the electrodeposition-displacement reaction with a pulsed current method. Bradley *et al.* (*30*) and Scharfe *et al.* (*31*) also studied the effects of metal displacement on electrodeposition. It has been shown that the properties of electrodeposited alloys differ from those of their cast analogs (*32*, *33*). Roy (*34*) also reported on alloy structures formed by the displacement reaction. Shibahara *et al.* (*28*) found that mixed-metal cubane-type clusters are involved in the displacement of a metal atom in the metal cluster by another metal atom, and Meuleman (*35*) reported that from one to four monolayers of nickel could be dissolved from Ni/Cu layers by displacement and dissolution.

Co-Electrodeposition Model

An electrochemical model, based upon a general approach for modeling the behavior of recirculating electrochemical reactors (*36*, *37*), and the single metal model developed to correlate/predict copper (*20*) and nickel (*21*) behavior in single metal solutions, was extended to simulate the co-removal of copper and nickel behavior with pH and temperature.

The principal reactions assumed to occur during copper and nickel electrowinning from acidic aqueous solutions are (*20*, *21*):

Main cathodic reactions: $$Cu^{2+} + 2e^{-} \rightarrow Cu \qquad (1)$$

$$Ni^{2+} + 2e^- \rightarrow Ni \qquad (2)$$

Cathodic side reaction: $$2H^+ + 2e^- \rightarrow H_2 \qquad (3)$$

Main anodic reaction: $$H_2O \rightarrow 2H^+ + 2e^- + ½ O_2 \qquad (4)$$

In addition to the preceding, the model must also take into account metal corrosion in the presence of oxygen and [H^+] which oxidizes deposited metal on the particles in acidic solutions *via* the same reactions as previously identified:

$$Cu + ½ O_2 + 2H^+ \rightarrow Cu^{2+} + H_2O \qquad (5)$$

$$Ni + ½ O_2 + 2H^+ \rightarrow Ni^{2+} + H_2O \qquad (6)$$

Also, as discussed above, it was found that the metal displacement reaction,

$$Cu^{2+} + Ni \rightarrow Ni^{2+} + Cu; (E° = +0.59V), \qquad (7)$$

is important in the behavior of copper and nickel during co-electrodeposition.

The assumptions that were used in developing the models for the electrodeposition behavior of the single metals (*20*, *21*) are retained in the current model, including mass transfer resistance and kinetic formulations. For galvanostatic operation, the corresponding total cathodic current balance is given by:

$$i = i_1 + i_2 + i_3 = \frac{(z_1F/a)k_1C_1}{(1 + k_1/k_La)} + \frac{(z_2F/a)k_2C_2}{(1 + k_2/k_La)} + (z_3F/a)k_3C_3 \qquad (8)$$

where the subscripts are: *1 = copper; 2 = nickel; and 3 = hydrogen*, respectively; z_i, i_i and C_i are the corresponding charge, cathodic current density, and bulk phase concentration; F is Faraday's constant; k_j is the electrochemical reduction rate constant, which depends on the electrode overpotential according to the Tafel approximation (*20*, *21*, *38*); k_L is the mass transfer coefficient given by Pickett (*39*) for a single layer packed bed electrode, and a is the interfacial surface area per unit volume. The resultant mass balances for the two metal cations are:

$$\frac{dC_1}{dt} = -k_1'C_1 + k_{c1} - k_d'C_1 \qquad (9)$$

$$\frac{dC_2}{dt} = -k_2'C_2 + k_{c2} + k_d'C_1 \qquad (10)$$

in which, $k_i' = k_i/(1 + k_i/k_La)$. Also, it is assumed that the metal displacement reaction is first order in the copper cation concentration, C_1, with the rate constant

k_d, and the k_{ci} are the apparent corrosion rate constants for the two metals, which are zeroth order in the metal cation concentration, and first order in DO and [H^+] (*20*, *21*, *40*).

Tafel kinetics parameter values for the copper, nickel and hydrogen cathodic reactions are presented in Table 1.

Table 1. Tafel Kinetics Parameter Values Used in the Cu/Ni Co-Electrodeposition Model (*38*)

Cathodic Reaction	*Transfer coefficient (α)*	*Exchange current density (A m^{-2})*	*Enthalpy of activation (kJ mol^{-1})*	*T (°C)*
Cu^{2+}/Cu	0.74 (*41*)	2.3 (*41*)[a]	41.7 (*41*)[a]	25
Ni^{2+}/Ni	0.49 (*42*)	0.068 (*42*)	37.2 (*43*)	25
H^+/H_2	0.63 (*44*)	0.002 (*44*)	42.2 (*44*)	20

[a] Calculated from data in Reference (*41*).

The model solution methodology is similar to that used previously in (*21*), modified for the metal displacement reaction, as follows. An initial estimate of the metal displacement reaction rate constant was determined by fitting the Cu and Ni data to polynomials. From these fits, values of C_1, C_2, and dC_1/dt at the nickel maximum where $dC_2/dt = 0$, were found. From the sum of Eqns. (9) and (10), evaluated at the nickel maximum, and the experimental value (slope) measured from the Ni corrosion data, $(k_d^{'}C_1 + k_{c2})_{\text{exp}}$ (obtained by shutting off the current during SPE operation; see below):

$$k_d^{'} = \frac{k_2^{'}C_2\big|_{\max} - (k_d^{'}C_1 + k_{c2})_{\exp}}{(C_1\big|_{\max} - C_1\big|_{\exp})} \tag{11}$$

$$k_{c2} = k_2^{'}C_2\big|_{\max} - k_d^{'}C_1\big|_{\max} \tag{12}$$

The sum of the slopes of the linear corrosion data for copper and nickel yield the value $(k_{c1} + k_{c2})_{\text{exp}}$, and

$$k_{c1} = (k_{c1} + k_{c2})_{\exp} - k_{c2} \tag{13}$$

Using these values for $k_d^{'}$, k_{c1}, and k_{c2}, determined as above, the model was then solved for the copper and nickel cation concentrations in the following manner. For constant current density, *i*, beginning with the initial metal ion concentrations, C_{10} and C_{20}, the transcendental current balance (Eq. (8)) is solved to yield the cathodic potential, E. Eqns. (9) and (10) are then solved for the first time step using a Runge-Kutta, 4th order method (*45*). These two steps are then repeated alternately, moving forward in time, until the desired time is attained.

A sum of least squares method was devised to determine the "best fit" set of parameter values for k_{c1}, k_{c2}, and $k_d^{'}$. First, from the measured copper and nickel corrosion rates, the rate of the metal displacement reaction was adjusted to minimize the sum of least squares deviation of the initial portion of the nickel removal curve up to the nickel maximum where it is dominant. Next, the copper corrosion rate was adjusted to provide the "best fit" for the copper removal curve. The same was then done for the nickel removal curve. This process was repeated with the new fit corrosion rates until the resultant parameter values converged.

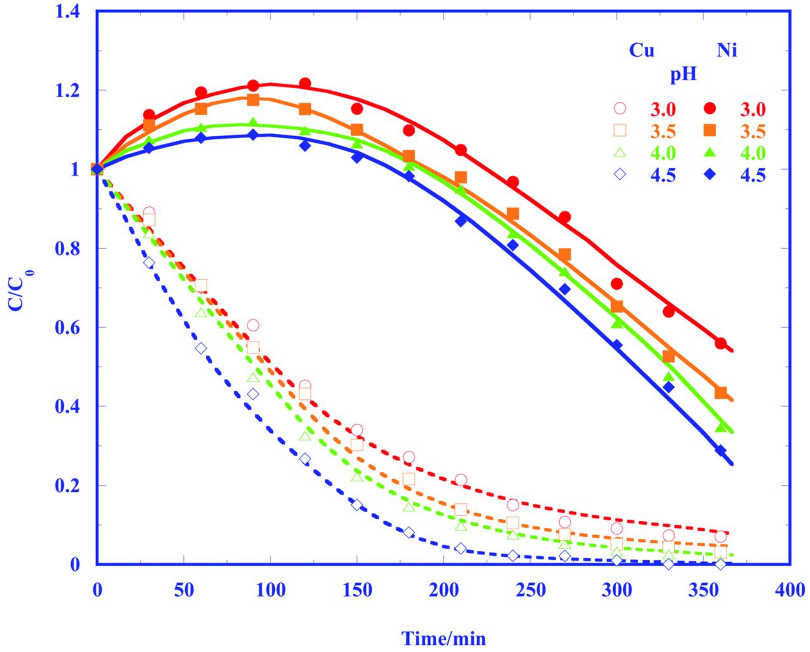

Figure 4. Galvanostatic co-electrodeposition of copper and nickel in the spouted particulate electrode as a function of pH at 40°C, 10A without nitrogen sparging. Adapted with permission from Ref. (23) (Copyright © 2011, ACS).

Results for co-electrodeposition of copper and nickel as a function of pH at 40°C are presented in Figure 4, and as a function of temperature at constant pH 4 in Figure 5, without nitrogen sparging. The data points are the measured values, and the curves are the model results for copper and nickel, respectively. As shown, the model results are in reasonable agreement with the data.

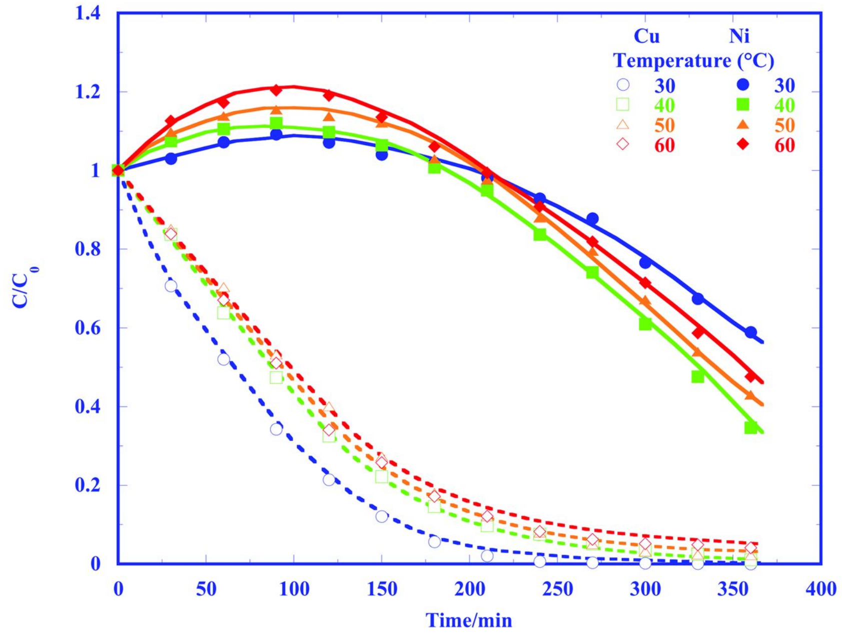

Figure 5. Galvanostatic co-electrodeposition of copper and nickel in the spouted particulate electrode as a function of solution temperature at pH 4, 10A without nitrogen sparging. Adapted with permission from Ref. (23) (Copyright © 2011, ACS).

These data show that copper deposits first and nickel second, consistent with their respective standard reduction potentials. The overpotentials ($\eta = E - E_e$) determined from the model, reflect these observations, exhibiting a larger, negative overpotential for copper than nickel over the entire experiment. A sharp change in the overpotential occurs for both metals over the region where copper deposition cuts off. For example, at pH 4, 40°C, 10A, copper initially deposits very rapidly up to about 110 min, which is where the nickel maximum occurs. Over this region, the overpotential for copper increases slightly (averaging about -230 mV), while that for nickel is positive and decreases slightly (averaging about +150 mV). Over the region where copper electrodeposition ceases (*ca.* 110 – 130 min), both the copper and nickel overpotentials are negative and decrease rapidly (i.e., become more negative) as nickel begins to electrodeposit. The results also indicate that the copper electrodeposition rate constant and the mass transfer coefficient become approximately equal (i.e., $k_La/k_1=1$) at about 110 min, while the same occurred for nickel (i.e., $k_La/k_2 = 1$) at about 400 min.

For electrodeposition of just copper from acidic solutions in the same apparatus used in the current work, it was found that the net rate increased with increasing pH and decreasing temperature (*20*), while for solutions containing just nickel (*21*), the behavior with pH was similar, but the net rate increased with temperature over the range of parameter values investigated. As shown in Figures 4 and 5, for co-electrodeposition, copper generally behaved as previously

(*20*), except with a much more rapid net removal rate. Nickel behavior, on the other hand, was more complex, such that the maximum net electrodeposition rate occurred at about pH 4. Also, from the results in Figure 5 at constant pH 4, the maximum co-electrodeposition rates occurred at a temperature of about 30°C for copper and about 40°C for nickel.

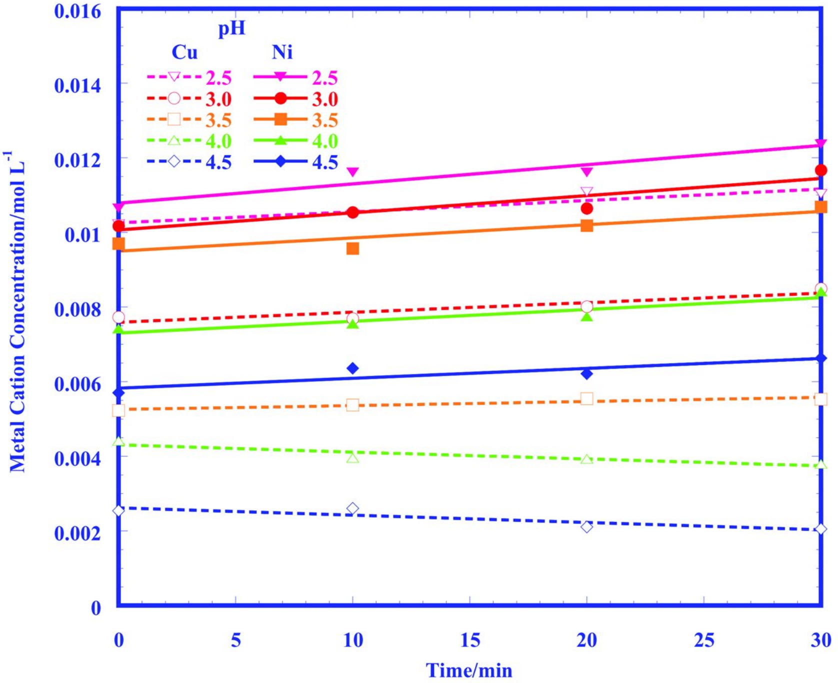

Figure 6. Copper and nickel ion concentrations during "corrosion" studies with no applied current as a function of solution pH at 40°C, without nitrogen sparging. Adapted with permission from Ref. (23) (Copyright © 2011, ACS).

The nickel maxima observed at relative concentration ratios *(C_i/C_{i0})* of about 1.05 - 1.2 in Figures 4 and 5 are attributed to the metal displacement (oxidation) reaction of Ni^0 by Cu^{++} [Eq. (7)]. Metal displacement reactions are well known (*46*, *47*) and are used commercially in applications such as the "cementation" of silver (*48*), for example. These reactions can also result in significant quantitative and qualitative differences between the electrochemical removal of metals from single metal aqueous solutions and from solutions of multiple metal mixtures.

In addition to the nickel maxima evident in Figures 4 and 5, the effects of the displacement reaction are quite evident in the metal corrosion experiments as well. In Figure 6 are presented corrosion results at 40°C as a function of solution pH without nitrogen sparging. As noted, the concentration of nickel ion increases with time at all the pH values, while the concentration of copper ion also increases with time at low pH (2.5 and 3.0). With increasing pH, however, the rate (i.e., the slope) decreases to zero, and the copper ion concentration thereafter decreases with time with increasing pH; and increasingly so with pH.

At pH 4, the copper concentration only decreases with time, and the rate (slope) becomes more negative with increasing temperature in the absence of an applied current. This behavior is directly attributable to the metal displacement reaction. With the current off, the electrodeposition rate terms are zero, and the resultant expressions can be solved to yield:

$$C_1 = (C'_{10} - \frac{k_{c1}}{k'_d})\exp(-k'_d t) + \frac{k_{c1}}{k'_d} \tag{14}$$

$$C_1 = (C'_{10} + C'_{20}) - \frac{k_{c1}}{k'_d} + (k_{c1} + k_{c2})t - (C'_{10} - \frac{k_{c1}}{k'_d})(\exp(-k'_d t)) \tag{15}$$

where C'_{10} and C'_{20} are, respectively, the copper and nickel cation concentrations at the point where the feeder current is turned off. From Eq. (14), it can be concluded that the copper cation concentration can exhibit two regimes of behavior, depending on the relative magnitudes of k_{c1} and k'_d: corrosion rate-control for $k'_d >> k_{c1}$ where the copper cation concentration increases with time after current shut-off; and displacement rate control for $k_{c1} << k'_d$ where the copper cation concentration decreases with time after current shut-off. The results here demonstrate both types of behavior depending on temperature, pH, and copper cation concentration at the time of current shut-off. If the argument of the exponential is relatively small, the resultant behavior will be approximately linear in time; i.e.,

$$C_1 = C'_{10} + (k_{c1} - k'_d C'_{10})t \tag{16}$$

$$C_2 = C'_{20} + (k_{c2} + k'_d C'_{10})t \tag{17}$$

From Figure 6, the corrosion data are indeed approximately linear in time, consistent with these expressions, and thus the kinetics are close to zeroth order, at least over this timescale.

Experimentally determined net corrosion rates for copper and nickel from experiments without nitrogen sparging are summarized in Table 2, along with the final “best fit” parameter values determined from the model, as described above. As shown, the experimental rates obtained by shutting off the current agree reasonably well with the values obtained from the model fits. The “fit” net corrosion values were consistently less than the measured values, but were quite close for the constant pH 4 data; however, they differ a bit more (by about a factor of 2-3 or so) for the isothermal 40°C data as a function of pH. This supports our conclusion that the essential elements of the system are reasonably well captured by the simple model.

Table 2. Measured and "Fit" Net Copper and Nickel Corrosion Rates without Nitrogen Sparging

	Measured Net "Corrosion" Rate ($\times 10^5$ mol L^{-1} min^{-1})			*"Fit" Net "Corrosion" Rate ($\times 10^5$ mol L^{-1} min^{-1})*			k'_d
	Cu	*Ni*	*Cu+Ni* ($k_{C1}+k_{C2}$)	*Cu*	*Ni*	*Cu+Ni* ($k_{C1}+k_{C2}$)	(min^{-1})
T (°C)	*pH 4, 10A*						
30	-1.6	2.5	0.9	-0.2	0.8	0.6	0.002
40	-1.9	3.2	1.3	-0.1	1.1	1.0	0.003
50	-2.5	3.9	1.4	-0.2	1.5	1.3	0.004
60	-3.9	5.5	1.6	-0.7	2.2	1.5	0.012
pH	*40°C, 10A*						
3.0	2.6	4.6	7.2	0.01	2.3	2.4	0.006
3.5	1.1	3.6	4.7	0.05	1.8	1.8	0.004
4.0	-1.9	3.2	1.3	-0.2	1.1	0.9	0.003
4.5	-2.0	2.6	0.6	-0.3	0.6	0.3	0.002

For the isothermal copper data (40°C) at low pH (3.0 and 3.5), the corrosion rate is greater than the metal displacement rate, while the reverse is true at higher pH (4.0 and 4.5) where the corrosion rates are less. Consequently, the resultant slopes for the isothermal "corrosion" data for copper exhibit a transition from positive to negative with increasing pH. As a function of temperature at a constant pH of 4, the copper behavior is dominated by metal displacement, such that the "corrosion" curves exhibit only negative slopes. These slopes become increasingly negative with increasing pH, reflective of the Arrhenius temperature dependence of the displacement rate constant. This differs from the behavior observed in acidic solutions containing just copper (*20*) or nickel (*21*), in which it was found that the corrosion rates were always positive; i.e., the metal ion concentrations always increased with time when the current was turned off. For nickel, however, both the corrosion and displacement reactions act in the same direction to monotonically increase the concentration of nickel ion in solution, such that the resultant slopes can only be positive, as previously discussed. As shown in Table 2, the corrosion rates for nickel increase monotonically with temperature and decreasing pH.

Fricoteaux and Douglade (*49*) and Pourbaix (*50*) found that Cu_2O formation can occur at pH ≥ 3.0 *via:*

$$2Cu^{2+} + 2e^{-} + H_2O \rightarrow Cu_2O + 2H^{+} \tag{18}$$

The deposited cuprous oxide would then further inhibit the metal displacement reaction. The higher the pH, the more facile the production of copper oxide, which may at least partially explain why the nickel displacement reaction rate decreases with increasing pH. A power law fit of the displacement reaction rate constant data as a function of pH from Table 2, indicates that the rate constant is proportional to $[H^+]^{-0.72}$ at 40°C. Also, from the results in Table 2, the metal displacement reaction rate constant is Arrhenius temperature-dependent with an apparent activation energy of 47.2 kJ/mol at a constant pH of 4.

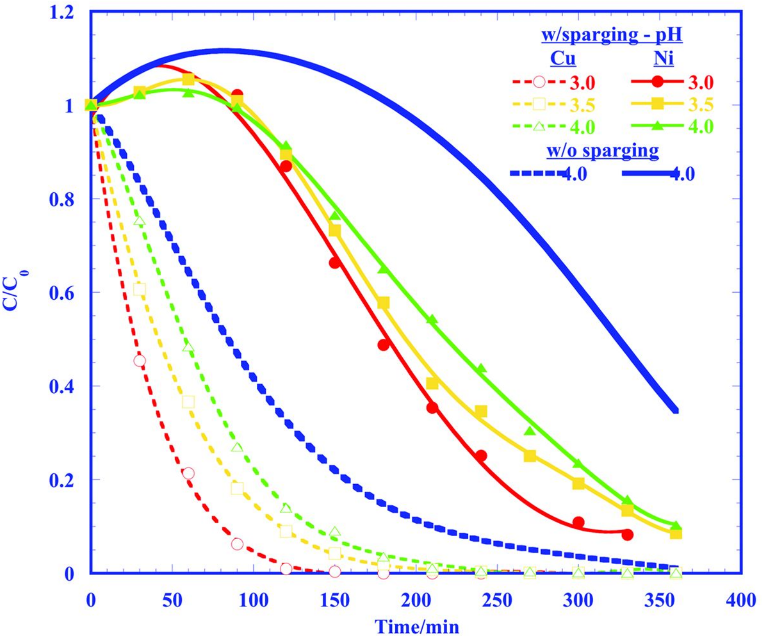

Figure 7. Normalized copper and nickel concentrations at 40°C. The bold solid and dashed curves without data symbols are the data without nitrogen sparging at pH 4, 40°C, 10A, from Figures 4 and 5. Adapted with permission from Ref. (23) (Copyright © 2011, ACS).

As was found for both copper and nickel solutions, sparging with an inert gas reduces the dissolved oxygen concentration and, consequently, the corrosion rate (*20*, *21*). In Figure 7 are presented co-electrodeposition data with nitrogen sparging for copper/nickel solutions as a function of pH at 40°C, 10A. The data from Figures 4 and 5 for pH 4, 40°C, 10A, are also presented for comparison. As shown, nitrogen sparging considerably increases the observed net electrodeposition rates for both metals – considerably more so than was observed from solutions with just the single metals alone (*20*, *21*).

Corrosion rate results following co-electrodeposition of copper and nickel are summarized in Table 3. As shown, the total corrosion rates for both metals were reduced by about a factor 2-3 with nitrogen sparging. The reduction in corrosion rates increases the negative slopes of the copper curves, and decreases the positive slopes of the nickel curves, decreasing the inhibition of the displacement reaction which accelerates copper and nickel removal rates to a greater degree than shown in Figures 4 and 5 without nitrogen sparging.

Table 3. Measured Net Copper and Nickel "Corrosion" Rates with Nitrogen Sparging

	Measured Net "Corrosion" Rate ($\times 10^5$ mol L^{-1} min^{-1})		
	Cu	*Ni*	*Cu + Ni* ($k_{C1}+k_{C2}$)
T (°C)	*pH 4, 10A*		
30	-2.2	2.6	0.4
40	-2.4	2.8	0.4
50	-3.1	3.3	0.2
60	-4.5	5.2	0.7
pH	*40°C, 10A*		
2.5	1.4	3.5	4.9
3.0	0.7	3.4	4.1
3.5	-0.03	2.9	2.8
4.0	-2.4	2.8	0.4
4.5	-2.6	2.8	0.2

The behavior of the dissolved oxygen (DO) concentration data with time, corresponding to the electrodeposition data in Figures 4 and 5, is presented in Figure 8. As shown, upon initiation of electrowinning, the DO concentration increases rapidly, exhibits a maximum, and then gradually decreases again. This behavior is similar to that observed for nickel electrodeposition alone (*21*). The DO concentration increases up to pH 4, and then decreases with increasing pH beyond that point. Also, as shown, it first increases with temperature (at constant pH 4) to 40°C, and then decreases thereafter. This behavior can be understood in terms of the model presented here, as discussed elsewhere (*21*).

As has been noted, in Figures 4 and 5 the net copper electrodeposition rate increases with increasing pH and decreasing temperature, which is similar to the behavior with just copper in solution (*20*). This differs somewhat from the behavior of solutions with just nickel present, where the electrodeposition rate increases with both increasing pH and temperature (*21*). These observations are attributed to the relative effectiveness of the net electrodeposition rate in comparison to the corrosion rate. In the case of nickel, the corrosion rate increases with both temperature and decreasing pH, but not as rapidly with temperature as observed for copper.

In Figure 9 are presented the sum of the copper and nickel cation concentrations as a function of time (at 40°C, 10A) with pH as a parameter from the results in Figure 4. Summation of the differential mass balances for the two cations (Eqns. (9) and (10)) eliminates the metal displacement reaction terms, so that these curves represent the net effect of just metal electrodeposition and corrosion. As shown, the resultant curves are approximately linear over the entire range, with a slope that gradually increases with pH, except for the data with pH 4.5. This behavior is attributed to galvanostatic operation under conditions where the operating current is less than the limiting current. Under these conditions, it has been shown that the concentration of the metal cations decreases linearly with time (*37*, *51*). The increasing (negative) slope with pH is attributed to diminution of the net corrosion rate with pH, with the exception of the slope for pH 4.5, where the effects of corrosion are minimal, but where the net metal electrodeposition rate is also slowing.

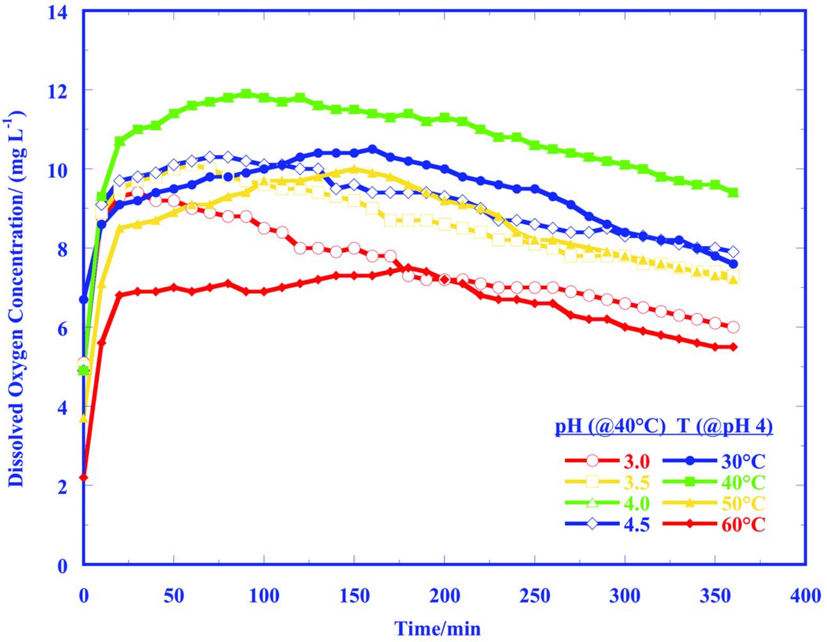

Figure 8. Dissolved oxygen (DO) concentrations corresponding to the Cu/Ni co-electrodeposition data presented in Figures 4 and 5. Adapted with permission from Ref. (23) (Copyright © 2011, ACS).

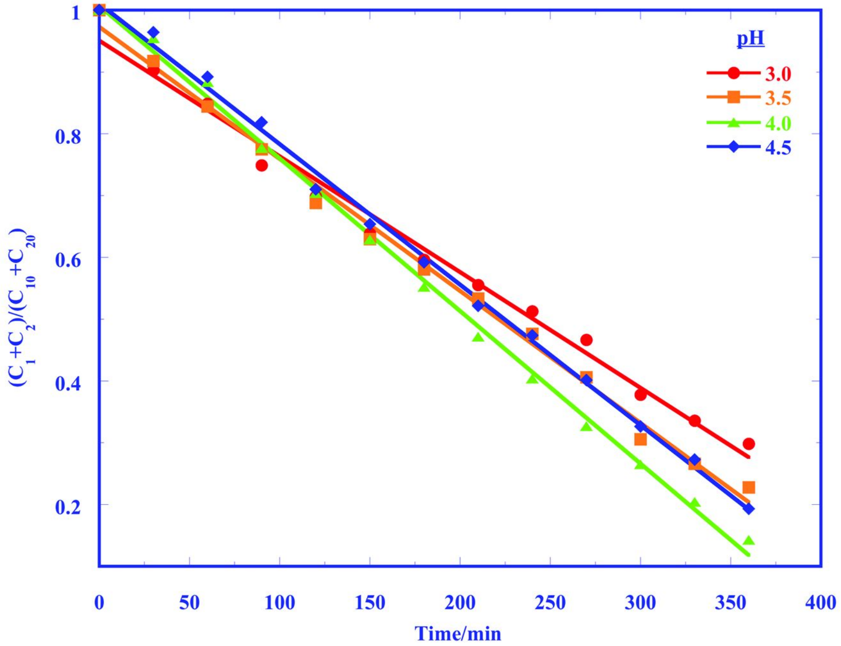

Figure 9. Normalized sum of copper and nickel ion concentrations from Figure 4 as a function of pH at 40°C, 10A. Adapted with permission from Ref. (23) (Copyright © 2011, ACS).

CEP System Performance and Analysis

During the electrowinning steps in the SPE, electrochemical reduction, corrosion, competing side reactions, and metal displacement reactions occur at the cathode particle surfaces (*20*, *21*, *23*). As shown above, the metal displacement reaction between Cu^{2+} and reduced nickel metal (Eq. (7)) was found to be important during the co-electrodeposition of copper and nickel from solution. In a similar fashion, in Cu/Ni/Cd mixtures, the following additional metal displacement reactions occur that play an important role in the overall removal of the three metals (*52*, *53*):

$$Cu^{2+} + Cd \rightarrow Cu + Cd^{2+};\ E° = 0.74V \tag{19}$$

$$Ni^{2+} + Cd \rightarrow Ni + Cd^{2+};\ E° = 0.15V \tag{20}$$

The P/R process steps are used to increase the metals concentrations to levels sufficient for efficient electrowinning, and as the final cleanup step for the discharged water. The increase in metal ion concentration with each P/R cycle was linear, as expected. For a cycle time of 8 min., and initial metal concentrations of 20 ppm each, the increase per P/R cycle was about 16 ppm, which is accounted for as follows: The inlet and outlet tubing of the P/R tank was located at about 1/5 of the distance from the bottom of the tank. Thus, for each P/R cycle, about 1/5 of the solution remains in the tank after discharge of the supernatant water. The accumulated concentration in a P/R/redissolution cycle is then (1-1/5) x 20 ppm = 16 ppm. For the current hardware, the precipitation process worked well for total metal ion concentrations less than about 200 ppm. For higher total concentrations, the amount of accumulated hydroxide precipitate sludge would exceed the level of the tank outlet tubing, and some precipitate would be carried over and lost upon draining the tank. Of course, the operating capacity can be increased by using a larger tank and/or relocating the tank outlet.

Metal ion concentrations in the filtered effluent water were also measured for the same runs as 0.23, 0.37, and 1.50 ppm for Cu^{2+}, Ni^{2+}, and Cd^{2+}, respectively, averaged over the 7 cycles. The solubility products of copper, nickel, and cadmium hydroxide at 25°C are $2.2x10^{-20}$ (*54*), $5.5x10^{-16}$ (*55*), $7.20x10^{-15}$ (*56*), respectively. Thus, the corresponding equilibrium concentrations at pH 11 should be $2.2x10^{-14}$ mol L^{-1} (0.0014 ppt), $5.5x10^{-10}$ mol L^{-1} (0.03 ppb), and $7.2x10^{-9}$ mol L^{-1} (0.8 ppb) for the Cu^{2+}, Ni^{2+}, and Cd^{2+} ion concentrations. These values are all many orders of magnitude less than the measured values, although the ordering is the same as observed.

The mean sizes of precipitate particles have been reported to be on the order of 0.1 - 5 µm (*57*), 20 - 50 µm (*58*, *59*), and 400 µm (*59*) for copper, nickel, and cadmium hydroxide, respectively. It was found that a 5 µm filter plugged quite easily, and a 50 µm filter passed an unacceptably large amount of precipitate material. Consequently, a 20 µm inline filter (ISC, model No SJC-40-20) was selected as a compromise to retain metal precipitate particles in the P/R tank. Apparently, however, a considerable amount of metal ions and fine colloidal precipitate particles were still carried over in the filtered water. However, the very large differences between measured and theoretical equilibrium values indicate that improvements in filtration and flocculation performance (e.g., use of more effective flocculants, increase in precipitation and settling times, etc.) can result in considerable improvements in metal retention in the P/R tank, and, consequently, in overall CEP performance.

USEPA MCLG (maximum contaminant level goal) values are 1.3 mg L^{-1} (TT, treatment technique) for copper; 0.1 mg L^{-1} for nickel (remanded 1995; currently under reconsideration), and 0.005 mg L^{-1} for cadmium (*60*). Thus, the current system, as is, reduces copper below its MCLG, and even modest improvements in P/R tank performance may be expected to enable the reduction of nickel and cadmium concentrations to below their respective MCLG values to drinking water standards, if so required.

One measure of CEP system performance is the net metal removal rate over the programmed number of P/R steps per electrodeposition step. For a single metal the intrinsic rate can be expressed as (*20*, *21*, *23*):

$$\frac{dC}{dt_e} = -\frac{kC}{1 + k / k_L a} + k_c \qquad (21)$$

where C is the metal ion concentration during electrowinning, t_e, is the electrowinning time, k is the electrochemical metal reduction rate constant, k_L is the interphase mass transfer coefficient, a is the specific interfacial surface area, and k_c is the metal corrosion rate. This expression cannot be solved analytically since k varies with overpotential, and thus with time. Consequently, the experimental data were fit to polynomials for the sake of convenience. Some typical C_e *vs* t_e data are presented for copper removal in the CEP SPE as a function of applied current in Figure 10(a).

The *net rate* at which a metal is removed in the CEP system, R (e.g., in g min^{-1}), is given by the expression:

$$R = \frac{(C_0 - C_e)V}{t_e + t_p} \tag{22}$$

where: C_0 is the initial metal concentration prepared for the electrodeposition cycle; C_e is the metal concentration at the end of the electrodeposition cycle, t_e; t_p is the time for P/R process associated with accumulating the metal for electrodeposition; and V is the solution volume in the SPE. The removal rate attains a maximum at $dR/dt_e = 0$. Thus, the optimal value of t_e occurs at the root of the transcendental equation:

$$\frac{kC_e}{1 + k / k_L a} - k_c - \frac{C_0 - C_e}{t_e + t_p} = 0 \tag{23}$$

For the data presented in Figure 10(a) for copper removal, $C_0 = 99.5$ ppm, which was accumulated from a 20 ppm solution over five P/R cycles. Each P/R cycle was 8 min, so for the five P/R cycles shown, $t_p = 5 \times 8 \text{ min} = 40 \text{ min}$. The net CEP removal rate, R, for these data as a function of total CEP process time, $t_e + t_p$, was calculated as a function of applied current from the polynomial curve fits of the data presented in Figure 10(a), and the results are presented in Figure 10(b). As shown, the net CEP removal rate exhibits a maximum. The reason for this behavior is as follows. For a fixed value of t_p (i.e., 40 min. in this case) at low CEP process times, or at low values of t_e, there is little metal removal by electrowinning, so $(C_0 - C_e)$ is low. As t_e increases, however, more metal is removed by electrowinning, such that $(C_0 - C_e)$ increases, and the effect of fixed t_p decreases in comparison to t_e. This behavior causes R to initially increase with CEP process time. However, since C_e decreases exponentially with t_e, the metal ion deposition rate decreases with t_e. That is, the rate of increase of $(C_0 - C_e)$ decreases with t_e. This causes the net CEP removal rate to exhibit a maximum, which represents the optimum net CEP removal rate achieved at this maximum.

From Figure 10(b) it is also noted that the optimal value of R increases and occurs at earlier times with increasing applied current. The observed net removal rate is the competitive result of metal removal by electrochemical reduction and metal redissolution *via* corrosion. The electrochemical reduction rate increases with current, while the corrosion rate remains approximately constant for fixed electrowinning conditions, such as temperature and pH. Thus, at a particular time, the removal rate increases with applied current. The higher electrowinning rate requires less time to process the results of P/R cycles at the maximum. Consequently, the optimal time decreases with applied current, while the optimal rate increases.

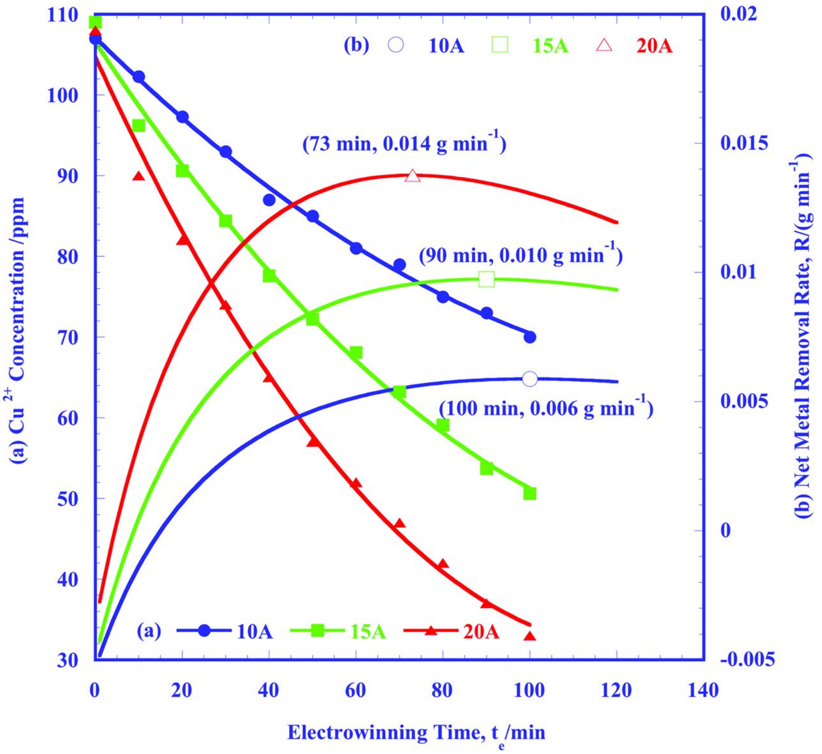

Figure 10. (a) Cu^{+2} electrowinning in the SPE as a function of current. The data symbols are the experimental data, and the curves are polynomial fits for electrowinning at 50°C, pH 4. (b) Net CEP copper removal rates, R, as a function of electrowinning time, t_e, constructed from the electrowinning data for a fixed value of t_p = 40 min., as a function of applied current. The values in parentheses are the optimal electrodeposition times, t_e, and the corresponding copper removal rates at the maxima for the same electrowinning conditions. Adapted with permission from Ref. (22) (Copyright © 2011, Elsevier BV).

Using the resultant polynomial curve fits from Figure 10(a), the corresponding optima for the copper data are 73, 90, and 100 min., corresponding to maxima in the copper removal rates of 0.014, 0.010, and 0.006 g min^{-1}, for 20, 15, and 10A, respectively. It is noted that the initial electrowinning concentration obtained with multiple P/R cycles was 99.5 ppm, while in Figure 10(a) the corresponding values are 107, 109, and 108 ppm for 10, 15, and 20A, respectively. The reason for this "discrepancy" is that after the solution is pumped to the SPE, a few minutes are required to heat the solution to the desired temperature (50°C in this case). During that time, some metal corrosion occurs which increases the initial concentration slightly. This also explains the initial "negative" removal rates in Figure 10(b).

Knowledge of the optimal times is useful for setting the electrowinning time for multiple CEP cycles. From Figure 10(a), at 15A, the net copper removal rate maximum occurs at 90 min. The results for copper removal at 15A over multiple CEP cycles are presented in Figure 11(a). For these data, four P/R steps were used to accumulate the initial Cu^{+2} concentration for electrowinning. After that, each CEP cycle consisted of one SPE and three P/R steps. Overall, the copper ion concentration in the feed water was reduced from 20.1 ppm to 0.23 ppm in the effluent water. The difference between these values is the total amount of copper deposited on the cathodic particles. The copper lost in the process was determined to be on the order of ±1.5%, such that the copper mass balance closes reasonably well.

As the reduction potential decreases, the metal becomes more sensitive to corrosion. In the current context this means that nickel and cadmium electrowinning is more sensitive to corrosion rate than copper. Consequently, nitrogen sparging plays a more important role in reducing dissolved oxygen in the electrolyte solution to reduce the corrosion rate, as discussed in References (*20*, *21*, *23*). The optimal time for nickel electrowinning was determined in the same manner as for copper. The optimal times and maximum net CEP removal rates for nickel were 112 min, 0.006 g min^{-1}, and 120 min, 0.004 g min^{-1} for 20A and 15A, respectively, and 173 min. for cadmium at 20A.

Slightly different than for copper, the nickel and cadmium electrowinning times for multiple CEP cycles are determined by both the optimal time and the final concentration at the end of each electrowinning step. Since an integral number of P/R cycles occur for each CEP cycle, the nickel and cadmium ion concentrations are not sufficiently depleted when shorter time intervals than the optimal time are used. Consequently, the initial ion concentration for the second CEP cycle will be greater than that for the first CEP cycle, etc., and the metal ion concentration would accumulate with each successive CEP cycle. Therefore, a time longer than the optimal time was used as the electrowinning time to maintain the initial metal ion concentration at the same level for the subsequent electrowinning step.

Nickel removal data at 20A over multiple CEP cycles are presented Figure 11(b). Four P/R cycles were employed to accumulate the initial Ni^{+2} concentration for electrowinning. After that, each CEP cycle consisted of one 180 min. SPE step (i.e., greater than the optimal time) and two P/R steps. With this program, no nickel ion accumulation occurs, while the electrodeposition rate remains close to the maximum rate at the optimal time), and three P/R cycles of 8 min. each for another 24 min. This program was effective for nickel removal. It is noted that the optimal time for nickel removal is greater than that for copper, and also that the maximum nickel removal rate is less than that for copper. The lower nickel electrodeposition rate means that less nickel is deposited over the same time interval, or a lower maximum removal rate for nickel. A lower removal rate requires a greater optimal time for the same initial metal concentration of 100 ppm.

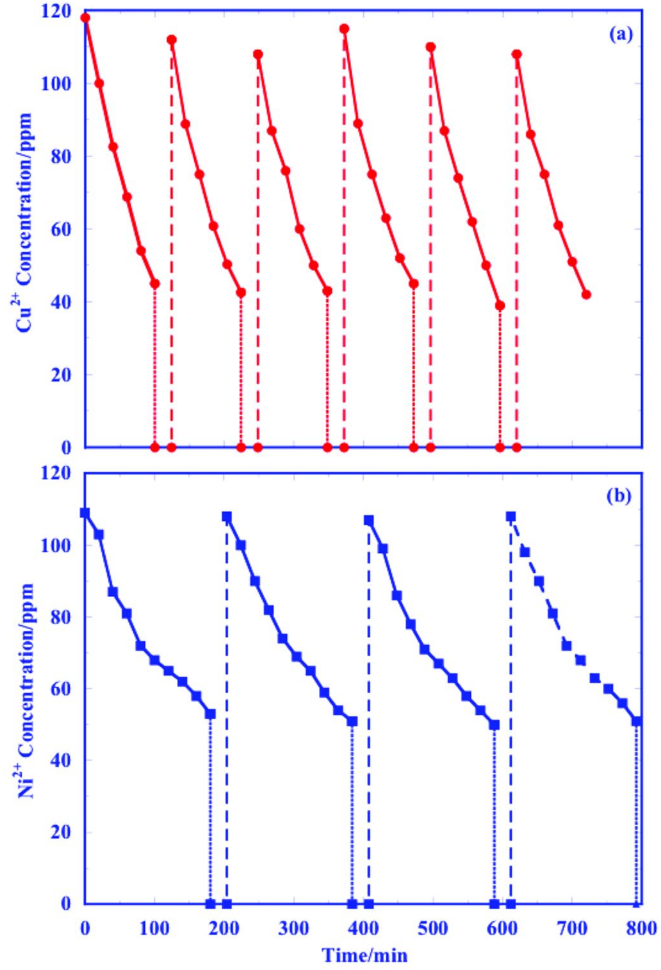

Figure 11. (a) Cu^{+2} concentration over multiple CEP cycles at 15A. (b) Ni^{+2} concentration over multiple CEP cycles at 20A. The solid curves are the electrowinning steps; the fine dashed vertical lines are precipitation; and the coarse dashed vertical lines are redissolution. Adapted with permission from Ref. (22) (Copyright © 2011, Elsevier BV).

The rate of cadmium removal is less than that of nickel. Cadmium electrowinning rates were found to increase with applied current, pH, and temperature. At 20A, pH 4.0, and 50°C, a 100 ppm cadmium solution was accumulated (from a 20 ppm solution) with five P/R cycles. The resultant optimal removal time and maximum rate were 340 min., 0.003 g min^{-1}, respectively. These values represent a greater time and lower maximum rate than were found for copper and nickel under similar conditions.

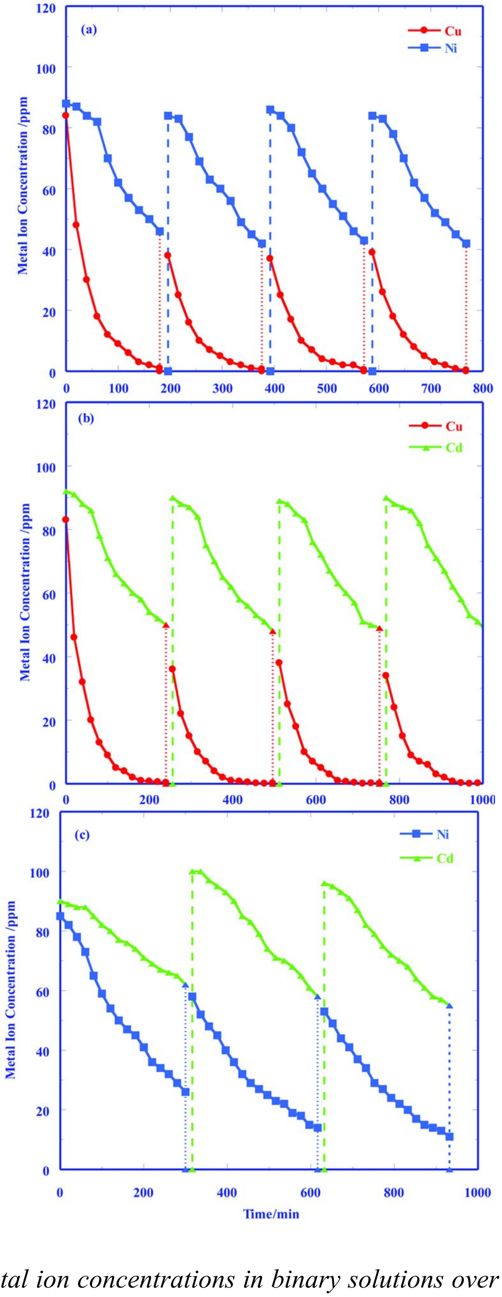

Figure 12. Metal ion concentrations in binary solutions over multiple CEP cycles: (a) Cu^{+2}/Ni^{+2}; (b) Cu^{+2}/Cd^{+2}; (c) Ni^{+2}/Cd^{+2}. Adapted with permission from Ref. (22) (Copyright © 2011, Elsevier BV).

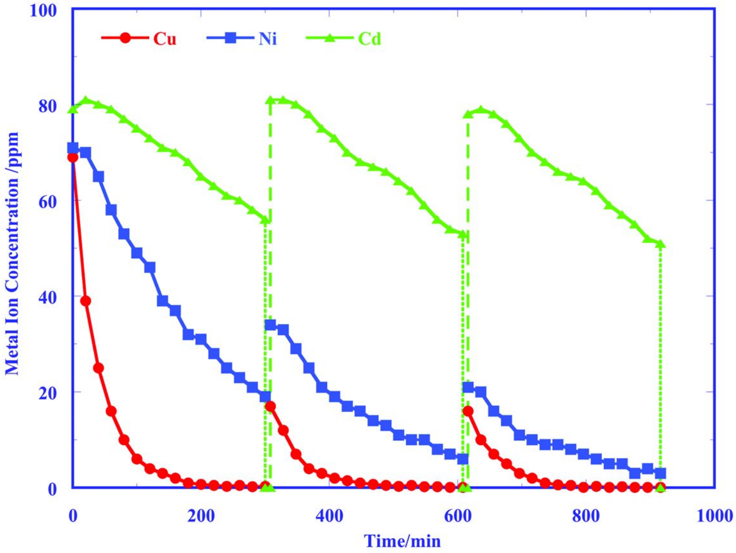

Figure 13. Cu^{+2}, Ni^{+2}, and Cd^{+2} concentrations in a ternary mixture over multiple CEP cycles. Adapted with permission from Ref. (22) (Copyright © 2011, Elsevier BV).

CEP data for three different binary mixtures of the metals over multiple CEP cycles are presented in Figures 12 under similar conditions. Three P/R steps were employed initially. After that, each CEP cycle consisted of one SPE step for the following te values, and two P/R steps: (a) Cu^{+2}/Ni^{+2}, t_e = 180 min.; (b) Cu^{+2}/Cd^{+2}, t_e = 240 min.; (c) Ni^{+2}/Cd^{+2}, t_e = 300 min.

CEP data for co-removal of a ternary Cu^{2+}/Ni^{+2}/Cd^{+2} mixture over multiple CEP cycles are presented in Figure 13. Three P/R steps were employed to accumulate the initial ion concentrations for electrowinning. After that, each CEP cycle consisted of one 300 min SPE step and one P/R step. The P/R pH values were 11.0 and 4.0, respectively, and electrowinning was conducted at 20A, 50°C, pH 4, with 3.5 SLM nitrogen sparging. The solid curves are the electrowinning steps; the fine dashed vertical lines are precipitation; and the coarse dashed vertical lines are redissolution. As shown, all the metal mixture co-removal data over multiple cycles exhibit a characteristic flattened curve at the inception of each electrodeposition step for the last metal to be removed. This characteristic is attributable to the metal displacement reactions. In Figure 14(a,b) are presented Cu^{+2}/Ni^{+2}/Cd^{+2} co-removal data at 20A, pH 4.0, 50°C. For these data, the initial solution concentration of about 100 ppm of each metal was prepared directly from the reagents, and not *via* a series of P/R steps, as previously. This was done simply for convenience due to the limited capacity of the P/R tank. As shown in Figure 14(a), the copper electrowinning rate is the greatest, while that of cadmium is the lowest, and that for nickel is intermediate between the two. In Figure 14(b) are presented the corresponding removal rates, R, of Cu^{+2}, Ni^{+2}, and Cd^{+2} determined from the data in Figure 14(a). The resultant corresponding optimal times and maximum removal rates are 65, 91, and 280 min., and 0.017, 0.006, and 0.002 g min^{-1}, respectively.

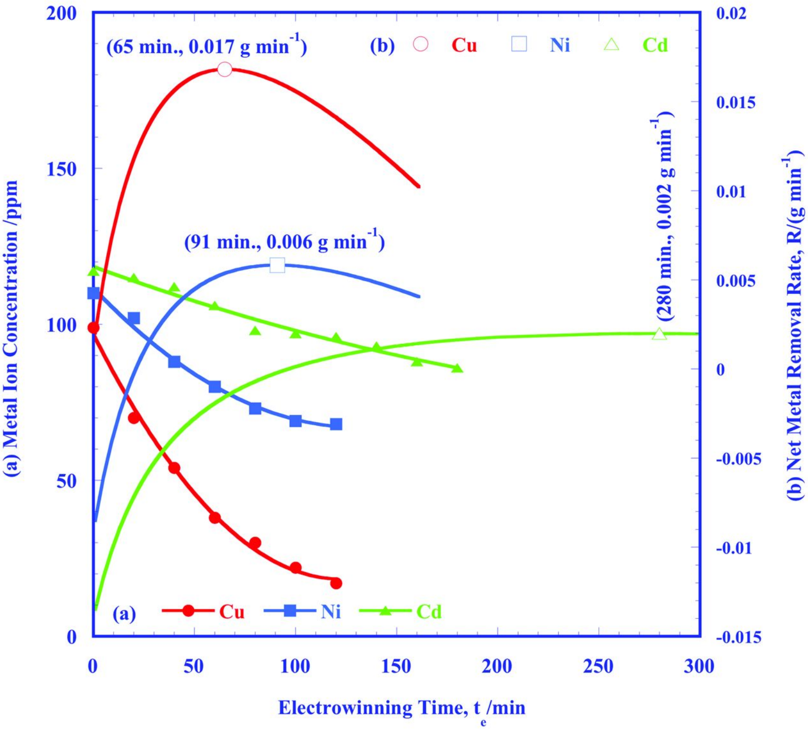

Figure 14. (a) Cu^{2+}, Ni^{2+}, and Cd^{2+} electrowinning in the CEP SPE at 50°C, pH 4, The symbols are the experimental data, and the curves are the polynomial fits. (b) Net Cu^{2+}, Ni^{2+}, and Cd^{2+} removal rates, R, calculated with the polynomial fits of the electrowinning data. The values in parentheses are the electrowinning times, t_e, and the corresponding metal ion removal rates at the maxima. Adapted with permission from Ref. (22) (Copyright © 2011, Elsevier BV).

Although not specifically shown here, it is noted that for the ternary mixture, the copper and nickel removal rates are greater, and the cadmium removal rates are less in comparison to their single metal behavior. This is also reflected in the optimal times that decrease for copper and nickel, and increases for cadmium. This behavior is due to the displacement reactions between copper ion and nickel and cadmium metal on the cathodic particles in a similar fashion as was found for Cu^{+2}/Ni^{+2} mixtures (*23*). In the ternary mixture, Cu^{+2} can be spontaneously reduced by both nickel and cadmium metal previously deposited on the surface of the cathodic particles, due to the positive standard potentials for the displacement reactions (Eqns. (7,19)). This enhances the net copper reduction rate, and decreases the optimal time. In a similar fashion, the nickel removal rate is enhanced by the cadmium displacement reaction, Eq. (20). However, since the standard potential difference between nickel ion and metal cadmium is less than that between copper ion and nickel, and copper ion and cadmium, its removal rate is enhanced somewhat less than that for copper. It is also noted that the displacement reactions all act in the same sense to increase the effective cadmium "corrosion" rate, such that its net removal rate decreases and its optimal time increases, in comparison to its single metal behavior.

The effects of the metal displacement reactions are also evident in modifying the initial electrowinning concentrations of the three metal ions. Even though the initial concentration of each metal ion was about 100 ppm, it is noted in Figure 14(a) that by the time the SPE was heated to the 50°C operating temperature and electrowinning was initiated, the metal ion concentrations had changed to 99, 110, 117 ppm for Cu^{+2}, Ni^{+2}, and Cd^{+2}, respectively. This is due to the action of the metal displacement and corrosion reactions over this period. That is, a small amount of copper was net removed, while both the nickel and cadmium ion concentrations increased due to corrosion.

The time interval selected for multiple co-deposition cycles for the $Cu^{+2}/Ni^{+2}/Cd^{+2}$ mixtures was greater than the optimal times of each of the single metals. Similar to the behavior of multiple CEP cycles with the binary mixtures, both the criteria of avoiding metal ion accumulation with subsequent cycles and maintenance of high electrowinning rates, were used to determine the optimal electrowinning time interval. That is, if a time shorter than the optimum for Cd^{+2} (but longer than those for Cu^{+2} and Ni^{+2}) is used, the concentration of Cd^{+2} (the last metal ion removed in the mixture), will increase with each subsequent electrowinning step, which is counter to the general overall desired effect. Consequently, the time interval for the electrowinning cycle was increased to sufficiently deplete cadmium to maintain decreasing cadmium concentrations with each successive electrowinning cycle. Of course, a number of other program strategies could also be employed as well. For example, the electrowinning time could be programmed so that it starts out as near optimal for Cu^{+2}, which allows Ni^{+2} and Cd^{+2} to accumulate with each cycle, while preferentially removing copper, and then operate on the resultant Ni^{+2} and Cd^{+2} - concentrated solution with an electrowinning time between the optimal values for Ni^{+2} and Cd^{2+2} to preferentially remove Ni^{+2} while accumulating Cd^{+2}, and then finally run at an optimal time for Cd^{+2} removal on the residual, etc., as well as other permutations thereof. The metal displacement reactions serve to "spread out" the removal of the different metals in time. This characteristic, coupled with the types of programs described above, can be used to allow the preferential accumulation of each metal on a different set of particles which, since they are entrained, can be removed and introduced hydrodynamically at appropriate times in the program, so that metal separation and recovery can also be achieved in a continuous fashion.

In order to further explore this possibility, experiments were conducted to separate metals from dilute aqueous solutions by concentrating each metal on a different cathodic particle set. Since the current SPE is not set up to automatically introduce and remove particles hydrodynamically, this was done manually. Some representative results are presented in Figures 15 and 16, in which the gray, vertical, double-arrow lines indicate where electrowinning was stopped and the particle sets changed. Conditions for these experiments were as follows:

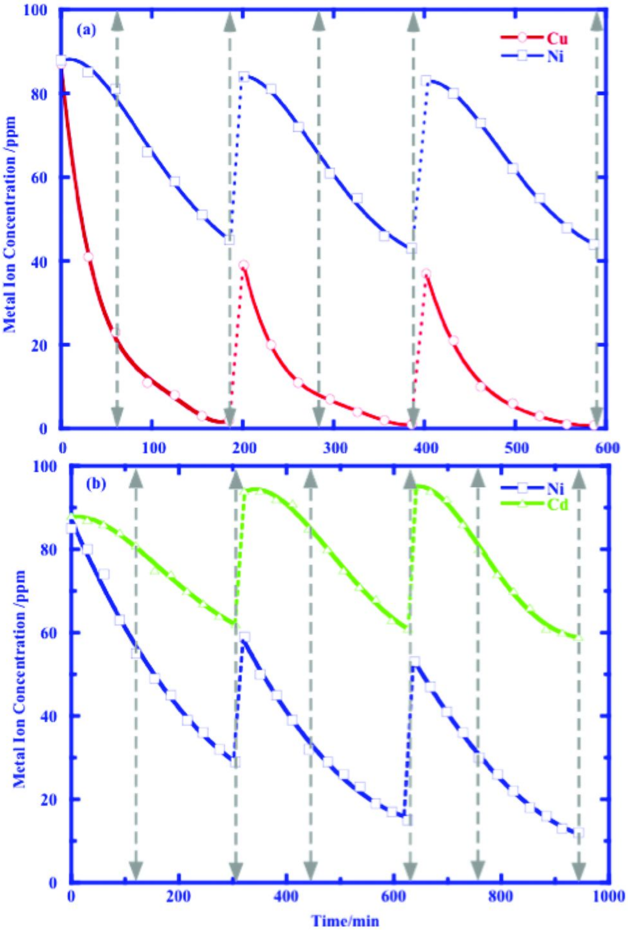

Figure 15. Metal ion concentrations during the separation of two metals on two different cathodic particle sets: (a) Cu+2/Ni+2; (b) Ni^{+2}/Cd^{+2}.

Figure 15(a) - Copper and nickel were recovered over multiple CEP cycles on two different cathodic particle sets. Five precipitation/dissolution cycles were used to accumulate the initial electrowinning metal cation concentrations to *ca.* 87 ppm from 20 ppm each. After that, each CEP cycle consisted of one 185 min. SPE electrowinning and two precipitation/redissolution steps (dashed lines) SPE electrowinning employed two different copper and nickel particle sets changed at 60 and 120 min., respectively, after the start of the step (gray, vertical double-ended arrow, dashed lines).

Figure 15(b) - Nickel and cadmium were recovered over multiple CEP cycles on two different cathodic particle sets. Five precipitation/dissolution cycles were used to accumulate the initial electrowinning metal cation concentrations to *ca.* 88 ppm from 20 ppm each. After that, each CEP cycle consisted of one 310 min. SPE electrowinning and two precipitation/redissolution steps (dashed lines). SPE electrowinning employed two different nickel and cadmium particle sets changed at 120 and 180 min., respectively, after the start of the step (gray, vertical double-ended arrow, dashed lines).

Figure 16 - Copper, nickel and cadmium were recovered over multiple CEP cycles on three different cathodic particle sets. Three precipitation/dissolution cycles were used to accumulate the initial electrowinning metal cation concentrations to *ca.* 71 ppm from 20 ppm each. After that, each CEP cycle consisted of one 310 min. SPE electrowinning and one precipitation/redissolution step (dashed lines). SPE electrowinning employed copper, nickel and cadmium particle sets changed at 60, 90, and 150 min., respectively, after the start of the step (gray, vertical double-ended arrow, dashed lines).

Each different cathodic particle set consisted of 200 cm^3 of the 2.0 mm diameter plastic spheres, metallized with a layer of copper (Bead House LLC, CMC02.0/CP). In all three cases, the particle set replacement time was 5 min. The precipitation/redissolution pH values were 11.0 and 4.0, respectively, and electrowinning was conducted at 20A, 50°C, pH 4, with 3.5 SLM nitrogen sparging of the solution. Images of some sample beads from the three different particle sets are shown in Figure 17.

In order to prove that metal separation was achieved, the three cathodic particle sets produced in the ternary metal experiment (i.e., Figures 16 and 17) were subjected to acid leaching in 200 ml sulfuric acid at pH 1 for 10 min. The resultant metal concentrations in the leaching solutions, determined by ICP, are presented in Table 4. The data confirm that each of the three particle sets concentrated its target metal.

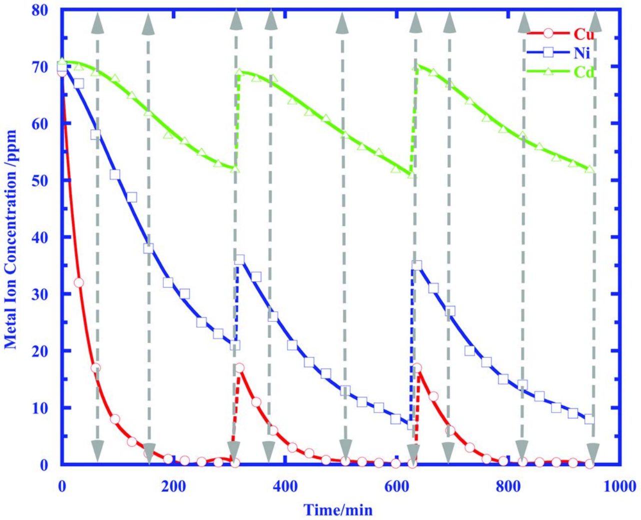

Figure 16. Metal ion concentrations during the separation of Cu^{+2}/Ni^{+2}/Cd^{+2} on three different cathodic particle sets.

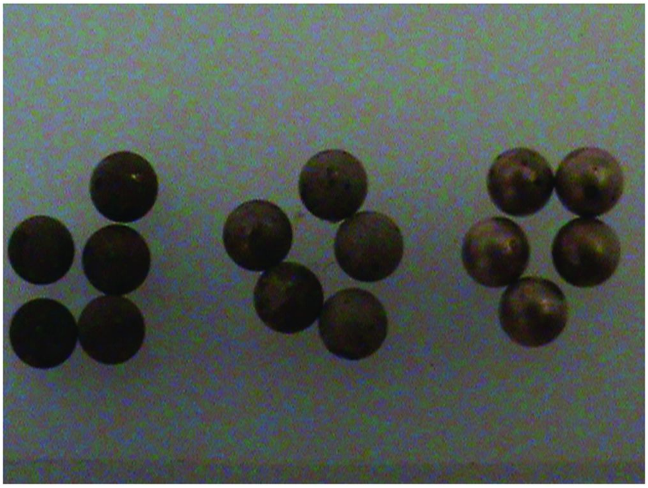

Figure 17. Sample particles from each of the three different particle sets used to separate three metals from solution with the CEP system. From left to right: copper, nickel, and cadmium particle sets following sequential Cu/Ni/Cd removal.

Table 4. Metal Ion Concentrations in Leaching Solutions from Three Different Cathodic Particle Sets

Particle Set	*Cu^{+2} (ppm)*	*Ni^{+2} (ppm)*	*Cd^{+2} (ppm)*
Copper	78.6	4.3	0.3
Nickel	21.1	40.9	3.6
Cadmium	1.3	10.1	46.8

CEP System Performance with Filtrate from Contaminated Soil Leachate

Most recently, the CEP System has been applied to heavy metal removal from leachates obtained from contaminated soils. Specifically, soil samples were obtained from the bank of the Seekonk River at Pitman St. in Providence, RI at an old municipal discharge point. Samples were taken at a few points located about 25 ft. from the stone wall lining the riverbank at low tide on 10/21/2011. The soil samples were treated with 1M sulfuric acid and 1M nitric acid for three days. They were then filtered, and the heavy metal content of the acidic filtrate solution was determined by ICP. It was found that these samples had relatively high heavy metal content, especially copper.

The filtrate also contained high concentrations of Fe^{2+} that oxidizes to Fe^{3+} at the SPE anode, and precipitates as $Fe_2(SO_4)_3$. Consequently, steps were taken to remove Fe^{2+} prior to CEP treatment. The pH of the filtrate was adjusted to 8, and hydrogen peroxide (Acros Organics, 35 wt.% solution in water, stabilized) was used to oxidize Fe^{2+} to Fe^{3+}. At this higher pH, Fe_3O_4 is the preferential reaction product (*61*). After complete oxidation, the solution pH was adjusted to 4.5, 400g of sodium sulfate were added, and the solution was then filtered. 400g of boric acid were added to this filtrate. This final solution was run in the CEP system. The resultant performance for copper removal is presented in Figure 18 over three electrodeposition cycles, showing almost complete removal/recovery of copper from the solution.

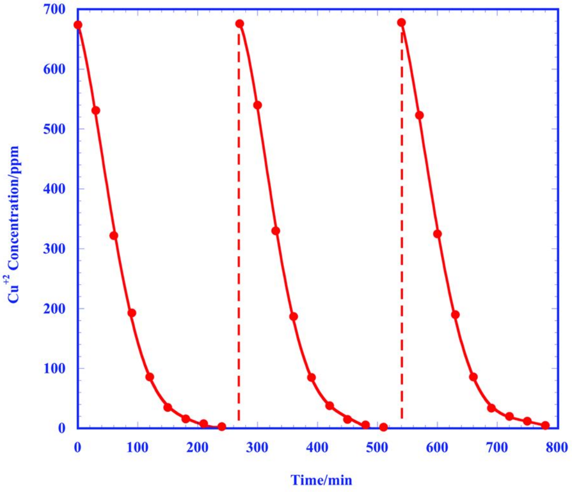

Figure 18. Cu^{+2} concentration in leachate filtrate solution from Pitman St. soil samples over multiple CEP cycles at 20A. Each CEP cycle consisted of one 240 min. SPE electrowinning step and one 30 min. precipitation/redissolution cycle (50°C; pH 4.5; 3500 cm^3 min^{-1} nitrogen sparging).

Conclusions

The work presented here has demonstrated the effective co-removal of the heavy metals copper, nickel, and cadmium from low concentrations in aqueous solutions *via Cyclic Electrowinning/Precipitation (CEP)*. This approach produces very large volume reductions from the original contaminated water (e.g., on the order of 10^6 for an initial metal ion concentration of 10 ppm) by electrochemical reduction of the ions to zero-valent metal on the surfaces of hydrodynamically-circulated cathodic particles. Although, the CEP approach is certainly not expected to be universally applicable to all heavy metals, there are a number of other heavy metals than the ones specifically investigated here that are also expected to be amenable to removal in an analogous fashion. In addition, the separation of the three metals onto different sets of cathodic particles, as well as recovery from leachate solutions obtained from contaminated soils were also demonstrated.

Acknowledgments

This work was supported by grant #5 P42 ES013660 from the National Institute of Environmental Health Sciences (NIEHS), NIH. The authors wish to thank Mr. A. Tente from the Chemistry Department for development and wiring of the CEP electrical systems, and Dr. I. Külaots for assistance with the development of the hardware and the LabView™ control program. The analytical assistance provided by Dr. D. Murray and Mr. J.R. Orchardo of the Geological Sciences Department is also gratefully acknowledged.

Appendix: CEP System Sequence of Operations

The *precipitation/redissolution process cycle* was conducted in the following manner (with reference to Figure 1):

(a) Valve 1 is opened and Pump 1 is activated, with all the other valves closed. Contaminated solution is pumped into the precipitation tank. Valve 1 is closed and Pump 1 is stopped automatically when the solution reaches a preset amount as indicated by a level sensor.
(b) Valve 3 is opened to charge base solution into the precipitation tank, and the mixer is activated. Valve 3 closes automatically when the pH reaches a preset level of 11 in the present work, and flocculant is added. Approximately 3 min. are required to allow the metal hydroxide precipitate to settle to the bottom of the tank.
(c) Valve 2 is opened and Pump 2 is activated, with all the other valves closed. The clean supernatant solution is pumped out of the precipitation tank. Pump 2 is stopped and Valve 2 is closed.
(d) Valve 4 is opened to add the acid solution to pH 4, and the mixer is activated. Valve 4 closes automatically when the solution pH attains the preset value. Approximately 4 min. are required to ensure that all the metal precipitate is redissolved.

The *electrowinning process cycle* was conducted in the following manner:

(a) Na_2SO_4 and H_3BO_3 are added to the solution in order to increase its conductivity and suppress hydrogen evolution during electrowinning.
(b) Valve 4 is opened to add the acid solution, and then closed automatically when the solution pH attains the preset value.
(c) Valves 5 and 6 are opened and Pump 3 is activated, with all other valves closed. The accumulated solution is pumped into the SPE.
(d) With Valve 6 open and Pump 3 running, Valve 5 is closed, and Valve 7 is opened. The solution then circulates continuously within the SPE. The SPE heater/cooler are turned on to achieve the desired preset temperature.
(e) The power is turned on and set to the selected current to begin electrowinning.

(f) After the electrowinning cycle is complete, Valve 6 is closed, and Valve 5 is opened, keeping Valve 7 open. The solution is drained into the precipitation tank. Valves 5 and 7 are then closed, and Pump 3 is stopped.

Each of the two types of cycles can be repeated as many times as required to achieve the desired metal removal results.

References

1. Sheikholeslami, R.; Bright, J. *Desalination* **2002**, *143* (3), 255–267.
2. White, C.; Sayer, J. A.; Gadd, G. M. *FEMS Microbiol. Rev.* **1997**, *20*, 503–51620.
3. Kaksonen, A. H.; Riekkola-Vanhanen, M. L.; Puhakka, J. A. *Water Res.* **2003**, *37*, 255–266.
4. Machemer, S. D.; Wildeman, T. R. *J. Contam. Hydrol.* **1992**, *9* (1−2), 115–131.
5. Machemer, S. D.; Reynolds, J. S.; Laudon, L. S.; Wildeman, T. R. *Appl. Geochem.* **1993**, *8* (6), 587–603.
6. Kim, B. R.; Gaines, W. A.; Szafranski, M. J.; Bernath, E. F.; Miles, A. M. *J. Environ. Eng. Div. (Am. Soc. Civ. Eng.)* **2002**, *128* (7), 612–623.
7. Shinohara, R.; Katoh, N. *Kogaku Kogaku Ronbunshu* **2005**, *31* (3), 217–221.
8. McIntryre, G. T.; Rodriguez, J. J.; Thackston, E. L.; Wilson, D. J. *Sep. Sci. Technol.* **1982**, *17* (5), 683–693.
9. Ilias, S; Schimmel, K. A.; Yezek, P. M. *Sep. Sci. Technol.* **1999**, *34* (6,7), 1007–1019.
10. Simonsson, D. *J. Appl. Electrochem.* **1984**, *14* (5), 595–604.
11. Chu, A. K. P.; Fleischmann, M.; Hills, G. J. *J. Appl. Electrochem.* **1974**, *4* (4), 323–330.
12. Houghton, R. W.; Kuhn, A. T. *J. Appl. Electrochem.* **1974**, *4* (3), 173–190.
13. Ferreira, B. K. *Miner. Process. Extr. Metall. Rev.* **2008**, *29*, 330–371.
14. Sequeira, C. A. C; Marques, F. D. S. In *Electrochemical Engineering: I. Chem. E.*; Symposium Series No. 112; Hemisphere Pub. Corp.: New York, 1989; pp 297−306.
15. Backhurst, J. R.; Goodridge, F.; Coulson, J. M.; Plimley, R. E. *J. Electrochem. Soc.* **1969**, *116*, 1600–1607.
16. Germain, S.; Goodridge, F. *Electrochim. Acta* **1976**, *21* (8), 545–550.
17. Fleischmann, M.; Oldfield, J. W.; Tennakoon, L. *J. Appl. Electrochem.* **1971**, *1* (2), 103–112.
18. Coeuret, F. *J. Appl. Electrochem.* **1980**, *10*, 687–696.
19. Hadzismajlovic, Dz. E.; Popov, K. I.; Pavlovic, M. G. *Powder Technol.* **1996**, *86* (2), 145–148.
20. Shirvanian, P. A.; Calo, J. M. *J. Appl. Electrochem.* **2005**, *35* (1), 101–111.
21. Grimshaw, P.; Calo, J. M.; Shirvanian, P. A.; Hradil, G. *Ind. Eng. Chem. Res.* **2011**, *50* (16), 9525–9531.
22. Grimshaw, P.; Calo, J. M.; Hradil, G. *Chem. Eng. J.* **2011**, *175*, 103–109.

23. Grimshaw, P.; Calo, J. M.; Hradil, G. *Ind. Eng. Chem. Res.* **2011**, *50* (16), 9532–9538.
24. Kelly, J. J.; Goods, S. H.; Talin, A. A.; Hachman, J. T. *J. Electrochem. Soc.* **2006**, *153*, C318–324.
25. Landolt, D. *Electrochim. Acta* **1994**, *39* (8−9), 1075–1099.
26. Chassaing, E.; Vu Quang, K. *J. Appl. Electrochem.* **1987**, *17* (6), 1267–1280.
27. Glibin, V. P.; Kuznetsov, B. V.; Vorobyova, T. N. *J. Alloys Compd.* **2005**, *386*, 139–143.
28. Shibahara, T; Asano, T.; Sakane, G. *Polyhedron* **1991**, *10* (19), 2351–2352.
29. Bradley, P. E.; Landolt, D. *Electrochim. Acta* **1997**, *42* (6), 993–1003.
30. Bradley, P. E.; Roy, S.; Landolt, D. *J. Chem. Soc., Faraday Trans.* **1996**, *92*, 4015–4019.
31. Scharfe, R. R.; Sastri, V. S.; Chakrabarti, C. L. *Can. J. Chem.* **1972**, *50*, 3384–3386.
32. Bories, C.; Bonino, J.-P.; Rousset, A. *J. Appl. Electrochem.* **1999**, *29* (9), 1045–1051.
33. Vorobyova, T. N.; Bobrovskaya, V. P.; Sviridov, V. V. *Met. Finish.* **1997**, *95* (11), 14–20.
34. Roy, S. *Surf. Coat. Technol.* **1998**, *105* (3), 202–205.
35. Meuleman, W. R. A.; Roy, S.; Péter, L.; Varga, I. *J. Electrochem. Soc.* **2002**, *149* (10), C479–C486.
36. Scott, K. *J. Chem. Technol. Biotechnol.* **1992**, *54*, 257–266.
37. Walker, A. T. S.; Wragg, A. A. *Electrochim. Acta* **1977**, *22* (10), 1129–1134.
38. Rieger, P. H. *Electrochemistry*; Prentice-Hall: Englewood Cliffs, NJ, 1987.
39. Pickett, D. J. *Electrochemical Reactor Design*, 2nd ed.; Elsevier, Amsterdam, 1979.
40. Ives, D. J. G.; Rawson, A. E. *J. Electrochem. Soc.* **1962**, *109* (6), 452–457.
41. Cifuentes, L.; Simpson *J. Chem. Eng. Sci.* **2005**, *60*, 4915–4923.
42. Mohanty, U. S.; Tripathy, B. C.; Singh, P.; Das, S. C. *J. Electroanal. Chem.* **2004**, *566*, 47–52.
43. Son, S. H.; Chung, D. W.; Kwon, D. C.; Lee, H. K. *Adv. Mat. Res.* **2008**, *47−50*, 754–757.
44. Conway, B. E. *Electrochemical Data*; Elsevier: Amsterdam, 1952.
45. Nakamura, J. *Applied Numerical Methods with Software*; Prentice Hall: Upper Saddle River, NJ, 1991.
46. Massé, N.; Piron, D. L. *J. Electrochem. Soc.* **1993**, *140* (10), 2818–2824.
47. Ritchie, I. M.; Roberston, S. G. *J. Appl. Electrochem.* **1999**, *27* (1), 59–63.
48. Timur, S.; Cetinkaya, O.; Ertürk, S.; Orhan, G. *Miner. Metall. Process.* **2005**, *22* (4), 205–210.
49. Fricoteaux, P.; Douglade, J. *Surf. Coat. Technol.* **2004**, *184* (1), 63–68.
50. Pourbaix, M. *Atlas des Equilibres Electrochirniques it 25°C*; Gauthiers-Villars & Cie: Paris, 1963.
51. Stankovic, V. D.; Wragg, A. A. *J. Appl. Electrochem.* **1995**, *25* (6), 565–573.
52. Piontelli, R.; Poli, G. *Z. Physik. Chem.* **1942**, *A190*, 317–330.
53. Berge, H.; Drescher, A.; Jeroschewski, P. *Fresenius' Z. Anal. Chem.* **1969**, *248* (1,2), 1–6.

54. Patnaik, P. *Handbook of Inorganic Chemicals*, 1st ed.; McGraw-Hill: New York, 2002; p 267.
55. Patnaik, P. *Handbook of Inorganic Chemicals*, 1st ed.; McGraw-Hill: New York, 2002; p 617.
56. Rai, D.; Felmy, A. R.; Szelmeczka, R. W. *J. Solution Chem.* **1991**, *20* (4), 375–390.
57. Ploss, H.; Lehne, J. Process of Producing Copper (II) Hydroxide. U.S. Patent 4,614,640, 1986.
58. Subbaiah, T.; Mohapatra, R.; Mallick, S.; Misra, K. G.; Singh, P.; Das, R. P. *Hydrometallurgy* **2003**, *68* (1-3), 151–157.
59. Feitknecht, W.; Studer, H. *Kolloid-Z.* **1949**, *115*, 13–16.
60. National Primary Drinking Water Regulations; EPA 816-F-09-0004; U.S. Environmental Protection Agency: Washington, DC, May 2009.
61. Mongan, B.; Lahav, O. *Chemosphere* **2007**, *68*, 2080–2084.

Chapter 10

Macronutrient Removal and Recovery from Tertiary Treatment of Wastewater

Sukalyan Sengupta*

**Department of Civil and Environmental Engineering,
University of Massachusetts, Dartmouth, 285 Old Westport Road,
North Dartmouth, Massachusetts 02747
*E-mail: ssengupta@umassd.edu**

Removal of two macronutrients, nitrogen (N) and phosphorus (P), from wastewater is critical before discharging the treated effluent to prevent eutrophication. But N and P are also essential components of any fertilizer; thus their recovery from wastewater will be an added bonus. This is especially critical for P since it is a non-renewable resource and its supply potential is getting diminished. For any process to have the ability to recover N and P from wastewater, it should be able to selectively remove the target ion containing N (NH_4^+-N in this case) from a background of competing cations that may be present at a higher concentration (primarily Na^+ and Ca^{2+}) and the target ion containing P ($H_2PO_4^-$ or HPO_4^{2-}) which faces strong competition from competing anions such as Cl^- and SO_4^{2-}. Moreover, selective removal of NH_4^+-N and P are not enough; the process should be efficiently able to desorb N and P to produce a small-volume, high concentration, regenerating solution. And finally, a solid-phase fertilizer of high purity should be extractable from the regenerating solution. On top of this, if the remaining regenerant solution can be reused in the next cycle, this process would be highly sustainable. Details of a process are provided where an inorganic zeolite (clinoptilolite) and a polymeric anion exchanger impregnated with iron oxide nanoparticles and preloaded with Cu as a selective ligand for phosphate are used to achieve selective N and P removal. The exchangers are efficiently regenerated with a combination of NaCl and NaOH and a solid-phase, high-purity fertilizer as

In Novel Solutions to Water Pollution; Ahuja, S., et al.;
ACS Symposium Series; American Chemical Society: Washington, DC, 2013.

$MgNH_4PO_4$ (struvite) is extracted. Three hybrid polymers were studied for P removal and recovery: HAIX, DOW-HFO, and DOW-HFO-Cu. Each material combines the durability, robustness, and ease-of-use of a polymeric ion-exchanger with the high sorption affinity of Hydrated Ferric Oxide (HFO) towards P. DOW-HFO-Cu was found to be the most efficient exchanger for removal of P. This was because both the HFO and the Cu, selective ligands for Cu sorption, acted in combination, thus providing maximum overall selectivity. The regenerating solution can be reused in the next cycle, thus creating a sustainable process with minimal waste effluent.

Keywords: clinoptilolite; orthophosphate; ligand; hydrated iron oxide; nanoparticle

Introduction

Eutrophication or the over-enrichment of global water bodies has grown from a rising concern to a major water quality impairment parameter over the past few decades. This phenomenon is mainly attributable to the influx of nitrogen (N) and phosphorus (P) into the water bodies from a variety of sources ranging from detergents to fertilizers to atmospheric deposition. Eutrophication is a key driver in a number of environmental problems including reduced light penetration resulting in seagrass mortality, increases in harmful algal blooms and hypoxic and anoxic conditions. It is generally agreed (*1–4*) that N is the rate-limiting nutrient in coastal ecosystems while P plays the same role in freshwater ecosystems. Lake water concentrations of phosphorus above 0.02 ppm generally accelerate eutrophication (*5*).

Coastal surveys of the United States and Europe found that a staggering 78 percent of the assessed continental U.S. coastal area and approximately 65 percent of Europe's Atlantic coast exhibit symptoms of eutrophication (*6*, *7*). In other regions of the word, the lack of reliable data hinders the assessment of coastal eutrophication. It can be safely concluded that due to the rising population, trends in agricultural practices, and the increasing energy usage, eutrophication will be an ever-growing problem. Control of point-sources of N and P has been a major focus of environmental regulatory agencies, and has resulted in stricter regulations for wastewater treatment. This communication will be restricted to reducing N and P concentration in effluent from waste water treatment plants (WWTPs). In many cases of discharge of WWTP effluent to "impaired waterways", limits of 3 mg/L as Total Nitrogen (TN) and 0.2 mg/L of Total Phosphorus (TP) are common (*8*).

Nitrogen in wastewater has an oxidation number of -3 and is approximately 60-70% ammonia-nitrogen and 30-40% organic nitrogen (*9*, *10*). Most of the ammonia-nitrogen is derived from urea, which breaks down rapidly to ammonia in wastewater influent (*8*). Secondary biological treatment processes (such as activated sludge, rotating biological contactor, trickling filter, etc.) in the waste water treatment plant convert ammonia and organic-N to nitrate (NO_3^-) through the process of nitrification. NO_3^- - is a highly mobile and persistent ion and almost all the N transported to bays and estuaries is in this form. Therefore, the issue of N control is essentially about controlling and containing the nitrification process and then converting the NO_3^-- to an innocuous form. However, once N is in the form of NO_3^-, it cannot be beneficially recovered. The focus of this research is not only to discuss technologies that can achieve stringent N discharge limits but also to present evidence of ability to recover the N present in the wastewater as a commercial-grade solid-phase fertilizer. For this reason the N has to be present in the trinegative form, as ammonia-N or organic-N. Organic-N is easily hydrolyzed to ammonia-N in the sewer system; therefore by the time the wastewater enters the primary treatment process in a WWTP all the N is in the form of ammonia-N (*9*). In this research N is removed from the wastewater by contacting the NH_4^+-rich wastewater with clinoptilolite, a natural zeolite that has high selectivity for NH_4^+ over competing cations in the wastewater such as Na^+ and Ca^{2+}. The selectivity of the material for the target cation (NH_4^+) is critical to the success of the process; this is explained in detail in a subsequent section.

Primary source of phosphorous in the environment is anthropogenic, present as both point sources (synthetic detergent in domestic wastewater) and non-point sources (agricultural run-off). About 95% of the phosphorus in municipal wastewater treatment plants (WWTPs) is as orthophosphate species (*11*). In response to the concern over eutrophication, its discharge by wastewater treatment facility is being increasingly limited. Consequently, tertiary treatment methods utilizing physicochemical and biological treatment methods have abounded to comply with the requirements. However, these methods suffer from the drawbacks of excessive sludge production, high operating costs and inability to attain complete nutrient removal due to thermodynamic and kinetic limitations. In addition, it might also be noted that if the current trend of phosphate rock mining is continued the stock is predicted to dwindle in next fifty years (*12*), which necessitates the recovery of phosphorus from the wastewater. Thus, what is needed is a process that can not only remove P from wastewater but also recover it as fertilizer. This research presents evidence of a technology that can achieve this goal. When combined with removal and recovery of N, this research shows how eutrophication can be prevented when wastewater is discharged to a receiving water body and at the same time a high-purity solid-phase fertilizer containing N and P can be generated. But for the process to be successful, selectivity of the target ion ($NH4^+$ over competing cations such as Ca^{2+}, Mg^{2+}, Na^+, and in $H_2PO_4^-/HPO_4^{2-}$ over competing anions such as Cl^-, SO_4^{2-}, HCO_3^-) is critical. The principles of a selective phosphate exchanger are presented below.

Anion Exchanger Development

With the constraints of the biological and chemical phosphorus removal processes and the complexity involved in recovery of phosphorus from the sludge produced in the processes, physical-chemical adsorption, or sorption as it is referred to in literature, can be a viable solution to the challenge faced by the global wastewater industry. Many natural and engineered sorbent media have been investigated in recent years; Granular activated alumina, zirconium oxide and iron oxide being a few well-studied inorganic sorbents in this regard (*13–17*). However, these metal oxide particles lack the mechanical strength and abrasion resistance properties for prolonged operation in fixed bed units and consequently form fines leading to increased head loss in the system (*18*). The metal oxides referred to above are also not amenable to efficient regeneration and are hence recommended for single-use applications (*16*).

While polymeric materials offer the requisite durability and mechanical strength, they lack the specific phosphate selectivity in the presence of competing sulfate ions ubiquitously present in both point and non-point sources of phosphorus. Earlier endeavors in this area include the REM NUT® process (*19*), and the development of a copper loaded polymeric ligand exchanger (PLE) (*20–22*). In spite of their advantages and promising pilot-scale applications they never reached full scale application due to techno-economic inefficiencies (*23*).

It has been well demonstrated through research in recent past that the oxides of polyvalent metals, namely, Fe(III), Ti(IV) and Zr(IV) exhibit strong ligand sorption properties (Lewis acids) through formation of inner sphere complexes (*24*, *25*). Of them, hydrated iron(III) oxide [FeOOH] or HFO is benign, inexpensive and stable over a wide pH range. Many previous studies confirmed that HFO or α-Goethite has high sorption affinity for phosphates (*13*, *26*, *27*) and their selective sorption is attributed to the ligand exchange in the co-ordination sphere of structural iron atoms.

In view of the economic constraints faced by the earlier PLEs and the preferential sorption affinity for phosphate exhibited by the HFO particles, attempts have been made to disperse or dope HFO nanoparticles within various support medias, like alginate, zeolite, cation exchange resin and activated carbon (*28–32*). A new hybrid anion exchange resin was developed by impregnating HFO nanoparticles within polymeric anion exchanger. It displayed significantly-increased sorption capacity (*18*, *33*), and is commercially available as ArsenX^{np} or LayneRT™.

Cation Exchanger (Clinoptilolite)

Clinoptilolite is a natural zeolite whose typical chemical formula is $Na_6[(AlO_2)_6(SiO_2)_{30}].24H_2O$ (*34*). It acts as a cation exchanger because often the cations in the zeolite structure compensate for the framework charges arising from substitution reactions, primarily that of substitution of silicon by aluminum. Ion-exchange in clinoptilolite proceeds in an isomorphous fashion. The primary reason clinoptilolite is chosen in this case is because *(a)* it is highly selective towards ammonium (compared to sodium, calcium, and magnesium, the three most commonly found cations in wastewater) during a cation exchange process, and *(b)* it is an abundant zeolite in the US and is fairly inexpensive. Various authors have studied the selectivity of clinoptilolite towards ammonium and based on a compilation of their published results (*34–37*), it may be stated that the selectivity series of cations as regards exchange on clinoptilolite is as follows:

$$NH_4^+ > Pb^{2+} > Na^+ > Ca^{2+} > Mg^{2+} > Li^+ > Cu^{2+} > Zn^{2+} \qquad (1)$$

Methodology

Separation Factor

The wastewater samples described before will have - apart from nutrients - ionic constituents which are innocuous from a regulation or health point-of-view, e.g., cations like Ca^{2+}, Mg^{2+}, Na^{+}, and anions like Cl^{-}, SO_4^{2-}, HCO_3^{-}, etc. These background ions are usually present at much higher concentrations than the ions of interest in this case, NH_4^+ and $H_nPO_4^{n-3}$. Thus, if removal of nitrogen and phosphorus species and their extraction as a fertilizer is the primary aim of a process, it is absolutely necessary that the ion-exchangers chosen for this process sorb the ions of interest preferentially over all the other competitors. Mathematically, the selectivity of an ion-exchanger for a particular ion (**A**) over that of another ion of the same charge (**B**) is given by the parameter "**Separation Factor**" which is denoted as follows:

$$\alpha_{A/B} = \frac{y_A x_B}{y_A x_B} \tag{2}$$

where "**y**" represents the fraction of the ion in the ion-exchanger and "***x***" represents the fraction of the ion in the aqueous phase. Let's look at an example:

Consider removing NH_4^+ from the wastewater. It is very likely that NH_4^+ will be swamped by other cations always present in the wastewater at much higher concentration like Ca^{2+}, Mg^{2+}, Na^+, etc. Therefore, "x_{NH4}" will be a very low fraction since

$$x_{NH_4} = \frac{C_{NH_4}}{C_{NH_4} + C_{Na} + C_{Mg} + C_{Ca}} \tag{3}$$

where "**C**" denotes the equivalent concentration of each species in the solution. If we consider the case of NH_4^+ selectivity with respect to another cation such as Ca^{2+}, it is apparent that "x_{Ca}" > "x_{NH4}" since the concentration of Ca^{2+} in the wastewater is much higher than NH_4^+ . The selectivity expression for NH_4/Ca system will be represented as:

$$\alpha_{NH4/Ca} = \frac{y_{NH4}\ x_{Ca}}{x_{NH4}\ y_{Ca}} \tag{4}$$

The ion-exchanger will be said to be selective towards NH_4^+ over Ca^{2+} if $\alpha_{NH4/Ca} > 1$. This means that "y_{NH4}" ≫ "y_{Ca}" since that is the only condition which will satisfy $\alpha_{NH4/Ca} > 1$. In other words, even though the fraction of NH_4^+ in the aqueous phase is less than that of Ca^{2+}, the fraction of NH_4^+ in the ion-exchanger is much higher than that of Ca^{2+}. This characteristic is absolutely critical to the success of this process. Since the targeted ions in our case are NH_4^+ and $H_nPO_4^{n-3}$, it is imperative that we choose:

- **a)** an ammonium selective cation-exchanger such that **$\alpha_{NH4/Ca} > 1$, $\alpha_{NH4/Mg} > 1$, and $\alpha_{NH4/Na} > 1$**
- **b)** a phosphate selective anion-exchanger such that **$\alpha_{PO4/Cl} > 1$, $\alpha_{PO4/SO4} > 1$, and $\alpha_{PO4/HCO3} > 1$**

Clinoptilolite was obtained from GSA Resources, Inc. Its characteristics are presented in Table I. The virgin material was pretreated with 1N NaCl for 2 hours, followed by a cyclic rinse of 1N HNO_3 and 1N NaOH as reported by Klieve and Semmens (*38*).

Table I. Clinoptilolite Characteristics

Pore Diameter	4.0 Angstroms
Pore Volume	15%
Specific Surface Area	40 m^2/g
Average Particle Diameter	0.4 mm
Bulk Density	760-1283 kg/m^3
Solid Density	100 lb/ft^3 (1603 kg/m^3)

Two combinations of transition metals and/or metal oxides were loaded onto the DOWEX ™ M4195 (referred to as DOW) resin to compare their performance with the ArsenX. Table II shows the properties of each PLE and Figure 1 shows the polymeric backbone onto which HFO nanoparticles are impregnated.

Table II. Properties of Iron Oxide-Impregnated PLEs

Characteristics	*HAIX*	*DOW-HFO*	*DOW-HFO-Cu*
Structure	Macroporous Polystyrene-Divinylbenzene	Macroporous Polystyrene-Divinylbenzene	Macroporous Polystyrene-Divinylbenzene
Appearance	Brown spherical beads	Tan to dark brown opaque beads	Tan to dark brown opaque beads
Functional group	Quaternary ammonium	Bis-picolylamine	Bis-picolylamine
Iron content	75-90 mg as Fe/ g resin	45 - 60 mg as Fe/ g resin	40 - 50 mg as Fe/ g resin
Bulk density	790 - 840 g/L	673 g/L	673 g/L
Particle size	300 - 1200 μm	297 - 841 μm	297 - 841 μm

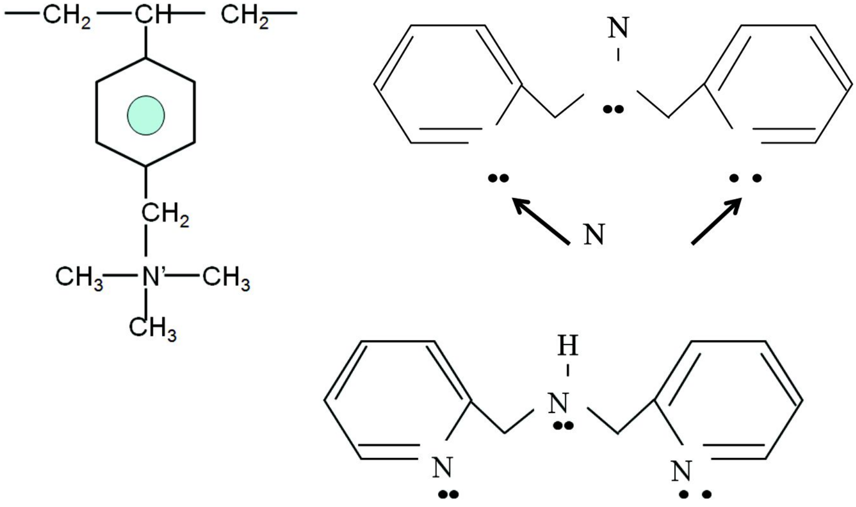

Figure 1. Polymeric Backbone onto which HFO Nanoparticles are Impregnated. Top left: ArsenX; Top Right: DOW-HFO-Cu; Bottom Right: DOW-HFO.

The configurations chosen and the justification of their choice are as follows:

1. Only HFO

Since DOW is a free form resin, it can be presumed that there would be no phosphate removal by ion exchange. The removal would be solely due to the ligand sorption onto HFO. This would give an estimate of relative distribution of the phosphate removal by ligand sorption and ion exchange in ArsenX.

For the impregnation of HFO nanoparticles onto the resin, a weighed mass of the dried virgin resin (10.0 *g*) was added to 1.0L of 1% solution of $FeCl_3.6H_2O$ (2.0 *g*/L as Fe) at pH $\approx$ 2.0 (to ensure that no $Fe(OH)_3$ precipitates out) and was vigorously stirred for 1 hr by a magnetic stirrer at 750 rpm. The pH of the solution was then stepwise increased to around 8 uniformly paced over 3 hours, by drop wise addition of 1.0N sodium hydroxide [NaOH] solution to form the FeOOH precipitate as per the following equation:

$$Fe^{3+} + 3OH^{-} \rightarrow FeOOH_{(s)} + H_2O \tag{5}$$

The mixing speed was reduced to around 200 rpm and was kept for 24 hours to optimize the contact of the resin beads with freshly formed HFO nanoparticles. After 24 hours, the resultant solution was repeatedly rinsed with deionized water to remove excess precipitate. The resin was then oven dried at 45±2 °C for 24 hours and stored in moisture free glass vials. The iron content of HAIX reported in Table II was determined by stirring 2.0 *g* of the dried material in a pH = 2.0 HNO_3 solution of 100 ml volume for 36 hours. 10 ml of the final solution was digested and diluted per Standard Methods (*39*) and the dissolved iron was measured by a spectrophotometer, details of which are provided in the "Analytical Procedures" section. The HFO impregnation range provided in Table II is based on 4 samples. This resin would be referred to as ***DOW-HFO*** this point forward for typographical convenience.

2. Both HFO Nanoparticles and Cu^{2+}

As both HFO and Cu^{2+} have shown high selectivity for PO_4^{3-}, this would allow demonstrating whether they can indeed be loaded in conjunction and if possible what would be the removal capacity.

The DOW resin was loaded with Fe using the protocol applied for DOW-HFO as explained earlier. Next, Cu^{2+} was loaded onto the resin by stirring weighed mass of the resin (10.0 *g*) in 1.0 L of 1% $CuCl_2.5H_2O$ (2.8 *g*/L as Cu) solution at a pH of 5.0 for 24 hours (though experiments indicated that the loading reaches equilibrium within 2-3hours). After 24 hours, the Cu^{2+} loaded resin was filtered out and repeatedly rinsed with distilled water followed by drying in oven at 45±2 °C for 24 hours. Once dry, it was stored in moisture-free glass vials. This resin would henceforth be referred to as ***DOW-HFO-Cu*** for typographical ease. The Fe loading capacity of DOW-HFO-Cu (40-50 mg Fe/*g* resin) is lower than that of DOW-HFO (45-60 mg Fe/*g* resin) but no significant conclusion can be drawn since the number of samples (n = 4 of each) is too small for any statistical significance. Cu-loading capacity of DOW-HFO-Cu was determined by equilibrating 2.0 *g* of it in a 200-ml- 2% (m/m) NH_3 solution. Zhao (*40*) has shown that the stripping solution is strong enough to desorb all the Cu from the exchanger. The Cu concentration of this solution was determined using atomic absorption spectrometry. From mass balance calculations, the Cu content was determined to be 35.0 mg Cu/*g* of dry exchanger. This material is hereafter referred to as DOW-HFO-Cu.

ArsenX^{np}, was obtained courtesy of SolmeteX Inc., Northborough, MA. DOWEX™ M4195 was obtained from Sigma-Aldrich Co. All chemicals used for this study were of analytical grade and were procured from Thermo Fisher Scientific Inc., Sigma-Aldrich or VWR International, LLC. The standards and other chemicals used for the ion-chromatograph (DIONEX ICS 900 Ion-Chromatograph) were purchased from DIONEX Corporation.

Batch Equilibrium Tests

Clinoptilolite

The pretreated clinoptilolite was used in batch tests to determine the NH_4^+ exchange capacity as a function of the aqueous phase equilibrium NH_4^+ concentration. 5.0 *g* (dry) of the Na^+-loaded clinoptilolite was introduced into a 1.0 L glass beaker that contained an aqueous solution containing varying concentration of NH_4^+ (40.0 - 190.0 mg/L as NH_4^+ - N). NO_3^- was chosen as the accompanying anion because of its poor ligand characteristics). All experiments were conducted at a temperature of 22 °C and with stirring accomplished by a magnetic stirrer at 400 rpm. The pH of the system was maintained at a pH of 7.5

by adding drops of 5.0 N HNO_3 when needed. pH of 7.5was chosen to ensure that all the trinegative N was in the form of NH_4^+; the p_{ka} for the NH_4^+ - NH_3 system is 9.3 (Snoeyink and Jenkins, 1980). After 48 hours of stirring, the concentration of NH_4^+ - N was determined, and the amount of NH_4^+ - N uptake by clinoptilolite was determined by mass balance, i.e.,

$$NH_4^+ - N\ loading\ on\ clinoptilolie = \frac{[(Init.aq.NH_4^+ - N) - (Fin.aq.NH_4^+ - N)] * Volume}{dry\ mass\ of\ clinoptilolie}$$

For calculation of separation factor of NH_4^+-Na^+ and Ca^{2+}-NH_4^+ binary systems, 1.0 *g* of a preloaded clinoptilolite was equilibrated in a glass beaker with a known concentration of the competing species in a 200-ml solution, with equilibrium being considered to be attained after 48 hours. The initial and equilibrium solutions were analyzed for binary cation concentrations using Ion Chromatograph (IC). Following this, the clinoptilolite was regenerated in 1.0 N NaCl and diluted regenerant was also analyzed on the IC for mass balance mass studies. For example, for a Na^+-preloaded clinoptilolite, 1.0 *g* of it was contacted in a well-stirred glass beaker with 200-ml of a solution that had a known concentration of NH_4^+ (within a range of 20 – 100 mg/l as NH_4^+-N) for 48 hours. The pH was maintained by adding drops of 5.0 N HNO_3 as needed. The initial and final solutions were analyzed for Na^+ and NH_4^+-N. The clinoptilolite was filtered (0.45 μm) and then regenerated with 50 ml of 1.0 N NaCl. Regeneration was carried out in a well-stirred glass beaker for 2 hours. The regenerant was analyzed for Na^+ and NH_4^+-N to confirm mass balance. For such a data point, the solution-phase fractions of Na^+ and NH_4^+-N were calculated (in milliequivalents/l) and also the solid-phase loading of Na^+ and NH_4^+-N (in milliequivalent/*g*). A binary isotherm was plotted; details of the isotherm profile vis-à-vis ion selectivity are discussed in a subsequent section.

Phosphorus-Selective PLE

Batch equilibrium tests were carried out in batch reactors (1.0 L or 2.0 L glass beakers) by adding 1.0 or 0.5 *g* of the Cl^--loaded resin(s) into 1.0 or 2.0 L of solution at either pH 8.0 or 5.0 containing different initial concentrations of PO_4^{3-} ranging from 5.0 to 75.0 mg as P/L. The pH was monitored constantly and the desired pH was maintained by adding a few drops of 5.0 N HCl or 5.0 N NaOH as needed.

Equilibrium tests were conducted on all resins, HAIX, DOW-HFO and DOW-HFO-Cu. The equilibrium tests were carried out at 22 °C. The reactors were agitated with magnetic stirrer at 400 rpm for 48 hours to ensure proper mixing and attainment of equilibrium. After equilibrium was attained, the resin was filtered out, rinsed with deionized water and was stirred with a small volume (25 mL) of regenerant solution containing 2.5% NaCl and 2.0% NaOH. Solute concentrations (chloride, phosphate or sulfate) in the initial, equilibrium and spent regenerant were analyzed using a DIONEX Ion Chromatograph Unit. Uptake of PO_4^{3-} or other solutes by the sorbents were determined from mass balance calculations.

Fixed-Bed Column Run

The conditioned clinoptilolite was used in a fixed-bed column to study its performance vis-à-vis removal of NH_4^+-N from septic tank effluent. 5.0 *g* of the conditioned clinoptilolite was poured into 100 ml of deionized H_2O and this slurry was loaded into an Adjusta Chrom® #11 (Ace Glass Inc., Vineland NJ) glass column 300 mm long with 10 mm inner diameter. The bed height was 7.0 cm; the bed volume (BV) was 5.5 cm^3. A septic tank effluent from a local residence (collected at the distribution box before it was distributed over the Soil absorption System was passed through this column at a flow rate of 1.2 ml/min, thus providing an Empty Bed Contact Time (EBCT) of 4.58 min. The average characteristics of the septic tank effluent are provided in Table III. The effluent was collected every day, brought to University of Massachusetts Dartmouth environmental lab, refrigerated, and then passed through the column continuously for 70 days, after which the column was stopped. The clinoptilolite column was regenerated with 1.0 N NaCl for 20 BV with an EBCT of 5.0 minutes.

Table III. Septic Tank Effluent Characteristics

BOD_5 (mg/L)	165
TSS (mg/L)	70
NH_4^+ - N (mg/L)	See Figure 2
Alkalinity (mg/L as $CaCO_3$)	185
pH	7.6

For the P-selective PLEs, fixed bed column runs were carried out in Adjusta Chrom® #11 (Ace Glass Inc., Vineland NJ) glass columns 300 mm long with 10 mm inner diameter. The influent was pumped into the column in a downflow direction using synchronous pumps, FMI Lab Pump, Model QSY (Fluid Metering Inc., Syosset, NY). Effluent sample from the column was collected by a Spectra/Chrom® CF-1 Fraction Collector (Spectrum Chromatography). The flow was adjusted to maintain constant empty bed contact time (EBCT) for all the column runs at 3.0 min.

An online pH meter was also connected in the system to monitor the effluent pH. Regeneration of the bed was performed similarly by passing the regenerant in a downflow direction and the spent regenerant samples were also collected in a similar fashion. The regenerated bed was rinsed with deionized water till the effluent pH was < 8.5. The regenerated bed was then used for another exhaustion run.

Regeneration of Exchanger and Recovery of N and P

Since the focus of this research is on recovery of N and P, efficient regeneration of the N and P-laden exchangers is critical. An ideal regeneration step should desorb 100% of the macronutrient of interest (N or P) in as few BVs as possible, thus providing the highest concentration of the macronutrient. After mixing the N-and P-regenerant solutions, a Mg source is added (as $MgCl_2$) into it to effect precipitation of $MgNH_4PO_4$ (struvite). These steps are represented in equations 6-8. Based on results of previous research, clinoptilolite was regenerated with 1% NaCl. 2.5% NaCl + 2.0% NaOH solution was chosen as the regenerant for all the regeneration runs for the P-selective PLEs. The sorbent media was regenerated with 20 BV (for clinoptilolite) or 25 BV (for P-selective PLE) of the regenerant solution in all cases.

$$\overline{\text{Clinop}^- - \text{NH}_4^+} + \text{NaCl} \longrightarrow \overline{\text{Clinop}^- - \text{Na}^+} + \text{NH}_4^+ \tag{6}$$

$$\overline{\text{Dow-HFO-Cu --PO}_4^{3-}} + \text{NaCl} \longrightarrow \overline{\text{Dow-HFO-Cu--Cl}^-} + \text{PO}_4^{3-} \tag{7}$$

$$\text{MgCl}_2 + \text{NH}_4^+ + \text{PO}_4^{3-} \longrightarrow \text{MgNH}_4\text{PO}_4\text{(s)} \tag{8}$$

The precipitate was allowed to settle for a couple of hours and the supernatant was decanted off and was analyzed for different solutes. Following the precipitation of PO_4^{3-} from the spent regenerant, 1.5% NaOH was added to it to compensate for the loss in OH^- ions in the regenerant, due to regeneration of the media and possible precipitation.

Analytical Procedures

All the chemicals were analyzed as per the Standard Methods (*39*). All anions such as chloride, nitrate, phosphate, and sulfate were analyzed using a DIONEX Ion Chromatograph (Model – ICS 900) coupled with an AS40 autosampler. Sodium, calcium, and ammonium were analyzed by Dionex ICS 900 as well. Dissolved organic carbon (DOC) was measured using a total organic carbon (TOC) analyzer (TELEDYNE TEKMAR Phoenix 8000 UV-Persulfate TOC Analyzer). The iron content in the resins was determined using a HACH spectrophotometer (Model - DV 4000 UV/Vis) by the FerroVer® method. Before analysis the samples were digested as per the Standard Methods (*39*). Cu was analyzed after acidification of the original sample as per the Standard Methods (*39*) in Perkin Elmer AAnalyst 300 Atomic Absorption (AA) Spectrometer in flame mode. X-ray photoelectron spectroscopy (XPS, PHI Quantum 2000, Physical Electronics, Inc., Chanhassen, MN, USA) was used to analyze the surface elemental composition of the struvite ($MgNH_4PO_4$) generated and compare its elemental composition to the same for pure struvite obtained from Sigma Aldrich.

Results and Discussion

Ammonium-Nitrogen uptake of clinoptilolite is shown in Figure 2. The maximum uptake capacity was determined to be 21.9 mg N/dry gm. of clinoptilolite for a corresponding aqueous-phase NH_4^+-N concentration of 78 mg/L. The maximum uptake capacity obtained for material used in this study (obtained from GSA Resources, Inc.) is almost the same as that obtained by Klieve and Simmons (*38*) but significantly higher than that reported by other researchers (*41–44*).

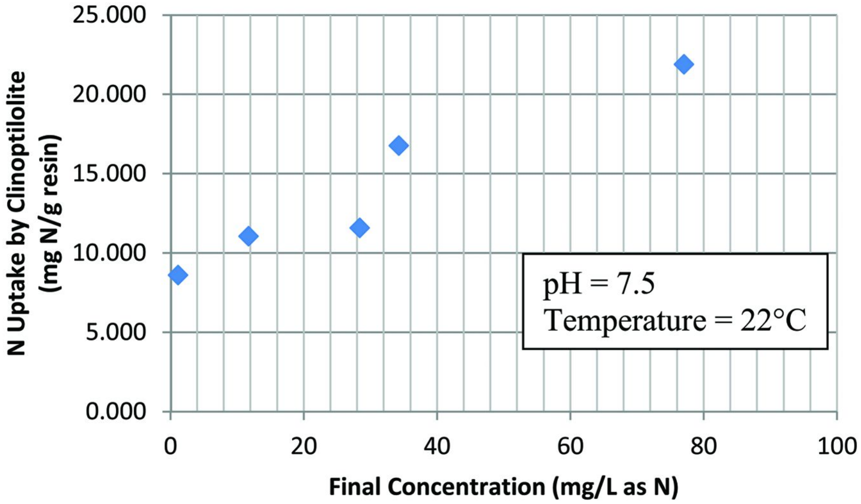

Figure 2. Ammonium-Nitrogen Uptake Isotherm by Na^+-loaded Clinoptilolite (Obtained from GSA Resources, Inc.) at a pH of 7.5.

Figure 3 presents NH_4^+/Na^+ and NH_4^+/Ca^{2+} binary selectivity data. From this figure it is clear that the cation exchanger chosen has **$\alpha_{NH4/Ca} > 1$**and **$\alpha_{NH4/Na} > 1$.** In Figure 3 the 45° line (dashed) represents a hypothetical zone where the exchanger material is not selective toward either of the binary component ions; i.e., its selectivity for one ion is the same as the other. For any binary isotherm point to the left of the 45° line, the ion represented (NH_4^+-N in this case) has a higher fractional occupancy in the exchanger phase compared to the same in the aqueous phase, and thus for this data point the exchanger is selective for the target ion compared to the competitor ion. The farther an isotherm point is to the left of the 45° line, the more selective is the material for the binary system. From Figure 3 it can be concluded that the clinoptilolite material used in this study (obtained from GSA Resources) is more selective toward NH_4^+-N compared to Ca^{2+} than compared to Na^+.

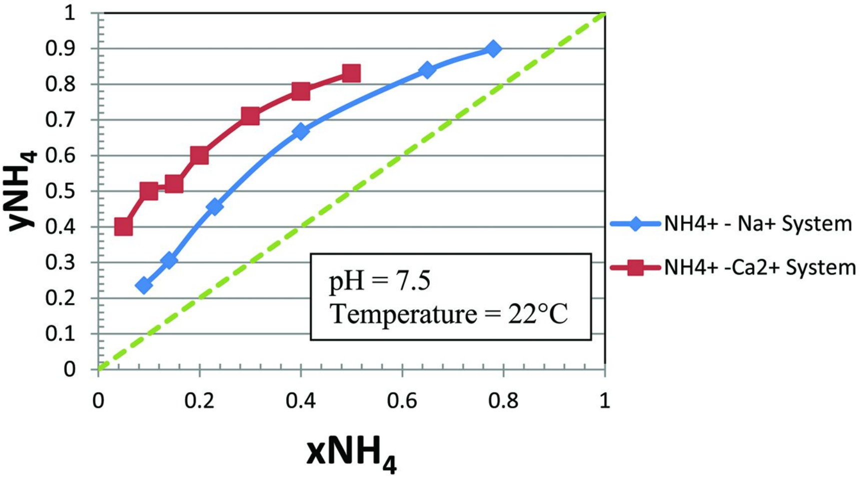

Figure 3. Ammonium-Nitrogen Selectivity for Clinoptilolite (Obtained from GSA Resources, Inc.) Over Sodium and Calcium. yNH_4 is the fraction of ion exchange sites on the clinoptilolite occupied by NH_4^+ (meq NH_4^+/g/maximum uptake capacity in meq./g) while xNH_4 is the fraction of NH_4^+ cations in the aqueous phase (meq NH_4^+/l /∑meq all cations/l).

Figure 4 shows the performance of the clinoptilolite column for the septic tank effluent. It is clear that clinoptilolite can be used to remove ammonium-nitrogen from a wastewater. The mass of clinoptilolite needed in the column would depend on the aqueous concentration of NH_4^+-N, the flow rate of the system, and the time allowed for exhaustion - design parameters that are outside the purview of this chapter.

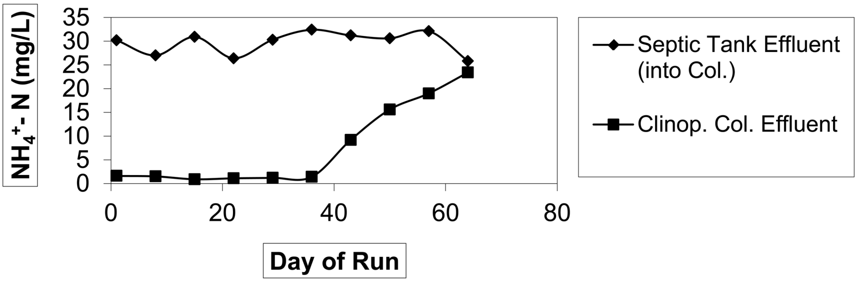

Figure 4. Clinoptilolite Column Performance with Septic Tank Effluent at a pH of 7.5. BV = 5.5 cm^3; EBCT = 4.58 minutes.

The following affinity sequence is generally obtained for Strong-Base Anion exchange resins and has been demonstrated in previous works (*18*, *20*) :

$$SO_4^{2-} > PO_4^{3-} > NO_3^- > Br^- > NO_2^- > Cl^-.$$

The ArsenX sorbent media showed remarkably high sorption affinity for P over high background concentration of SO_4^{2-}, which is evident from Figure 5. The column was fed an influent with 4.2 mg/l as P and 161.6 mg/l as SO_4^{2-}; thus the SO_4^{2-} concentration was almost 40 times as high as P, yet SO_4^{2-} broke through almost 300 BVs before P. It may be noted that selectivity of P over SO_4^{2-} is represented here with a column effluent profile. This is an alternative way to the batch isotherm experiment that was employed for the clinoptilolite selectivity. The column effluent curve provides additional information such as the dependence of selectivity on influent flow rate or Superficial Liquid Velocity (SLV). It might also be noted that the breakthrough behavior remained same for column runs with influent mg P: mg SO_4^{2-} = 1.0: 40.0 and influent mg P: mg SO_4^{2-} = 1.0: 60.0. This is illustrated in the breakthrough profile shown in Figure 6. It can be inferred from the following figures that ArsenX demonstrates high sorption affinity for P, when present as a trace species compared to ubiquitous SO_4^{2-}. The typical SO_4^{2-} and P concentration in the secondary effluent of a municipal wastewater treatment plant being in this range, little or no competition is expected from the increase in concentration of SO_4^{2-}. Also, Fe concentration of the effluent remained below detection limit, indicating no significant bleeding of Fe.

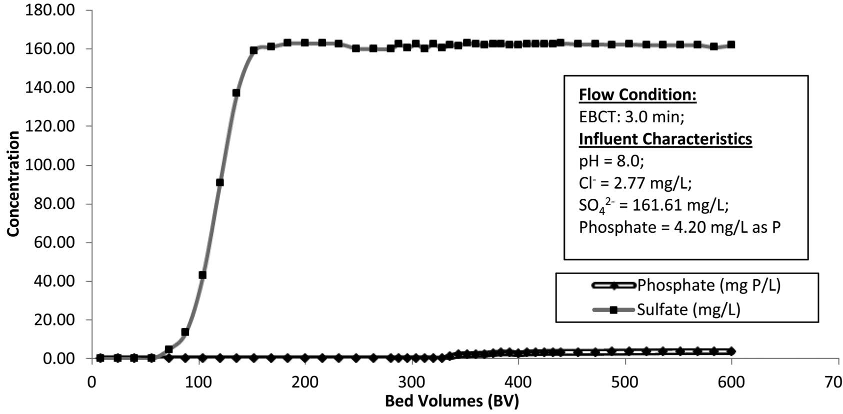

Figure 5. Comparison of breakthrough profiles of P and SO_4^{2-} for ArsenX. EBCT: Empty Bed Contact Time = 3.0 minutes.

Very similar breakthrough pattern was observed using DOW-HFO resin as the sorbent media. To be precise, the breakpoint was identical for identical influent. DOW being a free form resin without any exchange capacity, it reinstates the earlier postulation. Also, it might be noted that there was no sorption/exchange of SO_4^{2-}, which shows that SO_4^{2-} is not affected by LAB interaction. Thus it can safely be concluded that P is removed only by the HFO in this resin. This leads to the hypothesis that the higher the HFO impregnation, the better the P removal capacity of the exchanger.

With DOW-HFO-Cu, the capacity of the sorbent media was enhanced and the breakpoint of P was observed much later than (about 200 BVs) ArsenX and DOW-HFO. In this particular scenario, P was removed by LAB interaction with both the dispersed HFO nanoparticles and the Cu^{2+} ion immobilized on the surface. However, their share of the uptake cannot be determined conclusively. Nevertheless, this experimental data validates that if two different ligand exchangers could successfully be hosted on a polymeric backbone, increased sorption capacity could be attained as there is little or no compromise on the individual capacity of the ligand exchangers. Details of mechanisms of P uptake by the two exchangers are available in (*45*) and are not repeated here. Also, the concentration of Cu in the effluent remained below detection limit throughout the duration of the column run, indicating no significant bleeding of Cu from DOW-HFO-Cu. The same was noted for Fe also; i.e., no significant bleeding of Fe was noted from DOW-HFO-Cu. This observation is notable because any presence of Fe or Cu in the effluent would be undesirable and would make the process unacceptable.

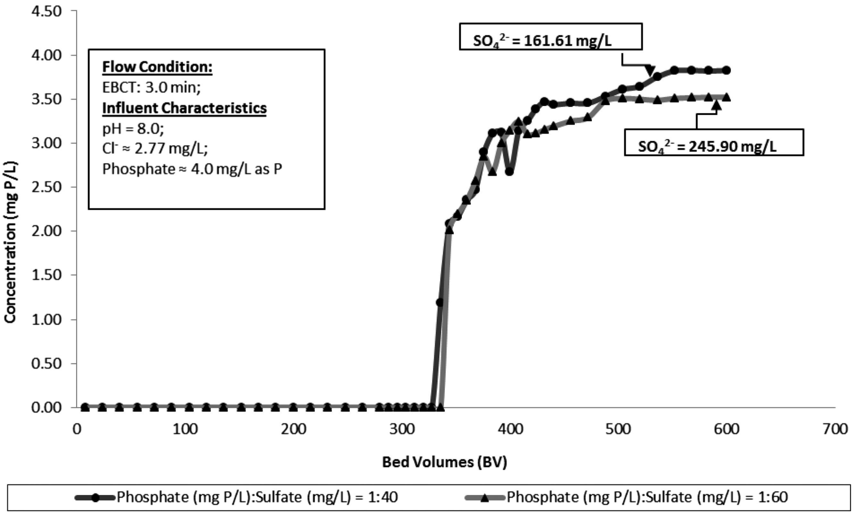

Figure 6. Comparison of breakthrough profiles of P for different background concentration of SO_4^{2-} (P is present as trace species compared with SO_4^{2-}). EBCT: Empty Bed Contact Time = 3.0 minutes.

A comparative breakthrough profile of all the three sorbent media utilized for this study is shown in Figure 7. It is clear that DOW-HFO-Cu provides the highest P removal capacity (milliequivalents of P per unit mass of the exchanger).

Figure 8 shows the column-run profile for DOW-HFO-Cu PLE with a synthetic containing Cl^- and SO_4^{2-} as competing anions for PO_4^{3-}. It may be noted that this material can be used to treat ≈2000 BVs of a wastewater containing ≈1.9 mg/L of P. A comparison of the performance of DOW-HFO-Cu in Figures 7 and 8 reveals an interesting result: the BV to breakthrough of P is inversely related to P concentration. While the P concentration in Figure 8 is 2.29 times lower than in Figure 7, the BV to breakthrough is almost 2.8 times higher. From an application perspective this has special significance in that the amount of material needed to run a packed-bed column for a design period before breakthrough is directly related to the P concentration in the wastewater.

Figure 9 shows the results of clinoptilolite regeneration for N recovery with 1% NaCl. Figures 10 and 11 show the results for P recovery from ArsenX and DOW-HFO-Cu respectively. Recovery of more than 90% of the sorbed N and P was attained in all cases. Also, no Fe or Cu was observed in the regenerant, thus confirming that the bound Cu and Fe are strongly attached to the exchanger and are not leached out even during aggressive regeneration conditions.

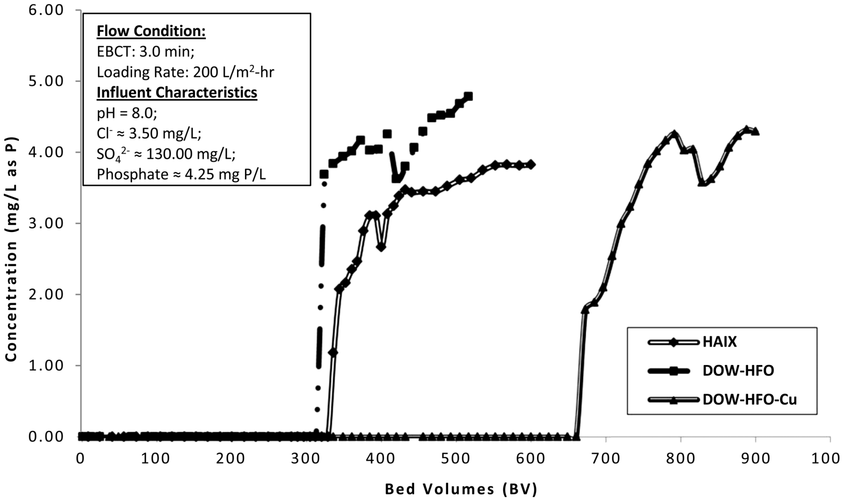

Figure 7. Comparative breakthrough profile of P with different sorbents. EBCT: Empty Bed Contact Time = 3.0 minutes.

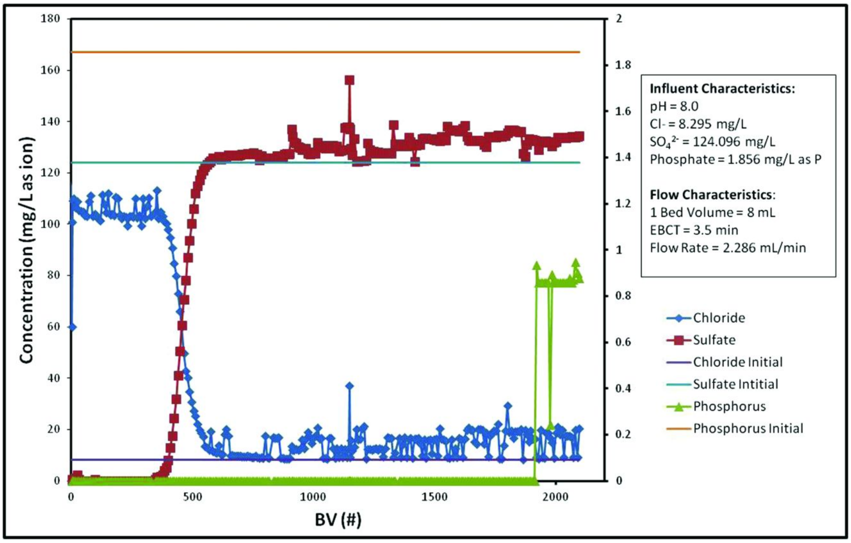

Figure 8. Breakthrough Profile for DOW-HFO-Cu. EBCT = 3.5 minutes.

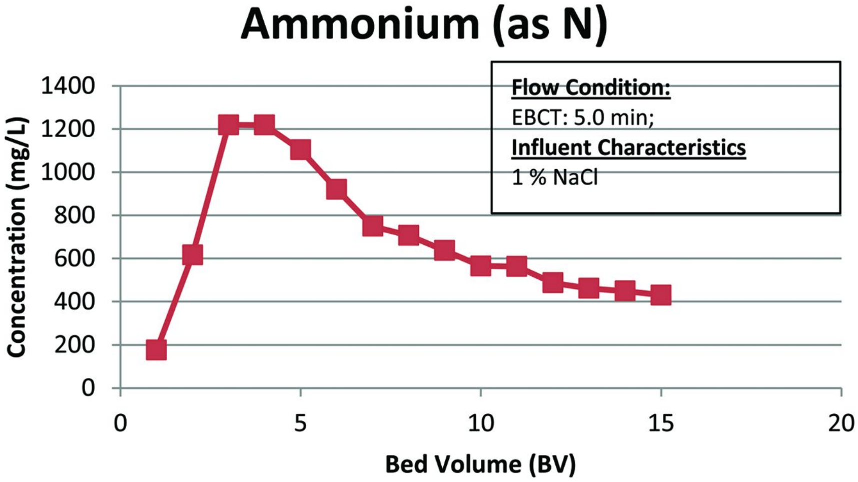

Figure 9. Typical Regeneration Profile of N using Clinoptilolite. EBCT: Empty Bed Contact Time = 5.0 minutes.

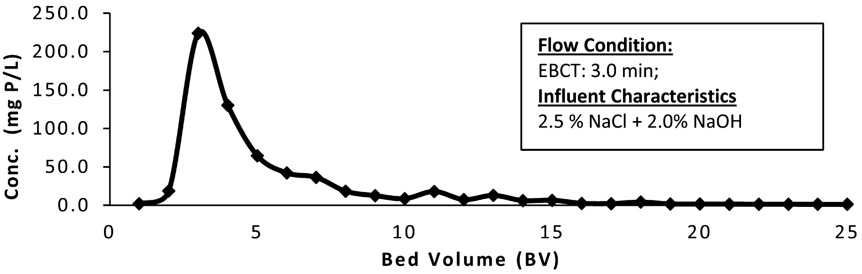

Figure 10. Typical regeneration profile of P using ArsenX. EBCT: Empty Bed Contact Time = 3.0 minutes.

Desorption of the SO_4^{2-} was also remarkable and > 89.0 ± 5.00 % of the sorbed SO_4^{2-} was desorbed within 15 BVs in all cases. Also, there was no compromise of the performance of the regenerated resin with that of the virgin resin. A decrease of about 1.5% in the breakpoint of PO_4^{3-} was observed after 10 cycles of exhaustion-regeneration of the same resin bed.

After addition of $MgCl_2$ to the mixture of the spent regenerant (from clinoptilolite and ArsenX/DOW-HFO-Cu), > 85.0 % of the N and P were recovered in the precipitate as $MgNH_4PO_4$, in high purity. Table IV presents XPS comparative results of elemental composition of the precipitate and pure struvite ($MgNH_4PO_4$) obtained from Sigma Aldrich. The solid-phase resource generated from the wastewater can be easily used as a fertilizer due to its high N and P content.

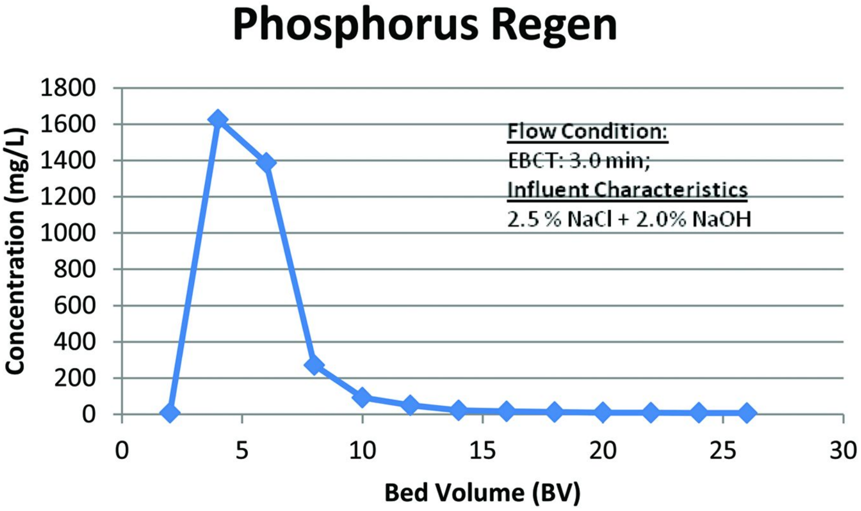

Figure 11. Typical regeneration profile of P using DOW-HFO-Cu. EBCT: Empty Bed Contact Time = 3.0 minutes.

Table IV. Elemental Composition of Fertilizer Precipitate and Pure Struvite

	Fertilizer from Regenerant Solution	*Struvite Standard*
Element	XPS Atom %	XPS Atom %
Oxygen	55.30	51.80
Phosphorus	16.40	14.90
Carbon	14.30	15.80
Magnesium	11.60	10.90
Nitrogen	2.40	6.60

Conclusions

Selective removal of trace N and P from a background of other competing cations and anions present in wastewater is a major challenge faced by water quality engineers and regulators. For N, biological nitrification followed by denitrification is a robust process but its drawback is that cannot recover N since the final N product is highly insoluble N_2 gas. Air stripping may remove ammonium-nitrogen from the aqueous phase but it merely transfers it to the gas phase and may cause air pollution concerns. Moreover, it also cannot recover the N. For P, chemical precipitation is limited by the production of excessive sludge and biological removal processes are restricted by the inability to remove trace concentration. Also, both chemical precipitation and biological P removal suffer from inadequate recovery of the removed phosphate, which is a non-renewable resource. Previous ion-exchange and fixed bed ligand sorption processes suffered from the low selectivity of the sorbent material towards phosphate and cost constraints. The overall goal of this study was to estimate the removal capacity of N and P by selective ammonium and phosphate exchangers at different background concentration of competing cations and anions and to assess their competitive effect on the removal process. Laboratory experiments were carried out to investigate the key features of the fixed-bed sorption process, which is capable of removing trace concentrations of N and P and to recover them as a commercial-grade, solid-phase fertilizer.

The major conclusions that can be drawn from this study are summarized below:

1. Clinoptilolite showed high selectivity toward ammonium-nitrogen compared to competing cations sodium, magnesium, and calcium.
2. ArsenX^{np} showed high selectivity towards phosphate when compared to sulfate consistent with the observation of other researchers (*18*). Experimentally determined phosphate-sulfate separation factors were significantly higher than those strong base anion exchangers previously used (Liberti, et al., 1976).
3. DOW-HFO-Cu showed superior P removal capacity in the presence of competing anions.
4. When phosphate is not present as a trace species compared to background sulfate, ion-exchange process is dominant over the ligand sorption process and sulfate gets a higher selectivity preference.
5. Lewis acid-base interaction (i.e. formation of covalent bond between the anionic ligand and the central metal atom forming inner-sphere complexes) accompanied by the electrostatic attraction (i.e. ion-pair formation) is the core mechanism leading to HAIX's and DOW-HFO-Cu's high sorption affinity toward phosphate. The mechanism was supported by thermodynamic data.
6. The sorbent is amenable to efficient regeneration. Single step regeneration with 2.5 % sodium chloride and 2.0 % sodium hydroxide consistently recovered more than 95.0 % of sorbed phosphate within 10 BV. Only minor capacity drop (about 1.5 %) was observed after 10 cycles of exhaustion-regeneration.
7. Clinoptilolite regeneration with 1% NaCl was able to recover >90% of ammonium-nitrogen.
8. The mixture of the two regenerant streams can be used to cover commercial-grade, solid-phase fertilizer; struvite.
9. No significant bleeding of the iron or copper was observed from regeneration of HAIX and/or DOW-HFO-Cu, negating any need for supplemental addition of iron and/or copper to the sorbent media during its life cycle.

Acknowledgments

This project received partial funding through the National Science Foundation Partnerships for Innovation Program (IIP -0650163).

References

1. Rhyther, J. H.; Dunstan, W. M. *Science* **1971**, *171*, 1008.
2. Goldman, J. C.; Tenore, K. R.; Stanley, H. I. *Science* **1973**, *180*, 955.
3. Valiela, I. *Marine Ecological Processes*; Springer-Verlag: New York, 1995.
4. Howarth, R. W.; Marino, R. *Limnol. Oceanogr.* **2006**, *5*, 367–376.
5. Sharpley, A. N.; Daniel, T.; Sims, T.; Lemunyon, J.; Stevens, R.; Parry, R. *Agricultural Phosphorus and Eutrophication*, 2nd ed.; U.S. Department of Agriculture, Agricultural Research Service: Washington, DC, 2003.
6. Bricker, S. B.; Longstaff, W. D.; Jones, A.; Boicourt, K.; Wicks, C.; Woerner, J. *Effects of Nutrient Enrichment in theNation's Estuaries: A Decade of Change*; NOAA Coastal Ocean Program Decision Analysis Series No. 26; National Centers for Coastal Ocean Science: Silver Spring, MD, 2007.
7. *OSPAR Integrated Report 2003 on the Eutrophication Status*; OSPAR: London: 2003.
8. *Nutrient Control Design Manual: State of Technology Review Report*; EPA/600/R-09/012; U.S. Environmental Protection Agency: Washington, DC, 2009.
9. Tchobanoglous, G.; Burton, F. L.; Stensel, H. D. *Wastewater Engineering: Treatment and Reuse*; McGraw Hill: New York, 2003.
10. Crites, R.; Tchobanoglous, G. *Small and Decentralized Wastewater Management Systems*; McGraw Hill: New York, 1998.
11. Snoeyink, V. L.; Jenkins, D. *Water Chemistry*; John Wiley and Sons: New York, 1980.
12. Herring, J. R.; Fantel, R. J. *Nat. Resour. Res.* **1993**, 226–246.
13. Seida, Y.; Nakano, Y. *Water Res.* **2002**, *36*, 1306–1312.
14. Tanada, S.; Kabayama, M.; Kawasaki, N.; Sakiyama, T.; Nakamura, T.; Araki, M. *J. Colloid Interface Sci.* **2003**, *257* (1), 13–140.
15. Zeng, L.; Li, X.; Liu, J. *Water Res.* **2004**, *38* (5), 1318–1326.
16. Genz, A.; Kornmüller, A.; Jekel, M. *Water Res.* **2004**, *38* (16), 3523–3530.
17. Chubar, N. I.; Kanibolotskyy, V. A.; Strelko, V. V.; Gallios, G. G.; Samanidou, V. F.; Shaposhnikova, T. O. *Colloids Surf., A* **2005**, *255* (1−3), 55–63.
18. Blaney, L. M.; Cinar, S.; SenGupta, A. K. *Water Res.* **2007**, *41* (7), 1603–1613.
19. Liberti, L.; Petruzzelli, D.; De Florio, L. *Environ. Technol.* **2001**, *22* (11), 1313–1324.
20. Zhao, D.; SenGupta, A. K. *Water Sci. Technol.* **1996**, *33* (10−11), 139–147.
21. Zhao, D.; SenGupta, A. K. *Water Res.* **1998**, *32* (5), 1613–1625.
22. SenGupta, A. K.; Zhao, D. U.S. Patent 6136199, 2000.
23. Petruzzelli, D.; De Florio, L.; Dell'Erba, A.; Liberti, L.; Notarnicola, M.; Sengupta, A. K. *Water Sci. Technol.* **2003**, *48* (1), 179–184.

24. Dzombak, D. A.; Morel, F. M. *Surface Complexation Modeling: Hydrous Ferric Oxide*; John Wiley and Sons, Inc.: Hoboken, NJ, 1990.
25. Stumm, W.; Morgan, J. J. *Aquatic Chemistry: Chemical Equilibria and Rates in Natural Waters*, 3rd ed.; John Wiley and Sons: New York, 1995.
26. Golterman, H. *Hydrobiologia* **1995**, *315*, 59–68.
27. Hiemstra, T.; van Riemsdjik, W. *J. Colloid Interface Sci.* **1999**, *210* (1), 182–193.
28. Huang, C. P.; Vane, L. M. *J. − Water Pollut. Control Fed.* **1989**, *61*, 1596–1603.
29. Katsoyiannis, I. A.; Zouboulis, A. I. *Water Res.* **2002**, *36* (20), 5141–5155.
30. Cumbal, L.; Greenleaf, J.; Leun, D.; SenGupta, A. K. *React. Funct. Polym.* **2003**, *54* (1−3), 167–180.
31. DeMarco, M. J.; SenGupta, A. K.; Greenleaf, J. E. *Water Res.* **2003**, *37* (1), 164–176.
32. Onyango, M. S.; Matsuda, H.; Ogada, T. *J. Chem. Eng. Jpn.* **2003**, *36* (4), 477–485.
33. Cumbal, L.; SenGupta, A. K. *Environ. Sci. Technol.* **2005**, *39* (17), 6508–6515.
34. Breck, D. W. *Zeolite Molecular Sieves*; Wiley, New York, 1974.
35. Jorgensen, S. E.; Libor, O.; Graber, K. L.; Barkacs, K. *Water Res.* **1976**, *10*, 213–224.
36. Blanchard, G.; Maunaye, M.; Martin, G. *Water Res.* **1984**, *18*, 1501–1507.
37. Beler-Baykal, B.; Allar, A. D.; Bayram, S. *Water Sci. Technol.* **2011**, *63*, 811–817.
38. Klieve, J. R.; Semmens, M. J. *Water Res.* **1980**, *14*, 161–168.
39. *Standard Methods for the Examination of Water and Wastewater*, 20th ed.; American Public Health Association, American Water Works Association, Water Environment Federation: Baltimore, MD, 1998.
40. Zhao, D. Ph.D. Dissertation, Lehigh University, Bethlehem, PA, 1997.
41. Koon, J. H.; Kaufman, W. J. *J. − Water Pollut. Control Fed.* **1975**, *47* (3), 448–465.
42. Schoeman, J. J. *Water SA* **1986**, *12* (2), 73–82.
43. Sirkecioglua, A.; Senatlara, A. *Turk. J. Eng. Environ. Sci.* **1995**, *19*, 399–405.
44. Demir, A.; Gunay, A.; Debik, E. *Water SA* **2002**, *28* (3), 329–336.
45. Sengupta, S.; Pandit, A. *Water Res.* **2011**, *45*, 3318–3330.

Chapter 11

Functionalized Nanoparticles as Removable Membrane Coatings

Megan A. Smith,[1] Carly A. Barnard,[2] and David A. Ladner[*,1]

[1]Department of Environmental Engineering and Earth Sciences,
Clemson University, 342 Computer Court, Anderson, South Carolina 29625
[2]Department of Mechanical Engineering, University of Colorado at Boulder,
Boulder, Colorado 80309
[*]E-mail: ladner@clemson.edu. Phone: 864-656-5572.

Membrane fouling plagues all types of membrane filtration, from large-pore microfiltration to nonporous reverse osmosis (RO). Here we investigate the feasibility of using a coating of one or two layers that serves as a barrier between the membrane and foulant. This coating is electrostatically bound to the membrane at operational pH and removed with a simple pH adjustment once fouling has reduced operational efficiency. The water treatment polymer polydiallyldimethylammonium chloride (polyDADMAC) was used to create a positive charge on the fully aromatic polyamide membrane surface. Carboxy-functionalized polyacrylate nanoparticles (NPs) composite with either silver [Ag-PA(-)] or titanium dioxide [TiO_2-PA(-)], both approximately 10 nm in size, were then adsorbed onto the polyDADMAC coating to reinstate an overall negative charge to the membrane surface. Acid washing removed the polyDADMAC coating by protonating the carboxyl groups on the membrane, promoting repulsion from the membrane surface. Coating and removal phases were characterized primarily by measurement of the surface zeta potential with an electrokinetic analyzer. Additional characterization was performed using scanning electron microscopy (SEM) and attenuated total reflectance Fourier-transform infrared (ATR-FTIR) spectroscopy. The overall results serve as a proof of concept that these materials could serve as removable coatings for RO membranes.

In Novel Solutions to Water Pollution; Ahuja, S., et al.;
ACS Symposium Series; American Chemical Society: Washington, DC, 2013.

Introduction

Background

Despite their promising abilities, membrane filtration processes are limited by fouling. Fouling is a broad term for inorganics, colloids, organic compounds and biological organisms that interact physically or chemically with the membrane surface, resulting in reduced flux. A fouled membrane from a laboratory test is shown in Figure 1. Fouling is largely considered an inevitable phenomenon, though fouling-resistant materials and membrane coatings have been developed to mitigate the problem. The diversity of fouling mechanisms is particularly challenging. Scaling occurs when mineral crystals form on the membrane surface and is often encountered in the treatment of surface water, groundwater and agricultural water (*1*). Colloidal fouling creates a cake layer, which blocks back diffusion of salt ions from the membrane surface, causing elevation of salt concentration and osmotic pressure at the membrane surface (*2*). Biofouling occurs when organisms in a groundwater or seawater supply grow on the membrane surface or in no-flow zones among the membrane spacer mesh (*3*). This fouling results in a characteristic pattern shown in Figure 1. Adsorption commonly occurs in the presence of organic compounds in the feed water, which contain functional groups that interact electrostatically with the membrane surface. These interactions can be strong enough to irreversibly foul the membrane despite vigorous or caustic washing (*4*).

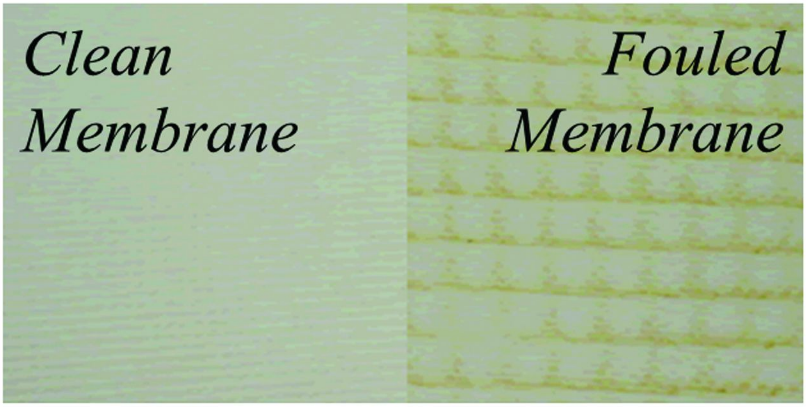

Figure 1. Images of clean and fouled membranes. The fouled membrane image clearly shows the impact of the feed spacer.

Much of the fouling prevention work done previously has been geared toward permanent surface modification (*5–7*). Permanent modification is useful, but even the most resistant membranes can eventually be fouled. This is especially true for feed waters like wastewater and surface water, which contain a wide variety of organic and inorganic material. For this work, a removable surface modification is sought. A removable coating would reverse fouling no matter the foulant characteristics because whatever is deposited on top of the coating could be released with the coating. If the coating could be released easily, it would reduce the costs for membrane cleaning and could increase the membrane lifetime.

There is potential to create a removable coating by electrostatically binding a material that can be released by pH manipulation. Polyvinyl alcohol has been investigated as a removable coating paired with a positively charged NF membrane (*4*). This resulted in a flux recovery of nearly 100% after low pH cleaning, however, the initial flux after coating was reduced compared to the uncoated membrane. A coating is sought that will be more permeable, yet still achieve the same fouling release capabilities.

Here the use of functionalized nanoparticles (NPs) as removable adsorptive coatings was investigated. Functionalized NPs have the potential to create a coating that is more porous than polymeric coatings because of the particle nature of the materials. Several inorganic-polymer composite NPs were examined in this study, including titanium dioxide coupled with polydiallyldimethylammonium chloride (polyDADMAC) to impart a positive charge, titanium dioxide incorporated with polyacrylate to impart a negative charge and silver incorporated with polyacrylate, again to incorporate a negative charge. PolyDADMAC was used as a positively charged binding layer atop the negatively charged membrane surface to adsorb negatively charged nanoparticles.

Membrane Characterization Methods

Chemical and physical effects and properties of fouling, coatings and modifications are determined by membrane characterization using an array of techniques from materials science, chemical engineering and traditional chemical analysis. Chemical (zeta potential, elemental composition and functional groups present) and physical (hydrophilicity, flux and roughness) properties are observed and compared to the virgin membrane to determine beneficial or detrimental effects. For chemical analysis, zeta potential indicates the overall surface charge and isoelectric point and attenuated total reflectance Fourier-transform infrared (ATR-FTIR) spectroscopy determines functional groups associated with the membrane surface and foulants. For physical analysis, contact angle measurement indicates hydrophilicity of the membrane material and scanning electron microscopy (SEM) visualizes the membrane surface and any coating or foulant aggregation.

Zeta Potential Measurements

Electrokinetic characteristics of reverse osmosis membranes have a significant influence on fouling performance and contaminant retention. Polyamide membranes, which have a slightly negative surface charge at neutral pH, can electrostatically repel negatively charged functional groups common to natural organic matter. In the presence of positively charged functional groups, however, the membrane charge is a hindrance and encourages electrostatic binding that can be difficult to remove (*4*). Significant progress has been made toward understanding the complex chemistries involved in membrane surface interactions, but fouling continues to plague desalination plants and other membrane filtration processes. Studies over the past several decades have investigated the fundamental chemical properties of the membrane surface layer (*8*, *9*). Zeta potential characterization of membrane cleaning studies has also been undertaken, though these studies use complex cleaning agents as used in large-scale operations and recommended by manufacturers (*10*).

This study uses an electrokinetic analyzer to determine the electrokinetic properties of the membrane surface by forcing an electrolyte solution through a sample cell containing the material of interest; electrodes at each end of the sample cell measure the resulting streaming current and zeta potential is calculated (*11*). The Fairbrother-Mastin (F-M) approach to calculating zeta potential (ζ), given in Equation 1, improves upon the earlier Helmholtz-Smoluchowski (H-S) approach, accounting for phenomena in the instrument that affect the reported measurements (*11*).

$$\zeta = \frac{dI}{dp} \times \frac{\eta}{\varepsilon \times \varepsilon_o} \times \frac{L}{A} \tag{1}$$

Here dI/dp is the measured slope of streaming current versus pressure, η is the electrolyte viscosity, ε is the dielectric constant of the electrolyte, ε_0 is the vacuum permittivity, L is the length of the streaming channel, and A is the cross-sectional area of the streaming channel.

Contact Angle Measurements

Contact angle measurement is used to assess the hydrophilic character of a membrane material and the change resulting from membrane modification or coating. The sessile drop method is most commonly used for membrane analysis. This method involves placement of a liquid droplet onto the membrane surface and photographic visualization with a contact angle goniometer (*12*). Software is used to determine the contact angle of the drop on the membrane. Titrations can be performed by varying the pH of droplets, allowing characterization of membrane surface chemistry throughout a range of pH values. The type of liquid used in the droplet can also be varied, and a "wettability" parameter can be identified based on the membrane's affinity for particular liquids (*13*). A second technique that can be applied to membrane surface characterization is the captive bubble method, in which the surface is immersed face-down in a liquid and a gas bubble is released onto the membrane surface from below (*14*).

In all contact angle measurements the shape of the drop/bubble is metastable and can be affected by outside pressures, evaporation and other factors. There is also a hysteresis described by Gao & McCarthy (*15*). An increasing droplet will cover a defined area with changing contact angle until reaching a certain volume, at which point it will increase in area with a constant contact angle; a decreasing droplet will decrease in volume with a changing contact angle until reaching a critical volume, at which point the area will decrease with a constant contact angle. In order to account for both aspects of this phenomenon, contact angle measurements often include additions and subtractions of drops/bubbles to find the constant contact angle (*14*).

Attenuated Total Reflectance Fourier-Transform Infrared Spectroscopy

ATR-FTIR spectroscopy is used to confirm functional groups present in the membrane, such as the carboxyl and amine groups expected for a polyamide membrane, or to determine functional groups associated with natural organic matter (NOM) or other foulant materials (*16*). In RO research, ATR-FTIR is often used to confirm that the membrane, coating or foulant is giving expected results (*17*). This technique is not often the primary analysis of membranes or membrane coatings, though some studies such as Belfer et al. (*18*)have demonstrated the benefits of utilizing peak emergence and absorbance changes for assessing membrane coatings. Without extremely sensitive instrumentation, it is difficult to discern the small quantities of coating layers over the dominant vibrational bands of the polysulfone support membrane and ATR-FTIR is of limited benefit (*19*).

Materials and Methods

Coatings

Three nanoparticles (NPs) of similar size but different composition and functionality were obtained from ViveNano Inc. (Toronto, Ontario, Canada): negatively charged silver-polyacrylate [Ag-PA(-)], negatively charged titanium dioxide-polyacrylate [TiO_2-PA(-)] and positively charged titanium dioxide-polyDADMAC [TiO_2-PD(+)]. Figure 2 gives a simplified visualization of nanoparticle surface charge. The NPs were manufactured such that the polymer was incorporated into the NP and functional groups imparted charge at neutral pH. TiO_2-PD(+) NPs were received in 20% w/w powder form. Ag-PA(-) NPs were received in an aqueous suspension of 1 g/L. TiO_2-PA(-) NPs were received in 18% w/w powder form. All nanoparticles had an average size of about 10 nm in diameter. Particle size was determined by the manufacturer via dynamic light scattering.

The quaternary ammonium polymer polydiallyldimethyl-ammonium chloride (polyDADMAC) Clarifloc C 308-P 20% solution was donated by Polydyne, Inc., a subsidiary of SNF Floerger (Riceboro, Georgia). The monomer structure of polyDADMAC is shown in Figure 3.

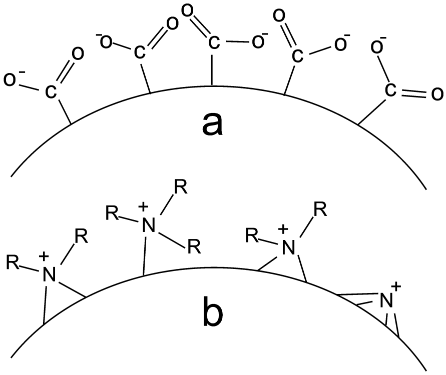

Figure 2. Simplification of functionalized nanoparticle charge groups. Acrylate (a) gives net negative charge to silver and titanium dioxide nanoparticles. PolyDADMAC (b) gives net positive charge to titanium dioxide nanoparticles.

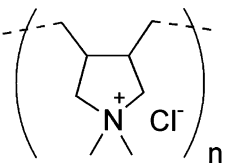

Figure 3. Monomer structure of polyDADMAC. The formulation used in this study, Clarifloc C 308-P, has an average length of 308 monomers.

Membranes

Two commercially available RO membranes were selected for this work: SW30HR from Filmtec, a subsidiary of Dow Chemical Company (Midland, Michigan), and SWC4 from Hydranautics, a Nitto-Denko company (Oceanside, California). Both membranes are thin-film fully aromatic polyamide formed from 1,3-benzenediamine and trimesoyl chloride; SWC4 is uncoated while SW30HR is coated with a polyvinyl alcohol layer (*20*). Both membranes were obtained as dry sheets and stored away from light in sealed plastic bags. Membrane coupons were cut from the same section of membrane to minimize the effects of membrane heterogeneity. One section of SWC4 was used for preliminary experiments. Several sections of SW30HR were used – one designated for Ag-PA(-) experiments, one designated for TiO_2-PA(-) and one designated for TiO_2-PD(+).

Membrane Coating Process

All coating, soaking and storage occurred in the refrigerator at 4°C. Membrane coupons of approximately 1.5 cm x 2.5 cm were used for all experiments. Coating was performed in 10 mL of coating solution in polypropylene petri dishes. Side-by-side coupons were used for contact angle and SEM measurements.

PolyDADMAC Coating Layer

PolyDADMAC was used as a positive binding layer to adhere negatively charged nanoparticles to the negatively charged membrane surface. Coating solution was prepared by a hundredfold dilution of the stock solution using doubly deionized (DDI) water, which is purified in house with a MilliQ water system (Millipore, Bedford, Massachusetts). Two dry membrane coupons were soaked in 10 mL of a 0.2% polyDADMAC solution for 24 hours. After 24 hours the membranes were rinsed in DDI water for at least 30 seconds and soaked in 10 mL of DDI water for 12 hours before further coating or analysis.

TiO_2-PD(+) NPs on Membrane Surface

TiO_2-PD(+) NPs were adsorbed directly to the membrane surface. A 1 g/L stock solution of TiO_2-PD(+) NPs was prepared by dispersing 100 mg powdered TiO_2-PD(+) NPs into 100 mL DDI water. No buffer was added due to concerns that a buffering species may interfere with NP adsorption to the membrane. A 10% coating solution was prepared by diluting 1 mL stock solution into 9 mL DDI water. Membranes were soaked in coating solution for 24 hours, rinsed in DDI for 30 seconds and soaked in DDI for at least 12 hours before analysis.

Negatively Charged NPs on PolyDADMAC-Coated Membranes

Negatively charged TiO_2-PA(-) and Ag-PA(-) were adsorbed onto the polyDADMAC coated membrane samples. A 1 g/L stock solution of TiO_2-PA(-) was prepared by dispersing 100 mg dry TiO_2-PA(-) into 100 mL DDI water. A 10% coating solution was prepared by diluting 1 mL stock solution into 9 mL DDI water. Ag-PA(-) was received as a 1 g/L solution and a simple tenfold dilution was performed for coating. Membranes were coated for 24 hours, rinsed in DDI for 30 seconds and soaked in DDI for at least 12 hours before analysis.

Control Samples

Control samples were prepared to confirm the electrostatic binding of the coating layers. Controls included TiO_2-PD(+) exposed to a polyDADMAC-coated membrane, TiO_2-PA(-) exposed to a virgin membrane and Ag-PA(-) exposed to a virgin membrane. In these controls the NPs were not expected to bind, since electrostatic repulsion should prevent it.

Coating Removal Process

Removal of single- and double-layer coatings was tested using simple strong acid and base. Hydrochloric acid (HCl) was used for acid washing at concentrations of 0.1 M (pH 1), 0.01 M (pH 2) and 0.001 M (pH 3). Sodium

Hydroxide (NaOH) was used for base washing at a concentration of 0.1 M (pH 13). Control samples of virgin membrane were washed at each pH to determine whether the acid and base solutions altered the properties of the membrane.

To promote coating removal a pair of membranes was vigorously shaken in acid or base for 5 minutes, rinsed thoroughly in DDI water and soaked in the acid or base solution for 6 hours. Kinetics experiments were performed by varying the soaking time to 2, 4, 6 and 8 hours to determine whether time had an effect on removal efficiency. Samples were rinsed for 30 seconds in DDI water after soaking, then soaked in 10 mL DDI water for at least 2 hours before analysis. As with coating, the removal, soaking and storage occurred in the refrigerator at 4°C.

Membrane Characterization

Zeta Potential Measurements

Membrane zeta potential was determined with a SurPASS electrokinetic analyzer (Anton Paar GMBH, Graz, Austria). Zeta potential, ζ, was calculated by VisioLab software (*21*) from streaming potential measurements using the Fairbrother-Mastin equation (Equation 1). Streaming potential measurements were collected using an adjustable gap cell (AGC) in which an electrolyte solution passed over the membrane surface in a channel 2 cm in length, 1 cm in width and 105±5 μm in height. Membrane coupons covered the 2 cm x 1 cm faces of the channel. Flow was directed through the AGC by linearly ramping pressure from 0 to 300 mbar in both directions. Electrodes measured the streaming current at each end of the sample cell. Two cycles of pressure ramping in each direction were performed and the average zeta potential was used in the titration curve. The electrolyte used was 0.001 M KCl. HCl (0.1 M) and NaOH (0.1 M) were used to adjust the pH. The instrument was fitted with a titration unit for customizable automated titration. Two titrations were performed for each full set of data: an acid titration from ambient pH (~5.5) to pH 3 and a base titration from ambient pH to pH 9. The system was rinsed with nanopure water between titrations to eliminate the buildup of ionic strength within the system. Single measurements were also taken at ambient pH for coated membranes and removal experiments.

Attenuated Total Reflectance Fourier-Transform Infrared Spectroscopy

ATR-FTIR was used to determine whether the coatings were present in sufficient quantity on the membrane surface to be detected. A Nicolet 6700 FTIR (Thermo Scientific, Waltham, Massachusetts) fitted with a diamond Smart-iTR plate was used with a scanning resolution of 2nm. A total of 32 scans were averaged for each reported spectrum.

Contact Angle Measurements

Contact angle measurements were taken with a drop shape analysis system (Easy Drop, Krüss, Hamburg, Germany) primarily through the sessile drop method. A volume of 6 µL of DDI water was used for each droplet. Video recording was employed to capture the drop's initial contact with the membrane. Video frames were subsequently analyzed to calculate the contact angle of the drop, fitting a general conic section equation to the drop's profile. Contact angle measurements were taken between 100 and 300 milliseconds after the drop's initial contact with the membrane surface.

The captive bubble method, in which the membrane was submerged in DDI water and an air bubble was deposited on its surface, was also employed to confirm the hydrophilic properties of the membrane and the coatings.

Scanning Electron Microscopy

SEM was employed to visualize the effects of the coating and removal processes on the membrane. Membrane samples were sputter coated in gold with a Hummer 6.2 sputtering machine (Anatech Ltd., Battle Creek, Michigan) prior to analysis. Images were taken at magnification of 2.5 k and 10.0 k with a tabletop TM3000 unit (Hitachi High Technologies America, Inc., Dallas, Texas).

Results and Discussion

Membrane Coatings

PolyDADMAC Coating and Removal

PolyDADMAC was extremely effective in creating a positive layer due to its strong interaction with dangling carboxyl groups in the membrane's polyamide layer. This interaction effectively neutralized the membrane surface charge and imparted the positive character of the polyDADMAC polymer. Because of the polymer's size and linear character, loops or chains of considerable length likely project from the membrane surface as well, exposing a considerable amount of positive charge to the feed solution. Cleaning with strong acid was effective in removing the polymer and nearly restoring the membrane to its virgin state (Figure 4). Acid washing to pH 1 for up to 30 minutes was approved by the manufacturer's technical specification sheet, but a titration performed after this control wash indicated significant changes in the membrane surface chemistry. It was determined that future acid washing should take place over short durations using the weakest effective acid solution. Use of surfactants and other complex cleaning solutions may be driven by similar results of damage to the virgin membrane with highly caustic solutions.

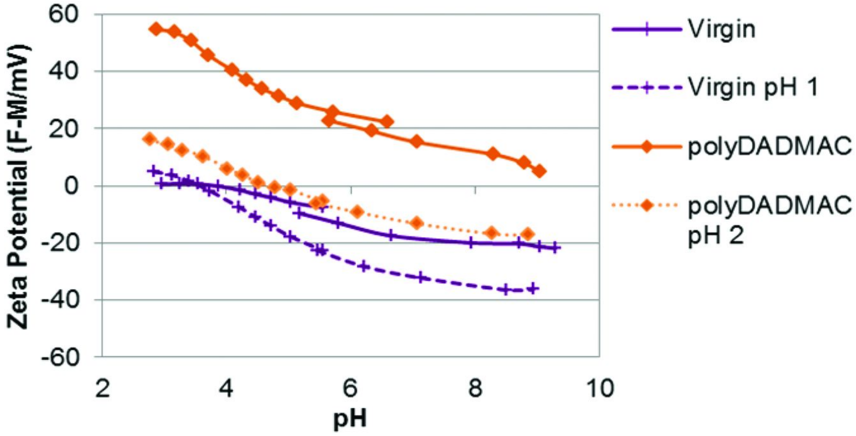

Figure 4. SurPASS titrations of virgin, polyDADMAC coated, and acid-washed membranes. PolyDADMAC imparted a strong positive charge and was nearly completely removed with a 30 minute pH 2 wash. Strong acid washing of the virgin membrane with a pH 1 wash altered the surface chemistry of the membrane.

TiO_2-PD(+) Coating and Removal

The TiO_2-PD(+) nanoparticle, despite containing polyDADMAC, had a very different physical character from the polymer. Coating of the virgin membrane with this positive NP was expected to impart a charge comparable to polyDADMAC but resulted in a significantly lesser positive charge, indicating a lower charge density (Figure 5). Acid washing was extremely effective in removing this coating, suggesting that the lower charge density may have been a beneficial property; whereas polyDADMAC was nearly removed with a strong acid wash, the TiO_2-PD(+) coating was removed as efficiently with a pH 3 wash as with pH 2 (Figure 6). In the control sample, layering the TiO_2-PD(+) over polyDADMAC decreased the positive character of the polyDADMAC polymer, confirming the lesser positive charge of the NP.

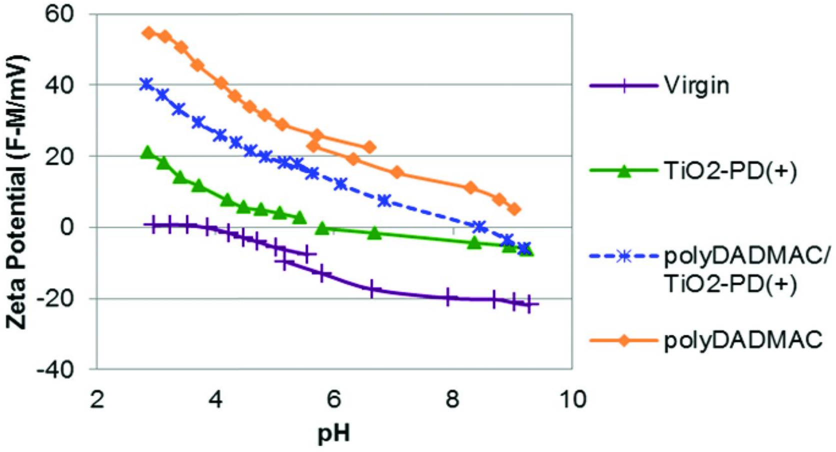

Figure 5. Comparison of TiO_2-PD(+) and polyDADMAC surface charge. TiO_2-PD(+) NPs decreased the positive character of the polymer layer, and was much less positively charged when coated onto the bare membrane.

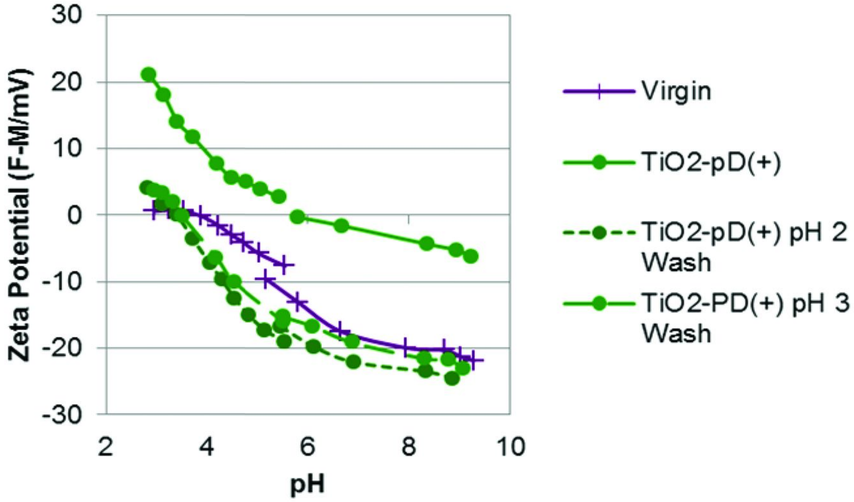

Figure 6. Acid cleaning results of TiO_2-PD(+) coating. NP coating was very effectively removed from the membrane at pH 2 as well as pH 3, which was equally effective.

Negatively Charged NPs Self-Assemble onto Polydadmac-Coated Membranes

Negatively charged NPs were self-assembled onto the membrane using polyDADMAC as a binding layer. Both NPs decreased the positive charge imparted by polyDADMAC, indicating the charged character of each NP. Ag-PA(-) decreased the positive charge much more than did the TiO_2-PA(-). It was discovered after these experiments that the Ag-PA(-) coating solution was a much higher concentration than the TiO_2-PA(-) coating solution, which may explain the greater effectiveness of the Ag-PA(-) coating. The Ag-PA(-) appears to have a more negative character in Figure 7, but this could be caused merely by the concentration difference.

Controls of both Ag-PA(-) and TiO_2-PA(-) increased both the overall charge of the membrane and the isoelectric point. Ag-PA(-) increased the isoelectric point from ~3.75 to ~4.5 and TiO_2-PA(-) increased the isoelectric point to ~5.0. These increases indicate that the NPs can bind to the membrane despite charge repulsion and need to be carefully monitored to ensure complete removal during cleaning.

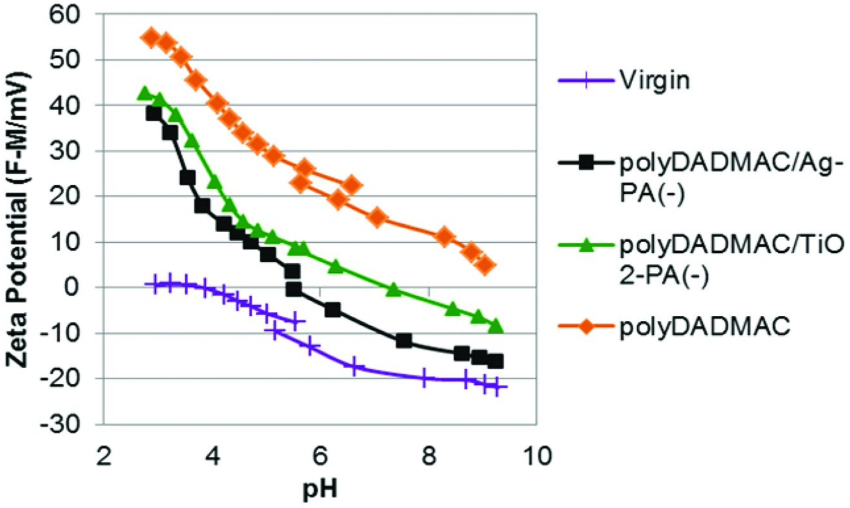

Figure 7. Zeta potential measurement of negative NPs after self-assembly onto a polyDADAMAC layer. Both negative NPs reduced the net charge of the membrane surface.

ATR-FTIR

ATR-FTIR measurements were taken for several membrane samples, including virgin membrane, polyDADMAC coated, and each negative NP coated onto polyDADMAC. No discernible differences among the spectra were observed. This is likely due to the mass of nanoparticles and polymer on the surface of the membrane being quite small. The full thickness of the active layer was penetrated by this analysis and the backing layer dominated the spectrum. Any contribution from polyDADMAC C-C or C-N bonds would be difficult to discern from those of membrane polyamide. Thus it was reasoned that the coatings were quite thin, even though they were able to significantly alter the surface charge. This bodes well for membrane flux (to be measured in future work), as the thin coatings would not be expected to greatly increase the inherent water transport resistance of the RO membrane.

Contact Angle Measurements

Contact angle measurements were made for most of the samples prepared for this study, but large standard deviation and results that were inconsistent with several literature studies made these results suspect. When sessile-drop method results were inconsistent with reported values the captive-bubble method was attempted, but the results were inconsistent with literature as well as with sessile-drop results. The results that were obtained showed very little deviation between the virgin membrane and double layer coatings, with a contact angle of approximately 80 degrees. Results for polyDADMAC showed an increase in contact angle to approximately 105 degrees. These results, if reliable, demonstrate that association with the membrane surface decreased the highly hydrophilic nature of polyDADMAC polymer. This decrease indicates that the charged ammonium group of the polymer interacts with negatively charged functional groups on the membrane surface, rather than van der Waals interactions of the hydrocarbon portions.

SEM Imaging

SEM imaging (Figure 8) was performed for virgin, coated and cleaned membranes. Images did not show significant presence of polyDADMAC or polyDADMAC/TiO_2-PA(-). Aggregates of Ag-PA(-) were observable, which led to the discovery that the coating solution was ten times more concentrated than originally calculated. The silver aggregates became a useful indicator of cleaning effectiveness in SEM imaging, however, as the lack of aggregates after high pH cleaning indicated that the nanoparticles had been successfully dissolved or removed. The lack of observable coating layers encourages the conclusion that polyDADMAC and functionalized NP coatings will not significantly alter the flux through the membrane.

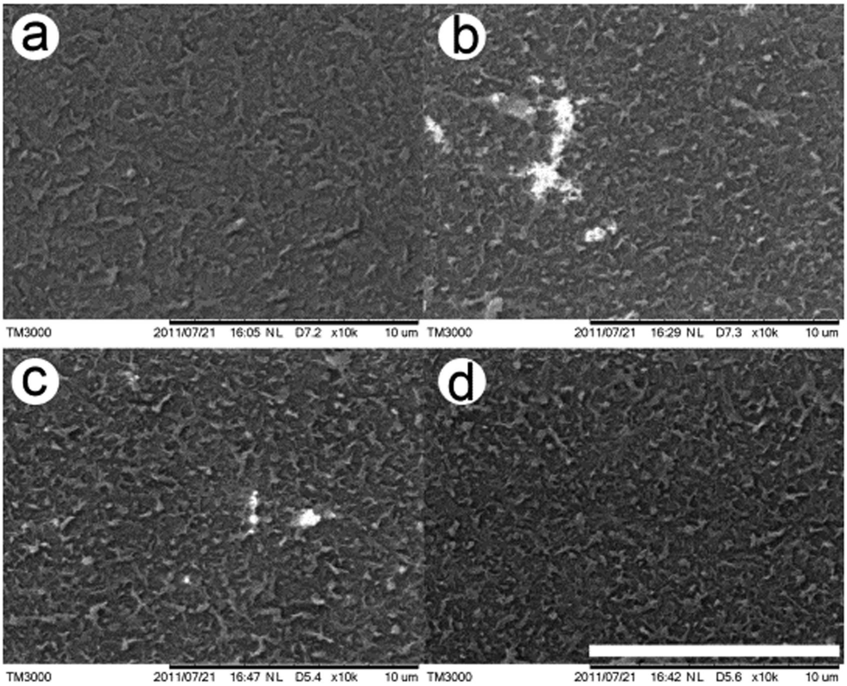

Figure 8. SEM images of (a) virgin RO membrane, (b) polyDADMAC/Ag-PA(-) coating, (c) Ag-PA(-) coating after pH 1 acid wash, and (d) Ag-PA(-) coating after pH 13 base wash. White scale bar is 10 µm.

Conclusions

The surface charge of RO membranes was made more positive by the addition of polyDADMAC and/or positively charged nanoparticles. The charge was further modified by adding a second layer of negatively charge functionalized NPs on top of the polyDADMAC. These layers were stable in deionized water overnight and in some cases for several days, but were readily removed by rinsing with an acidic solution. This indicates that these materials could potentially serve as easily washable coatings for RO membranes. However, it was unclear the extent to which the membrane was coated; patchy surface coverage was observed with silver NPs, and similar patchiness may occur with other materials. It is also unclear whether these coatings would be sufficient to prevent other foulants like natural organic matter from attaching irreversibly to the membrane. These questions will be explored in future work.

References

1. Van de Lisdonk, C.; Van Paassen, J.; Schippers, J. *Desalination* **2000**, *132*, 101–108.
2. Ng, H. Y.; Elimelech, M. *J. Membr. Sci.* **2004**, *244*, 215–226.
3. Khan, M. M. T.; Stewart, P. S.; Moll, D. J.; Mickols, W. E.; Burr, M. D.; Nelson, S. E.; Camper, A. K. *J. Membr. Sci.* **2010**, *349*, 429–437.
4. Ba, C.; Ladner, D. A.; Economy, J. *J. Membr. Sci.* **2010**, *347*, 250–259.
5. Taniguchi, M.; Kilduff, J. E.; Belfort, G. *J. Membr. Sci.* **2003**, *222*, 59–70.
6. Zhou, M.; Liu, H.; Kilduff, J. E.; Langer, R.; Anderson, D. G.; Belfort, G. *Environ. Sci. Technol.* **2009**, *43*, 3865–3871.
7. Gu, M.; Kilduff, J. E.; Belfort, G. *Biomaterials* **2012**, *33*, 1261–1270.
8. Childress, A. E.; Elimelech, M. *J. Membr. Sci.* **1996**, *119*, 253–268.
9. Childress, A. E.; Elimelech, M. *Environ. Sci. Technol.* **2000**, *34*, 3710–3716.
10. Al-Amoudi, A.; Williams, P.; Mandale, S.; Lovitt, R. W. *Sep. Purif. Technol.* **2007**, *54*, 234–240.
11. Buksek, H.; Luxbacher, T.; Petrinic, I. *Acta Chim. Slov.* **2010**, *57*, 700–706.
12. Hurwitz, G.; Guillen, G. R.; Hoek, E. *J. Membr. Sci.* **2010**, *349*, 349–357.
13. Brant, J. A.; Childress, A. E. *J. Membr. Sci.* **2004**, *241*, 235–248.
14. Drelich, J.; Miller, J. D.; Good, R. J. *J. Colloid Interface Sci.* **1996**, *179*, 37–50.
15. Gao, L.; McCarthy, T. J. *Langmuir* **2006**, *22*, 6234–6237.
16. Cho, J.; Amy, G.; Pellegrino, J.; Yoon, Y. *Desalination* **1998**, *118*, 101–108.
17. Coronell, O.; Gonzalez, M. I.; Marinas, B. J.; Cahill, D. G. *Environ. Sci. Technol.* **2010**, *44*, 6808–6814.
18. Belfer, S.; Purinson, Y.; Kedem, O. *Acta Polym.* **1998**, *49*, 574–582.
19. Gabelich, C. J.; Ishida, K. P.; Bold, R. M. *Environ. Prog.* **2005**, *24*, 410–416.
20. Tang, C. Y.; Kwon, Y.; Leckie, J. O. *Desalination* **2009**, *242*, 168–182.
21. *Instruction Manual SurPASS Electrokinetic Analyzer*; Anton-Paar GmbH: Graz, Austria, 2009.

Chapter 12

Hematite Nanoparticle Modified Granular Activated Carbon for Removal of Arsenic and Organic Co-Contaminants

Arti Jain, Jeremy Sanner, Robert Sandoval, and Kiril Hristovski*

**Environmental Technology, Department of Applied Sciences and
Mathematics, College of Technology and Innovation,
Arizona State University at the Polytechnic Campus,
6073 South Backus Mall, Mesa, Arizona 85212, United States
*E-mail: kiril.hristovski@asu.edu. Telephone: 1-480-727-1291**

The goal of this study was to determine whether hematite nanoparticles could be synthesized within the pores of granular activated carbon (GAC) media by hydrolysis of ferric salt to effectively remove arsenic and organic co-contaminant from water. Five task-oriented objectives were undertaken to address this goal: (1) hematite modified GAC media was fabricated; (2) properties of the fabricated media were characterized; (3) arsenic adsorption capacity was evaluated under batch pseudo-equilibrium conditions in different water matrices; (4) adsorption capacity of the fabricated media was evaluated for model organic co-contaminant (methylene blue) under batch pseudo-equilibrium conditions; and (5) short bed column tests were conducted to estimate adsorption capacity under continuous flow conditions. Four different hybrid media were fabricated characterized with iron contents ranging from 0.9% to 4.4% of Fe per dry weight. Longer hydrolysis times in solutions with lower concentrations of ferric salt allow for higher iron content, better distribution of the nanoparticles and formation of pore volume in the macropore region. Characterized by the low Freundlich intensity parameters ($1/n < 1$), the hybrid media with highest iron content exhibited better arsenic adsorption capacity and selectivity in waters with low arsenic concentrations than their counterparts. The introduction of nanoparticles within the

In Novel Solutions to Water Pollution; Ahuja, S., et al.;
ACS Symposium Series; American Chemical Society: Washington, DC, 2013.

pores of the granular activated reduced the adsorption capacity of the hybrid media for the model organic co-contaminant (methylene blue), but it did not affect the energy of adsorption.

Keywords: arsenic; activated carbon; adsorption; nanoparticle; hematite; iron

Introduction

Contamination of the water environment with arsenic from both natural and anthropogenic sources has been recognized as a problem in number of developing and developed countries, such as Bangladesh, Chile, Taiwan, India and the USA (*1–4*). Arsenic in drinking water represents a major health problem because of the ascertained health risks associated with low-level exposure to this contaminant (*5*). A number of epidemiological studies have documented the association between chronic exposure to arsenic in drinking water and cancer of the skin, liver, bladder, kidney, lung, and prostate (*6–11*). The International Agency for Research on Cancer has classified arsenic as a Class A human carcinogen by (IARC) (*12*). To protect consumers served by public water systems from the effects of long-term, chronic exposure to arsenic, the United States Environmental Protection Agency have reduced the standard for arsenic in drinking water from 0.05mg/L to 0.01mg/L, making it enforceable in January, 2006 (*13*).

To comply with the regulatory level, the USEPA has identified Best Available Technologies (BATs) to remove arsenic from groundwater (*14*). These include ion exchange, reverse osmosis, electro dialysis, enhanced coagulation/filtration, enhanced lime softening, etc. (*15–20*). Combinations of these technologies work well for removal of arsenic and other contaminants by large scale water treatment systems. However, technologies employed in large scale water treatment systems are economically not feasible for treatment systems serving small communities. Technologically simper and inexpensive point-of-use and point-of-entry systems are more suitable to provide safe drinking water for small communities.

According to the USEPA, adsorption has proven to be a fairly easy to operate, effective technology for small water treatment systems with low operating and maintenance costs. It has also been demonstrated that adsorption is successful in addressing the need for potable water in small communities (*14–21*). Granular activated carbon is one of the primary materials used in water treatment via adsorption because of its large surface area, porosity, and low cost (*22–24*). This adsorbent, however, is only efficient for removal of organic contaminants such as ones that cause undesirable taste, color and odor in water (*25–33*). Unfortunately, activated carbon is not a suitable adsorbent for removal of oxo-anions from water such as arsenate or arsenite. For these contaminants, ferric hydr(oxides) have been proven to be effective adsorbents (*34*). It has been reported that arsenic species form inner-sphere bidentate and monodentate ligands on the surface of these metal (hydr)oxides as they undergo ligand exchange reaction with iron species (*35*, *36*).

Starting with the premise that iron (hydr)oxide could be successfully combined with granular activated carbon (GAC) media to produce novel hybrid media, recently published research has demonstrated that these newly developed hybrid media are capable of removing arsenic in water along with organic co-contaminants (*37–41*). However, fabrication of such hybrid materials often involves multiple steps and generates large quantities of hazardous waste. So the need still exists to develop simpler and inexpensive approaches to fabricate these hybrid iron (hydr)oxide modified granular activated media (Fe-GAC).

In-situ hydrolysis of hematite nanoparticles within the pores of granular activated carbon media could possibly offer an alternative approach for simple fabrication of inexpensive Fe-GAC media. To this date, no study has been conducted to demonstrate the feasibility of this concept although generation of ferric (hydr)oxide particles has extensively been studied. Matijevic and his collaborators (*42*, *43*) have demonstrated that forced hydrolysis of ferric salts produces hematite particles (*42*). If synthesized within the pores of GAC media, these nanoparticles could used in removing arsenic from water while allowing the GAC to remove organic contaminants. Therefore, the goal of this study was based on the hypothesis that hematite nanoparticles could be synthesized within the pores of GAC media by hydrolysis of ferric salt to effectively remove arsenic and organic co-contaminant from water. To achieve this goal, the following task-oriented objectives were undertaken: (1) hematite modified GAC media was fabricated under two initial ferric salt concentrations and two hydrolysis periods to assess the effect of these parameters on nanoparticle formation and media performance; (2) properties of the fabricated media were characterized; (3) arsenic adsorption capacity was evaluated under batch pseudo-equilibrium conditions (a) in absence of competing ions to estimate the maximum adsorption capacity of the fabricated media, and (b) in presence of competing ions to estimate performance under realistic groundwater conditions; (4) adsorption capacity of the fabricated media was evaluated for model organic co-contaminant (methylene blue) under batch pseudo-equilibrium conditions; and (5) short bed column tests were conducted to estimate adsorption capacity under continuous flow and constant initial concentration conditions in model groundwater.

Experimental Approach

Fabrication of the Hematite Nanoparticle Modified Hybrid Granular Activated Carbon Media

HydroDarco 3000 (HD3000), a lignite based GAC obtained from NORIT Americas Inc. USA, was used to fabricate the hematite nanoparticle modified hybrid granular activated carbon media. Lignite based GAC was selected because of its superior macroporosity when compared to other carbon media such as bituminous coal based GAC (*37*, *44*).

Four types of hematite modified hybrid granular activated carbon media were fabricated via a modified synthesis method published by Matejevic et al. (*42*) in which it was demonstrated that hematite particles can be generated by forced hydrolysis of ferric chloride at elevated temperatures. In brief, two initial concentration of ferric chloride (0.5 M and 2 M) were prepared and used for in-situ synthesis of the hematite nanoparticles. Aliquots of 50 g of HD-3000 media and 500 mL of the appropriate ferric chloride solution were gently mixed together in amber bottles for a period of 15 hours to ensure equilibration of the ferric chloride solution and the GAC media. Upon equilibration, the amber bottles were covered with watch glasses to prevent evaporation and placed in a temperature controlled oven at 100 °C for periods of either 24 hours or 72 hours to synthesize the hematite nanoparticles within the pores of the GAC media. The hematite synthesis can be illustrated with Equation 1:

$$2Fe^{3+} + 3H_2O \rightarrow Fe_2O_3 + 6H^+ \qquad (1)$$

The hydrolysis process generates acid which was neutralized by repetitive rinsing of the fabricated media in 2% $NaHCO_3$ solution and ultrapure water (< 1 µS/cm) until the pH reached a value ≥ 5. Upon rinsing, the media was stored in ultrapure water and used wet.

Characterization of the Hematite Modified Hybrid Granular Activated Carbon Media

Moisture content of all media used in the study was determined using a picnometer measurements as described by Sontheimer et al. (*45*). Iron content of the dry media was determined by acid digestion according to USEPA SW 846, Method 3050B (*46*). Focus Ion Beam/Scanning Electron Microscopy (FEI NOVA 200 Nanolab UHR FEG-SEM/FIB) equipped with a backscatter detector was used to provide high magnification images of the deposited nanoparticles within the media pores. With the help of this backscatter detector heavier elements, like iron, and lighter elements, like carbon, nitrogen, and oxygen can be distinguished as light areas and dark areas, respectively. Zeta-potential analysis was conducted and the isoelectric point (IEP) was estimated on all synthesized hybrid media and untreated GAC media using Phase Analysis Light Scattering technique in 10 mM KNO_3 as a background electrolyte (ZetaPALS Brookhaven Instruments Corporation, Holtsville, NY). Pore size distribution and Brunauer Emmett and Teller (BET) surface area were estimated using Micrometrics Tristar-II 3020 automated gas adsorption analyzer.

Removal of Arsenic and Methylene Blue by the Hematite Modified Hybrid Granular Activated Carbon Media

To assess the arsenic removal capacity of hybrid media, batch equilibrium tests were conducted with two types of model water matrices: (1) model water with arsenic only (no competing ions) to estimate the maximum arsenic adsorption capacity of the media; and (2) model water simulating a challenge groundwater matrix to estimate arsenic adsorption capacity of the media under realistic conditions. The arsenic only model water was characterized by initial arsenate concentration of ~120 µgAs/L and 1 mM $NaHCO_3$ buffered ultrapure water.

Detailed composition of the model water simulating the challenge groundwater matrix is provided in Table 1.

Batch pseudo-equilibrium tests at pH = 7.7 ± 0.2 were conducted for arsenic with both model waters and dry media dosages ranging from 0.12 g/L to 5.6 g/L. Nalgene HDPE bottles, which contained 100 mL of model water, were used in the tests. The contact time was three days, which was considered sufficient for pseudo-equilibrium to occur. Upon equilibration, aliquots were filtered through GFF filter and analyzed for arsenic using Graphite Furnace Atomic Adsorption Spectroscopy (GF-AAS) (Varian Spectra 50B GTA-110).

Batch pseudo-equilibrium tests for both the model organic co-contaminant and the untreated GAC media were conducted to assess the effect of nanoparticle formation on the media's capacity to remove organic contaminants. The tests were conducted in Teflon capped amber bottles containing 100 mL aliquots of methylene blue solution with initial concentration of 50 mg/L. Dry media dosages ranging from 0.06 to 0.5 g/L dry mass were mixed with the methylene blue solution for a period of three days. Upon equilibration, aliquots were filtered through GFF filter and analyzed for methylene blue using UV spectroscopy (Jenway 6405 UV/Vis) with peak wavelength of 665 nm (*47*).

Isotherms were developed for arsenic and methylene blue adsorption and analyzed using Freundlich adsorption model (Equation 2):

$$q = KC_E^{\frac{1}{n}} \tag{2}$$

where q is the adsorption capacity ([M] adsorbate $[M]^{-1}$ adsorbent); K is the Freundlich adsorption capacity parameter ([M] adsorbate $[M]^{-1}$ adsorbent)($[L]^3$ $[M]^{-1}$ adsorbate)$^{1/n}$, C_E is the equilibrium concentration of adsorbate in solution ([M] adsorbate $[L]^{-3}$), and $1/n$ is the Freundlich adsorption intensity parameter (unitless), which is related to the energy of adsorption (*22*).

To assess the impact of contaminant mass transport on the adsorption capacity of the synthesized media under continuous flow conditions, short bed column tests with model groundwater were conducted. Briefly, a ~ 4 cm deep bed containing the synthesized media was packed on top of a quartz sand supported on hydrated glass wool and glass beads in 30 a cm long glass column with internal diameter of 1.1 cm (Ace Glass). Glass beads were placed above and below the support materials to provide evenly distributed flow. The continuous flow short bed adsorber tests were conducted at realistic hydraulic loading rates of 6.8 L/s/m^2 which represents the high end of the recommended hydraulic loading range for operating adsorbers packed with GAC media (*48*). The operating conditions for the continuous flow column tests conducted with different media are summarized in Table 2. The pH of the influent was 7.5 ± 0.2 and the initial arsenic concentration was ~ 130 μgAs/L. Samples were collected at predetermined time intervals and analyzed for arsenic.

The maximum adsorption capacities of the media obtained under continuous flow conditions were calculated using Equations 3 and 4.

$$\int_0^{m_{maz}} m_{As} = Q\int_0^t \left(C_0 - C_{ef}\right)(t)dt \tag{3}$$

where m_{As} is the mass of adsorbed arsenic [M]; C_0 and C_{ef} are initial and effluent concentrations of arsenic $[M][L]^{-3}$; Q is the flow rate of water $[L]^3[T]^{-1}$; and t is time of the collected sample [T].

$$q_{\max} = \frac{m_{\mathrm{As}}}{m_{\text{dry media}}} \qquad (4)$$

where q_{max} is the maximum adsorption capacity obtained under continuous flow conditions ([M] adsorbate $[M]^{-1}$ adsorbent); and $m_{dry\ media}$ is the mass of dry media used in the column test [M].

Table 1. Composition of the Model Groundwater Matrix

Ion Species	*Conc. of Ion (mg/L)*	*Added As*
N as NO_3^-	1.6	$NaNO_3$
F^-	1.1	NaF
PO_4^{3-}	0.069	$NaH_2PO_4.H_2O$
B^-	6.6	H_3BO_3
Pb(II)	0.002	$Pb(NO_3)_2$
Cr(III)	0.001	$CrK(SO_4)_2.12H_2O$
Fe(III)	0.075	$FeCl_3.6H_2O$
Mn(II)	0.029	$MnCl_2.4H_2O$
V(III)	0.007	Na_3VO_4
Se(IV)	0.003	$SeCl_4$
As(V)	0.12	$Na_2HAsO_4.7H_2O$
Al(III)	0.046	$Al_2(SO_4)_3.18H_2O$
Cu(II)	0.031	$CuSO_4.5H_2O$
Zn(II)	0.101	$ZnSO_4.7H_2O$
Mo(VI)	0.007	$Na_2MoO_4.2H_2O$
SiO_2	20	$Na_2SiO_3.9H_2O$
Mg^{2+}	12	$MgSO_4.7H_2O$
SO_4^{2-}	196.56	$MgSO_4.7H_2O$
Ca^{2+}	40	$CaCl_2$

Table 2. Operating Conditions for the Continuous Flow Column Tests Conducted with Different Media

Column Experiment	*Adsorbent media used*	*Column Depth (cm)*	*Mass of Media (g)*	*Flow rate (mL/min)*
C 1	0.5M-24hr	4	1.46	39
C 2	2M-24hr	4.1	1.63	39
C 3	0.5M-72hr	4	1.55	39.1
C 4	2M-72hr	3.9	1.45	39.5

Results and Discussion

Characterization of the Hematite Modified Hybrid Granular Activated Carbon Media

The iron content of the untreated GAC was < 0.002% of Fe per dry weight of the adsorbent. The in-situ hydrolysis of the hematite nanoparticles increased the iron content several orders of magnitude as illustrated in Figure 1. The iron content of the fabricated media by 24 hour hydrolysis with 0.5 M ferric chloride was 0.9% Fe per dry adsorbent weight, while the 2 M solution of ferric chloride contributed to approximate 1.7% of Fe per dry adsorbent weight under same hydrolysis time and temperature conditions. The 72 hour hydrolysis resulted in 2.2% and 4.4% of Fe per dry adsorbent weight for both 0.5 M and 2 M hydrolysis condition, respectively. While a small increase in the iron content was observed for the 2 M condition when the hydrolysis time was changed from 24 hours to 72 hours, the 0.5 M-72 hours condition yielded media with five times higher iron content than its counterpart media which was hydrolyzed for 24 hours.

Interestingly, however, the hybrid media with lowest iron content exhibited an increase in the surface area (Figure 2). This trend could be attributed to formation of very small nanoparticles inside the pores of the media causing an overall increase in surface area. Figure 3 demonstrates the existence such nanoparticles within the pores of the GAC media. As the hydrolysis progresses, these nanoparticles increase in size and numbers, providing for even distribution of the iron within the pores of the media, but also causing limited reduction in the media's surface area as illustrated in Figure 4. In contrast, during the hydrolysis with the more concentrated solution of ferric chloride, the surface area initially decreased probably because of formation of larger hematite nanoparticles that cause greater blockage of the smaller pores (micro- and mesopore region). However, prolonged hydrolysis caused increase in surface area. It could be hypothesized that once most of the Fe^{3+} is bound in the larger hematite nanoparticles and its concentration is reduced, smaller nanoparticles start growing which cause the similar trends observed during the hydrolysis of the 0.5 M solution.

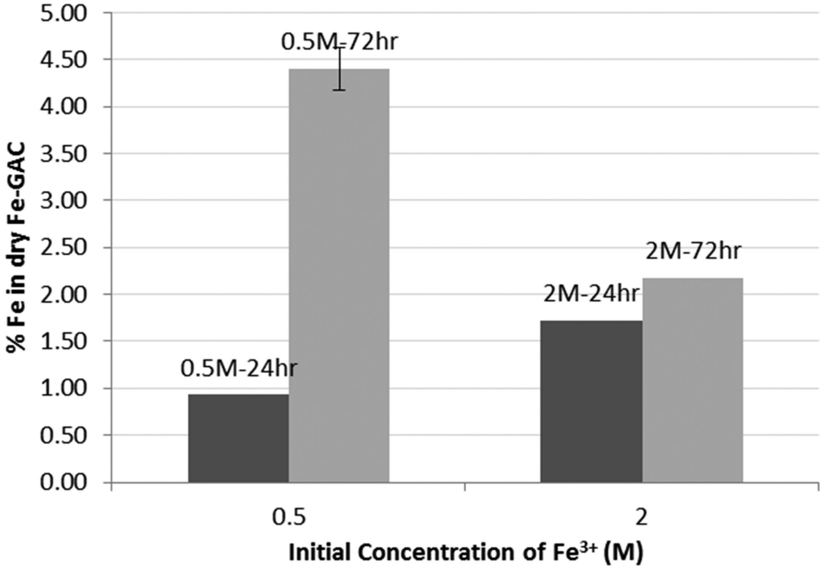

Figure 1. Iron content of the fabricated hematite modified hybrid granular activated carbon media. Error bars represent 95% confidence intervals based on a triplicate.

The pore blockage in the micropore and mesopore region is illustrated in Figure 5. In general, the hybrid media with the lowest surface area (2M-72HR) exhibited the greatest loss of pore volume, which provides additional support to the theory that the higher initial concentration of Fe^{3+} caused greater blockage of the smaller pores. In contrast, the 0.5M-72HR counterpart increase in pore volume in the region above 1200 Å although it followed the same trend in the micropore and mesopore region. This suggests that longer hydrolysis with less concentrated solutions could be more suitable for fabricating these hybrid media because it provides for media with higher iron content, negligible surface area loss and improved porosity in the macropores region. This disposition is further supported by the zeta potential data which is presented in Figure 6. Only 0.5M-72HR hybrid media exhibited increase in the iso-electric point of the media. While the iso-electric point of all other hybrid media did not change after the synthesis of the nanoparticles and remained at ~ 3.5, the iso-electric point of the media with highest iron content increased to ~ 5.2. Considering that metal (hydr)oxide nanoparticles have an iso-electric point of about 8.8-9 (*38*), only a large number of evenly distributed hematite nanoparticles onto the surface could sufficiently counterbalance the negatively charged surface of the lignite based GAC media to cause positive shift in the iso-electric point. Larger particles, like the one illustrated in Figure 7, contribute to greater positive charge localization and exhibit significantly lower specific surface area than smaller nanoparticles evenly distributed on the surface of the GAC media. These large hematite particles may be insufficient to cause an increase in the overall iso-electric point although they incorporate much of the iron within the hybrid media.

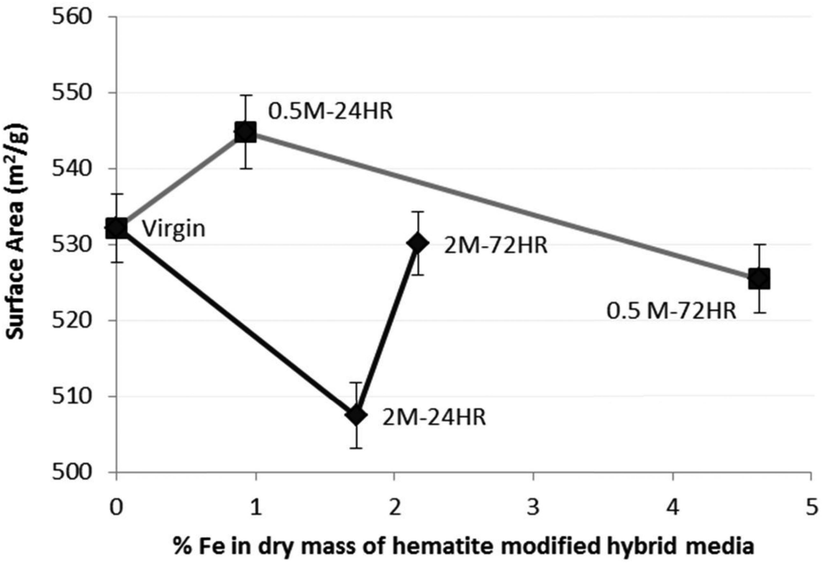

Figure 2. Relationship between surface area and the iron content of the fabricated hybrid media.

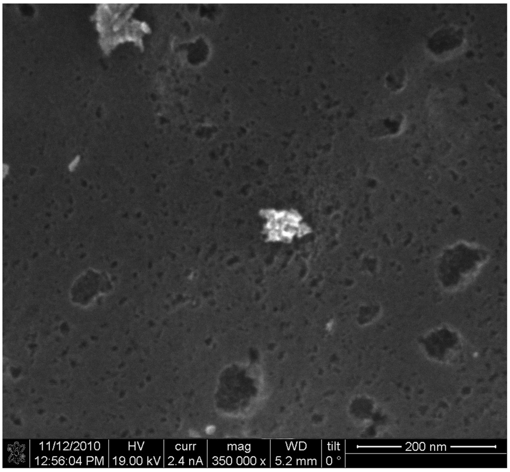

Figure 3. Existence of small hematite nanoparticles inside the pores of the hybrid granular activated carbon increasing its overall surface area.

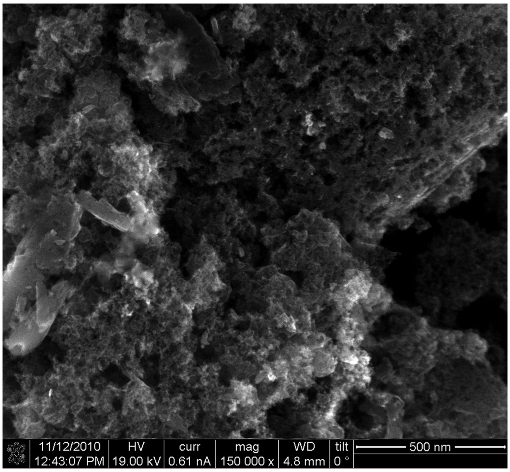

Figure 4. Hematite nanoparticles within the hybrid media granular activated carbon media evenly coating the pores and causing limited reduction in surface area.

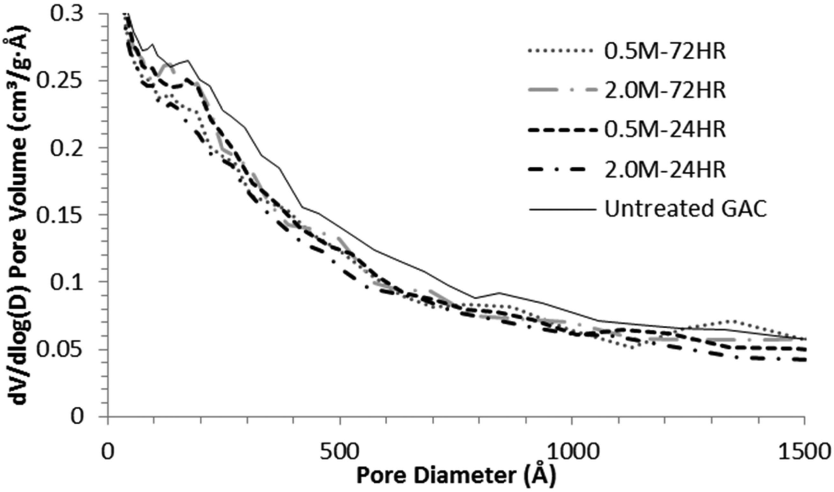

Figure 5. Differential pore volume as a function of pore diameter.

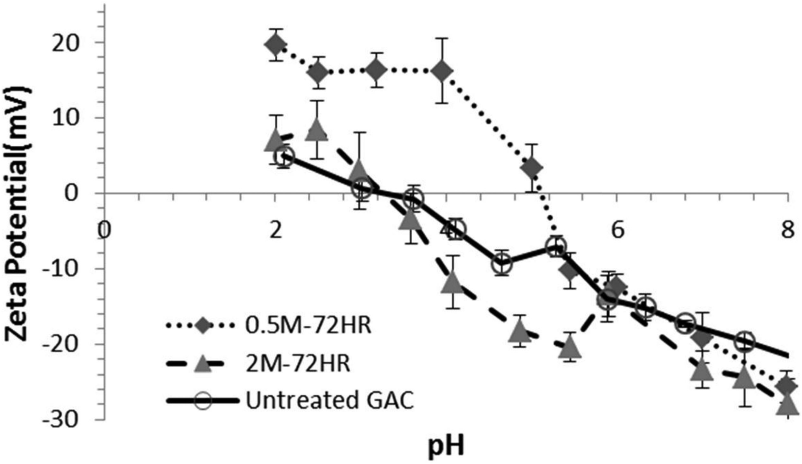

Figure 6. Change in the iso-electric point of 0.5-72HR hematite modified hybrid granular activated carbon media.

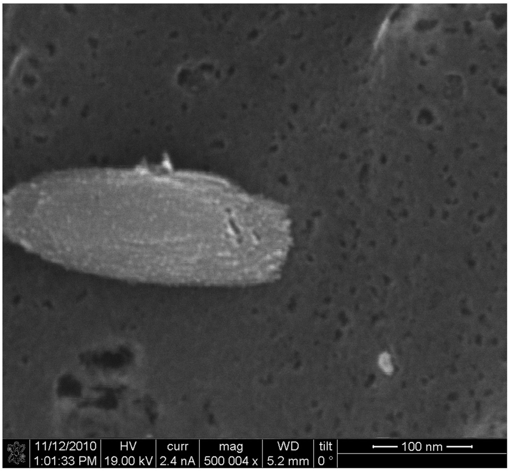

Figure 7. Large hematite particles within the pores of the hybrid granular activated carbon media.

Removal and Co-Contaminants by the Hematite Modified Hybrid Granular Activated Carbon Media

Table 3 summarizes Freundlich model parameters for the isotherms based on the data obtained from the batch tests conducted in both model waters. The Freundlich intensity parameters for 1 mM $NaHCO_3$ buffered ultrapure water with no arsenic co-contaminants were $1/n < 1$ for the media fabricated with 0.5 M solution of ferric chloride, which implies favorable adsorption for arsenic and good performance of these media in waters with low arsenic concentrations. In contrast, the media fabricated with 2 M solution of ferric chloride exhibited Freundlich intensity parameters $1/n \approx 1.1$, which are indicative of slightly unfavorable absorption of arsenic in low concentrations. However, the $1/n > 1$ suggests that the media may be suitable for treatment waters containing relatively high concentrations of arsenic. Table 4 summarizes the estimated maximum arsenic adsorption capacities under two initial arsenic concentrations, 5 μgAs/L and 100 μgAs/L simulating waters with very low and high arsenic concentrations, respectively. At low initial arsenic concentrations the 0.5M-72HR media exhibits highest maximum adsorption capacity of 19.4 μg As/$g_{\text{Dry Media}}$ probably because the electrostatic barrier is lower as a result of the even distribution of hematite the nanoparticles (described by increase in the iso-electric point). At these conditions, the energy necessary for arsenic to adsorb onto the media's surface is lower. This disposition coupled with the low ratio between dissolved arsenic species and available adsorption sites allows for formation of more thermodynamically stable inner-sphere bidentate ligands at low initial arsenic concentrations (*36*). With increase of the initial arsenic concentration, however; the ratio between dissolved arsenic species and available adsorption increases, consequently increasing the competition effect among dissolved arsenic species for the limited adsorption sites. The greater number of arsenic species attempting to adsorb on the media's surface, in turn, creates sufficiently high potential to overcome the necessary higher adsorption energy requirements, which are described by the higher 1/n values. This disposition causes the arsenic species to start forming thermodynamically less favorable complexes (e.g. monodentate), which consequently allows for denser packing of arsenic species and greater adsorption capacity of the media (*36*, *49*).

Similar effects can be observed in the presence of competing ions. The competing ions present in the model groundwater such as silica, phosphate and vanadate, decrease the adsorption capacity of the media by several fold (Table 4). With exception of the 0.5M-72HR media, this decrease is even more drastic, reaching an order of magnitude at low initial arsenic concentrations. It appears that the properties of the 0.5M-72HR media hybrid media (e.g. higher iso-electric point, greater iron content, high surface area and better pore size distribution) create a mitigating effect evidenced by negligible decrease of this media's adsorption capacity at low initial arsenic concentrations and its favorable Freundlich intensity parameter of $1/n < 0.47$ (Table 4).

Table 3. Freundlich Isotherm Parameters for Removal of Arsenic by the Hematite Nanoparticle Modified Hybrid Granular Activated Carbon Media Tested in the Two Model Water Matrices at pH ≈ 7.7 ± 0.2 and C_0 ≈ 120 μgAs/L

Media ID	*% Fe*	*1mM $NaHCO_3$ Matrix*			*Groundwater Matrix*		
		*K**	*1/n*	*R^2*	*K**	*1/n*	*R^2*
0.5M-24hr	0.93	2.5	0.86	0.82	0.2	1.32	0.94
2M-24hr	1.72	1.8	1.10	0.95	0.3	1.11	0.91
0.5M-72hr	4.4	6.8	0.65	0.94	8.0	0.47	0.97
2M-72hr	2.17	2.4	1.11	0.97	0.1	1.48	0.90

$$* \ \frac{\dfrac{\mu\text{g As}}{\text{g}_{\text{Dry Media}}}}{\left(\dfrac{\mu\text{g As}}{\text{L}}\right)^{\frac{1}{n}}}$$

Table 4. Maximum Adsorption Capacities under Equilibrium Conditions Estimated Using the Experimentally Obtained Freundlich Isotherm Parameters and Initial Arsenic Concentrations of 5 μg As/L (q_5) and 100 μg As/L (q_{100})

Media ID	*1mM $NaHCO_3$ Matrix*		*Groundwater Matrix*	
	q_5^*	*q_{100}^**	*q_5^**	*q_{100}^**
0.5M-24hr	10.1	137.4	1.9	100.4
2M-24hr	10.7	290.0	1.7	46.5
0.5M-72hr	19.4	136.3	17.0	69.4
2M-72hr	14.4	401.6	1.2	100.3

$$* \ \frac{\mu\text{g As}}{\text{g}_{\text{ Dry Media}}}$$

The competition effect created by the co-contaminants is further magnified by the mass transport limitations exerted under continuous flow conditions. Many co-contaminant species that are competing with arsenic, such as silica ($D_{l\text{–Silica}}$ ≈ 1.170 x 10^{-5} cm^2/s), phosphate ($D_{l\text{–Dihydrogen phosphate}}$ ≈ 0.959 x 10^{-5} cm^2/s), or selenate ($D_{l\text{–Selenate}}$ ≈ 1.008 x 10^{-5} cm^2/s), exhibit higher liquid diffusivities than arsenate ($D_{l\text{–Arsenate}}$ ≈ 0.905 x 10^{-5} cm^2/s) (*50*, *51*). Higher liquid diffusivities contribute to lower film and intraparticle mass transport resistance. Because of their lower mass transport resistance, these co-contaminants diffuse much faster inside the media pores than does arsenate. This allows them to reach unoccupied adsorption sites before the arsenic does; consequently magnifying the competition effect. This mass transport facilitated competition is more discernible under continuous flow conditions than under batch pseudo-equilibrium conditions because of the constant influent concentration and greater concentration gradient during continuous flow testing. Table 5 illustrates this effect by comparing the maximum adsorption capacities estimated at initial arsenic concentrations of 130 µg As/L and the observed maximum adsorption capacities under continuous flow conditions. For same initial arsenic concentration and the same model groundwater matrix, the arsenic adsorption capacity was decreased between ~2 to ~ 6 times when the testing mode was switched from batch mode to continuous flow mode, clearly emphasizing the mass transport facilitated co-contaminant competition. Under the given conditions, silica represents the greatest competitor for arsenic because its concentration is two orders magnitude greater than the one for arsenate in addition to higher liquid diffusivity.

Table 5. Comparison of the Maximum Adsorption Capacities under Equilibrium Conditions Estimated Using the Experimentally Obtained Freundlich Isotherm Parameters and Initial Arsenic Concentrations 100 µg As/L (q_{130}) in Model Groundwater and the Observed Maximum Adsorption Capacities under Continuous Flow Conditions

Sample ID	q_{130} ($\mu g\ As/g_{Dry\ Media}$)	$q_{max\ column}$ ($\mu g\ As/g_{Dry\ Media}$)
0.5M-24hr	141.9	77.4
2M-24hr	62.2	19.4
0.5M-72hr	78.5	29.6
2M-72hr	147.9	25.1

Table 6 summarizes the Freundlich isotherm parameters for removal of methylene blue by all media. The intensity parameters (1/n) of all media did not change significantly suggesting that the introduction of hematite nanoparticles within the media pores did not significantly affect the energy of adsorption. This relative constancy of the intensity parameter could be attributed to decrease in available surface area as a result of physical blocking by the hematite nanoparticles, and not as a result of change in thermodynamic states during adsorption. A linear relationship exists between the available surface area and the magnitude of the Freundlich capacity parameters for the hybrid media, which further supports the theory that the decrease in adsorption capacity is directly related to the physical blocking of the available adsorption sites by the hematite nanoparticles.

Table 6. Freundlich Isotherm Parameters for Removal of Methylene Blue (MB) by the Hematite Nanoparticle Modified Hybrid Granular Activated Carbon Media and the Untreated Media at pH ≈ 7.5 ± 0.2 and C_0 ≈ 50 mg MB/L

Sample ID	K^*	*1/n*	R^2
0.5M-24hr	82.9	0.14	0.97
2M-24hr	47.2	0.18	0.87
0.5M-72hr	56.8	0.19	0.86
2M-72hr	63.5	0.11	0.89
Untreated GAC	91.4	0.16	0.91

$$ {}^{*}\; \frac{\dfrac{\text{mg MB}}{\text{g}_{\text{Dry Media}}}}{\left(\dfrac{\text{mg MB}}{\text{L}}\right)^{\frac{1}{n}}} $$

Conclusions

Hybrid media can be fabricated by in-situ synthesis of hematite nanoparticles within the pores of granular activated carbon. Nanoparticle distribution and iron content of the hybrid media are directly related to the ferric salt hydrolysis conditions, and affect the adsorption capacity for arsenic and organic co-contaminants. Longer hydrolysis times in solutions with lower concentrations of ferric salt allow for higher iron content, better distribution of the nanoparticles and formation of pore volume in the macorpore region. Adequate selection of nanoparticle synthesis conditions could yield media that performs adequately in waters with specific arsenic concentrations and multiple co-contaminants. Although this study shows that the concept of fabricating hybrid media by -situ synthesis of hematite nanoparticles within the pores of granular activated carbon is feasible, further testing and optimization is needed to improve the arsenic adsorption capacity and overall performance of the media.

Acknowledgments

This work was supported by the Southwest Consortium for Environmental Research and Policy (SCERP) though a cooperative agreement with the U.S. Environmental Protection Agency. SCERP can be contacted for further information though www.scerp.org and scarp@mail.sdsu.edu.

References

1. Smedley, P.L.; Kinniburgh, D.H. *Appl. Geochem.* **2002**, *17* (5), 517–568.
2. Nickson, R.; McArthur, J.; Burgess, W.; Ahmed, K. M.; Ravenscroft, P.; Rahman, M. *Nature* **1998**, *395*, 338–338.
3. Nickson, R. T.; McArthur, J. M.; Shrestha, B.; Kyaw-Myint, T. O.; Lowry, D. *Appl. Geochem.* **2005**, *20*, 55–68.
4. Nickson, R.; Sengupta, C.; Mitra, P.; Dave, S. N.; Banerjee, A. K.; Bhattacharya, A.; Deverill, P. *J. Environ. Sci. Health, Part A: Environ. Sci. Eng.* **2007**, *42*, 1707–1718.
5. Jain, C. K.; Ali, I. *Water Res.* **2000**, *34* (17), 4304–4312.
6. Yoshida, T.; Yamauchi, H.; Sun, G. F. *Toxicol. Appl. Pharmacol.* **2004**, *198*, 243–252.
7. Smith, S. J. *Naturally Occurring Arsenic in Groundwater, Norman, Oklahoma, 2004, and Remediation Options for Produced Water*; Fact Sheet 2005-3111; U.S. Geological Survey: Oklahoma City, OK, 2005.
8. *Arsenic in Drinking Water. Background Document for Preparation of WHO Guidelines for Drinking Water Quality*; World Health Organization: Geneva, Switzerland, 2003.
9. Sams, R., II; Wolf, D. C.; Ramasamy, S.; Ohanian, E.; Chen, J.; Lowit, A. *Toxicol. Appl. Pharmacol.* **2007**, *222*, 245–251.
10. Mondal, D.; Adamson, G. C. D.; Nickson, R.; Polya, D.A. *Appl. Geochem.* **2008**, *23*, 2999–3009.
11. Lindberg, A. L.; Rahman, M.; Persson, L. Å.; Vahter, M. *Toxicol. Appl. Pharmacol.* **2008**, *230*, 9–16.
12. *Toxicological Profile for Arsenic*; U.S. Department of Health and Human Services: Washington, DC, 2007.
13. *EPA Basic Information about the Arsenic Rule*; U.S. Environmental Protection Agency: Washington, DC, 2012.
14. *Water Treatment Technology Feasibility Support Document for Chemical Contaminants for the Second Six-Year Review of National Primary Drinking Water Regulations*; EPA 815-B-09-007; U.S. Environmental Protection Agency: Washington, DC, 2009.
15. *Technologies and Costs for Removal of Arsenic from Drinking Water*; EPA 815-R-00-028; U.S. Environmental Protection Agency: Washington, DC, 2000.
16. *Arsenic in Drinking Water Rule: Economic Assessment*; EPA 815-R-00-026; U.S. Environmental Protection Agency: Washington, DC, 2000.
17. *Proven Alternatives for Aboveground Treatment of Arsenic in Groundwater*; EPA 542-S-02-002; U.S. Environmental Protection Agency: Washington, DC, 2002.
18. *Arsenic Treatment Technologies for Soil, Waste and Water*; EPA-542-R-02-004; U.S. Environmental Protection Agency: Washington, DC, 2002.
19. *Arsenic Removal from Drinking Water by Ion Exchange and Activated Alumina Plants*; EPA-600-R-00-088; U.S. Environmental Protection Agency: Washington, DC, 2000.

20. *Arsenic Removal from Drinking Water by Coagulation/Filtration and Lime Softening Plants*; EPA/600/R-00/063; U.S. Environmental Protection Agency: Washington, DC, 2000.
21. *Arsenic Treatment Technology Design Manual for Small Systems*; U.S. Environmental Protection Agency: Washington, DC, 2002.
22. Crittenden, J. C.; Trussell, R. R.; Hand, D. W.; Howe, K. J.; Tchobanoglous, G. *Water Treatment: Principles and Practice*, 2nd ed.; John Wiley and Sons: Hoboken, NJ, 2005.
23. Carter, M. C.; Weber, W. J. *Environ. Sci. Technol.* **1994**, *28* (4), 614–623.
24. Snoeyink, V. L.; Summers, R. S. Adsorption of Organic Compounds. In *Water Quality and Treatment. A Handbook of Community Water Supplies*; Letterman, R. D., Ed; McGraw-Hill: New York, 1999.
25. Vaughan, R. L., Jr.; Reed, B. E.; Viadero, R. C., Jr.; Jamil, M.; Berg, M. *Adv. Environ. Res.* **1999**, *3* (3), 229–242.
26. Zytner, R. G. *Water, Air, Soil Pollut.* **1992**, *65* (3−4), 245–255.
27. Crittenden, J.C.; Berrigan, J.K.; Hand, D.W. *J. Water Pollut. Control Fed.* **1986**, *58* (4), 243–259.
28. Crittenden, J.C.; Berrigan, J.K.; Hand, D.W.; Lykins, B. *J. Environ Eng.* **1987**, *113* (2), 243–259.
29. Crittenden, J.C.; Reddy, P.S.; Arora, H.; Trynoski, J.; Hand, D.W.; Perram, D.L.; Summers, R.S. *J. AWWA* **1991**, *83*, 77–87.
30. Hristovski, K. D.; Ngyuen, H. P.; Westerhoff, P. K. *J. Environ. Sci. Health, Part A:* **2009**, *44*, 354–361.
31. Baker, L. A.; Westerhoff, P.; Sommerfeld, M. *J. AWWA* **2006**, *98* (6), 113–126.
32. Lee, W.; Westerhoff, P.; Esparza-Soto, M. *J. AWWA* **2006**, *98* (10), 102.
33. Quinlivan, P.A.; Li, L.; Knappe, D.R.U. *Water Res.* **2005**, *39* (8), 1663–1673.
34. Mohan, D.; Pittman, C.U., Jr. *J. Hazard. Mater.* **2007**, *142*, 1–53.
35. Fuller, C.C.; Davis, J. A.; Waychunas, G.A. *Geochim. Cosmochim. Acta* **1993**, *57*, 2271–2282.
36. Sherman, D.M.; Randall, S. R. *Geochim. Cosmochim. Acta* **2003**, *67*, 4223–4230.
37. Nguyen, T.V.; Vigneswaran, S.; Ngo, H. H.; Pokhrel, D.; Viraraghavan, T. *Eng. Life Sci.* **2006**, *6* (1), 86–90.
38. Cooper, A.M.; Hristovski, K.D.; Moller, T.; Westerhoff, P. *J. Hazard. Mater.* **2010**, *183*, 381–388.
39. Reed, B. E.; Vaughan, R.; Jiang, L. *J. Environ. Eng.* **2000**, *126* (9), 869–873.
40. Hristovski, K.; Westerhoff, P.; Moller, T.; Sylvester, P. *Chem. Eng. J.* **2009**, *146* (2), 234–243.
41. Hristovski, K.; Westerhoff, P.; Crittenden, J.; Olson, L P. *Sep. Sci. Technol.* **2008**, *43* (11-12), 3154–3167.
42. Matijević, E.; Scheiner, P. *J. Colloid Interface Sci.* **1978**, *63* (3), 509–524.
43. Matijević, E. *Am. Chem. Soc.* **1981**, *14*, 22–29.
44. Sandoval, R.; Cooper, A.M.; Aymar, K.; Jain, A.; Hristovski, K. *J. Hazard. Mater.* **2011**, *193*, 296–303.

45. Sontheimer, H.; Crittenden, J.; Summers, S. *Activated Carbon for Water Treatment*, 2nd ed.; DVGW-Forschungsstelle, Engler-Bunte Institut, Universitat Karlsruhe: Karlsruhe, Germany, 1988.
46. *Test Methods for Evaluating Solid Waste*; Physical/Chemical Methods SW-846; U.S. Environmental Protection Agency: Washington, DC, 1996.
47. Raposo, F.; De La Rubia, M.A; Borja, R. *J. Hazard. Mater.* **2009**, *165*, 291–299.
48. Clark, R.M.; Lykins, B.W. *Granular Activated Carbon: Design Operation and Cost*; Lewis Publishers, Inc.: Chelsea, MI, 1991.
49. Pan, G.; Liss, P.S. Metastable-Equilibrium Theory I. Theoretical. *J. Colloid Interface Sci.* **1998**, *201*, 71–76.
50. Lide, D. *CRC Handbook of Chemistry and Physics*; Taylor and Francis Group: Baco Raton, FL, 2006.
51. Rebrenau, L.; Vanderborght, J.; Chou, L. *Marine Chem.* **2008**, *112*, 230–233.

Chapter 13

Titanium Dioxide-Based Hybrid Ion-Exchange Media for Simultaneous Removal of Arsenic and Nitrate

Jennifer Elton,[1] Kiril Hristovski,*,[1] and Paul Westerhoff[2]

[1]Environmental Technology, Department of Applied Sciences and Mathematics, College of Technology and Innovation,
Arizona State University at the Polytechnic Campus,
6073 South Backus Mall, Mesa, Arizona 85212, United States
[2]School of Sustainable Engineering and the Built Environment, Ira, Fulton Schools of Engineering, Arizona State University,
Interdisciplinary Science and Technology Building 4, Box 5306,
Tempe, Arizona, 85287, United States
***E-mail: kiril.hristovski@asu.edu. Telephone: 1-480-727-1291**

The goal of this study was to develop an inexpensive and easy to fabricate titanium dioxide-based hybrid ion-exchange media (Ti-HIX) and assess its potential to remove arsenic and nitrate from water. Different Ti-HIX media were fabricated via in-situ formation of TiO_2 nanoparticles within the pores of three different commercially IX resins; the Ti-HIX media were characterized; and the arsenic and nitrate removal potential of the most economically feasible Ti-HIX media was assessed in model water under batch pseudo-equilibrium conditions. The Ti-HIX media were characterized with content ranging between 11% and 21% TiO_2 per media dry mass. The TiO_2 exhibited form of anatase nanoparticles. The Freundlich adsorption intensity parameters (1/n) for all the Ti-HIX media were < 1 implying favorable adsorption for arsenic. The estimated maximum adsorption capacity for arsenic expressed per mass of titanium ranged between 16.6 mgAs g^{-1} Ti, 24.9 mgAs g^{-1}Ti, and 27.3 for different types of tested Ti-HIX media, and was several fold higher than similar reported values in the literature.

In Novel Solutions to Water Pollution; Ahuja, S., et al.;
ACS Symposium Series; American Chemical Society: Washington, DC, 2013.

Nitrate removal performance of the base ion-exchange resins used in synthesis of the Ti-HIX media was not adversely impacted by the synthesis process.

Introduction

Many small and rural communities around the world lack the financial and technical capabilities to construct, maintain and operate complex and expensive treatment systems capable of simultaneously removing multiple contaminants from their groundwater sources. However, with the ever-increasing need for potable water and increasing regulations impacting small systems, a possibility exists to employ small and simple point-of-entry or point-of-use treatment systems in small communities. These systems could offer an inexpensive and simple alternative which is capable of simultaneously removing a wide range of inorganic contaminants with different chemistries such as arsenic and nitrate.

Arsenic is widely naturally occurring element within the earth's crust, with an average abundance of approximately 2 ppm (*1*, *2*). Besides the natural geological sources, like the dissolution of arsenic-bearing rocks, soil erosion and weathering; various anthropogenic activities such as mining and smelting of metal ores, combustion of fossil fuels and use of arsenical pesticides are also contributing to groundwater contamination with arsenic (*2*, *3*). Because of its chronic and acute toxicities and carcinogenic properties, the International Agency for Research on Cancer, the US National research Council, and the US Environmental Protection Agency (US EPA) consider arsenic as toxin and human carcinogen prone to cause cancer in the bladder, lungs, skin, liver and prostate (*4–6*). To limit the exposure to arsenic, US EPA decreased its maximum contaminant level (MCL) in drinking water from 50 µg/L to 10 µg/L in 2002 and mandated all public water systems to comply with this 10 µg/L standard by 2006 (*7*).

Nitrate is one of the most widespread pollutants of groundwater in many developed and developing countries (*8*). In addition to occurring naturally, the main sources of nitrate contamination in groundwater include intensive use of chemical fertilizers and manure in crop production, and poor wastewater treatment and collection (*9*, *10*). Although traditionally nitrate itself has been considered relatively non-toxic to humans, new studies suggest that various types of cancer and disruption of the endocrine system have also been attributed to nitrate in drinking water in addition to the problems associated with methemoglobinemia (*11*, *12*). Currently, the Maximum Contaminant Level (MCL) set by the USEPA for nitrate in drinking water is 10 mg/L NO_3-N; however, it would not be surprising if the US EPA decreases the MCL value for nitrate in the near future.

Driven by the newest toxicological findings, the increase in regulatory pressure has spurred the need to develop new and inexpensive or improve existing technologies capable of better removing arsenic and nitrate, two anions with distinctly unique chemistries. Nitrate is a stable, highly soluble ion that does is difficult to remove by traditional coagulation or adsorption processes because of its unique non-coordinating ligand chemistry. With exception to biological treatment, which does not work for small drinking water systems, the only cost-efficient way for nitrate treatment is via strong base ion-exchange process. In contrast, arsenic has a unique chemistry which allows it to exist as an oxo-anion in natural waters regardless of whether it exists in arsenite (+3) or arsenate (+5) form (*13–15*). Both these species of arsenic can adsorb onto metal (hydr)oxide surfaces by forming stable inner-sphere bidentate ligands (*16*). This property of arsenic has made metal (hydr)oxides good candidates for use as absorbents for arsenic treatment (*17*). Because of their low cost, iron (hydr)oxides have been the primary candidates for development of hybrid media that could simultaneously remove arsenic and other contaminants from water (*17*, *18*). However, their dissolution at low pH and affinity for silica at high pH may limit their use and regeneration potential (*19*). Titanium dioxide has offered a promise as an alternative metal (hydr)oxide media that could replace iron (hydr)oxides, but the unique chemistry and high cost of titanium based precursors needed to inexpensively synthesize titanium dioxide have created a barrier for developing inexpensive and easy to fabricate titanium dioxide-based hybrid media capable of simultaneous removal of multiple contaminants (*20*).

The goal of this study was to develop an inexpensive and easy to fabricate titanium dioxide-based hybrid ion-exchange media (Ti-HIX) and assess its potential to remove arsenic and nitrate from water. To achieve this goal, three task-oriented objectives were addressed: (1) different hybrid ion-exchange (HIX) media were fabricated via in-situ formation of TiO_2 nanoparticles within the pores of three different commercially ion-exchange (IX) resins; (2) the Ti-HIX media were characterized; and (3) the arsenic and nitrate removal potential of the Ti-HIX media was assessed in model water under batch pseudo-equilibrium conditions.

Experimental Approach

Fabrication of the Titanium Dioxide-Based Hybrid Ion-Exchange Media

The hybrid media were fabricated by in-situ synthesis of TiO_2 nanoparticles within the pores of commercially available nitrate selective IX resins (Table 1). Briefly, 50 mL of strong base IX resin were soaked in 100 mL of ultrapure water ($< 1\ \mu S\ cm^{-1}$) for a period of 24 hours to achieve proper hydration of the resin. An aliquot of 100 mL of saturated TiO^{2+} precursor solution was prepared by slowly dissolving 124 g of $TiOSO_4$ salt (ACS grade, Sigma-Aldrich) in ultrapure water at an elevated temperature of 80°C. After decanting the excess water, the hydrated IX resin was mixed with 100 mL of the TiO^{2+} precursor solution. Two mixing times, 5 minutes and 6 hours, were used in mixing the precursor solution with the IX resin to assess the impact of mixing time on TiO_2 content of the Ti-HIX media. For large scale manufacturing, shorter mixing times are preferred because they allow process streamlining and cost reduction. Upon mixing, the TiO^{2+} precursor was converted to TiO_2 via a 24 hour hydrolysis at 80 °C. The hydrolysis process is illustrated with Equation 1:

$$TiO^{2+} + 2H_2O \rightarrow TiO(OH)_2 + 2H^+ \rightarrow TiO_2 + H_2O \qquad (1)$$

Two hydrolysis conditions were used to understand the effect that excess precursor solution might have on the TiO_2 content of the Ti-HIX media. The first condition entailed decanting of the excess TiO^{2+} precursor solution after the mixing, while the second condition involved hydrolysis without any removal of the excess TiO^{2+} precursor solution. The first condition is more economically sound from a cost reduction perspective than the second one because the decanted precursor solution could be reused for fabrication of other media.

Table 1. Strong Base Ion-Exchange Resins Used in Fabrication of the Titanium Dioxide-Based Hybrid Ion-Exchange Media

Media Name	*Manufacturer*	*Functional groups*	*Exchange capacity (meq/mL)*	*Dp (mm)*
Dowex NSR-1	Dow Chemical Co.	Quaternary amine	1.4	0.3-1.2
A-520E	Purolite	Quaternary ammonium	0.9	0.3-1.2
SIR-100-HP	Resintech	$R-N-R3^{+}Cl^{-}$	0.85	0.3-1.2

Using these synthesis variations, twelve different Ti-HIX media were fabricated from three commercially available IX resin. Upon fabrication, all Ti-HIX media were rinsed in ultrapure water to remove the excess sulfuric acid generated during the synthesis process and soaked in 5% NaCl overnight to convert the resin back in the chloride form. The Ti-HIX media was then repeatedly rinsed with ultra pure water to remove excess NaCl and stored wet.

Characterization of the Titanium Dioxide-Based Hybrid Ion-Exchange Media

The TiO_2 content of the media was quantitatively determined by a gravimetric analysis which involved drying of approximately 6g Ti-HIX media at 104 ± 1 °C to remove any moisture and consequent ashing at 550 °C until constant mass was achieved to remove any carbon content or impurities. This process produced pure TiO_2, which was confirmed by X-ray diffraction (XRD). High resolution XRD (Pananalytical X'Pert Pro) was used to determine the crystalline structure of the TiO_2, and focus ion beam and scanning electron microscope with energy dispersion X-ray microanalysis (FIB/SEM-EDX) techniques were employed to determine the size and the shape of the TiO_2 nanoparticles within the pores of the media (Nova 200 NanoLab UHR FEG-SEM/FIB).

Removal of Arsenic and Nitrate by the Titanium Dioxide-Based Hybrid Ion-Exchange Media

Batch equilibrium tests were conducted with the most economically feasible hybrid ion-exchange media at a final pH of 7.7 ± 0.2 in 5 mM $NaHCO_3$ buffered ultrapure water (<1 µS cm^{-1}). A realistic initial arsenate concentration of $C_0 \approx$ 120 µgAs L^{-1} was used to assess the arsenic removal capacities of the media and compare them to their untreated counterparts. To determine the best Ti-HIX media, two criteria, production cost and TiO_2 content, were considered. Additional batch equilibrium tests with the lowest performing hybrid ion-exchange media were conducted at four additional pH values, 6.3 ± 0.2, 7.7 ± 0.2, 8.3 ± 0.2, and 8.9 ± 0.2 to assess the impact of naturally occurring pH environments on arsenic adsorption capacity of the media. Nitrate removal potential of the media was assessed by conducting batch equilibrium tests in same water matrix (5 mM $NaHCO_3$ buffered ultrapure water) characterized with a final pH of 7.6 ± 0.3 and a low initial nitrate concentration of 5 mg L^{-1} (1.3 NO_3-N), to minimize the effects that high nitrate concentrations might have on the nitrate/chloride selectivity.

Isotherms were developed for arsenic and nitrate adsorption and analyzed using Freundlich adsorption model (Equation 2):

$$q = KC_E^{\frac{1}{n}} \tag{2}$$

where q is the adsorption capacity ([M] adsorbate [M]$^{-1}$ adsorbent; K is the Freundlich adsorption capacity parameter ([M] adsorbate [M]$^{-1}$ adsorbent)([L]^3 [M]$^{-1}$ adsorbate)$^{1/n}$, C_E is the equilibrium concentration of adsorbate in solution ([M] adsorbate [L]$^{-3}$), and $1/n$ is the Freundlich adsorption intensity parameter (unitless).

Arsenic was analyzed using inductively couple plasma mass spectrometry (ICP-MS) (ThermoScientific X-Series) according to US EPA method 200.8; while nitrate was analyzed using ion chromatography (IC) (Dionex IS-2000) according to method US EPA method 300.0 (*21*).

Results and Discussion

Media Characterization

Figure 1 illustrates the titanium dioxide content of the fabricated Ti-HIX media which ranged between 11% (6.7% as Ti) and 21% (12.9% as Ti) by dry resin mass. This broad range was caused to great extent by the high variability in the TiO_2 content of the Resintech media and suggests that this media might be the most susceptible to changes in fabrication conditions. In general, however, most of the Ti-HIX media were characterized with TiO_2 contents which were close to the average value of 16.4% (9.8% as Ti content).

The TiO_2 content data suggests that short mixing periods result in media with higher TiO_2 content. A mixing time of 6 hours without decanting the excess precursor solution resulted in similar TiO_2 contents as the 5 minute mixing times with or without decanting. However, when the excess precursor was decanted, the prolonged mixing of the media resulted in lower TiO_2 content probably because of attrition of the IX resin and/or reequilibration of the TiO^{2+} between the bulk solution and the pores of the IX resin. Higher metal (hydr)oxide content typically relates to higher adsorption capacity of the metal (hydr)oxide impregnated media. When the metal (hydr)oxide contents of the media are similar or higher, shorter mixing times are preferred if the fabrication process is to be scaled up because of lower fabrication costs. Additionally, reusing the excess precursor solution for fabrication of other Ti-HIX media further reduces the cost of production, which makes the Ti-HIX media fabricated by mixing the IX resin for 5 minutes and decanting the excess precursor solution most economically sound.

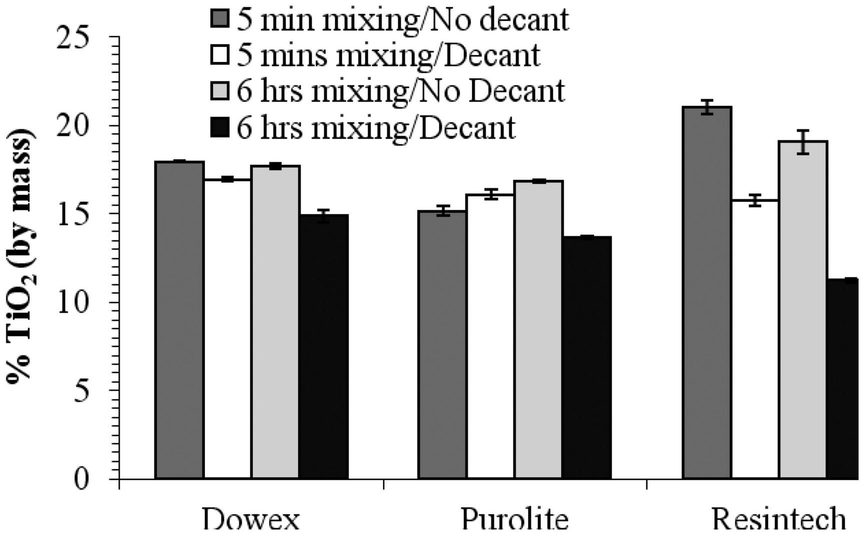

Figure 1. Titanium dioxide content of fabricated titanium dioxide-based hybrid ion-exchange media under different synthesis conditions and with three different ion-exchange resins. Error bars represent standard deviations.

FIB/SEM analysis revealed that titanium dioxide is evenly distributed through the Ti-HIX media (Figure 2a). The backscatter detector used during the FIB/SEM analysis differentiated between heavier elements such as titanium (white areas in Figures 2a and 2b) and lighter elements such as carbon, nitrogen, oxygen and hydrogen (darker areas in Figures 2a and 2b). As seen in Figure 2b, the in-situ hydrolysis resulted in formation of clusters of spherical nanoparticles within the pores of the IX resin. The nanoparticles ranged between 50 nm and 90 nm in size and had similar morphology as commercially available TiO_2 nanopowders (*20*). Although the FIB/SEM images suggested an amorphous TiO_2 structure, X-ray diffraction analysis revealed that the nanoparticles have the crystalline structure of anatase (Figure 3). Furthermore, the XRD data implied that the IX resin had no impact on the crystalline structure of the TiO_2 nanoparticles.

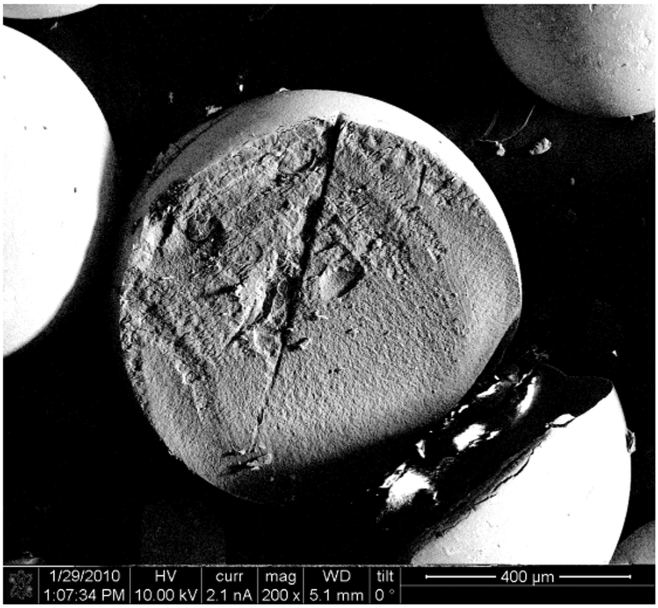

Figure 2a. Focus Ion Beam/Scanning Electron microscope image of a crossection of titanium dioxide-based hybrid ion-exchange media. Even distribution of white areas thoughout the media implies even distribution of heavier elements such as titanium.

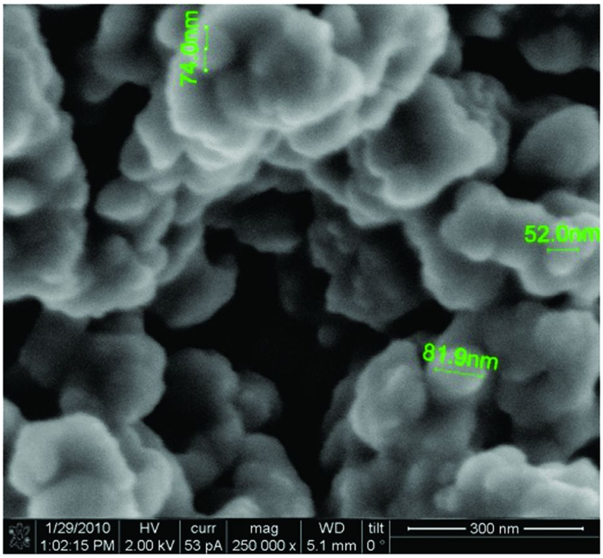

Figure 2b. Focus Ion Beam/Scanning Electron microscope image of a pore inside the titanium dioxide-based hybrid ion-exchange media showing white clusters of titanium dioxide nanoparticles coating the pores of the ion-exchange resin.

Arsenic Removal by the Titanium Dioxide-Based Hybrid Ion-Exchange Media

Figure 4 compares the arsenic adsorption isotherms for the untreated IX resin and the Ti-HIX media fabricated via the most economically sound synthesis conditions (mixing time of 5 minutes followed by decanting of the excess precursor solution and 24 hr hydrolysis). By the isotherms grouping, it is obvious that the Ti-HIX exhibit similar arsenic adsorption capacities, with Purolite Ti-HIX exhibiting negligibly higher adsorption capacity, and Resintech Ti-HIX exhibiting negligible lower adsorption capacity under these conditions. The arsenic removal performance of the untreated IX resin was one to three orders of magnitude lower than the hybrid media demonstrating the fact that high arsenic adsorption capacity is a direct result of the TiO_2 nanoparticle modification of the media.

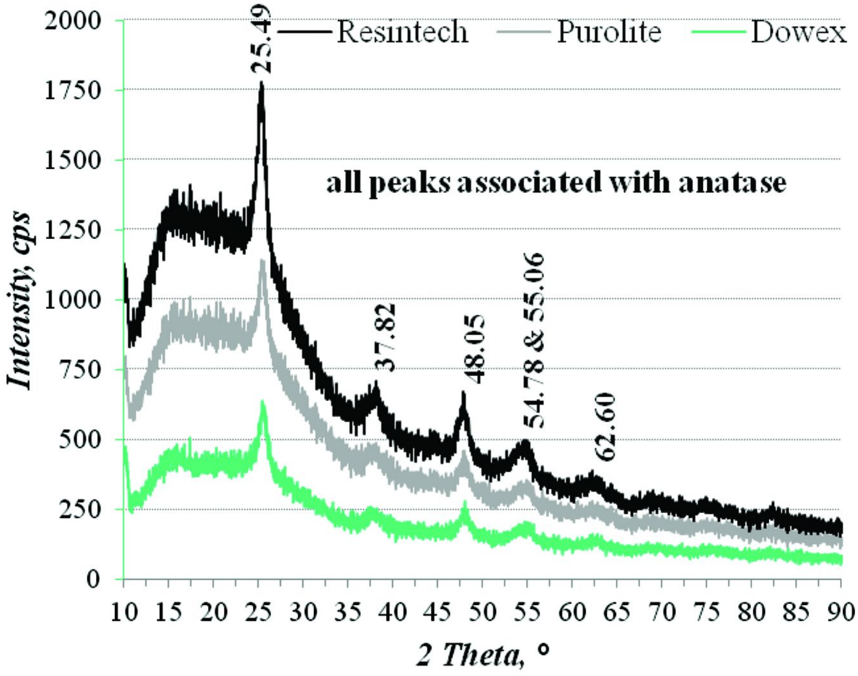

Figure 3. X-Ray diffraction peaks indicate existence of anatase crystalline structure of the synthesized titanium dioxide nanoparticles within the hybrid ion-exchange media.

Freundlich adsorption capacity parameters expressed per gram of dry mass of media are also presented in Figure 4; while normalized Freundlich capacity parameters expressed per gram of metal (titanium) are summarized in Table 2 together with the Ti contents of the tested media. For better comparison with other metal (hydr)oxide media used in arsenic adsorption, Table 2 also summarizes the maximum adsorption capacities expressed per gram of metal (titanium) and estimated for C_0 = 100 µgAs L^{-1}. The estimated maximum adsorption capacities (q_0) for the Ti-HIX media were 16.6 mgAs g^{-1} Ti, 24.9 mgAs g^{-1}Ti, and 27.3 mgAs g^{-1}Ti for the Resintech Ti-HIX, Dowex Ti-HIX and Purolite Ti-HIX, respectively. These values are several fold higher than the values published for other metal (hydr)oxide materials when normalized to gram of metal. The lowest performing Resintech Ti-HIX exhibited almost three times greater adsorption capacity per g of titanium than the commercially available TiO$_2$ nanopowder (*22*); while this factor was even greater for the ferric (hydr)oxide based media (Table 2).

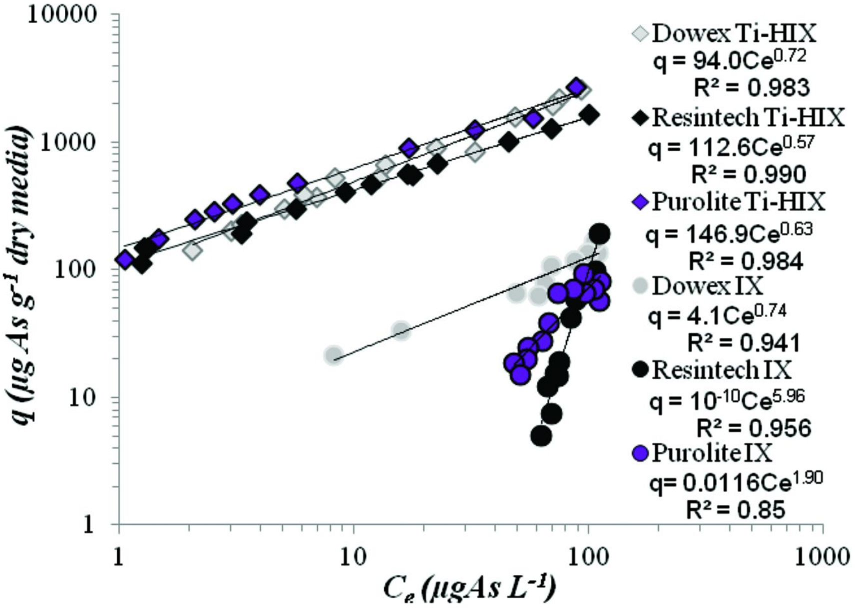

Figure 4. Arsenic adsorption isotherms for the untreated IX resin and the titanium dioxide-based hybrid ion-exchange media fabricated via the most economically sound synthesis conditions. Final pH = 7.7 ± 0.2; 5 mM NaHCO$_3$ buffered ultrapure water; $C_0 \approx 120$ µgAs L^{-1}.

The Freundlich adsorption intensity parameters (1/n) for all the Ti-HIX media were < 1 and were similar to the values reported for other metal (hydr)oxides (*19*, *22*, *23*). A value of 1/n < 1 implies a low energy of adsorption and good performance in waters with low arsenic concentrations (*24*).

Table 2. Comparison of Metal Contents and Estimated Maximum Arsenic Adsorption Capacity Values (q_0 for C_0 = 100 μgAs L^{-1}) for the Titanium Dioxide-Based Hybrid Ion-Exchange Media and Published Values for Other Metal (Hydr)oxide Based Media Evaluated under Comparable Conditions

Media Type	*Freundlich Capacity Parameter K**	*Metal Content (Fe, Zr, Ti)*	*Est. Max. Adsorption Capacity q_0 (mgAs g^{-1})*
Dowex Ti-HIX	924.5	~10.2%	24.9
Purolite Ti-HIX	1520.2	~9.7%	27.3
Resintech Ti-HIX	1191.7	~9.4%	16.3
TiO_2 nanopowder [pH ~ 6.7] (*22*)	NA	~60%	7.0
TiO_2 nanopowder [pH ~ 8.4] (*22*)	**NA**	**~60%**	**2.8**
Zr-GAC (lignite) (*23*)	**NA**	**~12%**	**8.6**
Zr-GAC (bituminous) (*23*)	**NA**	**~9.5%**	**12.2**
ZrO_2 nanopowder (*22*)	**NA**	**~74%**	**3.5**
ZrO_2 nanostructured spheres (*25*)	**NA**	**~74%**	**2.4**
Fe-GAC [pH ~ 6.4] (*26*)	**NA**	**~60%**	**6.4**
Fe-GAC [pH ~ 8.3] (*26*)	**NA**	**~60%**	**1.6**

* (μg As g^{-1} metal)(L μg^{-1} As$)^{1/n}$.

Figure 5 illustrates the effect of pH on arsenic adsorption for Resintech Ti-HIX, which exhibited negligibly lower adsorption capacity when compared to the other two HIX media. It is expected that arsenate adsorption would be the highest at pH ≈ 6.3 and lowest at pH ≈ 8.3 because anatase surface is more negatively charged at higher pH. Additionally, at pH ≈ 8.3, the $HAsO_4{}^{2-}/H_2AsO_4$ ratio is about 46 compared to 0.65 at pH ≈ 6.3, implying that almost all of the arsenate would be present in the more negative form, resulting in greater repulsion forces than at pH ≈ 6.3, and consequently causing greater energy required for the adsorption to occur. This increase in required energy for adsorption to occur would be manifested through reduced adsorption capacity and increase in the value of the Freundlich adsorption intensity parameter (1/n) at same sorben dosages and initial arsenic concentrations. Interestingly, however, the isotherm data suggests that that the adsorption capacity did not changed between pH ≈ 6.3 and 8.3 much, suggesting that electrostatic repulsion was abated probably as a result of the Donnan effect created by the positively charged quaternary amine ion-exchange groups (*27*). The expected trends associated with increase in pH were observed at pH ≈ 8.9, which is much higher than typically encountered for many metal (hydr)oxides (*23*), making the media suitable for arsenic treatment of waters with much higher pH.

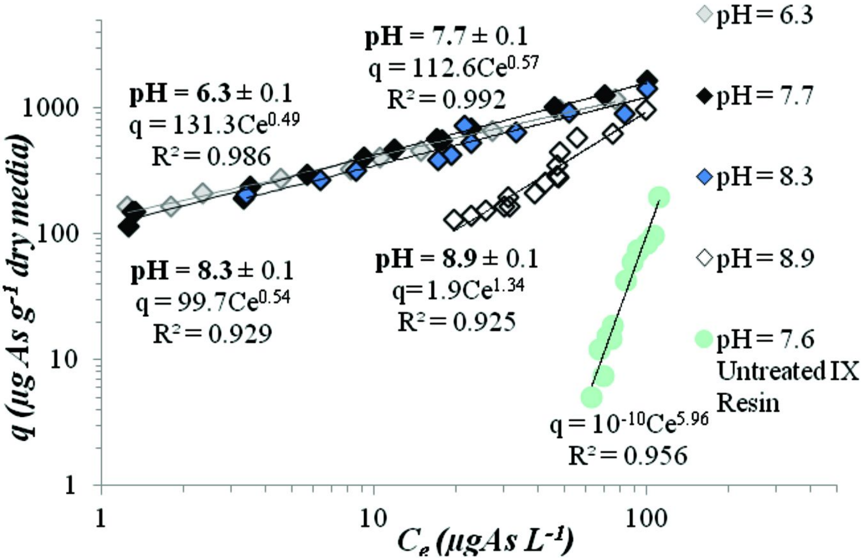

Figure 5. The effect of pH on arsenic adsorption for Resintech titanium dioxide-based hybrid ion-exchange media (5 mM $NaHCO_3$ buffered ultrapure water; C_0 ≈ 120 µgAs L^{-1}).

Nitrate Removal by the Titanium Dioxide-Based Hybrid Ion-Exchange Media

Figure 6 illustrates the nitrate removal performance of both hybrid ion-exchange media and the ion-exchange resins. The data fitted with the Freundlich isotherm model implies that there is negligible reduction in the nitrate removal performance after the media was impregnated with the TiO_2 nanoparticles. This suggests that the introduction of TiO_2 nanoparticles within the pores of the IX resin did not block the strong base ion-exchange sites responsible for removing the nitrate ions.

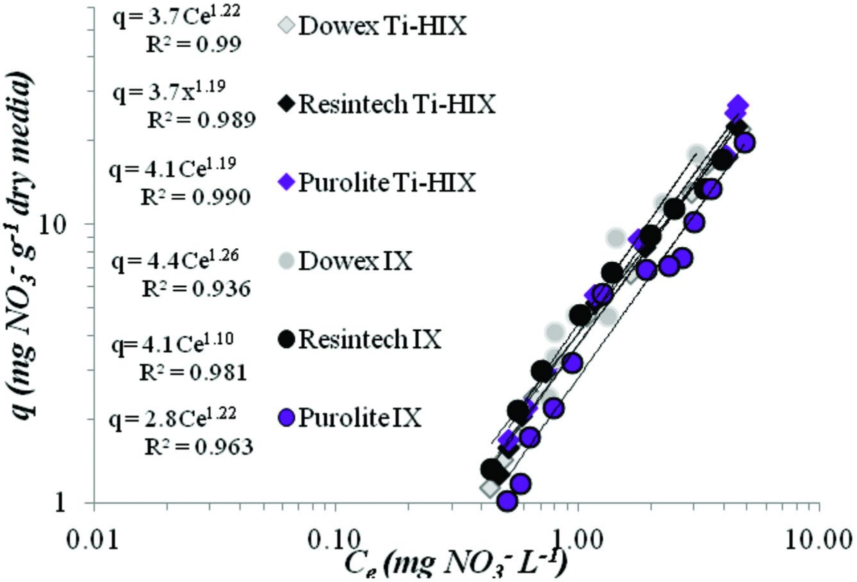

Figure 6. Nitrate removal performance of both titanium dioxide-based hybrid ion-exchange media and the ion-exchange resins.

Conclusions

This concept study demonstrated that a simple and inexpensive fabrication process can be developed to fabricate titanium dioxide-based hybrid ion-exchange media which exhibit high adsorption capacities for arsenic. The base ion-exchange resin could have a minor impact on titanium content of the final product and consequent arsenic removal performance, but an optimization study that engages in selection of the most suitable media could provide for even better performing hybrid media. It is imperative, however, that the media's performance is further examined under realistic conditions involving continuous flow test with naturally occurring water matrices to better understand and optimize the media.

Acknowledgments

Although the research described in the article has been funded in part by the U.S. Environmental Protection Agency's STAR program through grant (RD835175), it has not been subjected to any EPA review and therefore does not necessarily reflect the views of the Agency, and no official endorsement should be inferred. Gratitude to Mona Kamel, at the City of Tempe, Arizona, for the help with the ICP/MS analysis.

References

1. Sylvester, P.; Westerhoff, P.; Möller, T.; Badruzzaman, M.; Boyd, O. *Environ. Eng. Sci.* **2007**, *24* (1), 104–112.
2. Smedley, P. L.; Kinniburgh, D. H. *Appl. Geochem.* **2002**, *17* (5), 517–568.
3. Blssen, M.; Frimmel, F. H. *Acta Hydrochim. Hydrobiol.* **2003**, *31* (1), 9–18.
4. Goswami, A.; Raul, P. K.; Purkait, M, K. *Chem. Eng. Res. Design* **2011**, 0.
5. Guo, J.; Hu, L.; Yand, P.; Tanabe, K.; Miyatalre, M.; Chen, Y. *J. Environ. Sci. Health, Part A: Environ. Sci. Eng. Toxic Hazard. Subst. Control* **2007**, *42* (12), 1853–1858.
6. National Research Council (NRC). *Arsenic in Drinking Water*; National Academy of Sciences: Washington, DC, 1999.
7. Sylvester, P.; Westerhoff, P.; Möller, T.; Badruzzaman, M.; Boyd, O. *Environ. Eng. Sci.* **2007**, *24* (1), 104–112.
8. Hekmatzadeh, A. A.; Karimi-Jashani, A.; Talebbeydokhti, N.; Klove, B. *Desalination* **2012**, *284*, 22–31.
9. Rocca, C. D.; Belgiorno, V.; Meriç, S. *Desalination* **2007**, *204* (1−4), 46–62.
10. Kapoor, A.; Viraraghavan, T. *J. Environ. Eng.* **1997**, *123*, 371–380.
11. Fan, A. M.; Steinberg, V. E. *Regul. Toxicol. Pharmacol.* **1996**, *23* (1), 35–43.
12. Bruningfann, C. S.; Kaneene, J. B. *Vet. Hum. Toxicol.* **1993**, *35* (6), 521–538.
13. Smedley, P. L.; Kinniburgh, D. G. *Appl. Geochem.* **2002**, *17*, 517–568.
14. Cotton, F. A.; Wilkinson, G. *Advanced Inorganic Chemistry: A Comprehensive Text*, 3rd ed.; Interscience Publishers: New York, 1972.
15. Greenwood, N.; Earnshaw, A. *Chemistry of the Elements*, 2nd ed.; Reed Educational and Professional Publishing Ltd.: Woburn, MA, 1997.
16. Randall, S. R.; Sherman, D. M. *Geochim. Cosmochim. Acta* **2003**, *67*, 4223–4230.
17. Mohan, D.; Pittman, C. U., Jr. *J. Hazard. Mater.* **2007**, *142*, 1–53.
18. Hristovski, K.; Westerhoff, P.; Möller, T.; Sylvester, P.; Condit, W.; Mash, H. *J. Hazard. Mater.* **2008**, *152* (1), 397–406.
19. Badruzzaman, M. Ph.D. Dissertation, Arizona State University, Tempe, AZ, 2005.
20. Guan, X.; Du, J.; Meng, X.; Sun, Y.; Sun, B.; Hu, Q. *J. Hazard. Mater.* **2012**, *215–216* (0), 1–16.
21. *Water: CWA Methods. Approved General-Purpose Methods*, U.S. Environmental Protection Agency. http://water.epa.gov/scitech/methods/cwa/methods_index.cfm (accessed February 19, 2013).
22. Hristovski, K.; Baumgardner, A.; Westerhoff, P. *J. Hazard. Mater.* **2007**, *147* (1–2), 265–274.
23. Sandoval, R.; Cooper, A. M.; Aymar, K.; Jain, A.; Hristovski, K. *J. Hazard. Mater.* **2011**, *193*, 296–303.
24. Crittenden, J. C.; Trussell, R. R.; Hand, D. W.; Howe, K. J. *Treatment: Principles and Design*, 2nd ed.; Tchobanoglous, G., Ed.; Water Wiley & Sons, Inc.: Hoboken, NJ, 2005.
25. Hristovski, K. D.; Westerhoff, P. K.; Crittenden, J.; Olson, L. *Environ. Sci. Technol.* **2008**, *42*, 3786–3790.

26. Hristovski, K. D.; Westerhoff, P. K.; Möller, T.; Sylvester, P. *Chem. Eng. J.* **2009**, *146* (2), 237–243.
27. Cumbal, L.; SenGupta, A. K. *Environ. Sci. Technol.* **2005**, *39* (17), 6508–6515.

Chapter 14

Applications of Zero-Valent Iron (ZVI) and Nanoscale ZVI to Municipal and Decentralized Drinking Water Systems—A Review

Pei C. Chiu[*]

Department of Civil and Environmental Engineering,
University of Delaware, Newark, Delaware 19716, U.S.A.
[*]pei@udel.edu

Zero-valent iron (ZVI) has been used to treat contaminated groundwater for almost two decades, and its application in environmental engineering to date is still limited to site remediation. Work in recent years has shown that ZVI is also effective at removing contaminants that are relevant to drinking water, including viruses and bacteria, chlorine, disinfection by-products (DBPs), DBP precursors (e.g., natural organic matter), and metal ions. It is proposed that ZVI may represent a potential approach to address some of the drinking water problems. This review provides a brief summary of the recent work on the removal of these contaminants by ZVI and offers examples of potential applications to drinking water systems; i.e., in municipal water treatment plants and small-scale or portable point-of-use (POU) devices. In each example, the specific problems that ZVI may help address, and the expected benefits it may offer, are discussed. Preliminary results supporting these applications are presented, and possible uses of ZVI to other water-related problems are considered. The review closes by suggesting a number of research needs that shall be met prior to field implementation of the technology.

In Novel Solutions to Water Pollution; Ahuja, S., et al.;
ACS Symposium Series; American Chemical Society: Washington, DC, 2013.

Introduction

Drinking water quality has been recognized as an increasingly critical issue for the next decades. In addition to continued population growth and greater demand for potable water, a number of converging factors have been contributing to this looming crisis. These include increasing impact of wastewater discharge on drinking water sources, deteriorating water and wastewater infrastructure, growing number of emerging contaminants, heightened public awareness, and uncertainties due to climate change.

Given these considerations, it is unclear whether the conventional water treatment systems and processes can adequately remove a wide range of chemical and microbial pollutants to protect public health, and whether reliance upon a single source of piped water supply for consumption and other uses is a sustainable model for the future. What is certain, though, is that more, and more effective, barriers to the large number of traditional and emerging pollutants will be needed between contamination sources and finished water to ensure water quality and protect human health. Here we proffer that zero-valent iron represents a novel approach that could potentially address some of the drinking water problems.

Zero-valent iron (ZVI), in the form of either granular or nanoscale particles, has been applied to remediate contaminated groundwater since the mid-1990s. Granular ZVI, typically in the form of scrap iron filings, is commonly used as a reactive material in subsurface permeable reactive barriers (PRBs) to remove groundwater contaminants (*1*). Since the installation of the first full-scale PRB in Sunnyvale, CA in 1995, more than 200 PRBs have been installed in North America, Europe, and elsewhere (*2*). The PRB technology is a passive and in situ remediation method that relies on the natural groundwater flow and requires relatively low maintenance. In existing PRBs, ZVI granules have been shown to remain effective at degrading contaminants in groundwater for many years (*3*). While initially proposed to treat chlorinated solvents such as tetrachloroethene (PCE) and trichloroethene (TCE), ZVI-based PRBs have since been used to remove a broad range of organic and inorganic contaminants (*1*) including Freons, metals (e.g., Cr(VI), arsenic, and cadmium), radionuclides (e.g., U(VI)), and nutrients (e.g., nitrate).

A more recent approach to use ZVI for site remediation involves addition of nano-scale (1–100 nm) ZVI (or nZVI) particles to contaminated subsurface (*4*). Introduction of nZVI is typically accomplished through direct injection and may involve recirculation, pressure pulsing, or fracturing (*5*). One major advantage of nZVI as compared to granular ZVI is the significantly greater contaminant degradation rates. This is due primarily to the smaller particle size and higher specific surface area per unit iron mass (on the order of 35 m^2/g, (*4*)) relative to granular ZVI (1–4 m^2/g, (*6*)).

Through research, development, and field experience over the last two decades, the ZVI/nZVI technology has become increasingly understood, mature, and accepted. However, application of ZVI in environmental engineering to date is still limited almost exclusively to site remediation, even though its potential use in other areas, such as drinking water and wastewater treatment, have been demonstrated.

With respect to drinking water, the contaminants of primary concern are, in addition to those that are also relevant to groundwater; e.g., PCE, TCE, and Cr(VI), are microorganisms (bacteria, viruses and protozoa), disinfection by-products (DBPs, including trihalomethanes and haloacetic acids), and disinfectants (e.g., free chlorine). Depending the source water quality and treatment system/process used, other contaminants such as arsenic and lead may also be of concern.

Below we shall first review briefly the recent studies on the removal of drinking water pollutants and their precursors by ZVI. This is followed by discussion of two potential applications of ZVI or nZVI for drinking water treatment, the expected benefits and potential drawbacks of each, and future research needs.

Removal of Drinking Water Contaminants by ZVI

Studies in the last decade have demonstrated that ZVI is effective at treating many contaminants relevant to drinking water. You et al. (*7*) first illustrated the ability of ZVI to remove viruses from water. The bacteriophages MS-2 and φX-174, which are commonly used indicator viruses, both broke through sand columns quickly but were removed from synthetic groundwater at high efficiency when 35% (v/v) of the sand was replaced by Peerless™ ZVI granules. Within 20 min of ZVI contact time, the removal efficiency for both viruses was initially 4 logs (i.e., 99.99%) and subsequently increased to between 5 and 6 logs. The 10- to 100-fold improvement for both viruses was attributed to continuous formation of new surface iron (hydr)oxides, which were formed through gradual oxidation of ZVI by the water that passed through. Iron (hydr)oxides are known to serve as adsorption sites for virus particles (*8*)

In a parallel batch experiment, these authors compared the observed virus removal rate constants and collision frequency calculations and showed that the removal rates of MS-2 and φx-174 by ZVI was rapid, approaching the mass transfer limit. Zhang (*9*) subsequently found that most (>99.8%) of the MS-2 and φX-174 removed by ZVI were either inactivated or irreversibly bound to ZVI, suggesting that additional interactions took place following the initial adsorption of virus particles to the surface (hydr)oxides. Similarly high removal of pathogenic viruses by Peerless™ ZVI from actual drinking water was recently reported by Shi et al. (*10*). Adenovirus 41 and Aichi virus, as well as MS-2 and φX-174, were removed at efficiencies between 3.5 and 6 logs from both synthetic groundwater and actual water treatment plant samples using a sand column containing 15% ZVI (v/v) with a 9.3 minute ZVI contact time.

ZVI has also been shown to remove and inactivate bacteria, although the organisms investigated have been limited to *Escherichia coli*. Using a experimental setup similar to that used by You et al. (*7*), Derevianko (*11*) observed enhanced removal of the pathogenic bacterium *E. coli* O157:H7 from water when ZVI filings were incorporated into a sand filter. Ingram et al. (*12*) reported significantly greater removal of *E. coli* O157:H12 from irrigation water by adding ZVI to a field-scale sand filter. The crops and soil that received ZVI-treated water also had lower *E. coli* O157 counts than the control. Pachocka (*13*) evaluated the effect of ZVI amendment on the performance of a creek water-ripened biosand filter. Both *E. coli* and MS-2 were removed more thoroughly after the water had passed through a layer of ZVI than after passing the top section containing a schmutzdecke.

Compared to granular ZVI, nZVI can achieve the same virus removal efficiency at a lower mass because of its higher specific surface area. Using conditions similar to those for the batch studies by You et al. (*7*) except 0.1 g of nZVI (instead of 1.0 g of ZVI filings) per bottle, we obtained comparable removal rate constants for MS-2 and φX-174 as those with 1.0 g of ZVI granules. As shown in Figure 1, removal of these viruses by 0.1 g of nZVI was pseudo-first-order and the rate constants were 0.83 h^{-1} for MS-2 and 1.1 h^{-1} for φX-174 (re-plotted from ref (*14*)). These numbers compare well with those (1.4 and 0.78 h^{-1}, respectively) observed using 1.0 g of granular ZVI (*7*), which had a specific surface area more than 10 times smaller.

In investigating the biocidal effects of nZVI, Sedlak and coworkers (*15*, *16*) showed that, while direct interactions with nZVI particles played a key role, soluble Fe(II) released from nZVI contributed significantly to the observed bactericidal (*E. coli*) and virucidal (MS-2) effects of nZVI. Zhang (*9*) demonstrated that aqueous Fe(II) released from ZVI was able to rapidly inactivate φX-174 but had no observable effect on MS-2 under anoxic conditions. It thus appears that, while virus interactions with nZVI and aqueous Fe(II) both depend on nZVI surface area (and hence the relationship between rate constant and surface area noted above), the mechanisms for viral and bacterial inactivation are manifold and remain to be further elucidated.

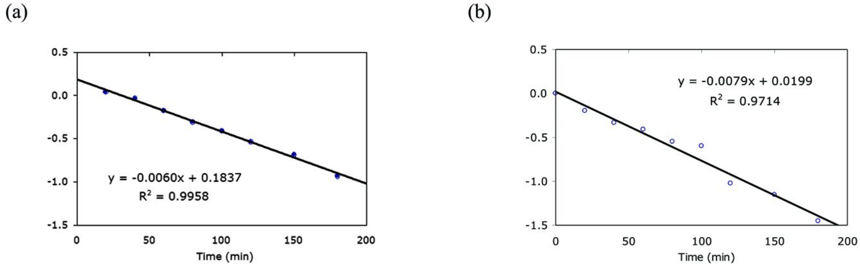

Figure 1. Removal of MS-2 and φX-174 by 0.1 g of nZVI in 250-mL amber batch reactors (14). The pH of degassed artificial groundwater was 6.84 and the shaker speed was 60 rpm. No removal of either virus was observed over three hours without nZVI addition.

In addition to microorganisms, other contaminants of great importance to drinking water, such as DBPs and their precursors, free chlorine, and metal ions, have also been shown to be treatable by ZVI. For example, in an effort to identify feasible alternatives to sulfite for dechlorinating water, Bedner et al. (*17*) reported that ZVI was a highly effective reducing agent that consumed free chlorine as rapidly as sulfite. Indeed, because chlorine reacts instantly with both ZVI and Fe(II) species, oxidizing them completely to Fe(III), we have been able to use chlorine to determine the overall oxidation state of synthesized nZVI particles (unpublished data). ZVI has also been shown to reductively degrade chlorination and ozonation DBPs, including haloacetic acids (*18*, *19*), chloropicrin (*20*), bromate (*21*), and *N*-nitrosodimethylamine (*22*). The degradation rates of these DBPs vary by several orders of magnitude, ranging from mass transfer-limited kinetics to rates that correspond to half-lives of many days. For water treatment purposes, the potential kinetic limitations for slow-degrading DBPs may be overcome, at least in part, by using the more reactive nZVI and/or a second, catalytic metal (*22*).

Natural organic matter (NOM) is arguably the most important and ubiquitous precursor of DBPs. It would not only consume chlorine but also produce trihalomethanes (THMs), haloacetic acids (HAAs) and many other DBPs during chlorination and chloramination (*23*, *24*). ZVI, through its corrosion in water to form iron (hydr)oxides, is known to adsorb and remove NOM such as humic acid from water. However, many studies have focused on the effect of NOM on contaminant removal/degradation by ZVI, rather than on the removal of NOM itself (*25–27*).

Using humic acid as a model NOM, we assessed the ability of sand and ZVI columns to remove NOM from synthetic groundwater continuously for a month. As shown in Figure 2(a), sand alone did not adsorb or retard the transport of NOM, which broke through completely after one pore volume (PV) (*9*). In contrast, with 35% ZVI (v/v) in the column, NOM removal was 70% initially, decreased to 40% over 3-4 days, and maintained at about 40% on the average for the remainder of the month. This is consistent with the explanation for virus removal suggested by You et al.(*7*): As water passed through and ZVI corroded, new iron hydroxides formed continuously on the surface to serve as sorption sites for NOM. The efficiency of NOM removal would likely depend on ZVI contact time, NOM loading, and water chemistry.

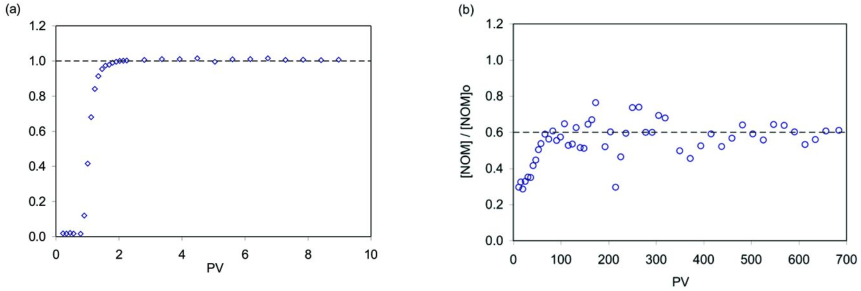

Figure 2. Breakthrough curves of NOM (0.45 μm-filtered IHSS humic acid) for sand-only and ZVI-sand columns (9). The pH of degassed groundwater was 7.5 and the input TOC was 2.41 ppm. The ZVI-sand column contained 35% ZVI by volume. One PV corresponds to ~1 h residence time.

Collectively, the above results suggest the potential applicability of ZVI to water treatment. Two specific applications are discussed below, where ZVI's ability to remove microbes, free chlorine, NOM, DBPs, and/or other contaminants from drinking water would be relevant.

Application of ZVI to Municipal Water Treatment

Most people in the U.S. obtain their drinking water from public water systems (PWS). There are approximately 161,000 PWS in the U.S., producing 34 billion gallons of drinking water each day for 90% of the U.S. population (*28*). These PWS are singularly important to society and their contribution to public health cannot be over-stated. Chlorine (i.e., Cl_2, HOCl and OCl^-) is the most common disinfectant to treat drinking water, used by approximately 80% of large water systems and almost all of the small PWS (i.e., systems serving fewer than 10,000 people). While larger utilities typically use processes such as coagulation, flocculation, sedimentation, filtration, and activated carbon in addition to chlorination, water treatment at some small PWS is limited to chlorination only.

Its many benefits notwithstanding, chlorination presents a serious public health problem: It forms DBPs through reactions with NOM and other constituents in source water. More than 600 DBPs have been reported (*24*) that are derived from oxidative disinfectants (chlorine, chloramines, ozone, and chlorine dioxide). Most of these DBPs are associated with chlorine, and many chlorination DBPs have been linked to bladder, rectal, and colon cancers, and reproductive and developmental effects including fetal losses and heart and neural tube defects (*29*). Approximately 280 million people in the U.S. are exposed to DBPs on a daily basis.

A daunting problem facing many PWS today is how to control microbial pathogens and DBPs simultaneously – and to do so at an acceptable cost. On the one hand, high chlorine dosage can produce excessive amounts of DBPs; on the other hand, low chlorine doses may not sufficiently protect the distribution system and consumers against harmful pathogens. Although alternative methods of disinfection are available, such as UV, ozone, chloramine, and membrane filtration, some of them require significant capital investment and process modifications, or are more complex and expensive to operate. Ozone and chloramines also form DBPs of serious health concerns including bromate, N-nitrosodimethylamine, bromo- and iodo-organics. Many of these DBPs are more toxic than the chlorinated DBPs currently regulated (*24*).

Unlike large utilities that can invent in non-oxidant-based disinfection technologies such as ultra-filtration (e.g., Columbia Heights Filtration Plant, Minneapolis, 78 MGD) and UV disinfection (e.g., Catskill-Delaware UV Disinfection Facility, New York, ~2,000 MGD), most small PWS are operated by municipalities and do not have the necessary resources and support to invest in or migrate to a more advanced disinfection technology. Hence, it is particularly challenging for small and medium-size PWS to manage both microbial and DBP risks simultaneously.

Given the importance of PWS to society and the constraints under which many of them operate, there is a pressing need to improve the current process and to help PWS meet multiple treatment goals at an affordable cost. Ideally, such a process should, in addition to helping PWS to control both microbes and DBPs, be easy to use, inexpensive to install and operate, non-oxidant-based and thus producing little DBPs, compatible with existing treatment processes, and applicable to both existing or new facilities.

These criteria may all be met by a simple application of ZVI, as was recently suggested by Shi et al. (*10*): ZVI particles may be added to a granular filter as another medium besides anthracite coal, sand, and gravel. Because in many PWS filtration precedes chlorination, ZVI could on the one hand enhance the removal of viruses and bacteria in the filter, and on the other hand remove a portion of the organic precursor (i.e., NOM) that would otherwise contribute to DBP formation during chlorination. NOM removal prior to chlorination is believed to be the most effective approach to control DBP formation and may provide the added benefits of sustained chlorine residuals and lower DBP concentrations in distribution systems (*30*). Further-more, having ZVI in a filter may help to remove other contaminants such as chromium, arsenic, and lead (*31*, *32*).

This envisioned application of ZVI could potentially reduce chlorine burden/use and improve the chemical and microbiological quality of finished water. It would not require significant capital investments or process modification and hence may represent a simple and affordable alternative for PWS to meet multiple treatment goals – an option that might be especially attractive to small and medium-size plants for whom processes such as UV and membrane are not viable options. ZVI would be particularly feasible for PWS that use groundwater, which typically has low dissolved oxygen concentrations and thus may yield longer ZVI service lives. For PWS that use aerobic surface water, ferric oxides formed, and the adsorbed microbes, NOM, and metals, could be removed from the filter through periodic backwashing.

Application of Nanoscale ZVI to Point-of-Use Water Filters

In situations where piped water is not available or additional treatment is desired, decentralized systems, such as point-of-use (POU) and point-of-entry (POE) devices, can be used to provide additional protection at/near the point of consumption, offering direct benefits to the consumer. POU devices are intended to purify only the portion of incoming water that is used for drinking or cooking, whereas POE devices treat all the water entering into a house, building, or facility. Technologies such as reverse osmosis (RO), nano-filtration (NF), ozonation and ultraviolet (UV) are available for many POE/POU systems; however, these technologies are relatively expensive and require either a power source and/or a large pressure head to work. In contrast, POU filters that rely on granular media, such as activated carbon and cation exchange resins, are popular due to their low cost and ease of use, manufacture, maintenance, and media replacement. Granular filters require minimal pressure heads and are often gravity-fed. They are prevalent in pitcher-style and faucet-mounted household POU systems, as well as in portable water filters for outdoor activities (camping and hiking), foreign travels, and engineering or military operations in regions where piped water and/or power are not available or reliable. In addition, POU/POE devices are potentially useful, and have been evaluated, as a means of ensuring water security and protecting the public (*33*); e.g., in case of intentional release of chemical or biological agents to water supply.

While granular media such as granular activated carbon (GAC) and cation exchange resin (CER) are effective at removing organic and inorganic contaminants, a major deficiency of these media relative to RO and UV is their inability to remove microbial contaminants, particularly viruses. Most carbon- and resin-based media are 0.2 to 1.0 mm in size, which means the pores are 100-1,000 times that of bacteria and 10,000 times that of viruses. Few granular media-based filters currently on the market claim to be effective at removing viruses.

It is possible that, by adding nZVI onto the granular media in POU filters, one could significantly improve the ability of these filters to remove viruses, bacteria, and other microbes from drinking water. Because of nZVI's high specific surface area and reactivity, successful virus removal may be achieved by coating only a small fraction of activated carbon or resin surface with nZVI. This would add little mass of iron but a critically important, yet currently lacking, ability to granular POU filters (i.e., to remove microbes), while preserving the existing functions of the media (i.e., to remove chemical pollutants). This modification may improve the capability of granular media and make them potentially effective and low-cost alternatives to UV- and RO-based devices.

This idea was evaluated in a laboratory study using GAC (20 x 50 mesh) from Calgon Carbon (Pittsburg, PA) and Amberlite® IR-120 CER (sodium form, 16 x 45 mesh) from Sigma Aldrich (St. Louis, MO). The methods for coating nZVI to these media have been published elsewhere (*34*) and are described briefly here. Ferric nitrate or ferric chloride was used as a source of iron for nZVI. The coating of nZVI on GAC involved addition of a known mass of ferric nitrate solution to a target amount of GAC. For CER, an adsorption isotherm for Fe(III) was first obtained, based on which a target amount of ferric chloride was adsorbed. By using different Fe(III) masses we could control the nZVI loading from 0.5 to 8% (w/w) for both media.

Reduction of Fe(III) on GAC to nZVI was carried out at high temperatures (<800 °C, (*35*, *36*)) under H_2 in a stainless steel reactor (78 cm^3) manufactured at the University of Delaware's Machine Shop and configured to fit inside a modified furnace. Fe(III)-coated GAC was placed in the reactor connected to a compressed gas delivery line. The heating time was varied as needed depending on the target temperature. After reduction, the product was cooled under nitrogen. Upon exposure to air, a pyrophoric effect indicated successful reduction of Fe(III) to nZVI. In contrast to GAC, CER is heat-labile, and thus reduction of Fe(III) on CER was carried out in an anaerobic glove box (Coy Laboratory, MI) under N_2/H_2 (95/5) with $NaBH_4$ as a reducing agent (*37*). $NaBH_4$ solution (0.05 M) was introduced drop-wise into a shaken flask containing Fe(III)-laden CER. The nZVI-coated CER produced was washed with deoxygenated deionized water and dried in a vacuum oven under N_2.

Scanning electron microscopic (SEM) analysis of the original and nZVI-coated CER shows that roughly 10-15% of the surface was covered by fairly evenly distributed individual and clusters of 25-50 nm nZVI particles (Figure 3a and 3b). Presence of nZVI on GAC was less discernible based on morphology due to the uneven surface of GAC (Figure 3c), but was clearly confirmed by X-ray diffraction (XRD, Figure 3d). The BET surface areas of GAC and nZVI-coated GAC were also measured, and the results show that the change in BET surface area (and presumably adsorption capacity) was limited, decreasing only slightly from 798 to 792 m^2/g after addition of 3 wt% nZVI. The limited surface coverage of CER and GAC by nZVI suggests the adsorption capacities of CER and GAC for cationic and organic pollutants would remain largely the same, although this needs to be verified experimentally.

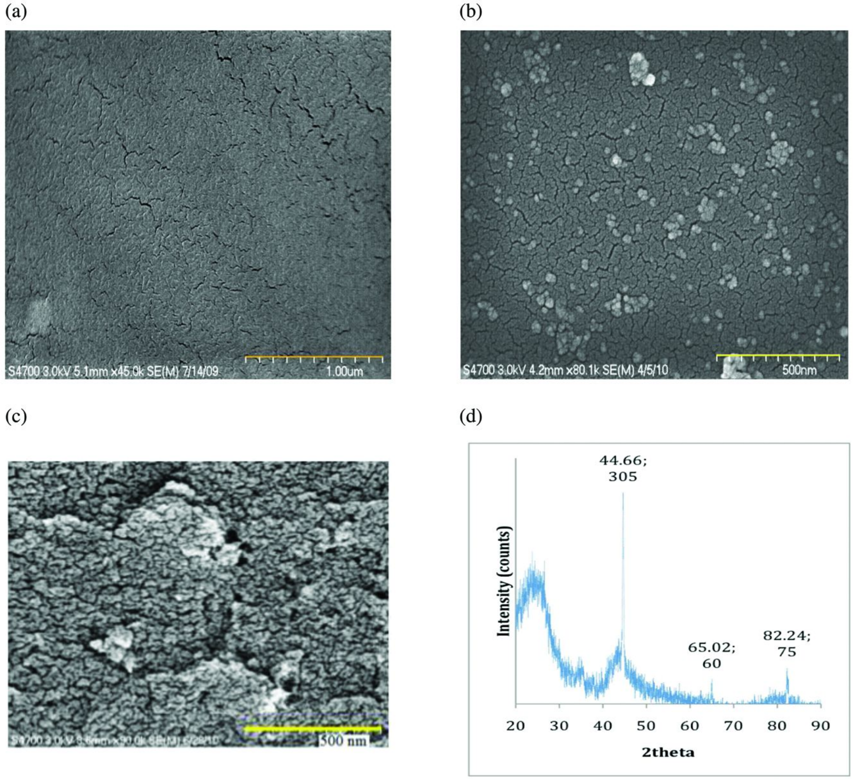

Figure 3. SEM images of original CER (a), nZVI-coated CER (b), and nZVI-coated GAC, and XRD result of nZVI-coated GAC (d).

The proposed addition of nZVI to GAC and CER can provide these media with a new, important ability – the ability to remove viruses and bacteria from water, without negatively affecting their capacities to adsorb organic and metallic pollutants. If used in a drinking water treatment pouch or a portable filter for outdoor activities, the nZVI-fortified media may provide greater protection against microbial pathogens in natural waters. If used in a household to treat chlorinated tap water, the nZVI-coated media could improve water quality by removing chlorine, DBPs, and metals such as arsenic and lead. The nZVI media may be readily adopted commercially, simply through direct substitution for the original, uncoated media in a POU system, with little change in weight, size, or other properties.

Other Potential Applications and Research Needs

In addition to the two applications discussed above, ZVI may help to address other water-related problems. ZVI was recently explored as a simple and low-cost method to remove bacteria from irrigation water (*12*). While the study focused mainly on *E. coli* removal, ZVI-amended filters are expected to also remove other microorganisms and metals, thus reducing the conveyance of these contaminants to crops and soil through irrigation and preventing foodborne illnesses.

Furthermore, as suggested by Pachocka's study (*13*), incorporation of ZVI into a biosand filter could improve the filter's effectiveness to remove bacteria and viruses. Biosand filters are one of the few effective low-cost household water treatment technologies for the world's poor (*38*). Some of the drawbacks of biosand filters, such as long filter ripening time and highly variable, daily charge-dependent performance, may be ameliorated through ZVI addition. ZVI can not only augment the bio-active layer (i.e., schmutzdecke) to improve the overall efficiency in pathogen removal, but provide a baseline treatment before a filter ripens and/or when the schmutzdecke is disrupted or fails. Thus, ZVI amendment could potentially minimize performance variations among individual biosand filters.

To realize the full potential of ZVI and achieve broad adoption of the technology for drinking water treatment, additional research is necessary to bridge the current knowledge gaps. First, ZVI needs to be evaluated against a wider range of microorganisms, particularly those important to drinking water and human health. These include bacteria besides *E. coli* (e.g., *Salmonella* and *Legionella*), and the protozoa *Giardia lamblia* and *Cryptosporidium*. Second, the mechanisms responsible for the removal and inactivation of viruses and bacteria need to be better understood. These mechanisms appear complex and dependent on the characteristics of water (oxygen level, pH, organic content, etc.) and the microorganism (isoelectric point, presence and properties of spikes, sensitivity to Fe(II) and reactive oxygen species) (*7*, *10*, *15*, *16*). ZVI would become a robust drinking water treatment technology only if a fuller, better understanding of these mechanisms is developed. Third, the long-term performance of ZVI needs to be assessed in pilot- and full-scale systems under realistic operation conditions (e.g., in the presence of other media such as anthracite and sand, and with periodic backwashing) in order to determine its effectiveness over time and therefore its service life and replacement frequency. Fourth, as above noted, whether and how nZVI addition may affect the treatment capacities of CER and GAC for chemical contaminants need to be further studied to understand the trade-off, if any exists. Finally, as an application may depend on ZVI's ability to remove multiple contaminants simultaneously, and because some preliminary results suggest that different contaminants may be removed through similar processes on the same adsorption sites (*9*), it is essential to evaluate the extent of competition and/or interference among microorganisms, NOM, and other contaminants such as arsenate.

In summary, as the world becomes increasingly populated and water-stressed, ZVI may represent a simple, effective, versatile, and low-cost material that can help improve drinking water quality and protect human health. While the recent studies have shown much promise, further work is necessary to develop robust ZVI-based drinking water processes for large-scale implementation.

References

1. *Remediation Technologies Development Forum (RTDF)*. www.rtdf.org (accessed 2009).
2. *Permeable Reactive Barrier: Technology Update*; Interstate Technology & Regulatory Council (ITRC): Washington, DC, June, 2011.
3. Phillips, D. H.; Van Nooten, T.; Bastiaens, L.; Russell, M. I.; Dickson, K.; Plant, S.; Ahad, J. M. E.; Newton, T.; Elliot, T.; Kalin, R. M. Ten year performance evaluation of a field-scale zero-valent iron permeable reactive barrier installed to remediate trichloroethene contaminated groundwater. *Environ. Sci. Technol.* **2010**, *44*, 3861–3869.
4. Zhang, W. X. Nanoscale iron particles for environmental remediation: An overview. *J. Nanopart. Res.* **2003**, *5*, 323–332.
5. *Nanotechnology: Applications for Environmental Remediation*; CLU-IN Technology Focus Area Fact Sheet; U.S. Environmental Protection Agency: Washington, DC, November, 2011.
6. Alowitz, M. J.; Scherer, M. M. Kinetics of nitrate, nitrite, and Cr(VI) reduction by iron metal. *Environ. Sci. Technol.* **2002**, *36*, 299–306.
7. You, Y.; Han, J.; Chiu, P. C.; Jin, Y. Removal and inactivation of waterborne viruses using zero-valent iron. *Environ. Sci. Technol.* **2005**, *39*, 9263–9269.
8. Ryan, J. N.; Harvey, R. W.; Metge, D.; Elimelech, M.; Navigato, T.; Pieper, A. P. Field and laboratory investigations of inactivation of viruses (PRD1 and MS2) attached to iron oxide-coated quartz sand. *Environ. Sci. Technol.* **2002**, *36*, 2403–2413.
9. Zhang, L. Removal and Inactivation of Waterborne Viruses Using Zerovalent Iron. M.S. Thesis, University of Delaware, Newark, DE, 2008.
10. Shi, C.; Wei, J.; Jin, Y.; Kniel, K. E.; Chiu, P. C. Removal of viruses and bacteriophages from drinking water using zero-valent iron. *Separ. Purific. Technol.* **2012**, *84*, 72–78.
11. Derevianko, A. Effect of Zero-Valent Iron on the Removal of *Escherichia coli* O157:H7 from Water. M.S. Thesis, University of Delaware, Newark, DE, 2008.
12. Ingram, D. T.; Callahan, M. T.; Ferguson, S.; Hoover, D. G.; Chiu, P. C.; Shelton, D. R.; Millner, P. D.; Camp, M. J.; Patel, J. R.; Kniel, K. E.; Sharma, M. Use of zero-valent iron biosand filters to reduce *Escherichia coli* O157:H12 in irrigation water applied to spinach plants in a field setting. *J. Appl. Microbiol.* **2012**, *112*, 551–560.

13. Pachocka, M. Intermittent Slow Sand Filters: Improving Their Design for Developing World Applications. M.S. Thesis, University of Delaware, Newark, DE, 2010.
14. Zhang, L.; Jin, Y.; Chiu, P. C. Removal and Inactivation of Viruses by Elemental Iron, Platform presentation. *231st American Chemical Society National Meeting*, Atlanta, GA, March, 2006.
15. Lee, C.; Kim, J. Y.; Lee, W. I.; Nelson, K. L.; Yoon, J.; Sedlak, D. L. Bactericidal effect of zero-valent iron nanoparticles on *Escherichia coli*. *Environ. Sci. Technol.* **2008**, *42*, 4927–4933.
16. Kim, J. Y.; Lee, C.; Love, D. C.; Sedlak, D. L.; Yoon, J.; Nelson, K. L. Inactivation of MS2 coliphage by ferrous ion and zero-valent iron nanoparticles. *Environ. Sci. Technol.* **2011**, *45*, 6978–6984.
17. Bedner, M.; MacCrehan, W. A.; Helz, G. R. Making chlorine greener: Investigation of alternatives to sulfite for dechlorination. *Wat. Res.* **2004**, *38*, 2505–2514.
18. Hozalski, R. M.; Zhang, L.; Arnold, W. A. Reduction of haloacetic acids by Fe(0): Implications for treatment and fate. *Environ. Sci. Technol.* **2001**, *35*, 2258–2263.
19. Zhang, L.; Arnold, W. A.; Hozalski, R. M. Kinetics of haloacetic acid reactions with Fe(0). *Environ. Sci. Technol.* **2004**, *38*, 6881–6889.
20. Pearson, C. R.; Hozalski, R. M.; Arnold, W. A. Degradation of chloropicrin in the presence of zero-valent iron. *Environ. Toxicol. Chem.* **2005**, *24*, 3037–3042.
21. Xie, L.; Shang, C. Role of humic acid and quinone model compounds in bromate reduction by zerovalent iron. *Environ. Sci. Technol.* **2005**, *39*, 1092–1100.
22. Odziemkowski, M. S.; Gui, L.; Gillham, R. W. Reduction of *N*-nitrosodimethylamine with granular iron and nickel-enhanced iron. 2. Mechanistic studies. *Environ. Sci. Technol.* **2000**, *34*, 3495–3500.
23. Hrudey, S. E. Chlorination disinfection by-products, public health risk trade-offs and me. *Wat. Res.* **2009**, *43*, 2057–2092.
24. Krasner, S. W.; Weinberg, H. S.; Richardson, S. D.; Pastor, S. J.; Chinn, R.; Sclimenti, M. J.; Onstad, G. D.; Thruston, A. D., Jr. Occurrence of a new generation of disinfection byproducts. *Environ. Sci. Technol.* **2006**, *40*, 7175–7185.
25. Giasuddin, A. B. M.; Kanel, S. R.; Choi, H. Adsorption of humic acid onto nanoscale zerovalent iron and its effect on arsenic removal. *Environ. Sci. Technol.* **2007**, *41*, 2022–2027.
26. Dries, J.; Bastiaens, L.; Springael, D.; Agathos, S. N.; Diels, L. Competition for sorption and degradation of chlorinated ethenes in batch zero-valent iron systems. *Environ. Sci. Technol.* **2004**, *38*, 2879–2884.
27. Gu, B.; Schmitt, J.; Chen, Z.; Liang, L.; McCarth, J. F. Adsorption and desorption of natural organic matter on iron oxide: Mechanisms and model. *Environ. Sci. Technol.* **1994**, *28*, 38–46.
28. *Water On Tap: What You Need to Know*; EPA-816-K-09-002; U.S. Environmental Protection Agency: Washington, DC, December, 2009.

29. *Stage 2 National Primary Drinking Water Regulations: Disinfectants and Disinfection Byproducts Rule*; EPA-HQ-OW-2002-0043; U.S. Environmental Protection Agency: Washington, DC, January, 2006.
30. Kristiana, I.; Joll, C.; Heitz, A. Powdered activated carbon coupled with enhanced coagulation for natural organic matter removal and disinfection by-product control: Application in a western Australian water treatment plant. *Chemosphere* **2011**, *83*, 661–667.
31. Chen, W.; Parette, R.; Sheehan, W.; Cannon, F. S.; Dempsey, B. A. *Arsenic Removal with Iron-Tailored Activated Carbon Plus Zero-Valent Iron*; WERC and Water Research Foundation: Denver, CO, 2010.
32. Ponder, S. M.; Darab, J. G.; Mallouk, T. E. Remediation of Cr(VI) and Pb(II) aqueous solutions using supported, nanoscale zero-valent iron. *Environ. Sci. Technol.* **2000**, *34*, 2564–2569.
33. *Research Report on Investigation of the Capability of Point-of-Use/Point-of-Entry Treatment Devices as a Means of Providing Water Security*; EPA/600/R-06/012; U.S. Environmental Protection Agency: Washington, DC, February, 2006.
34. Chiu, P. C.; Jin, Y. *Filtration Media Coated with Zero-Valent Metals, Their Process of Making, and Use*. USPTO Patent Application No. US 2011/0139726.
35. Mackenzie, K.; Schierz, A.; Georgi, A.; Kopinke, F.-D. Colloidal activated carbon and carbo-iron–novel materials for in-situ groundwater treatment. *Global NEST J.* **2008**, *10*, 54–61.
36. Hoch, L.; Mack, E.; Hydutsky, B.; Hershman, J.; Skluzacek, J.; Mallouk, T. Carbothermal synthesis of carbon-supported nanoscale zero-valent iron particles for the remediation of hexavalent chromium. *Environ. Sci. Technol.* **2008**, *42*, 2600–2605.
37. Li, A.; Tai, C.; Zhao, Z.; Wang, Y.; Zhang, Q.; Jiang, G.; Hu, J. Debromination of decabrominated diphenyl ether by resin-bound iron nanoparticles. *Environ. Sci. Technol.* **2007**, *41*, 6841–6846.
38. Elliott, M. A.; Stauber, C. E.; Koksal, F.; DiGiano, F. A.; Sobsey, M. D. Reductions of *E. coli*, echovirus type 12 and bacteriophages in an intermittently operated household-scale slow sand filter. *Wat. Res.* **2008**, *42*, 2662–2670.

Chapter 15

Decentralized Wastewater Treatment for Distributed Water Reclamation and Reuse: The Good, The Bad, and The Ugly—Experience from a Case Study

**A. L. Prieto,[1] D. Vuono,[1] R. Holloway,[1] J. Benecke,[1] J. Henkel,[1]
T. Y. Cath,[1] T. Reid,[2] L. Johnson,[2] and J. E. Drewes*,[1]**

**[1]NSF Engineering Research Center *ReNUWIt*, Department of Civil and
Environmental Engineering, Colorado School of Mines, 1500 Illinois Street,
Golden, Colorado 80401, United States
[2]Aqua-Aerobic Systems, Inc., Rockford, Illinois 61111, United States
*E-mail: jdrewes@mines.edu**

Cities worldwide are facing a growing water crisis with challenges from climate change, population growth, and deteriorating infrastructure that threatens economic development, social welfare, and environmental sustainability. New strategies are needed for water/wastewater treatment and distribution that will reduce the need to pump water over long distances and provide opportunities to reuse wastewater locally. A full-scale pilot hybrid sequencing batch membrane bioreactor (SBMBR) wastewater treatment system serving 400 residential units at Colorado School of Mines (Colorado) was used as a case study to assess the technical feasibility of using the SBMBR process as a sustainable approach for onsite water reclamation and reuse of domestic wastewater effluents. The system was first tested in its capability to produce an effluent quality adequate for landscape irrigation applications. Further, the authors examined the applicability of the SBMBR as a decentralize treatment technology in terms of local water demand, infrastructure requirements, energy consumption and environmental impact. The technical challenges related to the operation of the SBMBR were also evaluated. Findings

In Novel Solutions to Water Pollution; Ahuja, S., et al.;
ACS Symposium Series; American Chemical Society: Washington, DC, 2013.

of this study demonstrated that the SBMBR system had the operational flexibility to generate effluent qualities that differed with respect to nitrogen concentrations tailored to local needs. These were generated within a few days without major system disturbances or negative impact on membrane fouling. Similar to other decentralized treatment technologies, the application of the SBMBR for water reuse purposes is challenged by uneven/seasonal local water needs, use-specific distribution systems, and energy requirement for treatment. The largest challenge for implementation of decentralized systems is the need for a much better process control that can lead to "smarter" SCADA systems for remote operation.

Introduction

In 2005, a total of 410 billion gallons per day were withdrawn from different sources or fresh water in the United States. While public supply and domestic uses correspond to approximately 12% of this water (48 billion gallons per day) (*1*), it is safe to assume that the majority is disposed as wastewater. To protect public and environmental health, the volumes of wastewater are treated every day in centralized wastewater treatment plants (CWWTP) meeting effluent discharge standards that require reduction of organic matter and nutrients. Considering the resources trapped in wastewater (i.e., water, energy, and nutrients), most CWWTP do not engage in recovering these resources (*2*).

Adding to that, the water demand for irrigation and industrial activities in the U.S. have exceeded 146 billion gallons per day. Irrigation (agricultural and urban) consumed an estimated 31 percent of the total water uses in the U.S. in 2005 (*1*), yet, local outdoor water use may be as high as 70 percent of the total residential water uses (*3*). In the United States, turfgrass represents the predominant component of urban landscapes and is the single largest irrigated crop in the U.S. (*4*). Turfgrass areas include residential lawns, commercial plantings, public roadside areas, parks, athletic fields, cemeteries and golf courses. With the exception of turfgrass grown in wet humid regions, the majority of turfgrass areas receive supplemental water at least during peak summer months (*3*). Among the fertilizing nutrients in turfgrass, nitrogen is present in greatest quantities and must be applied routinely for a quality stress tolerant turfgrass (*5*). Nitrogen application further accounts for the highest cost of a turfgrass fertilization.

Managing and preventing the excessive use of freshwater resources becomes a major concern. Fortunately, a feasible opportunity to cope with the current water supply needs lies in water reclamation and reuse (*6*). Water reuse practices are well established in the U.S. and elsewhere, providing water for numerous activities, such as irrigation, industry and potable supply. However, water reuse accounts only for less than 1 percent of the national water use in the U.S. (*6*). With many communities already overcommitting or approaching the limits of their locally available freshwater supplies, water reuse has become an attractive and many places sole option for conserving and extending available water supplies (*7*).

As a recognized and cost-effective alternative to CWWTP, decentralized treatment offers a wide array of treatment technologies, which could be effectively integrated into urban and rural settings (*8*). For example, different types of decentralized treatment technologies, such as soil treatment units, packed-bed biofilters, constructed wetlands, or membrane bioreactors (MBRs), can produce high quality effluent for local reuse. Historically in the U.S., distributed systems were used as a temporary treatment option for rural and sub-urban communities until the developments could be tied into the public sewer network serving a CWWTP. Since these systems were not designed for permanent use with specific aims to achieve treatment and reuse objectives, inadequate management and performance deficiencies led to the perception that these systems were not reliable (*9*). However, with increasing environmental consciousness and advancements in the science and standard-of-practice, the utility of decentralized treatment systems as a permanent component of a sustainable water infrastructure are now being recognized (*9*, *10*). Nonetheless, it is unrealistic that centralized water and wastewater treatment will ever become obsolete. Instead, a diverse and flexible urban water portfolio that integrates many treatment options (e.g., flexible and robust treatment technologies, stormwater management, energy and nutrient recovery, and water conservation at various scales) should be considered. Distributed systems that integrate decentralized treatment and centralized conveyance are already recognized as a promising and sustainable approach for urban, suburban and rural water challenges (*11*).

On-site water reclamation provides a local resource that could prevent the high costs of importing freshwater and conveying it over a long distance or high elevation differences (*12*). In fact, the high cost associated with water conveyance is not only determined by the energy employed in pumping and distribution. As the water distribution network reaches the end of its design life, the replacement and expansion of the current infrastructure has been estimated to cost up to $1 trillion over the next 25 years (*13*).

Another advantage of distributed treatment systems is related to their proximity to the final reuse application. This proximity offers the opportunity that the reclaimed water quality can be *tailored* to local needs, such as landscape irrigation, groundwater recharge, streamflow augmentation, or service water used in households (e.g., toilet flushing). The concept of *tailored water* is then conceived as an alternative to meet effluent discharge standards or simply finding a beneficial use for large volumes of wastewater effluents, as currently practiced by most CWWTP. One main characteristic that defines a tailored water system is its required flexibility. The treatment technology should be capable to provide various qualities of water depending upon costumer demand. Treatment performance, in this case, plays an important role in the cost-effectiveness of the system. In contrast, a CWWTP can also provide a specific water quality for specific reuse applications, but this practice comes with significant increases in capital and operational costs for the new treatment process, which is only cost effective for a year round application with similar demand.

It is clear that decentralized systems offer significant advantages for local tailored water reuse. However, additional operational challenges arise, compared to those offered by centralized systems, depending on the complexity of the treatment technology employed. In this study, a decentralized water reclamation system was investigated. The system was tested to produce water tailored for local urban irrigation needs. The applicability of this system as a decentralized water reclamation technology, as well as barriers to its implementation and technical challenges encountered in its operation, are discussed in this chapter.

Methodology

The decentralized hybrid sequencing batch/membrane bioreactor (SBMBR) facility (Aqua-Aerobic Systems, Inc., Rockford, IL, USA) is located on the Colorado School of Mines campus in Golden, Colorado, USA. This facility receives raw wastewater from about 400 units of the Mines Park Student Housing Complex (MPSHC) through a sewer diversion (Figure 1). During the course of this study, influent wastewater entered a 9.5 m^3 (2,500 gallons) underground holding tank, and a submerged grinder pump transferred mixed sewage to the demonstration-scale SBMBR system in 1.14 m^3 (300 gallon) batches, which were screened (3 mm) prior to entering one of two bioreactors. Mixing and aeration were provided by a submersible centrifugal pump with bi-directional jet nozzles and two coarse bubble aerators on the bottom of each SBR, respectively. The two bioreactor tanks were paired with two submerged membrane tanks each containing a PURON® hollow fiber ultrafiltration membrane cassette (Koch Membrane Systems, KMS, Wilmington, MA). Each membrane cassettes contained 9 bundles with a total of 31 m^2 surface area. The characteristics of the membranes used in this study are summarized in Table 1. The membrane cassettes were intermittently aerated during operation through a diffuser nozzle located at the center of each bundle of fibers. Frequent backwashing was provided to control the transmembrane pressure (TMP). The SBMBR is equipped with a supervisory control and data acquisition (SCADA) system which enables the operator to monitor and control process parameters and equipment.

SBMBR influent was characterized by COD, sCOD, NH_4-N and ortho-P concentrations in mg/L ranging from 270-560, 110-210, 24-37, and 8-16, respectively. Influent wastewater was subjected to SBR cycles consisting of a non-aerated fill stage (Mix/Fill), an intermittently-aerated fill stage (React/Fill), and an intermittently aerated discharge phase (React/Draw) (Figure 2). When one bioreactor was in Mix/Fill or React/Fill mode, activated sludge was pumped from the second bioreactor (React/Draw) to the shared membrane tanks for permeate production and sludge recycle via gravity. The total cycle lasted two hours, allowing the continuous permeate production and the treatment of 24 batches per day (for a total of 7200 gal/day). The dissolved oxygen concentration (DO) in the SBRs was set at 0.6 mg/L and controlled by in-line feedback dissolved oxygen (DO) measurements in the SBRs.

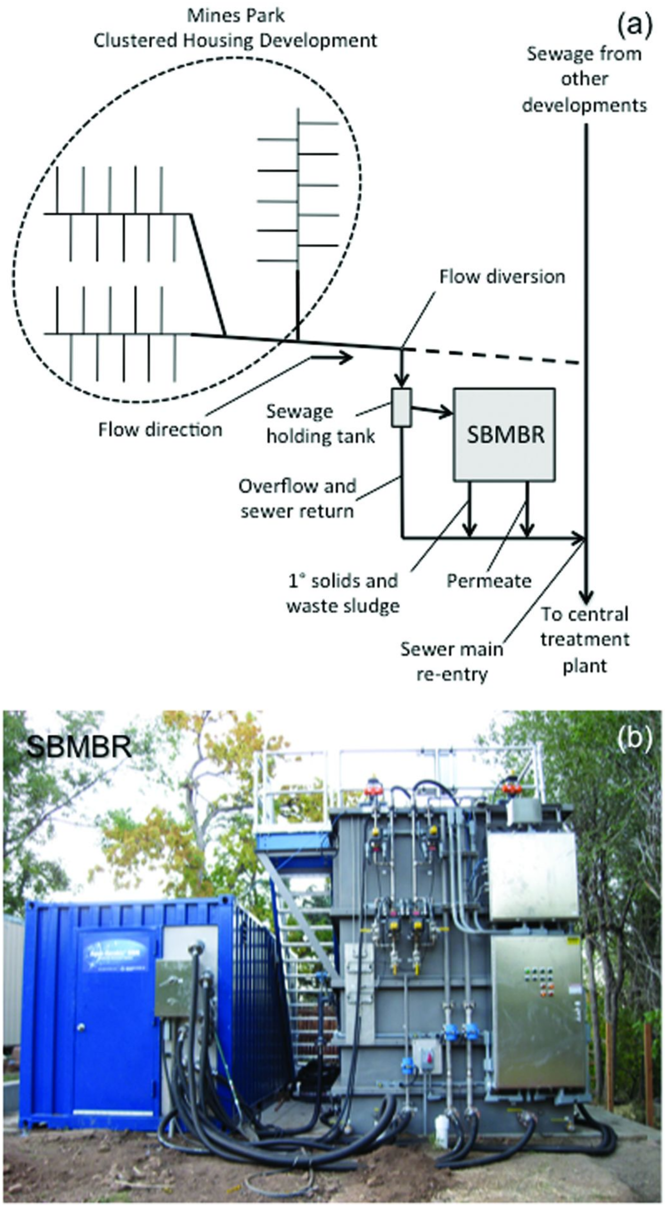

Figure 1. Schematic of the process flow (a). Photograph of the SBMBR (b).

Table 1. Select SBMBR System Parameters and PURON® Membrane Properties and Operating Parameters

SBMBR		*PURON® Membranes*	
Parameter	*Value*	*Parameter*	*Value*
Total SBR Volume	17.5 m^3	Nominal Pore Size	0.05 µm
Total MBR Volume	6.4 m^3	Membrane Surface Area	61.3 m^2
Recirculation Flow (RAS)	76 L/min	Membrane Material	PVDF
Volume exchange ratio (VER)	10%	Permeate Flow Direction	Outside-In
		Driving Force	Vacuum
		Net Design Flux	19 L/(m^2h)
		Permeate Mode Duration	300 s
		Backflush Mode Duration	20 s

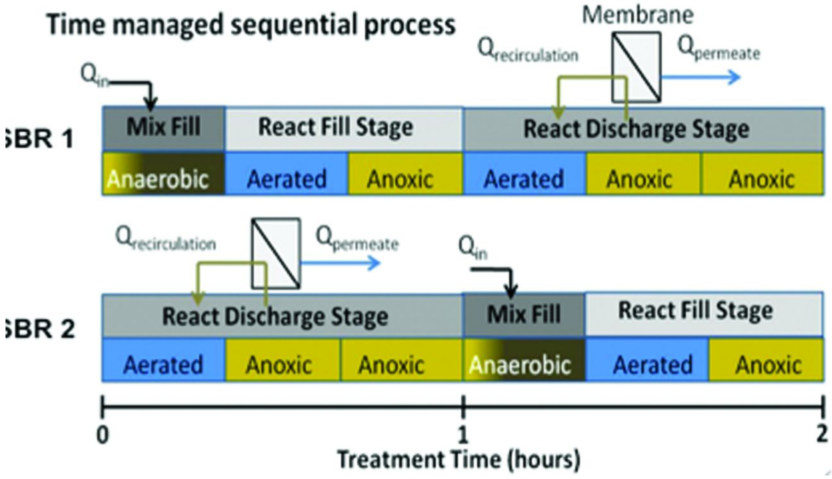

Figure 2. Treatment cycle of the two parallel SBRs. The cycle consists of 3 treatment stages (Mix Fill, React, Fill and React Draw/Discharge). During React Fill and React Draw, intermittent aeration steps are provided to allow oxic and anoxic conditions in the reactors.

Operating Conditions for Tailored Water Reuse

To produce water of various qualities, two treatment approaches were evaluated. First, the system was operated to completely remove organic matter and nutrients from the influent. The SBMBR system was operated at a wastewater exchange rate of 10 percent, thus a 90 percent removal of nitrogen was expected. The first aeration set up, aeration setup 1, featured an initial non-aerated Fill/React period of 20 min, followed by aeration and an additional second non-aerated phase, finalizing with a non-aerated period to assure anoxic conditions for the subsequent treatment cycle (Figure 2). The sludge retention time (θ_x) and MLSS were 35 days and 5.1 ± 0.4 g/L, respectively.

Second, the SBMBR was operated to produce water with concentrations of nitrogen suitable for landscape irrigation. Four experiments to retain NO_3-N in the effluent were conducted at $\theta_x \geq 35$ d, testing different lengths of aeration setups. The major difference in the aeration setups lies in the total duration of the non-aerated treatment periods. Setups 2 and 3 featured an initial non-aerated Fill/React period of 3 min and 6 min, respectively, followed by continuous aeration (full aeration) and a final 5 min non-aerated period to assure anoxic conditions for the subsequent treatment cycle. In contrast, setups 4 and 5 (9 min and 6 min Fill/React period) offered an additional second non-aerated phase, which allowed for further denitrification to occur (intermittent aeration). In between the tailored water experiments, the SBR aeration setup was reset to full-denitrification (i.e. set up 1). Table 2 summarizes the aeration set-ups tested in this study.

Table 2. Summary of the SBMBR Aeration Set-Ups Tested in This Study

Aeration setups	*Phase duration in a 2 hr cycle (min)*				
	Anoxic	*Oxic*	*Anoxic*	*Oxic*	*Anoxic*
(1) 20 minutes anoxic + intermittent aeration	20	25	20	30	25
(2) 3 minutes anoxic + continuous aeration	3	62	–	50	5
(3) 6 minutes anoxic + continuous aeration	6	59	–	50	5
(4) 6 minutes anoxic + intermittent aeration	6	39	20	45	10
(5) 9 minutes anoxic + intermittent aeration	9	36	20	45	10

Results and Discussion

The Good: Advantages of Distributed Water Reclamation and Reuse

The Mines Park SBMBR hybrid system has been put to the challenge to produce various effluent qualities that are tailored to local needs (i.e., fully denitrified effluent for streamflow augmentation or groundwater recharge in the winter and non-nitrified effluent for landscape or agricultural irrigation in the summer). This tailored water approach is challenging for several reasons. First, in times when the effluent is not needed for landscape irrigation, the water quality has to comply with effluent discharge regulations, which require sufficient carbon and nutrient removal. Second, if the effluent is periodically used for agricultural irrigation, although nutrient removal is not desired, certain hygienic aspects have to be met. And third, in the case the water is reused for urban landscape irrigation or toilet flushing, both nutrient removal and hygienic aspects have to be considered.

Our first step towards this approach to generate different effluent qualities using the same treatment system was to determine the maximum nutrient removal potential of a SBMBR system without adding chemical coagulants. Under aeration set-up 1, the SBMBR efficiently removed COD, nitrogen (TN), and phosphorous (TP) by more than 97 percent, 95 percent and 90 percent removal, respectively.

For tailored water generation, some operational variables were drastically changed in the SBMBR, mostly to demonstrate the flexibility and resilience of the system. The strategy to tailor the SBMBR effluent was to limit denitrification through changes in the SBR aeration setup and thus retaining NO_3-N in the treated effluent (Table 2). The experimental period investigating tailored water generation through the limitation of denitrification is illustrated in Figure 3.

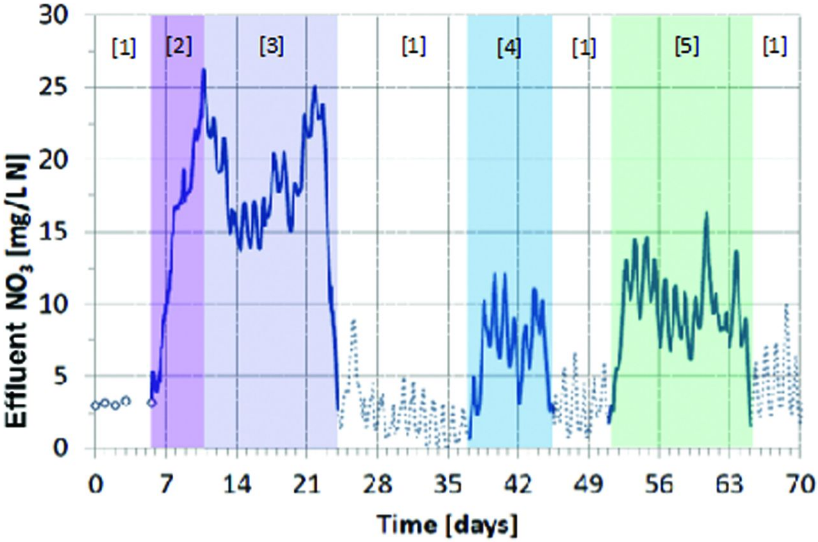

Figure 3. Effluent nitrate concentration at different aeration settings $\theta_x \geq 35$ d. Aeration setups are [1] 20 minutes anoxic + intermittent aeration, [2] 3 minutes anoxic + full aeration, [3] 6 minutes anoxic + full aeration, [4] 9 minutes anoxic + intermittent aeration, and [5] 6 minutes anoxic + continues aeration. The dotted lines indicate when the system is left to recover to the initial performance or aeration setup [1].

The SBMBR responded immediately to the change of the aeration setup from 1 to 2. Effluent NO_3-N concentrations ($[NO_3\text{-}N]_e$) increased steadily and reached values of > 26 mg/L NO_3-N after 4 days. At this time, $[NO_3\text{-}N]_e$ was still increasing. However, the pH dropped drastically to a value of 5.0 after two days. Because of adverse impacts on the microbial community associated with low pH values, the aeration setup was changed to 3. After three days, aeration set up 3 allowed $[NO_3\text{-}N]_e$ of 15.3 ± 1.1 mg/L NO_3-N and a pH of 5.8 ± 0.3. Since nitrification is the most pH-sensitive biological process in the system, it is expected that the process rate will decrease significantly at pH values below the neutral range (*14*, *15*). Although effective in producing tailored water with high NO_3-N concentration, set ups 2 and 3 were not considered sustainable.

Two additional aeration setups (4 and 5) were tested that featured a shortened Fill/React period in the beginning of the cycle (6 min and 9 min), but maintained a second non-aerated treatment period starting after 45 min (Figure 2). As expected, operation of the SBMBR under 4 resulted in an immediate increase of $[NO_3\text{-}N]_e$ from 1.3 ± 1.0 mg/L NO_3-N to 8.1 ± 2.0 mg/L NO_3-N within two days. pH remained stable at 6.6 ± 0.1. Full denitrification was recovered within a day after aeration was changed back to 1 with an average $[NO_3\text{-}N]_e$ of 3.0 ± 1.3 mg/L NO_3-N. The response of the system to the change of 1 to 5 was similar. $[NO_3\text{-}N]_e$ increased to values of 10.3 ± 2.2 mg/L NO_3-N within one day while pH remained stable at 6.6 ± 0.2. The operation of the system could be easily changed back to full denitrification performance without affecting initial removal efficiencies (i.e., 97%, 95% and 90% percent removal for COD, TN and TP, respectively). A summary of the effluent concentrations tested in this study are presented in Table 3.

Tailored effluent NO_3-N concentrations could be generated in the Mines Park facility within less than 48 hours by tuning the duration of the Fill/React period of the SBMBR. This flexibility and the quick response behavior of the SBMBR are fundamental when aiming for several water reuse applications in an urban setting (e.g. irrigation and toilet flushing).

Table 3. Summary of the SBMBR Nitrate Effluent Concentrations at the Operational Set-Points Tested in This Study

Aeration setups	*Effluent concentrations (mg NO_3-N/L)*
SBMBR Influent	<1
(1) 20 minutes anoxic + intermittent aeration	1.3 ± 1.0
(2) 3 minutes anoxic + continues aeration	> 26
(3) 6 minutes anoxic + continues aeration	15.3 ± 1.1
(4) 6 minutes anoxic + intermittent aeration	8.1 ± 2.0
(5) 3 minutes anoxic + intermittent aeration	10.3 ± 2.2

The Bad: Barriers to Implementation of Decentralized Treatment and Distribution

In a recent report published by the National Research Council, the current challenges of implementing water reuse practices in United States were discussed with regard to the advancement and implementation of new technologies, to public education, conservation, and sociopolitical factors (*6*). The system at Mines Park is not oblivious to these challenges. From a more technical perspective, some of the limiting factors for water reuse applications can be easily identified in our case study.

Uneven Seasonal Demand and Treatment Requirements

As one component of the decentralized treatment tool-kit, an SBMBR hybrid configuration can be operated with flexibility such that effluent quality can be tailored to local or seasonal needs. But with local or seasonal water needs, demand may be irregular or uneven, which would result in plants that are operating below capacity over extended periods of time or require additional treatment processes that can be brought online if needed. If secondary effluent is suitable for surface discharge than stream augmentation may be an appropriate option. But if secondary effluent has elevated nitrate concentrations for landscape irrigation than a separate treatment train may be needed to remove nutrients from tailored water. Otherwise storage capacity would be needed to supply water for later use. Separate treatment trains may include constructed or existing wetlands or soil-aquifer treatment, all of which require additional capital costs, land area, expertise, and operation and maintenance costs.

Dual Distribution Systems Costs

In addition to uneven seasonal demand and excess treatment capacity, conveyance systems to facilitate local reuse may be costly in retrofit a decentralized application such as the Mines Park site. Reuse can take shape in a number of ways, which would require different infrastructure for different reuse applications. For example, reuse for household service water, such as toilet flushing, would require a dedicated in-house piping system beyond a conveyance system needed for other reuse applications, such as landscape irrigation. In-house retrofits would not likely be economically feasible for existing developments. However, if reuse is planned for new developments, infrastructure costs can be factored into the overall design along with a time frame to recover capital investments through resource recovery. Thus, a major barrier for implementing a distribution system for reclaimed household service water is the economic cost of retrofitting existing infrastructure. On the other hand, exterior retrofits, such as drip-irrigation within green-space, can be installed unobtrusively. The only major barrier to implementation, both economically and socially, would be costs of installing conveyance systems across roadways, which could also lead to the inconvenience of road closures for occupants.

Energy Demand

The specific energy demands of usually less than 1 kWh/m^3 of water treated for full-scale centralized MBRs are comparable to conventional activated sludge plants if process optimization is achieved (*16*, *17*). However, MBRs scaled to decentralized applications have yet to reach cost-effective energy demands. In an energy audit of major system components, the Mines Park SBMBR system showed disproportionate energy consumption by mixing devices (>50%), rather then aeration (25%) (Figure 4), which is likely a function of scale and key process components selected. At times, the overall specific energy demand reached as high as 5 kWh/m^3 water treated. It is important to note that the SBMBR configuration was initially designed to ensure system robustness as a prototype installation. Identification of major energy consuming devices has thus helped to guide more efficient design by replacing the initial 2.4 horsepower (HP) submersible centrifugal mixing pumps with more energy efficient paddle mixing devices. Nonetheless, wastewater treatment at such a small scale (7,200 gal/day) is subject to "scale-down" effects and these results suggest that the market for energy efficient devices is not yet fully developed (*18*). Cost savings would be gained at the system level by a need for smaller conveyance systems to distribute to reclaimed water and lower pumping costs, not counting the benefits by using less potable water for the same application.

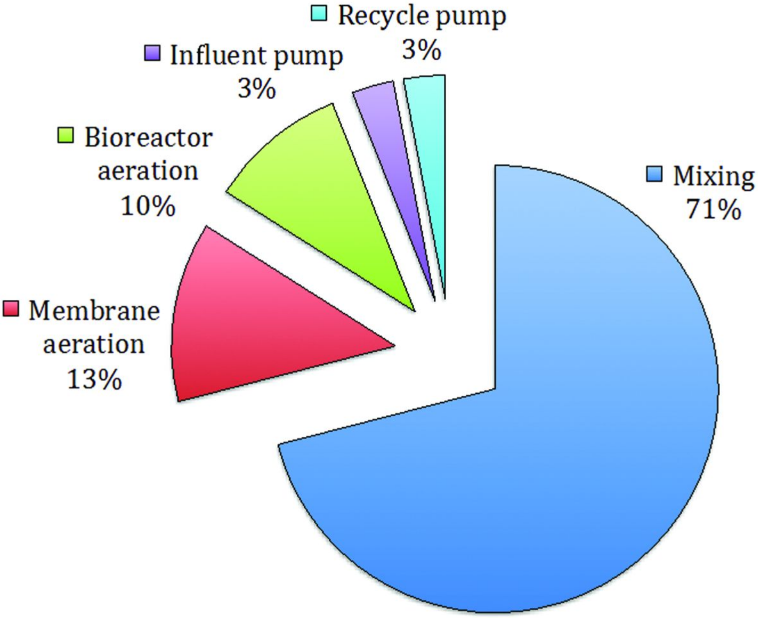

Figure 4. Energy consumption by consumer in in the SBMBR.

Environmental/Ecological Impacts

High-performance treatment technologies such as hybrid SBMBR treatment systems have great potential for recovering reclaimed water and nutrients. The recovery of water and nutrients for onsite reuse, streamflow augmentation, and/or groundwater recharge within the urban environment can greatly enhance the environmental and ecological health of aquatic systems within and outside of urban environments. However, the specific energy demand of distributed high-performance treatment solutions remains as the major barrier to implementation and are not currently economically and environmentally viable as a long-term solution. However, a detailed Life-Cycle Assessment (LCA) that includes the benefits from reuse and provides a system-level assessment considering treatment, conveyance, and associated carbon footprints may improve long-term outlook and improve investor confidence, economics, and environmental viability of decentralized water infrastructure.

The Ugly: Operational Challenges of Decentralized Systems

In this section, the operational and mechanical requirements of the SBMBR are examined from the viewpoint of the operators that have been monitoring and maintaining the Mines Park decentralized plant over the last four years.

Effect of Environmental Conditions

The temperature in the Colorado Front Range can vary greatly throughout the year. The average low and high temperatures for the summer are 14°C and 29°C and for the winter months are -8°C and 6°C. The SBMBR was designed and built to be operated outside as it was equipped with weatherproof enclosures but not necessary for cold weather operation. The system piping was insulated, heat traced, and PVC pipe sections were replaced with stainless steel before the first winter of operation. These precautions were successful in protecting many of the system components during the coldest Colorado winter months. However, brass ball valves and a short PVC pipe stub that were exposed to the elements caused serious operational problems (Figure 5).

The systems brass ball valves would freeze during cold snaps, thereby, preventing them from being automatically actuated. In one severe case, a brass ball valve cracked (Figure 5). Operators, armed with heat guns, would be forced to address the frozen actuators at all hours, day or night. PVC pipes are also sensitive to drastic changes in temperature, which can cause pressure losses, spills, and, in the worst-case scenario, shut down the system.

The subfreezing temperatures not only impact the system performance but required immediate operator attention. Furthermore, system failures oftentimes occurred late at night when the temperatures were the lowest. A large insulated structure was then constructed around the SBMBR to alleviate the mechanical and operational strains caused by the environmental conditions (Figure 6). Although the system performed admirably while operating outside, the designs for similar systems in similar climates should include appropriate weather protection. This will significantly decrease the burden on the system and operation staff and increase system reliability.

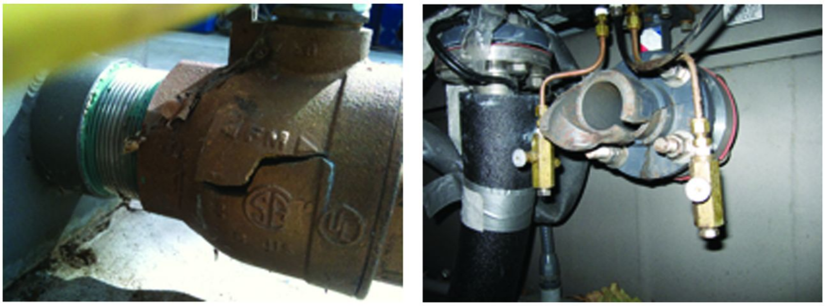

Figure 5. Brass ball valve (left) and PVC pipe stub (right) broken due to freezing temperatures.

Figure 6. SBMBR before (left) and after (right) the construction of the weather protection structure.

Monitoring

Since the system was automated and controlled by a supervisory control and data acquisition (SCADA) system, a series of sensors were continuously monitoring the reactor's performance. When some of the real-time operational values differed from the set design values, or there was a malfunction in the system; the SCADA system run an alarm and notified the operators through an auto-dialer. Depending on the severity of the case, the alarms varied from minor to major. Minor alarms included low influent flow, low RAS flow, low permeate tank level, high permeate turbidity, among others. These alarms did not trigger the system's auto-dialer and generally did not require immediate operator's attention. Alternatively, major alarms will engage the auto-dialer and require immediate operator attention. The frequency of major alarms can range from once every couple of months to a couple of times in a month. Standard major alarms included very low influent flow, low bioreactor level, high TMP, and membrane shutdown. These alarms can occur for a multitude of reasons including both mechanical failure and operator's error. Low-low influent flow can be caused by influent grinder pump wear (mechanical failure) or failure to turn the pump back on after maintenance (operator's error). Diagnosing more complex alarms (e.g., membrane shutdown) required extensive operational experience. Furthermore, correcting such alarms generally require staff with operational and maintenance experience to perform the necessary repairs.

Maintenance Requirements

Routine maintenance was conducted on a daily, weekly, and monthly basis to system's components such as the influent sump, the influent screening collection system, membrane influent line, and online probes all require regular maintenance and/or calibration. Solids can easily accumulate and clog the influents lines, which in most cases required manual cleaning. Online probes must be maintained and calibrated on a routine basis due to the unpredictable and variable nature of the waste strength.

Some components of the system under continuous usage and wearing require repair more often than others. These components include the influent submersible pump (with a grinder), hollow-fiber membranes, low-pressure blowers, and oil-less air compressor. In particular, the influent pump is exposed to the harshest conditions. Its failure was typically associated with the blade wear or improper installation of the blade. Maintenance of this pump normally required at least two operators to pull the pump from the sump, to remove any fibrous material (i.e., hair, paper towels, tissue, dental floss) from the grinder, and to inspect and assure. The SBMBR operated without any influent flow during the pump repair. Ideally, similar systems should be equipped with a redundant influent pump so that pump maintenance can be performed without disrupting system operation.

The hollow-fiber membranes generally operated without flaw unless another system parameter fell outside of its design criteria. The primary system parameters that can significantly affect membrane fouling were the membrane tank solids concentration (TSS) and membrane air scour flow. Extended operation of the system with these parameters being outside of design specification will result in membrane sludging (Figures 7). After sludging, the membrane cassettes had to be cleaned manually, which includes separating the membrane fibers by hand and rinsing them with low-pressure water.

Figure 7. Hollow-fiber membranes after a sludging episode (left). Operator cleaning sludged membranes (right).

Low-pressure blowers supply air for membrane air scouring and bioreactor oxygen demand. The blowers can overheat and fail during summer months operation. Without the blowers, membrane sludging is imminent, not to mention that the bioreactors can turn anaerobic.

Conclusions

The operation of a decentralized wastewater treatment facility to generate effluent of high quality for water reclamation is challenging. The modification of the SBR aeration setup and the induced prevention of denitrification proved to be a promising strategy to recover water and nitrogen from domestic wastewater. The SBMBR proved to be a flexible and robust treatment technology for tailored water reuse applications and landscape irrigation in particular. However, mayor challenges to implementation of this technology are related to the uneven year round demand for reclaimed water, distribution infrastructure for specific end-user, and the energy consideration inherent to decentralized treatment technologies (i.e., scale down effect).

While the system was able to generate highly flexible effluent qualities on demand, it requires close supervision and proper maintenance. The complexity of the system requires a deeper understanding of the process and its dependencies than usually required for larger-scale installations that are staffed 24/7. This knowledge should be integrated into a smart SCADA system that appropriately responds to out-of-specification behavior before the system fails or triggers major maintenance issues. Operational strategies need to be developed that can address any equipment deficiencies or failures that can have a detrimental effect on the produced water quality and quantity including early warning systems that would facilitate a remote operation of highly complex distributed water reclamation facilities.

References

1. Kenny, J. F.; Barber, N. L.; Hutson, S. S.; Linsey, K. S.; Lovelace, J. K.; Maupin, M. A. *Estimated Use of Water in the United States in 2005*; USGS Circular 1344; U.S. Geological Survey: Reston, VA, 2009.
2. Wilderer, P. A. Sustainable water management in rural and peri-urban areas: What technology do we need to meet the UN millennium development goals? *Water Sci. Technol.* **2005**, *51* (10), 1–6.
3. Leinauer, B.; Devitt, D. A. *Irrigation Sci. Technol.* **2012**, in press.
4. Milesi, C.; Elvidge, C. D.; Dieta, J. B.; Tuttle, B. T.; Nemani, R. R.; Running, S. W. A strategy for mapping and modeling the ecological effects of US lawns. *J. Turfgrass Manage.* **2005**, *1*, 83–97.
5. Carrow, R. N.; Waddington, D. V.; Rieke, P. E. *Turfgrass Soil Fertility and Chemical Problems: Assessment and Management*, 1st ed.; Sleeping Bear Press: Chelsea, MI, 2002.

6. National Research Council of the National Academies. *Water Reuse: Expanding the Nation's Water Supply Through Reuse of Municipal Wastewater*; The National Academies Press: Washington, DC, 2012.
7. Asano, T; Burton, F.; Leverenz, H.; Tsuchihashi, R.; Tchobanoglou, G. *Water Reuse: Issues, Technologies, And Applications*, 1st ed; McGraw-Hill: New York, 2007.
8. *Guidelines for Water Reuse*; U.S. Environmental Protection Agency: Washington, DC, 2004.
9. Siegrist, R. L; Lowe, K. S.; McCray, J. E.; Munakata Marr, J.; Drewes, J. E.; Spear, J. R.; Tomaras, J. M. B. *Advancing the Science and Engineering and Integration of On-Site Wastewater Systems*. Proceedings of the Onsite '07 International Conference, Armidale, Australia, 2007; pp 27−34.
10. Daigger, G. T. Evolving urban water and residuals management paradigms: Water reclamation and reuse, decentralization, and resource recovery. *Wat. Environ. Res.* **2009**, *81* (8), 809–823.
11. D'Amato, V.; Clerico, E.; Dietzmann, E.; Clark, M.; Striano, E. When to consider distributed systems in an urban and suburban context. *Proc. Water Environ. Fed. Annu. Conf. Expo.* **2009**, *20*, 5441–5460.
12. Levine, A. D.; Asano, T. Peer reviewed: Recovering sustainable water from wastewater. *Environ. Sci. Technol.* **2004**, *38* (11), 201A–208A.
13. *Buried No Longer: Confronting America's Water Infrastructure Challenge*; AWWA Report; American Water Work Association: Denver, CO, 2012.
14. *Manual: Nitrogen Control.* U.S. Environmental Protection Agency, Office of Water: Washington, DC, 1993.
15. Henze, M.; van Lossdrecht, M. C. M.; Ekama, G. A. and Brdjanoviv, D. *Biological Wastewater Treatment: Principles, Modeling, and Design: Principles, Modelling and Design*, 1st ed; IWA Publishing: London, UK, 2008.
16. Krzeminski, P.; Langhorst, W.; Schyns, P.; de Vente, D.; van den Broeck, R.; Smets, I. Y.; van Impe, J. F. M.; van der Graaff, J. H. J. M.; van Lier, J. B. The optimal MBR configuration: Hybrid versus stand-alone—Comparison between three full-scale MBRs treating municipal wastewater. *Desalination* **2012**, *284*, 341–348.
17. Lesjean, B.; Tazi-Pain, A.; Thaure, D.; Moeslang, H.; Buisson, H. Ten persistent myths and the realities of membrane bioreactor technology for municipal applications. *Water Sci. Technol.* **2011**, *63* (1), 32–9.
18. Stüber, J.; Schallehn, F.; Lüdicke, C.; Lesjean, B.; Gnirss, R.; Kraume, M. Economical Evaluation of Decentralized MBRs Achieving Varying Effluent Qualities. *IWA World Water Congress 2010*; Montreal, Canada.

Editors' Biographies

Satinder Ahuja

Satinder Ahuja (Ph.D. from the University of Sciences in Philadelphia) worked at Novartis Corporation for 25 years in various leadership positions and simultaneously served as adjunct professor for several universities. For the last decade, he has been helping solve arsenic contamination of groundwater problem in Bangladesh, India, and the United States. As a founder of Ahuja Academy of Water Quality at UNC Wilmington, he encourages research on various water quality issues. His books include *Monitoring Water Quality* (in press), *Handbook of Water Purity and Quality* (Elsevier 2009), and *Arsenic Contamination of Water: Mechanism, Analysis, and Remediation* (Wiley 2008).

Kiril Hristovski

Kiril D. Hristovski (Ph.D. Civil and Environmental Engineering from Arizona State University) is currently an assistant professor in the College of Technology and Innovation and a senior sustainability scientist with the Global Institute of Sustainability at Arizona State University. His research focuses on environmental implications and applications of nanomaterials and developing simple and novel water treatment technologies. Since 2007, he has produced over 35 peer reviewed research articles and four patents. Dr. Hristovski is a recipient of a Fulbright Specialist Program Fellowship.

In Novel Solutions to Water Pollution; Ahuja, S., et al.;
ACS Symposium Series; American Chemical Society: Washington, DC, 2013.

Subject Index